Cations on Board, Ready for Takeoff: Using Vanadyl and Its Terminal Oxo to Probe Ligand Donor Strength in Heterobimetallic Complexes

Thesis by Claire M. Dopp

In Partial Fulfillment of the Requirements for the Degree of
Bachelor of Science with Honors in Chemistry

University of Kansas
Lawrence, KS
May 2023

Table of Contents

Acknowledgements

I have said it once, and I'll say it again: I truly do not believe that I would be where I am today if it weren't for the mentorship of James Blakemore. As a high school student freshly admitted to KU, I remember surfing through the Emerging Scholars job descriptions, trying to find one that stood out to me. After reviewing about 100 pages, the Blakemore Group was heavily weighing on my mind, as it was the only environmentally beneficial chemistry lab that was focused on sustainable energy. Fast forward months later, and I'm working with Riddhi and hearing someone different every week ask "so when are you switching your major?" Long story short, I believe James's willingness to invest in undergraduates truly changes lives, because I know it changed mine. Thank you for taking the time to invest in me, and I hope I've made (and will make) you proud.

To Riddhi and Shaun, I've gone back and forth between you two quite a bit, but I couldn't have been luckier to have the help of two graduate students. Riddhi, you taught me every reaction I needed to know for my synthetic procedure and put up with SO many questions from freshman me. You've helped get this publication over the finish line, and I'm so thankful to have your support. Shaun, we're so alike that it's scary. From working through syntheses all sophomore summer to our endless life rants, I'm really lucky to have gotten to work with you. Thanks for always checking in on me and caring about my life, and I still need to meet your daughter (really don't want to move away without that happening!)

To Blakemore Group members, present and past, thank you for everything. I know I asked for a few things over and over ("Joe, I can't remember how to change a high pressure" or "Alex, how do I baseline correct an IR") but I hope you never got too sick of me. Joe, you're a wonderful TA and an even better lab mate. Thanks for keeping an eye on me when we both knew I was

messing something up. Emily, you're a fantastic teacher. You deserve so much in this world and I hope you take everything that comes your way, because it all belongs to you. Christian, when the going gets tough, you get tougher. Your engineering-like challenges have never ceased to confuse me, but I know you'll go on to an amazing career in reactors and scary stuff like that. Alex, you're a great friend to have in the lab. Thanks for never making me feel stupid, yet always making me feel stupid. I guess that's what friends are for. Davis, you joke around yet you're so meticulous in your work, it's been so funny getting to know you. I hope the lab keeps you supplied with calendars and planners for ages. Fynn, I feel like you've finally broken out of your quiet little shell this semester. You fit in so well with the group and I believe you'll make a great leader once passed the torch. To Cecelia and Celine, I admire you girls so much. You bring so much light to the group, and your willingness to learn and be successful will take you far. Never forget your lab big sister, but you'll both be great mentors to undergrads as well. To our past members, thank you for supporting me as a younger student. It's been sad to watch you go, but I'm so proud to get to watch you and your careers from afar. Don't forget me when I call in a few years needing a job!

Thank you to my committee members, James, Misha, and Meredith: I was never quite sure if this defense would occur, but I'm very grateful to have had your support to make it happen. It's been so much fun taking classes and learning from you, and I look forward to keeping in touch and coming back to say hi.

Thank you to Dr. Justin Douglas and Sarah Neuenswander for putting up with me running to them every time something is wrong with an NMR instrument. I was never too independent in that realm, sadly. Thanks also to Dr. Victor Day and Dr. Allen Oliver for their extensive help with crystallography. This thesis is a behemoth and it's all thanks to hours spent on these structures. Thank you!

To my friends, while you will probably never read this document, it's important to mention you all. Thank you for being the glue that has kept college together through the chaos and stress. While my friends represent a wide range of majors on campus, we all work to support each other through each semester, and I'm lucky that we now get to support each other's careers.

To Keirian, you've been my absolute rock throughout all of undergrad. Meeting you was the luckiest thing that has ever happened to me, and I'm so glad we've held onto each other through all the uncertainty of the last 4 years. You're an important piece of my life and I will forever cherish getting to spend this part of my life (and hopefully a whole lot more) with you.

Finally, my family. Mom, Dad, and Maddie: thank you for supporting me since, quite literally, day 1. You've trusted me to figure things out and take the driver's seat. I know I'm a lot, but you never let it show. Thank you for supporting my career and life goals, and for always listening no matter how long I ramble on. I promise to visit often and fly you out to visit me. I love you all, and I'm so proud to be your daughter and sister.

Abstract

The coordination chemistry of heterobimetallic complexes has become a highly studied research topic in the broader field of inorganic chemistry. This can be attributed in part to the exciting opportunities that are afforded by assembly of well-defined complexes containing two (or more) different metals. In particular, it has been shown that the properties of a core metal center can be systematically varied by incorporation of secondary metal cations in close proximity. In this thesis, a possible origin of these tuning effects has been explored though use of the vanadyl moiety, $[VO]^{2+}$, as a spectroscopic and structural probe. $[VO]^{2+}$ is a paramagnetic species bearing a terminal oxo ligand that is quite chemically robust, making it ideal for use as a probe moiety. The studies presented in this thesis represent an extended examination of the origin of such tuning effects, with a particular attention paid to adapting synthesis and characterization methods to complexities that arise due to inclusion of vanadyl. Chapter 1 describes structural, spectroscopic, and electrochemical studies conducted with heterobimetallic vanadyl complexes containing a series of mono-valent cations (Cs^+, Rb^+, K^+, Na^+) and a di-valent cation (Ca^{2+}). This chapter mentions the synthesis of a heterobimetallic complex incorporating Li^+, but this compound and its speciation profile are described in detail in Chapter 2. The complex containing Li^+ appears to behave differently than the other heterobimetallic complexes reported here and thus it is described separately. Chapter 3 describes spectroscopic experimentation on heterobimetallic complexes based on the same ligand framework as those in Chapters 1 and 2 but presents expansion of our previous series of complexes to analogues containing trivalent cations (La^{3+}, Y^{3+}, Lu^{3+}). Taken together, the results assembled in this thesis paint a comprehensive picture of the tuning effects that Lewis acidic metal cations can exert on the vanadyl ion.

Chapter 1

Vanadyl as a Spectroscopic Probe of
Tunable Ligand Donor Strength in Bimetallic Complexes

This chapter is adapted from a manuscript that has been accepted for publication:
Dopp, C.M., Golwankar, R.R., Kelsey, S.R., Douglas, J.T., Erickson, A.N., Oliver, A.G., Day, C.S., Day, V.W., and Blakemore, J.D., Vanadyl as a Spectroscopic Probe of Tunable Ligand Donor Strength in Bimetallic Complexes, *Inorg. Chem.,* **2023**, *in press*, doi: 10.1021/acs.inorgchem.3c00724; also available as a pre-print on *ChemRxiv*, doi: 10.26434/chemrxiv-2022-t8p04

1.1 Abstract

Incorporation of secondary metal ions into heterobimetallic complexes has emerged as an attractive strategy for rational tuning of compounds' properties and reactivity, but direct solution-phase spectroscopic interrogation of tuning effects has received less attention than it deserves. Here, we report assembly and study of a series of heterobimetallic complexes containing the vanadyl ion, $[VO]^{2+}$, paired with mono-valent cations (Cs^+, Rb^+, K^+, Na^+) and a di-valent cation (Ca^{2+}). These complexes, which can be isolated in pure form or generated *in situ* from a common monometallic vanadyl-containing precursor, enable experimental spectroscopic and electrochemical quantification of the influence of the incorporated cations on the properties of the vanadyl moiety. The data reveal systematic shifts in the V–O stretching frequency, isotropic hyperfine coupling constant for the vanadium center, and V(V)/V(IV) reduction potential in the complexes. These shifts can be interpreted as charge density effects parametrized through the Lewis acidities of the cations, suggesting broad potential for the vanadyl ion to serve as a spectroscopic probe in multimetallic species.

1.2 Introduction

Tracking and systematically analyzing the tunable properties of multimetallic coordination complexes attracts significant attention in a variety of fields, as understanding the origin of tunability in metal complexes could assist researchers in rational design of new materials with tailored properties. Multimetallic complexes often afford access to structural and chemical properties that are inaccessible in their homometallic analogues, making them attractive for development as catalysts or as platforms for bespoke reactivity manifolds. Divergent synthetic protocols enable development of a wide range of complexes built from monometallic precursors, as secondary, effectively Lewis acidic metals can often be readily incorporated when appropriate

ligands are utilized. Progress in understanding the precise roles that the secondary metal cations play in multimetallic systems has come from studies of such compounds, particularly those based on first-row transition metals.[1,2]

As charged species that do not readily engage in significant covalent bonding, electropositive metal cations such as Na^{+}, Ca^{2+}, and Y^{3+} have been envisioned to exert electrostatic effects in multimetallic complexes, giving rise to changes in chemical reactivity,[3] catalytic behavior,[4,5,6] and in many cases, electrochemical reduction potentials.[7,8] These effects have been parametrized through a variety of descriptors, including the cations' charges, their ionic radii,[9] or their effective Lewis acidities, as estimated from the pK_a values of their corresponding metal aqua complexes.[10] Other parametrizations based on spectroscopic measurements have also been proposed because of the influence that solvent effects and metal ion speciation can exert over quantitative descriptors. For example, Fukuzumi and co-workers have explored systematic differences among cations with electron paramagnetic resonance (EPR) experiments on *in situ* generated superoxide species.[11] Caputo and co-workers have developed an approach to measuring Lewis acidity with fluorescence measurements,[12] and our group has been examining use of phosphine oxide probes and ^{31}P nuclear magnetic resonance (NMR) methods to quantify the properties of diamagnetic cations.[13,14] In all these cases, there is motivation to pursue a quantitative measure of the tendency of a given chemical species (*e.g.*, electropositive metal cation) to serve effectively as a Lewis acid. Such behavior can be thought to arise from the induced shift in charge density distribution that results from interaction of a given Lewis acid with a molecule of interest.

Along this line, the properties and reactivity of molecular vanadium complexes and catalysts can be readily tuned through modification of both their ligand sets and conditions under which they are utilized.[15] Homomultimetallic vanadium species have important applications in oxidative

catalysis in particular,[16] and can take part in reactions such as diketone cleavage,[17] sulfide oxidation,[18] and deoxydehydration of vicinal-diols such as glycols.[19] In catalytic systems based on vanadium, both homo- and hetero-multimetallic systems can play critical roles; for example, sodium vanadate is a commonly utilized precursor complex and polymeric [VO_4] species are believed to be the active catalysts in reactions such as the oxidative dehydration of alkanes.[20] The work of Matson and co-workers has afforded access to well-defined polyoxovanadate clusters[21] that can be "doped" or substituted with single heterometals such as iron,[22] titanium, hafnium, zirconium, or gallium to interrogate the consequences of incorporating secondary metal cations into vanadium-based materials.[23] In these systems, the secondary metal has been shown to modulate the electronic properties of the parent clusters, affording electrochemical properties for multiple vanadium-centered redox events that depend linearly on the pK_a values of the corresponding aqua complexes of the incorporated secondary metal cations.[24] These results underscore the recognized ability of secondary metals to tune the properties of vanadium-based materials, and encourage further developments in this area.

Considering the established interest in the field toward pursuit of systematic analysis of tuning effects and their precise origins,[25] further development of molecular vanadium-containing heterometallic systems could offer additional benefits that merit exploration. In particular, our focus was drawn to the vanadyl ion, $[VO]^{2+}$ or oxovanadium(IV), for incorporation into heterobimetallic complexes. This species is chemically robust[26] (attributable to the formal V–O triple bond[27]) and affords a variety of unique spectroscopic handles that are readily addressed in complex systems.[28,29] These handles include unique electronic absorption properties in the UV and visible regions as well as well-resolved asymmetric V–O stretching frequencies that are typically found near 990 cm^{-1}. Additionally, $[VO]^{2+}$ is inherently paramagnetic due to its $3d^1$ configuration,

giving rise to a distinctive eight-line electron paramagnetic resonance (EPR) spectrum for the resulting $S = 1/2$ and $I = 7/2$ spin system when $[VO]^{2+}$ is placed into otherwise diamagnetic environments.[30] The vanadyl ion is also redox active, and can often be reversibly oxidized from V(IV) in neutral complexes to V(V). Consequently, incorporation of a single vanadyl ion into systematically tuned heterobimetallic complexes could *i)* afford the ability to interrogate the species with multiple techniques and *ii)* provide comprehensive experimental data to aid in identifying the origin of tuning effects measured in the complexes.

We envisioned that taking a hybrid approach could be fruitful to take advantage of these opportunities, in that use of a tailored ligand could enable installation of the vanadyl moiety into a monometallic precursor as well as enable binding of secondary metals through inclusion of an appropriate ancillary binding site. The ligand frameworks developed by Reinhoudt and co-workers[31] and elaborated upon by Vigato and co-workers[32] that feature [N_2,O_2] and [O_6] binding sites seemed ideal for this purpose, as they enable stable binding of cations in solution.[33,34] We thus anticipated that installation of the vanadyl ion into such a ligand would enable us to capitalize on its spectroscopically addressable nature, with an eye on understanding how ligand field strength varies across a series of heterobimetallic complexes wherein a modular series of electropositive metal cations are held in close proximity.

Here, we report the assembly of a series of heterobimetallic complexes that pair the vanadyl ion with a secondary electropositive metal cation (Cs^+, Rb^+, K^+, Na^+ or Ca^{2+}) and solution-phase spectroscopic and electrochemical measurements which quantify the influence of the secondary metal cations on the vanadyl core. The vanadyl ion, $[VO]^{2+}$, appears robust in these systems, and the complexes themselves can be either *i)* isolated and characterized as powdered samples or *ii)* prepared *in situ* and used directly for solution-phase spectroscopic investigations. Findings from

electronic absorption, infrared, and EPR spectroscopies as well as electrochemical studies have enabled us to quantify the decrease in ligand donor power that is driven by the effective Lewis acidity of the incorporated secondary metals, establishing a general model of the role that secondary metals play in heterobimetallic systems. Our results underscore that the vanadyl ion can serve as a readily addressable spectroscopic probe in heterobimetallic complexes, suggesting that this species could be used as a probe of coordination environment-dependent tunability in other systems.

1.3 Results

Synthesis of the Heterobimetallic Series

Syntheses of the heterobimetallic vanadyl complexes were accomplished with a monometallic precursor denoted **[VO]** (see Scheme 1.1). **[VO]** was prepared by stirring **[H_2,Ba]** dissolved in chloroform with an excess of guanidinium sulfate in water (resulting in extraction of Ba^{2+})[18,15] followed by addition of 1 equiv. of $VO(acac)_2$ (acac = acetylacetonate)[35] along with a few drops of triethylamine. **[VO]** was isolated (see Synthetic Procedures Section) in good yield (76%) as a green powder and is soluble in acetonitrile (CH_3CN) and tetrahydrofuran. The ^1H NMR spectrum of **[VO]** features a set of distinctive albeit broad resonances (see Appendix 2, Figure S1). The chemical shift values of the resonances for both the aromatic and aliphatic protons of our macrocyclic ligand are shifted from where they would be anticipated to be in diamagnetic complexes,[34] in line with the paramagnetic nature of **[VO]**. The elemental analysis results and structural data from X-ray diffraction (XRD) analysis confirmed the desired formulation of **[VO]**, including the presence of the free crown-ether-like [O_6] site that appears poised for binding of secondary metal cations.

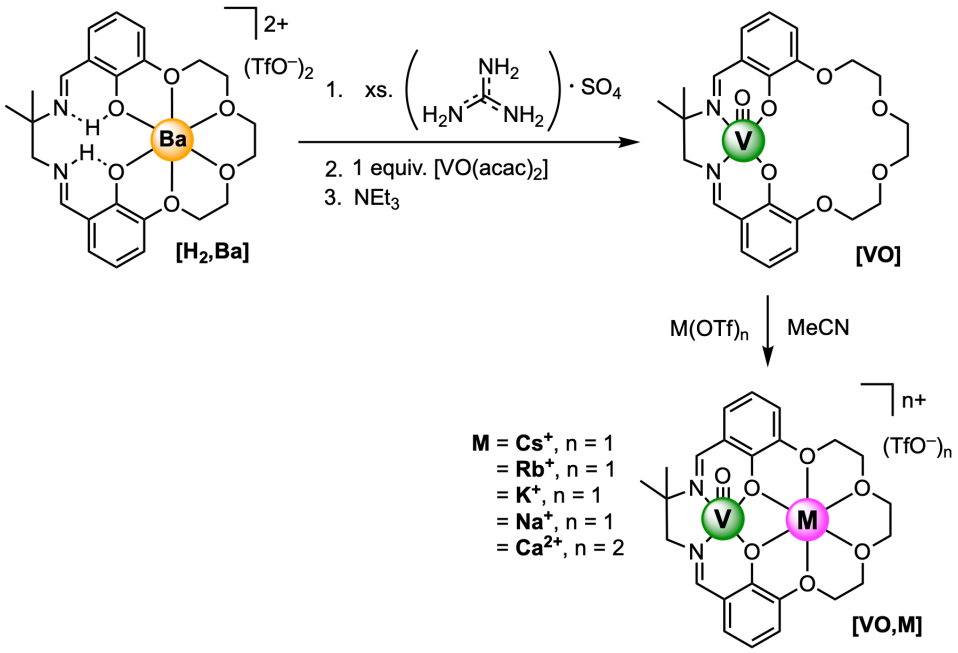

Scheme 1.1. Synthetic strategy for preparation of heterobimetallic vanadyl complexes.

To demonstrate the ability of **[VO]** to cleanly incorporate secondary metal cations, **[VO,Cs]**, **[VO,Na]**, and **[VO,Ca]** were also isolated and fully characterized (see Synthetic Procedures Section for details). These compounds could be readily prepared by addition of 1 equiv. of the corresponding triflate (OTf^-) salts of the desired secondary metal cations (Cs^+, Na^+, and Ca^{2+}) to solutions of **[VO]** in CH_3CN. The heterobimetallic species were isolated in good yields (>85%) in each case, in line with clean reactivity in solution. **[VO,Cs]**, **[VO,Na]**, and **[VO,Ca]** were fully characterized, including by elemental analysis, while solid-state structural data from XRD for **[VO,Na]**, and **[VO,Ca]** confirmed the ability of the pendant crown-ether-like [O_6] site in **[VO]** to effectively bind both monovalent and divalent secondary metals in the solid state.

X-ray Crystallography

Single-crystals of **[VO]**, **[VO,Na]**, and **[VO,Ca]** suitable for XRD analysis were grown by vapor diffusion of diethyl ether into CH_3CN in all three cases. See Table 1.1 for metrical data from XRD and Appendix 2 pp. S43-S86 for details. On the one hand, the solution and refinement of the structure of **[VO]**, described in **a03a**, was straightforward, with a clear-cut space group assignment of $P2_1/c$ and a quite acceptable final R_1 value of 4.0% (see Figure 1.1). **[VO]** is overall neutral in the solid state, co-crystallizing with only two outer-sphere acetonitrile molecules in our structure. The pendant crown-ether-like [O_6] site is clearly poised for binding of secondary metals in the compound, and as desired, the geometry about the vanadium metal center orients the two phenoxide (i.e., phenolate) oxygen atoms such that they could serve as bridging ligands to incoming secondary metal cations.

Table 1.1. Comparison of structural parameters from X-ray diffraction (XRD) analysis.

Compound	**[VO]**	**[VO,Na]**	**[VO,Ca]**
Structure code	**a03a**	**a04d-No1**	**b31b-No7**
pK_a of $[\mathbf{M}(H_2O)_m]^{n+}$ [a]	-	14.8	12.6
Ionic radius of **M** [b]	-	1.18	1.12
C.N. of M^{n+}	-	8	8
V–O_{oxo} (Å)	1.605(1)	1.595(7) [c]	1.589(10) [c]
V•••M (Å)	-	3.532(4) [c]	3.524(4) [c]
O1•••O2 (Å)	2.650(2)	2.603(12) [c]	2.580(15) [c]
M•••$O_{phenoxide}$ (Å) [d]	-	2.495(9) [c]	2.452(11) [c]
V–$O_{phenoxide}$ (Å) [e]	1.924(1)	1.926(8) [c]	1.943(11) [c]
τ_5 geometry index [f]	0.074	0.103 [c]	0.018 [c]
ω_{salmen} [g]	0.035	0.046 [c]	0.008 [c]
ω_{crown} [h]	0.246	0.273	0.257
ψ_V (Å) [i]	0.595	0.595 [c]	0.568 [c]

[a] From reference 10. [b] From reference 9. [c] Average values of parameters for **[VO,Na]** and **[VO,Ca]** were calculated as the arithmetic mean of the relevant values for the four independent molecules of **[VO,Na]** and two independent molecules of **[VO,Ca]** present in their structures' respective asymmetric units. Stated e.s.d.'s on distances were taken as the largest of the individual values in the refined data for the independent molecular species. [d] Defined as the average of the interatomic distances between the secondary metal cations Na^+ and Ca^{2+} and the O-atoms of the bridging phenoxide moieties. [e] Defined as the average of the interatomic distances between the vanadium center and the O-atoms of the bridging phenoxide moieties. [f] Geometry index for five-coordinate complexes, with the values ranging from 1.00 for a perfect trigonal bipyramidal geometry to zero for a perfect square pyramidal geometry. Calculated as described in references 36 and 37. [g] Defined as the root mean square deviation (RMSD) of the atoms O1, O2, N1, and N2 from the mean plane of their positions. [h] Defined as the RMSD of the atoms O1, O2, O3, O4, O5, and O6 from the mean plane of their positions. [i] Absolute value of the distance between the vanadium atom and the mean plane defined by O1, O2, N1, and N2.

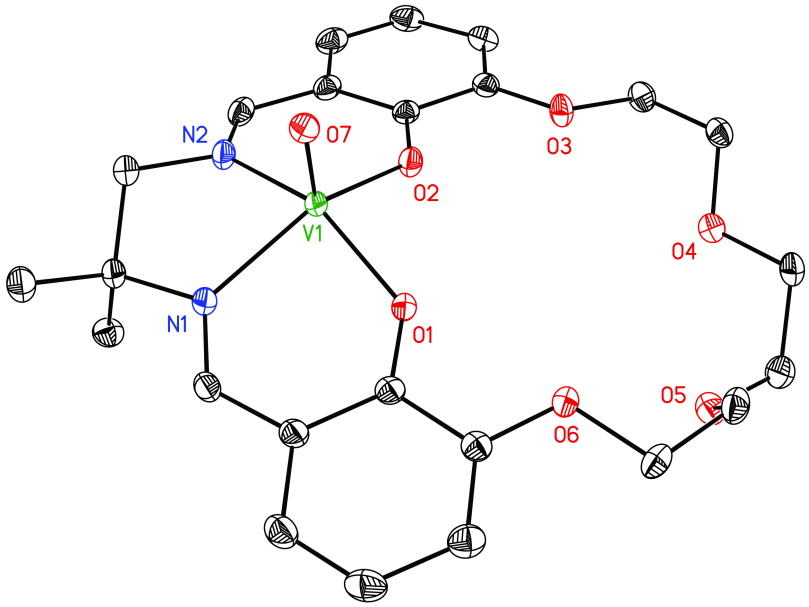

Figure 1.1. Solid-state structure of **[VO]** from **a03a**. Two outer-sphere co-crystallized acetonitrile solvent molecules and hydrogen atoms are omitted for clarity. Displacement ellipsoids are shown at the 50% probability level.

On the other hand, the solution and refinement of the structures of **[VO,Na]** and **[VO,Ca]**, given in **a04d** and **b31b**, were not routine due to crystallographic *pseudo*-inversion symmetry that affects both systems. In essence, the structures of **[VO,Na]** and **[VO,Ca]** (see Figures 1.2 and 1.3) display inversion symmetry that is not rigorous, in that it is obeyed by large numbers of atoms in the asymmetric unit of each structure but not all. While at first glance this situation might be thought to resemble those involving re-assignment of space groups from ambiguous determinations highlighted by the late R.E. Marsh,[38] instead it is rather the opposite. Marsh's efforts were often focused on correcting structures by finding and imposing unrecognized rigorous symmetry elements; our cases in **a04d** and **b31b** involved assigning the preferable and correct solutions that avoid imposition of non-rigorous centers of symmetry. Consequently, although Dr. Marsh stated at least once that "the most reasonable procedure is to describe [a structure] in the centrosymmetric

space group if at all possible," this prescription[40] does not apply to our structures. Structures appearing to contain approximate centers of inversion were the focus of another particularly insightful study[39] from Dr. Marsh; he noted that in such cases, "the moral is clear: if an approximate center is present, extra care must be taken." We have found this advice to ring true in the present work. In **b31b**, imposing rigorous symmetry results in a single crystallographically-independent cationic moiety with significant disorder. The molecular cation has two half-occupancy orientations for the polyether chain and obtaining a metrically reasonable structure required an unacceptably high ratio of restraints to parameters (1272 to 802). On the other hand, the non-centrosymmetric refinement produced two crystallographically-independent ordered cationic moieties that were metrically reasonable with many fewer restraints. In **a04d**, imposition of inversion symmetry results in at least one *apparently* unreasonable short intermolecular packing contact between a disordered methyl group (associated with C23B) of the heteroditopic ligand of **[VO,Na]** and a fully ordered triflate counter-anion.[40] By being involved in a C-H•••O hydrogen bond that presumably stabilizes the structure, the C23B methyl group would *not* be expected to be disordered, as it was in the centrosymmetric structure. The specifics of these issues are discussed in the Special Refinement Details in Appendix 2 and are briefly summarized in the next paragraph in light of their unusual nature and scholarly interest (p. S46-S49 for **a04d** and p. S69-S70 for **b31b**).

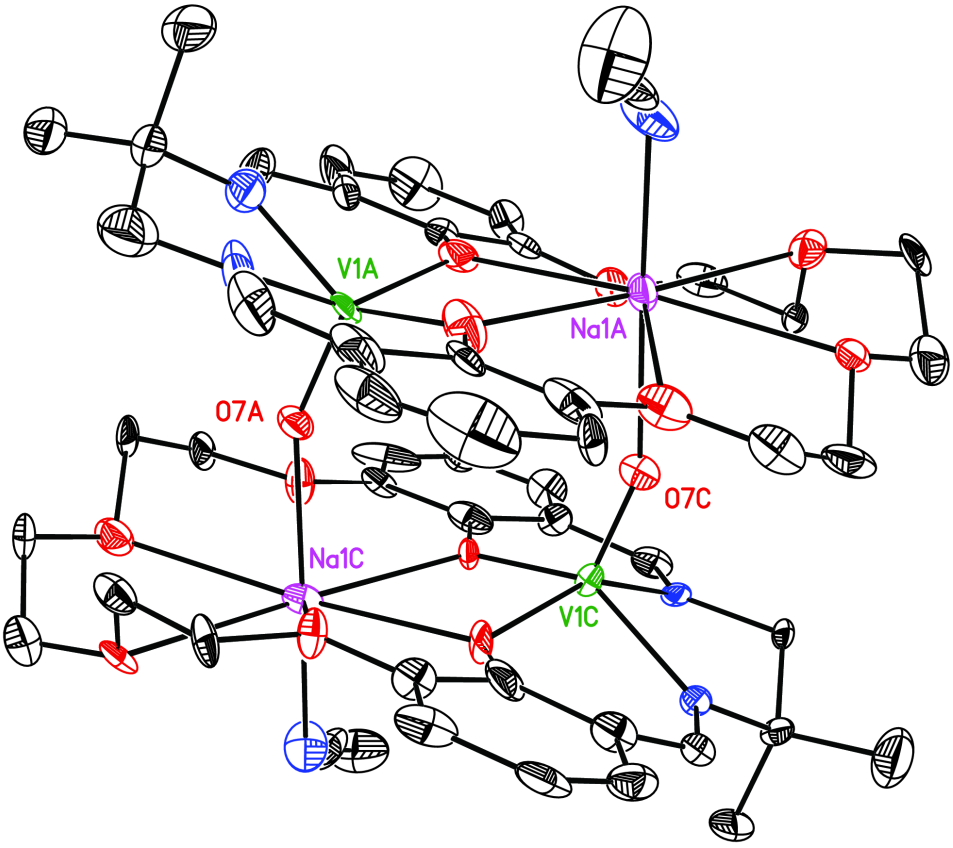

Figure 1.2. Solid-state structure of the *pseudo*-centrosymmetric **[VO,Na]** dimer from **a04d-No1**. Four outer-sphere triflate counter-anions, an outer-sphere water molecule, and a second dimeric species that is chiral (due to one of the two *pseudo*-inversion-related 4-carbon diimine bridges being "flipped") are omitted for clarity, in addition to hydrogen atoms; displacement ellipsoids shown at the 50% probability level.

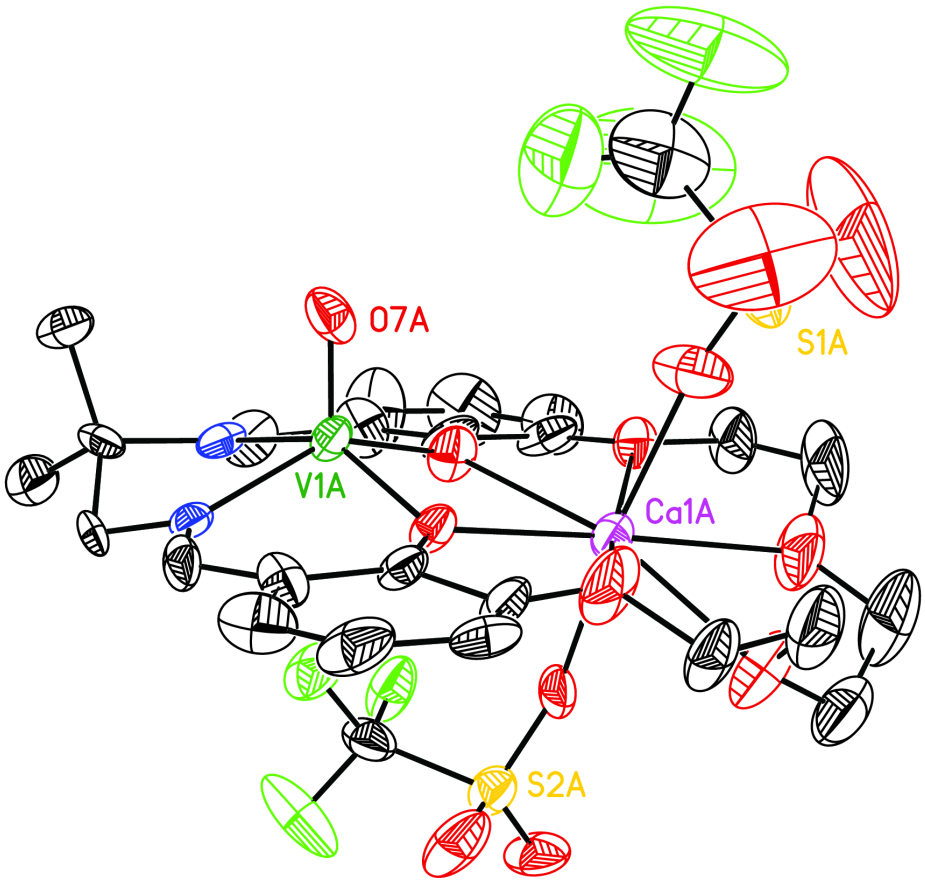

Figure 1.3. Solid-state structure of **[VO,Ca]** from **b31b-No7**. All H-atoms, a co-crystallized molecule of acetonitrile solvent, a second molecule of **[VO,Ca]** found in the asymmetric unit, and triflate disorder (associated with S2A) are omitted for clarity. Displacement ellipsoids are shown at the 50% probability level.

Both structures could be fully refined to give reliable geometric information and bond metrics through selection of appropriate space groups: *P1* for **a04d-No1** and *Pc* for **b31b-No7**. These refinements avoid imposition of non-rigorous symmetry and return acceptable R_1 values of 6.4% and 6.8%. More importantly, they eliminate all macrocycle disorder in both structures, much of the triflate disorder in **b31b** and reveal the presence of two structurally distinctive dimeric species present in the solid-state for **a04d**. The observation that the crystal of this compound contained

two distinctive types of dimers was unexpected; this finding, along with the presence of an important co-crystallized water molecule, was obscured when the structure was solved in centrosymmetric space group *P-1* but unambiguous in the final refinement using the non-centrosymmetric space group *P1*. This water molecule appears to be critical because it engages in hydrogen bonding with two outer-sphere triflate molecules, orienting these species and presumably affording stabilization to the solid-state asymmetric unit. Of additional note, a short and apparently critical intermolecular packing contact between a fully ordered methyl group of the heteroditopic ligand of **[VO,Na]** and a fully ordered triflate counter-anion was clearly resolved in the lower-symmetry non-centrosymmetric structure in *P1*. With both the methyl group and triflate being ordered in the *P1* structure, it was possible to identify this interaction as an inherently weak C-H•••O hydrogen bond. In an analogous refinement in *P-1*, the methyl group was disordered while the triflate remained fully ordered, a dissonant finding that caused us to suspect that the refinement in *P1* was the preferred and most correct solution. In light of all these considerations, we have used the final structures in lower-symmetry space groups for discussion of the properties of **[VO,Na]** and **[VO,Ca]** given below, but have also included further details in the SI regarding the competing centrosymmetric and non-centrosymmetric refinements for these cases.

The vanadyl moiety coordinates to the [N_2,O_2] site in both **[VO,Na]** and **[VO,Ca]**, and does not interact directly with atoms of the crown-ether-like [O_6] site. The Na^+ and Ca^{2+} cations occupy the [O_6] site in the structures of **[VO,Na]** and **[VO,Ca]** as expected, and the cations are both eight-coordinate in the solid-state data. In addition to the six oxygen donors, Ca^{2+} is ligated by two inner-sphere κ^1 triflate counter-anions while Na^+ is ligated by one inner-sphere acetonitrile molecule and the oxo of a nearby vanadyl moiety, resulting in the triflate counter-anions being found in the outer sphere. **[VO,Na]** forms dimeric species in the solid-state data, driven by the long, weak Na•••O_{oxo}

interactions of ca. 2.304(3) Å. The vanadyl moiety adopts a square pyramidal geometry in the complexes; quantification of the τ_5 geometry index for the vanadium centers in the three structures reported here returns values that are close to zero in all cases, consistent with near-perfect square pyramidal geometries. **[VO,Na]** deviates most significantly with τ_5 = 0.103, suggesting that the weak interaction of the vanadyl oxo with the nearby sodium cations drives a mild distortion of the vanadium coordination sphere.

Inspection of the interatomic distances between vanadium and the Na^+ and Ca^{2+} ions reveals that the smaller Ca^{2+} (Shannon ionic radius 1.12 Å) can nestle more tightly than Na^+ (ionic radius 1.18 Å) into the nascent diamond core motif (see Table 1). This position allows the secondary cations to interact closely with the bridging phenoxide moieties, a tendency likely driven by these groups' partial anionic character that arises from deprotonation and binding of $[VO]^{2+}$. In accord with this model, the distance between the phenoxide donors (O1•••O2) decreases upon incorporation of the secondary metal cations, with the smallest O1•••O2 and V•••M distances being associated with the more Lewis acidic calcium ion. There is minimal change in the out-of-plane deformation of the crown-ether-like site upon binding of the secondary metal cations (quantified by ω_{crown}, see Table 1.1), whereas the out-of-plane deformation of the atoms defining the vanadyl binding site (quantified by ω_{salmen}, see Table 1.1) is minimized in the case of **[VO,Ca]** (ω_{salmen} = 0.008) vs. in the cases of **[VO]** and **[VO,Na]** (ω_{salmen} = 0.035 and 0.046, respectively). Consistent with this observation, the vanadium center moves significantly closer toward the plane of the macrocycle (quantified by ψ_V parameter, see Table 1.1) upon coordination of the Ca^{2+} ion.

These observations suggest that the properties of the vanadyl core are indeed measurably perturbed upon incorporation of Lewis acidic cations into **[VO]**. Additional evidence for this perturbation comes from examining the bond distances about the vanadium center. Indeed,

coordination of the more Lewis acidic Ca^{2+} results in a pronounced elongation of the $V–O_{phenoxide}$ distance (1.943(11) Å in **[VO,Ca]** vs. 1.924(1) Å in **[VO]** and 1.926(8) Å in **[VO,Na]**. More significantly, however, the $V–O_{oxo}$ bond undergoes a contraction upon binding of Na^+ or Ca^{2+}, giving data for this bond distance that decrease in the order **[VO]** > **[VO,Na]** > **[VO,Ca]**; the values of the $V–O_{oxo}$ distance for the compounds in this order are 1.605(1) Å, 1.595(7) Å, and 1.589(10) Å, respectively. These measured changes in the $V–O_{phenoxide}$ distance and $V–O_{oxo}$ distance are consistent with attenuation of the electron donor power of the bridging phenoxide atoms upon binding of Lewis acidic cations, a proposal that we anticipated could be investigated through spectroscopic and electrochemical studies which address the suggested changes occurring at the vanadium site. Thus, we next turned to solution-phase spectroscopic investigations to provide further quantitative evidence for such perturbations.

Electronic Absorption Spectroscopy

We first considered electronic absorption to spectroscopically interrogate the properties of the heterobimetallic complexes containing the vanadyl ion. Assembly of the complexes *in situ* with CH_3CN, rather than bulk isolation and solid-state characterization of all complexes, was pursued to enable screening of a range of metal cations, including Cs^+, Rb^+, K^+, Na^+, Li^+, and Ca^{2+}. The spectral signatures in the UV-visible region were used to confirm the formation and stability of the complexes in solution. Therefore, we prepared 1:1 vanadium:**M** solutions over a vanadium concentration range of 0.025 to 0.5 mM, and measured these solutions' UV-visible spectra under inert atmosphere in our glove box. Two main types of transitions were immediately apparent in the measurements of the starting **[VO]** complex, and these transitions were also observed for the heterobimetallic species, albeit shifted to higher energies (blue shifted) in all cases (see Figures 1.4 and 1.5, and see Appendix 2, Figures S9-S15 for more details). The first transition was found

for **[VO]** at λ_{max} = 386 nm, and was assigned as having charge-transfer (CT) character on the basis of its intense molar absorptivity (ε = 4,500 M^{-1} cm^{-1}). The second transition was found for **[VO]** at 593 nm, and on the basis of its position[41] as well as lower intensity ($\varepsilon \approx 130$ M^{-1} cm^{-1}),[20] we assigned it as a d-d transition associated with the vanadyl moiety.

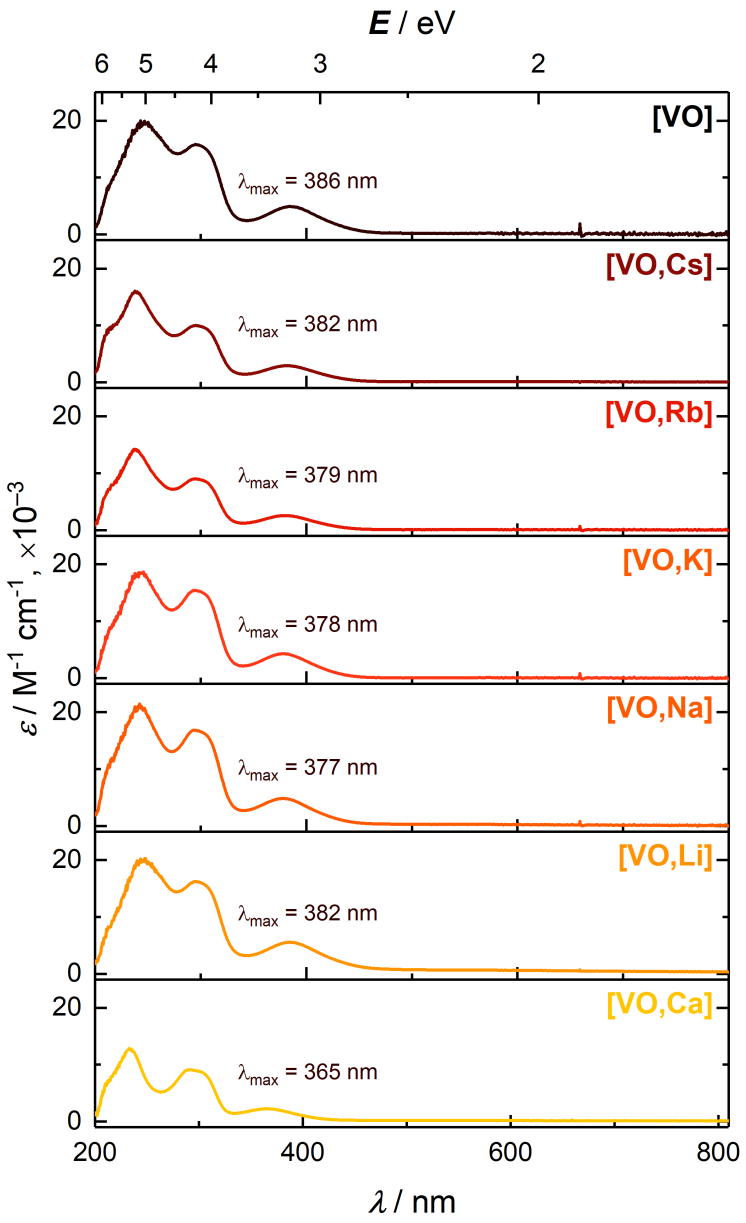

Figure 1.4. UV-visible spectra highlighting charge transfer transitions in the complexes. The spectra of the heterobimetallic species are given in order of increasing pK_a of the corresponding metal aqua complexes. The concentration of vanadium in each case was 100 μM.

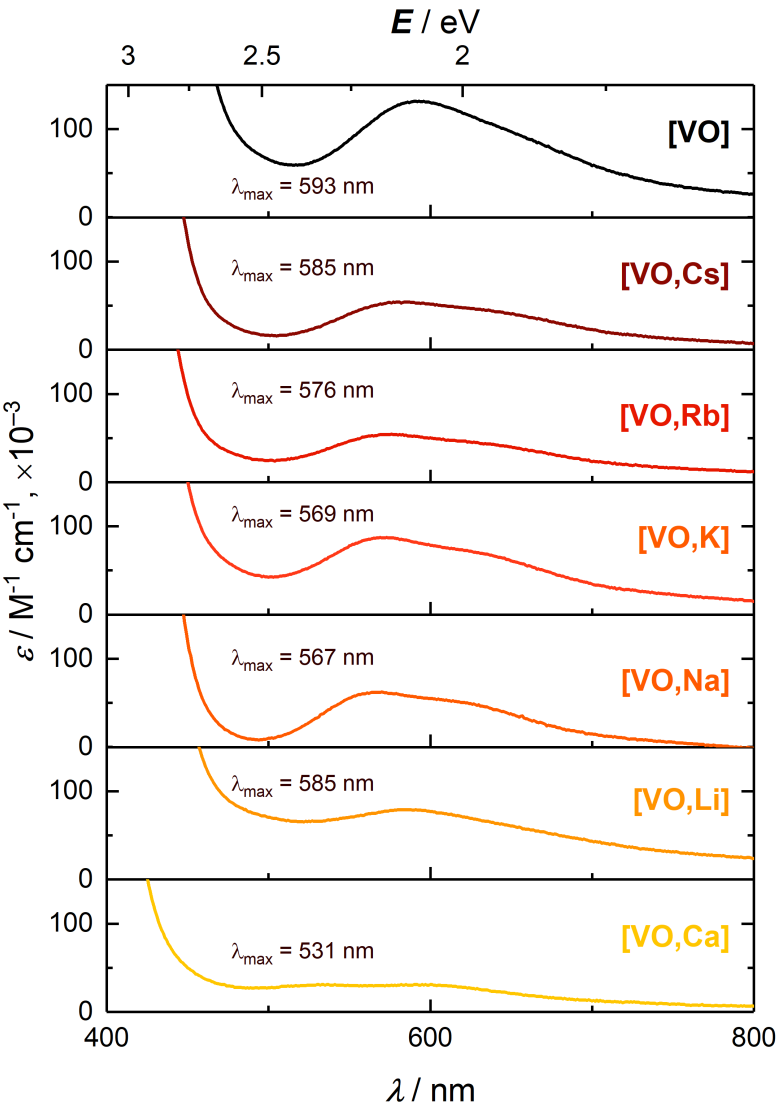

Figure 1.5. UV-visible spectra highlighting the d-d-type transitions measured for the complexes.

As mentioned above, examination of the electronic absorption spectra of the heterobimetallic complexes revealed similar transitions to those measured in **[VO]** in each case. The lowest-energy charge transfer transition was found at 382 nm for **[VO,Cs]** and at further blue-shifted wavelengths for the other heterobimetallic complexes, up to 365 nm for **[VO,Ca]**. The d-d transition measured at 593 nm for **[VO]** was also found to blue shift in the heterobimetallic derivatives, shifting as far as 531 nm in the case of **[VO,Ca]**. Plotting the energies of the two tabulated types transitions (CT and d-d) as a function of Lewis acidity (parametrized by pK_a values as described above) results in linear trends in both cases, with the exception of the data for **[VO,Li]** (see Figure 1.6).

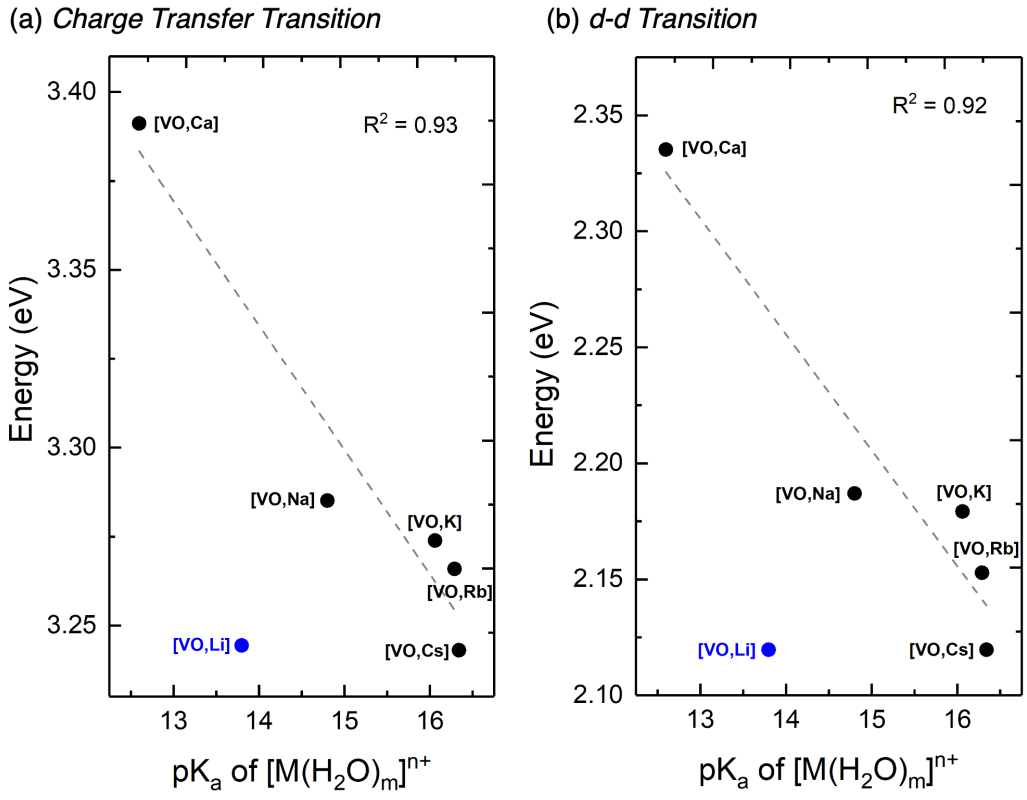

Figure 1.6. Dependence of the energies of charge transfer (panel a) and d-d (panel b) transitions on the pK_a values of the corresponding aqua complexes of the incorporated secondary metal cations. Data for **[VO,Li]** are given in the blue points, and were not included in the linear fits.

Setting aside the case of **[VO,Li]** for the moment, the dependence of the CT transition energy for the adducts of Cs^+, Rb^+, K^+, Na^+, and Ca^{2+} on Lewis acidity was found to be −30±5 meV/pK_a, whereas the value was found to be −50±10 meV/pK_a for the d-d transition. The values of these slopes are not unlike the prior dependences that we have measured in related Ni,[33] Pd,[34] and uranyl[42] heterobimetallic complexes (–46±5, –45±3, and –22±1, respectively), in line with the similar structure of the ligands used in each case. The use of vanadyl here, however, enabled us to measure the dependence of its d-d energy on the Lewis acidity of nearby cations; the higher dependence of this energy on Lewis acidity suggests, at least, that the close proximity of the vanadium(IV) center to the site for binding of the secondary metal cations results in a significantly greater sensitivity to the influence of these cations in comparison to their influence over the CT transition energies in the same compounds.

For the **[VO,Li]** complex, although the UV-visible data qualitatively resemble those for the other cation adducts, the shifts in the transitions for **[VO,Li]** are more modest than what would be expected on the basis of Lewis acidity. These observations suggest that the cation interacts with the parent **[VO]** complex in a different manner than that of the other cations in this study. Looking to the literature, Li^+ has an established preference to bind in smaller crown ethers such as 15-crown-5, and thus likely does not bind tightly to the larger crown-like site in **[VO]**.[43] Li^+ could also prefer to interact directly with the terminal oxo of the vanadyl moiety.[44] In accord with the possibility of distinctive speciation for **[VO,Li]**, we found that preparation of concentrated solutions (ca. 10 mM) resulted in precipitation of an insoluble material. Consequently, we elected to separate further experiments with Li^+ in order to focus on cation adducts that systematically and reliably feature binding in the crown-like site. Information on **[VO,Li]** spectroscopic and electrochemical characterization can be found in Chapter 2.

Our observation of shifted electronic transitions upon binding of secondary metal cations in the 18-crown-6-crown-like site of our macrocyclic resembles observations made in prior work. For example, addition of 1 eq. of scandium(III) to a manganese(IV) oxo complex resulted in the blueshift of an electronic transition for the complex from 940 nm to 680 nm.[45] On the other hand, addition of 1 eq. of scandium(III) to a TAML-ligated manganese(V) oxo complex resulted in a smaller red-shift of an electronic transition from 430 to 465 nm.[46] In this latter case, the scandium(III) ion was suggested to interact with the parent complex through a remote (CO) group in the ligand backbone; this was supported by DFT calculations as well as EXAFS analysis showing changes in ligand back scattering upon addition of scandium(III). On the other hand, less Lewis acidic cations such as Zn^{2+} and Ca^{2+} did not result in changes to the UV-visible absorption profile of the Mn(V) oxo system. In our own prior work with a family of heterobimetallic palladium complexes, systematic shifts in a CT transition were observed across a family of seven cations, including K^{+}, Ca^{2+}, and Lu^{3+}.[34] These observations underscore the important role of the crown-ether-like site in our macrocyclic ligand, which was used in both the work with palladium and the work here with vanadyl. We conclude that the crown-ether-like moiety in our ligand system enables direct interaction of the cations Cs^{+}, Rb^{+}, K^{+}, Na^{+}, and Ca^{2+} with the vanadyl core. As mentioned earlier, we hypothesize that placement of cations in this site is particularly impactful on the properties of the vanadyl core owing to interaction with the two bridging phenoxide ligands. Modulation of the ability of these ligands to serve as donors to the vanadyl moiety can be predicted to impact the properties of vanadyl, and to investigate this possibility we turned next to infrared (IR) spectroscopy.

Infrared Absorption Spectroscopy

The solution phase IR spectrum of **[VO]** collected in CH_3CN exhibits a feature at 989 cm^{-1} which can be assigned on the basis of prior work with vanadyl complexes[47] to be associated with the asymmetric stretch of the V–O moiety (see Figure 1.7, black line, and see Appendix 2, Figure S21). On the one hand, the asymmetric stretch measured for our complex **[VO]** matches well with those from prior literature on both salen-type vanadyl complexes, in line with the similar ligand environment about **[VO]** in our macrocyclic ligand,[48] and other vanadyl complexes.[28,49,50] On the other hand, however, the V–O stretching mode in **[VO]** does exhibit a noticeable shoulder on the low wavenumber side of the main peak. This could be attributed to interaction of the free 18-crown-6-like unit with the vanadyl moiety in an intermolecular fashion. This possibility is supported by observations attesting to occupation of the crown unit by secondary metals in the other complexes, disfavoring intermolecular interactions of this type. Additionally, we found that the V–O stretching mode of **[VO]** does not exhibit a noticeable shoulder in the solid state (see Appendix 2, Figure S33), suggesting that the shoulder is induced by intermolecular interactions in the solution state.

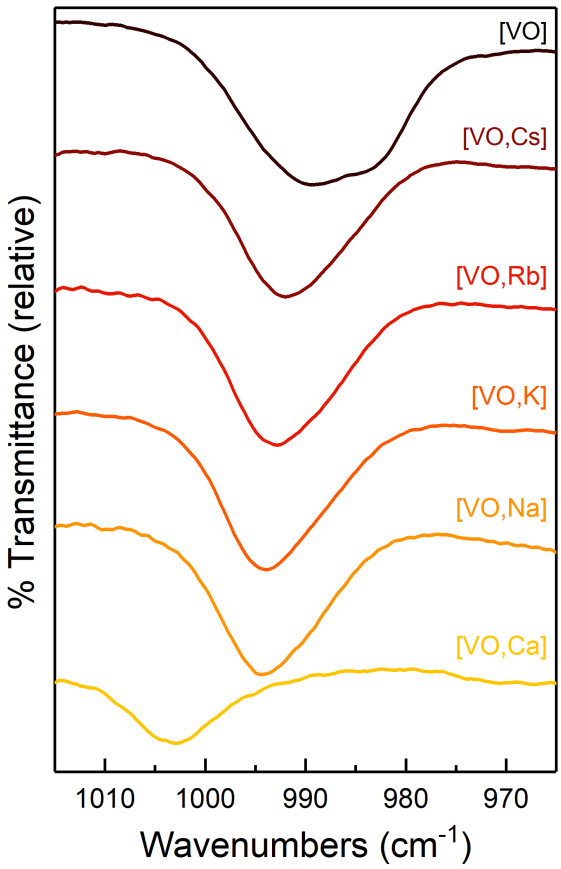

Figure 1.7. Infrared spectra of the **[VO,M]** complexes. Conditions: CH_3CN solvent; **[VO]** = 10 mM; KBr window cell.

A shift of the V–O stretching frequency to higher wavenumbers was observed upon incorporation of more Lewis acidic cations to form the heterobimetallic complexes, with the greatest shift of 12 cm^{-1} being encountered in the case of **[VO,Ca]** (see Figure 1.7, Table 1.2, and Appendix 2 Figures S21-S26 for full spectra in CH_3CN). This observation is consistent with deformation of the electron density of phenoxide parentage in the heterobimetallic complexes, resulting in an attenuation of electron donation to the vanadyl moiety. To confirm these results, we also collected infrared spectra of solid-state (powder) samples of the heterobimetallic complexes prepared in solution followed by removal of solvent *in vacuo*. These solid-state IR

spectra (see Appendix 2, Figures S27-S33) show a similar shift of the V–O stretching frequency to higher wavenumbers upon incorporation of secondary metal cations, with the great shift of 22 cm^{-1} being measured for the case of **[VO,Ca]**.

Table 1.2. Comparison of quantitative data from infrared spectroscopy and fitted parameters from EPR analysis.

Compound	pK_a of $[\mathbf{M}(H_2O)_m]^{n+}$ [a]	ν_{V-O} (cm^{-1}) [b]	Δg [c]	A_{iso} (MHz) [d]	g_{avg} [e]
[VO]	-	991	0.395	271.9	1.9695
[VO,Cs]	16.34	992	0.398	274.0	1.9702
[VO,Rb]	16.29	993	0.399	274.9	1.9705
[VO,K]	16.06	994	0.401	275.9	1.9708
[VO,Na]	14.8	995	0.403	277.7	1.9713
[VO,Ca]	12.6	1003	0.407	280.1	1.9727

[a] From reference 10. [b] Asymmetric $V–O_{oxo}$ stretching frequency. Measured at the transmittance minimum of the assigned peak. Uncertainty measured in triplicate runs (±1σ) was ±1 cm^{-1}. [c] Measured as the difference in *g* between the maxima of the derivative low-field and high-field features in the EPR spectra. (see Appendix 2, Figures S42). [d] Isotropic hyperfine coupling constant from fitting of spectral data according to the equation $A_{iso} = (2 \bullet A_{\perp} + A_{\parallel})/3$. Uncertainty was determined from triplicate runs (±1σ) to be ±0.1 MHz. [e] Average *g*-value from fitting of spectral data, corresponding to the arithmetic mean of the *g*-values of the eight individual spectral features. Uncertainty was determined from triplicate runs (±1σ) to be ±0.001.

Based on the infrared spectra, we can conclude that the $V–O_{oxo}$ bond strengthens upon incorporation of secondary metal cations into **[VO]**, and we hypothesize that this is due to a charge density effect induced by the nearby secondary metal cations that interact with the bridging phenoxide ligands. The strength of the $V–O_{oxo}$ bond increases as the Lewis acidity of the secondary metal cations increases (see Figure 1.8), indicating that this descriptor can be used to interpret the observed spectroscopic changes. Noticeably, the V–O stretching frequency increases across the series of monovalent cations, indicating that charge alone cannot predict the strength of the V–O stretch. In terms of the linear fit shown in Figure 1.8, the slope of the trend line was found to be –

2.69±0.35 cm^{-1} $(pK_a)^{-1}$, and the R^2 goodness of fit was found to be 0.95. The estimated uncertainties thus compare reasonably well with those from the other trends measured here. We are not aware of any other examples showing tuning of asymmetric stretching vibrations for metal oxo moieties with Lewis acidic secondary metal cations, excluding the prospect of comparing uncertainties at this stage. However, we emphasize that these results suggest that attenuated charge donation from the bridging phenoxide moieties results in a more electron-deficient vanadium(IV) center and this drives an increase in the measured $V–O_{oxo}$ stretching vibration frequency. Our structural data (*vide supra*) support this claim as well.

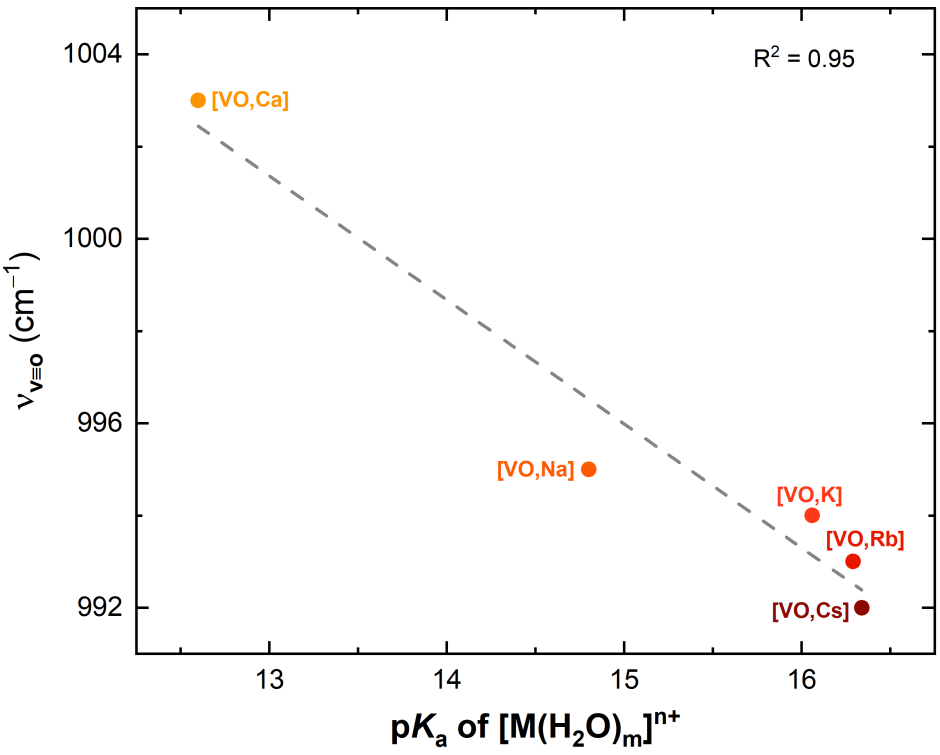

Figure 1.8. Plot of V–O stretching frequency for the heterobimetallic complexes as a function of the pK_a values of aqua complexes of the corresponding metal aqua cations.

Electron Paramagnetic Resonance Spectroscopy

Further support for the hypothesis that incorporation of secondary metal cations into our macrocyclic species results in attenuated donor strength of the bridging phenoxide ligands comes from X-band electron paramagnetic resonance (EPR) spectra collected in CH_3CN solution at room temperature (25°C). As we desired to use CH_3CN as the solvent for this work, we prepared capillaries containing the heterobimetallic complexes in CH_3CN and loaded these into conventional quartz EPR tubes in our glovebox prior to transferring the sealed samples to the spectrometer for data collection. The spectra thus obtained (see Figure 1.9) reveal a distinctive eight-line signal centered near $g = 2.0$ in each case, consistent with the formal +IV oxidation state and $S = 1/2$ configuration of the vanadyl ions in each heterobimetallic complex.[52] However, there is a subtle but nonetheless measurable widening of the spectral profile when comparing the spectra of the heterobimetallic complexes to that of the **[VO]** precursor, consistent with an increase in the difference between the high- and low-field g values (Δg) that is driven by the incorporation of secondary metal cations (see Table 1.2).

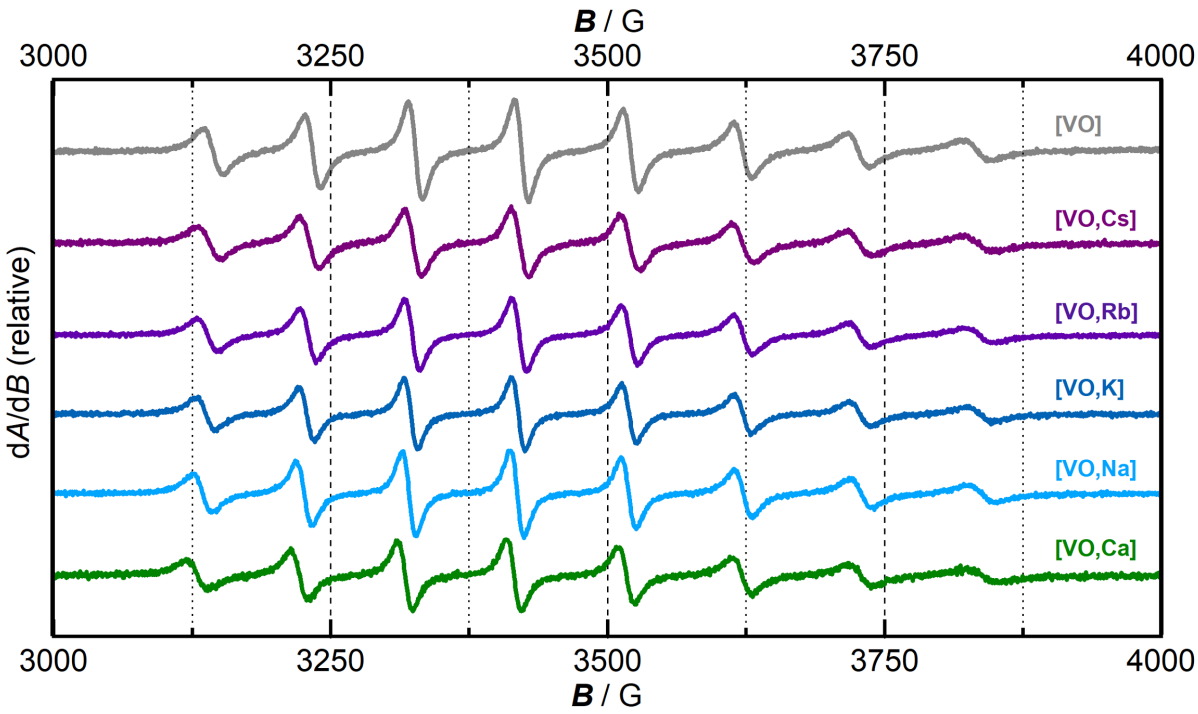

Figure 1.9. Experimental X-band EPR spectra of **[VO]** and the **[VO,M]** complexes in CH_3CN. [Vanadium] was ca. 10^{-3} M in each case. (Conditions: modulation amplitude = 4.0 G; time constant = 1.28 ms; T = 25°C). Simulated spectra (EasySpin) that were fitted with the experimental data are given in Appendix 2, Figures S36–S41.

Our vanadyl complexes are five-coordinate at vanadium on the basis of the solid-state structures from XRD, and the quantitative τ_5 geometry index confirms that the geometry about the vanadium center is close to ideal square pyramidal in all cases. The oxo ligand is typically used to define the *z*-direction of coordination polyhedra in complexes of this type, and the strong interaction with this ligand has been found in prior work to give rise to large, approximately axial anisotropy in the hyperfine characteristics of the vanadyl ion. It has also been recognized in prior work that the identity of the four equatorial ligands can give rise to differences in hyperfine coupling constants in those *x* and *y* coordinates (A_x and A_y), and also that the identity or absence of a sixth ligand *trans*

to the oxo group often results in little change to the hyperfine characteristics of a given system.[47,51] Our spectra fit well in the context of these prior findings, although we note that because our data were collected in liquid solution, these individual anisotropies should manifest as perturbations to the intensities and *g*-values of the separate features within the eight-line pattern associated with the vanadyl moiety, rather than through powder averaging as would be observed in work carried out in frozen solution.[52]

In order to fully quantify the magnetic properties underlying our spectral data and any changes to them induced by the secondary metal cations, we turned to spectral simulation and fitting with the *garlic* function in the EasySpin package,[53] an approach which allowed us to extract the value of the isotropic hyperfine coupling constant ($A_{iso} = (2 \bullet A_{\perp} + A_{\parallel})/3$) for each complex as well as the values of $g_{\parallel}$ and $g_{\perp}$ for the vanadyl moiety in each complex (see Appendix 2, pp. S22-S33 for details).[52] In our simulations, the spectra could be modeled well with a single $S = ½$ radical species displaying axial anisotropy in the fast motion regime. The EPR simulations reveal a distinctive increase in the value of A_{iso} for the vanadyl ion in the heterobimetallic complexes studied here (see Figure 1.10). This increase in hyperfine coupling constant gives rise to the noted anisotropic widening of the spectral profile described above, with the largest values being measured for the derivatives incorporating Na^+ and Ca^{2+}. Thus, as the Lewis acidity of the secondary metal cation increases, A_{iso} increases in our complexes.

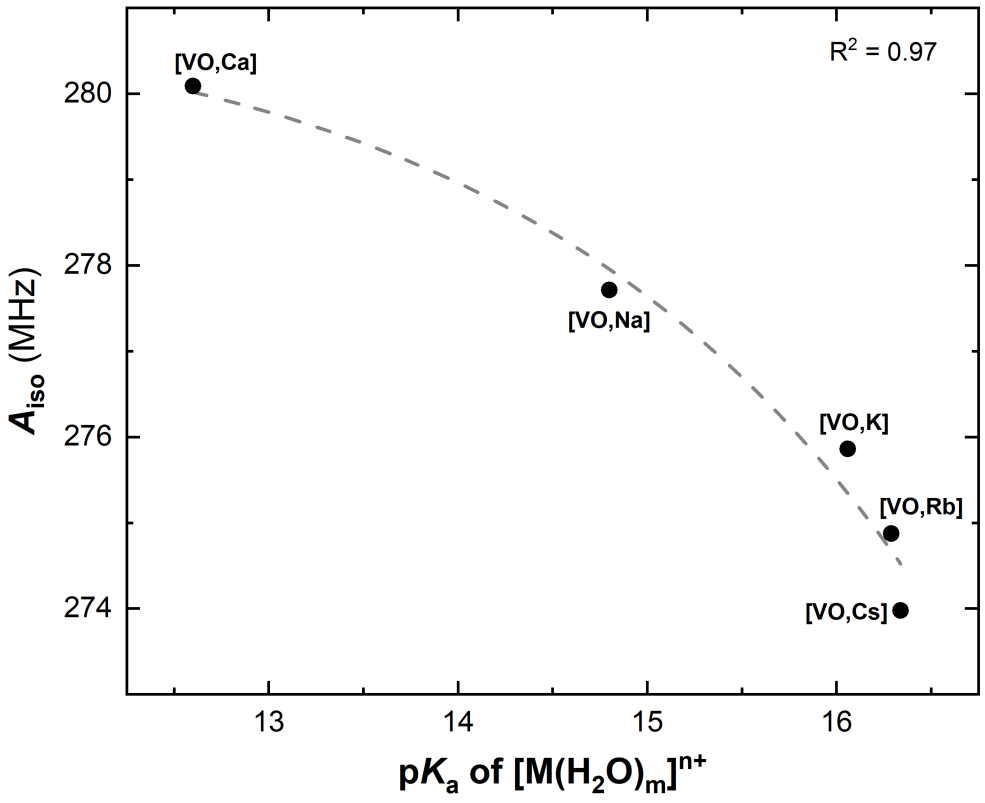

Figure 1.10. Plot of A_{iso} (MHz) for the **[VO,M]** complexes vs. pK_a of [**M**$(H_2O)_m]^{n+}$. The gray dashed line corresponds to an exponential fit of the data and is intended primarily as a guide to the eye for the monotonic relationship in the data.

Our approach of using the vanadyl ion as a spectroscopic probe or reporter in heterobimetallic complexes represents a strategy reminiscent of prior work from the field of the bioinorganic chemistry of vanadium-containing enzymes and proteins.[54,55] In particular, pioneering work from Wüthrich and co-workers[56] demonstrated that controlled substitution of the ligand environment around the vanadyl ion in protein matrices resulted in measurable changes in hyperfine coupling. The theory regarding vanadyl EPR spectra has evolved considerably since this pioneering work was initiated,[57,58] enabling use of hyperfine coupling constants as a sensitive probe of electronic environment.[59] In particular, an additivity relationship has been developed which correlates the

number and types of ligands present in the equatorial plane of the vanadyl ion to its spectral properties in a given system. The magnitudes of the hyperfine components are quite sensitive to the electron-donating ability of the equatorial ligands, and within this paradigm, EPR measurements carried out on biological systems with known (or presumed) identities have been useful for assigning the identity of coordinating ligands in vanadyl-containing biological systems.[60] In our family of complexes, this relationship appears to be manifest as a monotonic dependence of the A_{iso} values of the **[VO,M]** complexes on the pK_a values of the incorporated secondary metal cations (Figure 1.10). This is consistent with the prior work on biological systems, in that weaker electron donors (e.g., oxides) generally result in wider spectra and larger A_{iso} values whereas stronger donors (e.g., sulfides) give smaller A_{iso} values.[57] Thus, our EPR data reveal a quantitative measure of diminished electron donation from the bridging phenoxide ligands to the vanadium(IV) center in the vanadyl ion when secondary electropositive metals are present.

Linear relationships between A_{iso} and $g_{average}$ have also been measured in prior explorations of the role of ligand environment in influencing the EPR properties of vanadium-containing systems.[58] In these prior measurements, linear trends could be plotted between A_{iso} and $g_{average}$, where the underlying experimental origin for the changing A_{iso} and $g_{average}$ values is the changing identity of the ligands around the vanadyl moiety; changing the identity of the ligands results in the noted trend in which the magnetic properties of the complexes systematically shift as a function of ligand electron donor ability. Considering the monotonic dependence of the A_{iso} values of the **[VO,M]** complexes on the pK_a values of the incorporated secondary metal cations, we were curious if we would also find a correlation between the A_{iso} and $g_{average}$ values for our system that could resemble the correlation found in the literature data.[58,60] Indeed, we confirmed a strong linear correlation ($R^2 = 0.95$) between these parameters in our system as well (see Appendix 2, Figure

S44). As our values for A_{iso} and $g_{average}$ were extracted from the raw spectra using the *garlic* function of EasySpin, this linear correlation further strengthens our conclusions. Considering this trend together with the monotonic dependence of the A_{iso} values of the **[VO,M]** complexes on the pK_a values of the incorporated secondary metal cations, the EPR results support the central hypothesis of this work: incorporation of secondary electropositive metal cations results in diminished electron donation from the bridging phenoxide ligands to the vanadium(IV) center in our macrocyclic complexes.

Electrochemical Studies

As mentioned in the Introduction, the vanadyl ion is redox active, and can often be reversibly oxidized from V(IV) to V(V) in neutral complexes. We were curious to investigate the possibility of oxidative electrochemistry for our complexes in light of the spectroscopic results described above, in that electrochemical data have not previously been available for heterobimetallic vanadyl complexes for which a library of related spectroscopic data is also available for comparison. This is of special interest in our system in light of the hypothesis that incorporation of secondary metal ions into the 18-crown-6-like site results in attenuated donation from the bridging phenoxide groups to the vanadium(IV) center. As a result, we predicted at the outset that incorporation of Lewis acidic metals would result in a positive shift of the V(V)/V(IV) reduction potential, corresponding to a vanadium(IV) center that is more difficult to oxidize due to reduced stabilization from the bridging phenoxide ligands. We further anticipated that any trends in such behavior between our metal cations of interest here could shed light on oxidation-induced reactivity of our range of complexes.

Cyclic voltammograms collected for **[VO]** revealed a single, chemically reversible anodic wave at a modest positive potential of $E_{1/2}$ = 55 mV vs. the ferrocenium/ferrocene couple, denoted hereafter as $Fc^{+/0}$ (see Figure 1.11, black line). A return cathodic peak is evident in the data at all scan rates measured from 50 to 500 mV/s (see Appendix 2, Figure S49), indicating that the vanadium(V) form of our complex **[VO]** is stable on the electrochemical timescales in this work and persists in solution following electro-oxidation of the starting vanadium(IV) complex. Thus, we assign this process as chemically reversible, as no obvious chemical reaction or EC-type behavior is implicated by the data.[61] Scan-rate dependent studies confirm that both the V(IV) and V(V) forms of the complex are freely diffusing at the electrode surface, consistent with the good solubility of **[VO]** in MeCN. And, finally, we note that the V(V)/V(IV) couple appears electrochemically quasi-reversible on the basis of its peak-to-peak separation (ΔE_p) of 118 mV (see Appendix 2, Table S3).

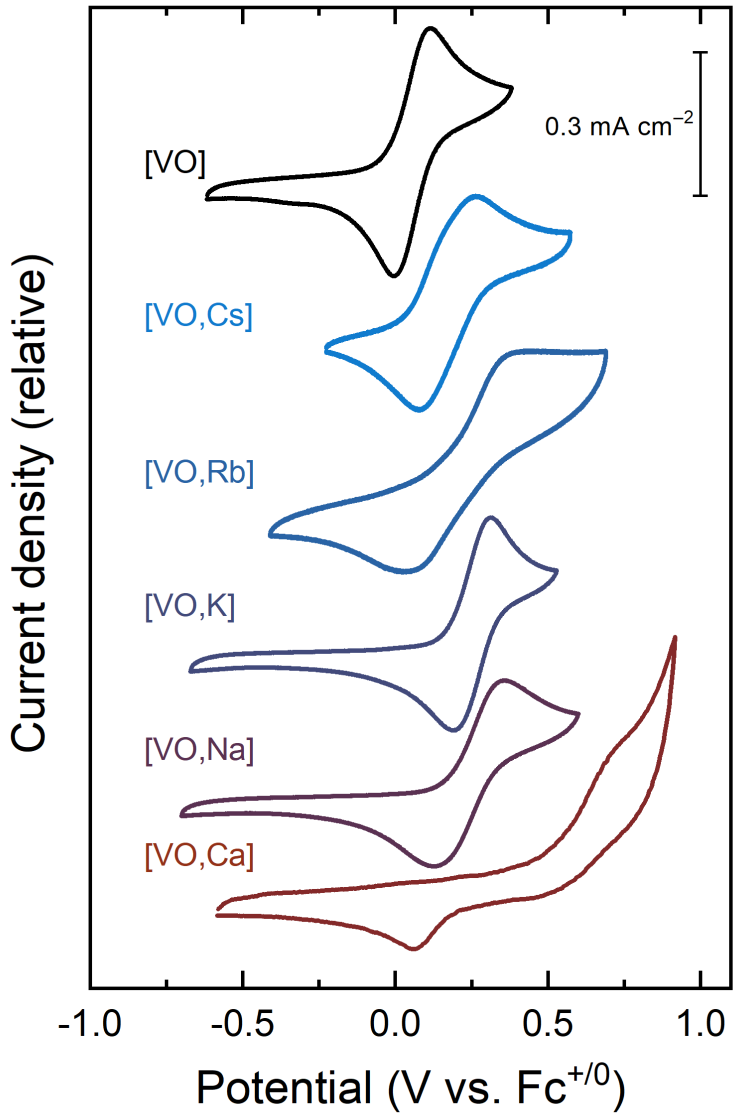

Figure 1.11. Cyclic voltammetry data for the complexes. Conditions: 0.1 M tetrabutylammonium hexafluorophosphate in CH_3CN; scan rate: 100 mV/s; [vanadium] = 2 mM.

Following the electrochemical study of **[VO]**, we investigated the influence of the installed electropositive metal cations on the V(V)/V(IV) couple for the heterobimetallic derivatives. On the one hand, oxidation and reduction waves could be measured for all the complexes explored here that were generally shifted to more positive potentials compared to that of the parent **[VO]** (see Table 3 for all data). On the other hand, the specific appearance of the data was unique in each

case, implying the V(V) forms of the compounds investigated here display particular behaviors. These behaviors, however, can be understood on the basis of the Lewis acidity and other properties of the incorporated cations Cs^+, Rb^+, K^+, Na^+, and Ca^{2+}, in that the generation of the V(V) species with a higher cationic charge could result in diminished binding strength of the secondary cations to the crown-ether-like site. Such diminished binding strength or even cation loss could be influenced, in particular, by the size and charge of the individual cations. Thus each cation could display unique behaviors in this case. Before discussing the redox couples in turn, we note however that the anodic and cathodic peak currents were linearly dependent upon scan rate for the complexes of Cs^+, Rb^+, K^+, and Na^+, showing the freely diffusing nature of the oxidized and reduced forms of the complexes at the electrode in each case (see Appendix 2, Figures S51, S53, S55, and S57). The case of **[VO,Ca]** is more complex and consequently is discussed last in the series.

Table 1.3. Comparison of $E_{1/2}$, $E_{p,a}$, and ΔE_p values for complete series of complexes.

Complex	pK_a of $[M(H_2O)_m]^{n+}$	$E_{1/2}$ (mV vs. $Fc^{+/0}$)	$E_{p,a}$ (mV vs. $Fc^{+/0}$)	ΔE_p (mV) [a]
[VO]	-	55	114	118
[VO,Cs]	16.34	172	270	190
[VO,Rb]	16.29	232	436	409
[VO,K]	16.06	252	312	120
[VO,Na]	14.8	241	319	138
[VO,Ca]	12.6	429	800	743

[a] ΔE_p was measured at a scan rate of 100 mV/s in all cases.

In line with the similar effective Lewis acidities and ionic radii of Cs^+ and Rb^+, the cyclic voltammetric behavior of **[VO,Cs]** and **[VO,Rb]** are rather similar (see Figure 1.11). **[VO,Cs]** undergoes redox cycling with $E_{1/2}$ = 172 mV while **[VO,Rb]** cycles at $E_{1/2}$ = 232 mV. The overall chemical reversibility of these waves appears reasonable, in that clear oxidation and reduction waves are apparent in each case. However, the electrochemical reversibility of the two systems is rather different, with a ΔE_p value of 190 mV measured in the case of **[VO,Cs]** and a much larger 409 mV measured for **[VO,Rb]**. Considering the anodic wave of **[VO,Rb]** is significantly broadened in comparison to the other waves in our study and that the peak reduction potential for the couple is shifted negative of that of **[VO,Cs]**, we anticipate that the appearance of this wave could be influenced by diminished electron transfer rates.

On the other hand, the cyclic voltammetric behavior of **[VO,K]** shows a higher degree of chemical and electrochemical reversibility, with an $E_{1/2}$ value of 252 mV and a ΔE_p value of 120 mV. This peak-to-peak separation is similar to that of the parent monometallic complex **[VO]** and suggests limited reorganization upon oxidation/reduction. This observation is consistent with the binding constants that are known to be high for incorporation of the potassium ion into 18-crown-6-like moieties.[43] With regard to reduction potential, the $E_{1/2}$ value for **[VO,K]** at 252 mV compares well with those of **[VO,Cs]** and **[VO,Rb]**, in that the more effectively Lewis acidic potassium ion results in a more pronounced shift than the less acidic cesium and rubidium ions. However, we note here that the diminished electrochemical reversibility for the wave measured in the case of **[VO,Rb]** complicates such comparisons.

Moving on to the case of **[VO,Na]**, the V(V)/V(IV) couple for this complex was observed at $E_{1/2}$ = 241 mV. The electrochemical reversibility of this wave was decreased in comparison to that

of **[VO,K]**, a phenomenon that we ascribe to the better fit of K^+ in the 18-crown-6-like site of our macrocyclic ligand that drives minimal reorganization upon oxidation to V(V). Examination of the data does not obviously suggest loss of the sodium cation from the 18-crown-6 like site upon oxidation, however, as the peak cathodic process is shifted considerably positive of that of the parent monometallic complex **[VO]** (see Figure 1.11). On the other hand, this cathodic process is visibly broadened in comparison to that of the analogous process in **[VO,K]**, suggesting that the equilibrium for binding of the cation in the crown-like site could be diminished in the V(V) form of **[VO,Na]** relative to the strong binding of Na^+ in the V(IV) form of the complex that could be reliably synthesized and isolated, as well as crystallized successfully.

In line with the placement of Ca^{2+} in our series as the most effectively Lewis acidic cation investigated, the electrochemical properties of **[VO,Ca]** were the most significantly perturbed relative to the starting monometallic complex **[VO]**. **[VO,Ca]** displays a set of oxidation and reduction waves with a very high peak-to-peak separation, ΔE_p, of 743 mV (see Figure 1.11 and see Appendix 2, Figure S58). This indicates a low degree of electrochemical and chemical reversibility in this case. Looking at the data in detail, the peak cathodic potential which nominally corresponds to re-reduction of the V(V) form of the complex produced at the electrode surface is found near 0 V vs. $Fc^{+/0}$, a position more consistent with the re-reduction of the V(V) forms of **[VO,Cs]** and **[VO,Rb]**. Considering that the isolated V(IV) form of **[VO,Ca]** is demonstrably stable on the basis of the synthetic work, the observation of a very wide peak-to-peak separation from the corresponding anodic peak potential ($E_{p,a}$) of 800 mV suggests to us that the Ca^{2+} ion is not stably bound in the V(V) form of the macrocylic complex. Under this working model, the rather dramatic positive shift of $E_{p,a}$ to 800 mV for **[VO,Ca]** (cf. $E_{p,a}$ for **[VO]** is 114 mV) is the result of the incorporation of the calcium dication but the corresponding reduction process

measured in this case cannot be used to reliably report on the properties of the V(V) form of the compound as it was not isolated in this study and may not be stable in solution. Similar to the case of the Rb^+ complex of V(V) (*vide supra*), the high degree of electrochemical irreversibility casts doubt on the stability of the V(V) form of **[VO,Ca]**.

Considering the very positive shift in the oxidation wave for **[VO,Ca]**, we became concerned that other processes beyond V(IV)/V(V) redox cycling might impact the cyclic voltammetry data obtained for this compound. Our suspicions were confirmed upon increasing our scan window to more positive potentials, in that we were able to measure a further anodic process near 1.2 V (Figure S59). As this process was not apparent in the corresponding blank electrolyte voltammogram, we tentatively assign it as a ligand centered oxidation process for our macrocyclic ligand framework. We have found that such ligand-centered processes result in decomposition of our complexes in prior work,[33,34,42] and thus the close localization of the ligand- and vanadium-centered oxidation processes for **[VO,Ca]** could diminish the ability of the CV data to report on the properties of the V(V)/V(IV) system. Scan rate dependent data, while confirming that the oxidized and reduced forms of **[VO,Ca]** are freely diffusional at the electrode surface, display greater scatter than other sets in our study. This could be consistent with electrode fouling behaviors that we measured in other heterobimetallic complexes based on phenoxide-containing macrocyclic ligands studied by our group.[33,34,42]

With this full view of the redox behaviors of the heterobimetallic complexes in our studies in hand, we wished to examine the electrochemical data for evidence supporting or disproving our hypothesis (based on the spectroscopic data) that incorporation of secondary electropositive metal cations results in diminished electron donation from the bridging phenoxide ligands to the

vanadium(IV) center in our macrocyclic complexes. Appealingly, we were able to confirm two different trends in the electrochemical data that align affirmatively with our hypothesis. First, tabulation and comparison of the $E_{1/2}$ values for the V(V)/V(IV) couples measured for all the heterobimetallic complexes could be used to estimate the influence of the effective Lewis acidity of the incorporated metal cations on the redox properties of the complexes. A satisfying linear relationship was revealed (see Appendix 2, Figure S61) by plotting $E_{1/2}$ as a function of the pK_a values of the metal aqua complexes of the corresponding incorporated metal cations and displays a slope of –56(±13) mV/pK_a. Thus, when effectively Lewis acidic metal cations are coordinated to **[VO]**, there is a uniform trend in a positively modulated potential for metal-centered oxidation. The similarity of the value of this slope to others that we have measured for metal-centered redox processes is likely attributable to the comparable nature of the macrocyclic ligands used across our recent studies.[33,34]

Second, comparison of the $E_{p,a}$ values for the V(V)/V(IV) couples measured for the complexes for which we have structural data from X-ray diffraction analysis could be used to estimate the role of the bridging phenoxide ligands in modulating the redox properties of the complexes. A second linear trend was thus obtained when plotting the $E_{p,a}$ values for the complexes as a function of the V–O(phenoxide) bond distance measured by XRD analysis (see Figure 1.12). In this plot, there is a linear correlation ($R^2 = 0.94$) between the estimated potentials required for oxidation of the V(IV) complexes to their V(V) analogues and the bond distance between the vanadium center and the bridging phenoxide donor ligands. The slope of this trendline is ca. +16 V/Å, meaning that lengthening of the V–O(phenoxide) bonds is associated with a more positive potential for vanadium oxidation in each case.

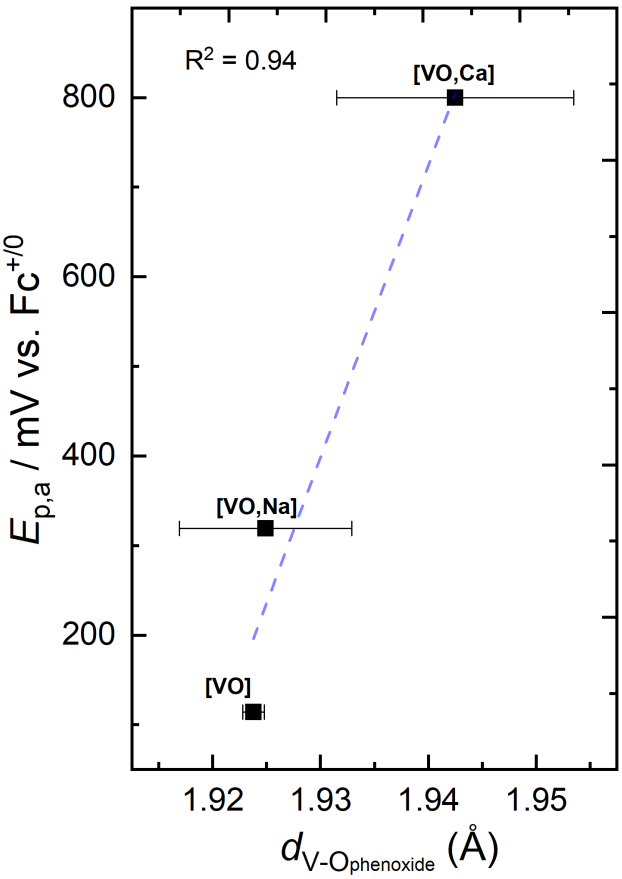

Figure 1.12. Dependence of the peak anodic reduction potentials for **[VO]**, **[VO,Na]**, and **[VO,Ca]** on V–O(phenoxide) bond length. The bond lengths for the individual compounds were derived from the structures reported here: **a03a**, **[VO]**; **a04d-No1**, **[VO,Na]**; **b31b-No7**, **[VO,Ca]**. Uncertainties associated with the bond lengths are represented with the error bars, which are the e.s.d.'s determined in the indicated structures. Details on determination of these e.s.d.'s are given in Table 1.

Taken together with the trend measured between $E_{1/2}$ and pK_a measured above, the dependence of $E_{p,a}$ on V–O(phenoxide) bond distance provides further support for our hypothesis that incorporation of metal cations into our macrocyclic vanadyl complex results in diminished electron donation from the bridging phenoxide ligands to the vanadium(IV) center. From the electrochemical data, we can confirm that the vanadium center indeed displays potentials that are

more positive for V(IV) oxidation in the heterobimetallic derivatives and vary as a function of the effective Lewis acidity of the incorporated cations. Moreover, from the dependence of potential on V–O(phenoxide) bond distance, we can confirm a direct role for the bridging phenoxide ligands in this behavior and harmonize the analysis of the heterobimetallic complexes with that of the monometallic species.

1.4 Discussion

In planning the studies described here, we hoped that incorporation of a single vanadyl ion into tunable heterobimetallic complexes would enable collection of comprehensive experimental data that could aid in identifying the origin of tuning effects measured for the complexes. Indeed, we have found that the spectroscopically addressable nature of the vanadyl ion coupled with the observable V(V)/V(IV) redox system observable for the complexes reported here afford the opportunity to explore how secondary metal cations affect the properties of the redox-active vanadium center from a variety of perspectives. Chief among our goals in this study was to leverage the paramagnetic nature of the vanadyl center to obtain comprehensive EPR data for a series of heterobimetallic complexes; the desired spectra were obtained through room temperature studies using capillaries filled with CH_3CN solutions of the compounds and avoiding a need for costly cryogenic conditions.

The relationship measured here between the measured A_{iso} values from EPR studies and the pK_a values of the corresponding aqua complexes of the incorporated secondary metals is supportive of our hypothesis that diminished donor power from the phenoxide ligands results from incorporation of the cations into the macrocyclic structure of **[VO]**. The total span of hyperfine coupling constants measured here from 274 to 280 MHz (ΔA = 6 MHz from **[VO,Cs]** to **[VO,Ca]**) is

indicative of tuning of the phenoxide donor ligands that bridge between V and **M** in all cases. Notably, inspection of the relevant literature[58] reveals that A_{iso} values for a wider range of vanadyl coordination environments and ligand donor strengths vary from 250-294 MHz. This wider range of A_{iso} values (ΔA_{iso} = 44 MHz), arising when the inner-sphere ligands to vanadium are wholly substituted, compares well with the narrower measured range of A_{iso} values (ΔA_{iso} = 6 MHz) for our own complexes. The values for our complexes appear appropriate within the full spread of literature values that is more widely varying because our complexes could be reasonably expected to span a much more compact range of properties since the identity of the core ligand framework around the vanadium center is invariant in the complexes and only varies due to binding of electropositive metal cations in the nearby crown-ether-like site. We also confirm here that replicate measurements and simulations suggest the uncertainty on our fitted A_{iso} values is ±0.1 MHz (reported as ±1σ), suggesting that we can reliably interpret the span of values obtained for the full series of **[VO,M]** complexes (see Appendix 2, Figure S45 and Table S2).

In this work, we chose to quantify A_{iso} values through EasySpin simulation of our experimental spectroscopic data. These data were obtained in liquid solution, giving rise to spectra that could be readily compared amongst themselves. Our viewpoint for the analysis carried out here relies on the prior observation that the equatorial contributions to hyperfine coupling (A_x and A_y) in the case of the vanadyl ion have been shown to be quite sensitive to ligand donor power as well as geometric perturbations.[29,62] From our X-ray crystallographic data collected on **[VO]**, **[VO,Na]**, and **[VO,Ca]**, we can observe geometric changes in the bimetallic cores of our complexes as a function of the identity of the secondary metals. In particular, the phenoxide-to-phenoxide O•••O distances (denoted O1•••O2 in Table 1) decrease from 2.650(2) Å for **[VO]** to 2.604(4) Å for **[VO,Na]** and 2.583(5) Å for **[VO,Ca]**. We have noted similar contractions in our prior work with

heterobimetallic complexes of uranyl[27] and zinc.[63] In any case, the EPR data described here cannot be used to distinguish between changes in ligand donor power and the associated structural changes in the heterobimetallic complexes. We note that these are synergistic changes however, and that future work could additionally focus studies in frozen solution to distinguish specific axial and equatorial effects for the vanadyl ion in these complexes. In this work, we have found that isotropic hyperfine coupling constant values do report, however, on the donor power in the equatorial plane as a function of the identity of the incorporated secondary metal cations.

To further deepen the connection between the structural and spectroscopic work carried out here, we also compared the vibrational data on the V–O_{oxo} asymmetric stretches measured for **[VO]**, **[VO,Na]**, and **[VO,Ca]** to the V–O_{oxo} bond distances in these compounds as determined by XRD. We wished to carry out this analysis for two reasons. First, it could allow us to glean information in the context of Badger's Rule,[64] which states that the strength of a given bond (in terms of stretching frequency) is correlated with the bond length, where shorter bonds are stronger bonds. Second, this analysis could be used to bridge the gap between the spectroscopic properties of the monometallic complex **[VO]** and the heterobimetallic complexes studied here, bringing their vibrational data onto a common axis for interpretation. In accord with our expectations, we found a tight linear correlation (see Figure 1.13) between the V–O_{oxo} bond distance and V–O_{oxo} stretching frequency, wherein the measured contraction of this bond is correlated with increased V–O_{oxo} stretching frequencies. Notably, this trend appears reliable across the monometallic and bimetallic complexes for which we have structural data, implying support for our hypothesis regarding induced diminishment of the phenoxide electron donor power to vanadium upon incorporation of the secondary cations. This is because the data would suggest that the phenoxides are best able to

serve as electron donors when no secondary metal is bound in the crown-ether-like site of our complexes.

This conclusion is in accord with the positive shifts in reduction potentials that we have measured in the current work, and also that we have measured in prior work for heterobimetallic uranyl complexes.[27] Incorporation of more effectively Lewis acidic cations (especially trivalent cations such as Y^{3+}) results in more facile reduction of U(VI) to U(V) and also in shift of the potential for V(IV) to V(V) oxidation to more positive values. These parallel findings underscore the shared features of the vanadyl and uranyl ions, species that have long been viewed through a common lens in light of their similar, strongly bonded terminal oxo ligands. Additionally, we anticipate that the approach of using a paramagnetic probe to understand electronic changes brought about by secondary metal cations appears to be a useful strategy. As the U(V) oxidation state is associated with $S = ½$ species, exploration of such effects in this less common oxidation state of uranium appears to be worthy of investigation.

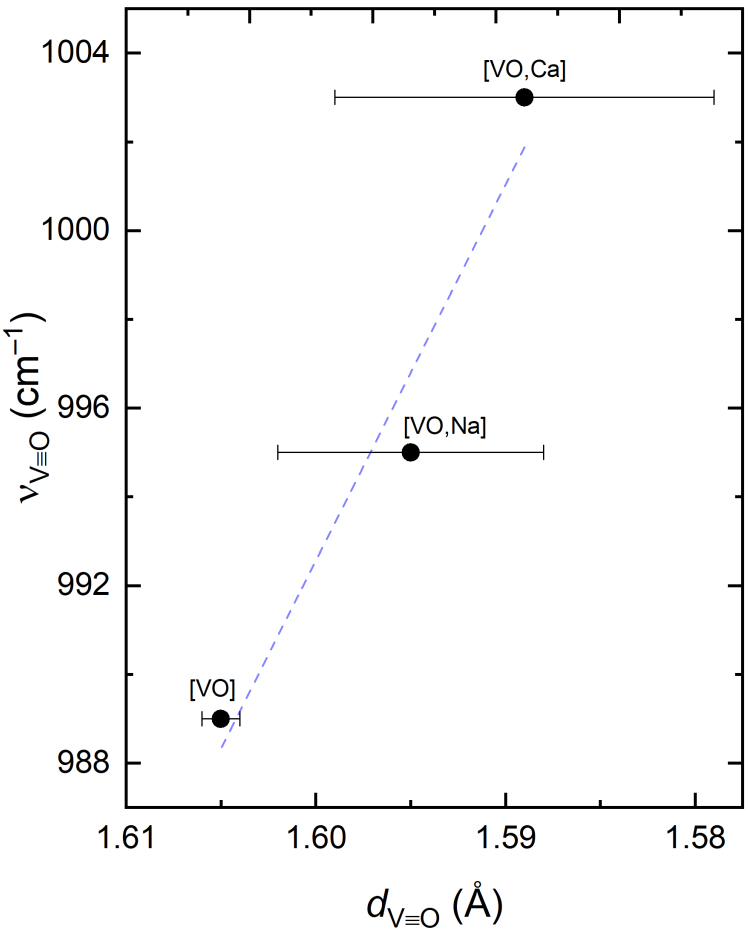

Figure 1.13. Dependence of the V–O stretching frequency measured with infrared spectroscopy on V–O bond length. The bond lengths for the individual compounds were derived from the structures reported here: **a03a**, **[VO]**; **a04d-No1**, **[VO,Na]**; **b31b-No7**, **[VO,Ca]**. Uncertainties associated with the bond lengths are represented with the error bars, which are the e.s.d.'s determined in the indicated structures. Details on determination of these e.s.d.'s are given in Table 1.

Bringing the threads together, the primary lesson from this work is that installation of secondary metal cations into complexes in which those cations interact with a central (often redox-active) metal through bridging ligands results in changes in the ability of those bridging ligands to donate to the central metal. Although this claim has been implicit in our prior work and perhaps that of

other investigators in the field, the use of the paramagnetic vanadyl ion as the central species in this work has enabled us to obtain synergistic structural, spectroscopic, and electrochemical support for the hypothesis. The conclusion that this is a valid hypothesis is important because it could enable further development of tunable heterobimetallic complexes that rely on incorporation of secondary electropositive metals to afford the desired tunability. In our own ongoing work, this concept is being applied in several projects, all united under the umbrella of leveraging tuning effects for particular purposes, including control over the reduction potentials of actinide elements as these are important drivers in the nuclear fuel cycle. The present work can also be distinguished by its experimentally derived insights into the properties of the vanadyl complexes explored here. It is our hope that the support offered for our hypothesis will spark further development of multimetallic coordination complexes and favor the development of reliable models to interpret the behaviors displayed by such species.

1.5 Conclusion

Spectroscopic measurements of heterobimetallic complexes using the vanadyl ion as a probe demonstrate that attenuated electron donor power results from ligands that bridge between the vanadium center and the incorporated secondary metal cations. Use of the chemically robust vanadyl ion as a spectroscopic reporter has enabled the measurements made here, and these in turn highlight that tunable properties become uniquely accessible through incorporation of secondary metal cations; these cations can themselves display a wide range of structural properties and effective Lewis acidities, making a wide space for future explorations on this platform. The placement of two metal centers in close proximity results in electronic tuning that appears to be related to intermetallic distance as well as the effective Lewis acidities of the secondary metal cation partners. These observations highlight that both the spatial arrangement of the metals

involved as well as the influence of interactions driven by bridging ligands should be considered in future efforts aimed at generating tunable multimetallic materials.

1.6 Synthetic Procedures

Synthesis of [VO]. To a suspension of **[H_2,Ba]** (0.40 g, 0.46 mmol) in $CHCl_3$ prepared according to reference 18 was added an excess of guanidinium sulfate (0.49 g, 2.28 mmol) dissolved in water. The mixture was allowed to stir for 72 h, after which the organic layer was separated and concentrated to a total volume of 10-15 mL. A solution in $CHCl_3$ containing 1 equiv. of [$VO(acac)_2$] (0.12 g, 0.46 mmol) was added slowly, followed by 4 drops of triethylamine. The solution was allowed to stir at room temperature for 2 h, at which time the solution was concentrated and chilled (–20°C) overnight to encourage precipitation of the product. After chilling overnight, ice-cold ether was added dropwise to the flask, and the green precipitate was isolated by vacuum filtration. Yield: 76% (0.18 mg, 0.35 mmol). Anal. Calcd for $C_{24}H_{28}N_2O_7V$ (**[VO]**): C 56.81, H 5.56, N 5.52; Found: C 54.46, H 5.56, N 5.71. Calcd for $C_{24}H_{28}N_2O_7V + H_2O$: C 54.86, H 5.76, N 5.33. This analysis is consistent with the incorporation of 1 equiv. of H_2O during sample transport and handling.

Synthesis of [VO,Na]. 1 equiv. of Na(OTf) salt (33.9 mg, 0.20 mmol) dissolved in 10 mL CH_3CN was added to a 10 mL CH_3CN solution containing **[VO]** (100 mg, 0.20 mmol). The combined solution was allowed to stir overnight. The product was then filtered and isolated by *in vacuo* solvent removal. This compound could also be isolated by vapor diffusion of diethyl ether into a concentrated CH_3CN solution, resulting in crystals that could be isolated by vacuum filtration. Yield: 89% (119 mg, 0.18 mmol). Anal. Calcd for $C_{25}H_{28}F_3N_2NaO_{10}SV$ (**[VO,Na]**): C 44.19, H 4.15, N 4.12; Found: C 44.09, H 4.27, N 4.59. Calcd for $C_{25}H_{28}F_3N_2NaO_{10}SV$ + 0.3

CH_3CN: C 44.45, H 4.21, N 4.66. This analysis is consistent with the incorporation of 0.3 equiv. of CH_3CN during preparation of **[VO,Na]**, as well as the observation of coordinated CH_3CN in the solid-state structure of the compound.

Synthesis of [VO,Ca]. 1 equiv. of $Ca(OTf)_2$ salt (33 mg, 0.10 mmol) dissolved in 10 mL CH_3CN was added to a 10 mL CH_3CN solution containing **[VO]** (50 mg, 0.10 mmol). The combined solution was allowed to stir overnight. The product was then filtered and isolated by *in vacuo* solvent removal. This compound could also be isolated by vapor diffusion of diethyl ether into a concentrated CH_3CN solution, resulting in crystals that could be isolated by vacuum filtration. Yield: 92% (77 mg, 0.91 mmol). Anal. Calcd for $C_{25}H_{28}F_3CaN_2O_{10}SV$ (**[VO,Ca]**): C 36.93, H 3.34, N 3.31; Found: C 36.92, H 3.64, N 3.52.

Synthesis of [VO,Cs]. 1 equiv. of Cs(OTf) salt (56 mg, 0.20 mmol) dissolved in 10 mL CH_3CN was added to a 10 mL CH_3CN solution containing **[VO]** (100 mg, 0.20 mmol). The combined solution was allowed to stir overnight. The product was then filtered and isolated by *in vacuo* solvent removal. This compound could also be isolated by vapor diffusion of diethyl ether into a concentrated CH_3CN solution, resulting in a powder that could be isolated by vacuum filtration. Yield: 88% (137 mg, 0.17 mmol). Anal. Calcd for $C_{25}H_{28}CsF_3N_2O_{10}SV$ (**[VO,Cs]**): C 38.04, H 3.58, N 3.55; Found: C 38.35, H 4.03, N 3.63. Calcd for $C_{25}H_{28}CsF_3N_2O_{10}SV$ + 0.1 Et_2O: C 54.86, H 5.76, N 5.33. This analysis is consistent with the observation of Et_2O in the ^1H NMR spectrum of isolated **[VO,Cs]**, which was presumably incorporated during isolation of the solid compound.

***In Situ* Preparation of [VO,M] Complexes**. In a typical experiment, 1 equiv. of the desired metal triflate salt was dissolved in 10 mL of CH_3CN and added to a 10 mL solution in CH_3CN

containing **[VO]** (100 mg, 0.20 mmol). The resulting homogeneous mixture was allowed to stir overnight, filtered, and used as needed for experimentation on the *in situ* produced complex.

1.7 Acknowledgements

The authors thank the generous faculty of the American Crystallographic Association's Summer Course in Chemical Crystallography for helpful discussions and technical assistance with the structural data reported in this manuscript. The authors also thank Sarah Neuenswander for assistance with NMR spectroscopy. This work was supported by the U.S. Department of Energy, Office of Science, Office of Basic Energy Sciences through the Early Career Research Program (DE-SC0019169). C.M.D. was supported by the Beckman Scholars Program at the University of Kansas, funded by the Arnold & Mabel Beckman Foundation. X-ray facilities at Wake Forest University were supported by the US National Science Foundation through award CHE-0234489.

Chapter 2

Synthetic and Spectroscopic Studies Targeting a Heterobimetallic Vanadyl Complex Containing the Lithium Monocation

This chapter is adapted in part from a manuscript that has been accepted for publication:
Dopp, C.M., Golwankar, R.R., Kelsey, S.R., Douglas, J.T., Erickson, A.N., Oliver, A.G., Day, C.S., Day, V.W., and Blakemore, J.D., Vanadyl as a Spectroscopic Probe of Tunable Ligand Donor Strength in Bimetallic Complexes, *Inorg. Chem.,* **2023**, *in press*;
doi: 10.1021/acs.inorgchem.3c00724; also available as a pre-print on *ChemRxiv*,
doi: 10.26434/chemrxiv-2022-t8p04

2.1 Abstract

In this chapter, the synthesis and characterization of a heterobimetallic complex pairing the vanadyl ion, $[VO]^{2+}$, with the lithium monocation (Li^{+}). Studies of this complex containing lithium can be distinguished from those of the other cations mentioned in Chapter 1 in part due to the apparent placement of **[VO,Li]** as an outlier in results from all of the spectroscopic characterization methods utilized here. Once the heterobimetallic analogue was synthesized using LiOTf, a complete set of spectroscopic information was obtained with electronic absorption, infrared (IR), and electronic paramagnetic resonance (EPR) spectroscopies. Along with interrogation of the redox properties of the complex with cyclic voltammetry experiments, these studies were conducted in order to better understand the behavior of the lithium ion in comparison to the others. The results of these studies are presented and analyzed in this chapter, with the overall conclusion being that lithium behaves strangely compared to the other ions. This is attributable to its small size, which drives a mismatch with the rather large 18-crown-6-like receptor site in the monometallic vanadyl precursor. The apparent size mismatch results in solution speciation that is not fully understood at this time; in essence, the site(s) at which the lithium cation interacts with the vanadyl ion cannot be confidently assigned.

2.2 Results

*Synthesis of the **[VO,Li]** analogue*

The Li^{+} containing heterobimetallic complex was generated using the same divergent synthetic pathway as outlined in Chapter 1. **[VO]** monometallic and LiOTf were stirred together in a 1:1 ratio to generate **[VO,Li]** *in situ*. This material was then utilized in the characterization methods that follow.

Electronic Absorption Spectroscopy

As mentioned in Chapter 1, electronic absorption spectroscopy (EAS) experimentation was pursued with the Li^+ analogue, but its low solubility and poor fit in a trendline with its neighboring cations (when considering their Lewis acidity) were concerns that merited removal of the complex from further consideration of tuning behaviors. Figure 2.1 depicts the obtained spectroscopic measurements in the UV-visible region for **[VO,Li]**, along with the corresponding Beer's Law plot. A charge transfer band is observed at λ_{max} = 384 nm and a d-d transition at λ_{max} = 585 nm, both values of modest energy when considering the quite Lewis acidic nature of Li^+ (pK_a = 13.8). When examining the slope of both trendlines in Figure 1.7, we would expect these values to be closer to 360 nm and 450 nm, respectively.

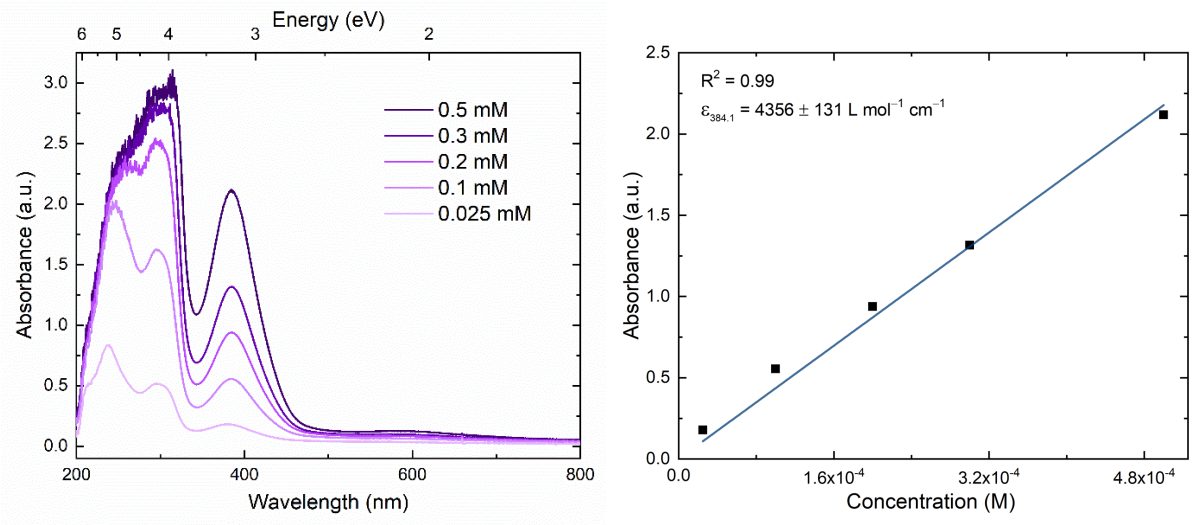

Figure 2.1. Left panel: Electronic Absorption Spectroscopy data for **[VO,Li]**. Right panel: Absorbance vs. concentration plot of **[VO,Li]** in CH_3CN monitored at 384.1 nm.

Infrared Spectroscopy

Infrared spectra of **[VO,Li]** were obtained in both the solution and solid states. Solution-phase measurements were conducted at 1.25 mM, a value that is only a fraction of the 10 mM concentration at which other mono-valent cations mentioned in Chapter 1 were measured. This is attributable to the poor solubility of the Li^+ analogue in comparison to other heterobimetallics. The low solubility, in practical terms, resulted in the requirement of extensive dilution to obtain homogeneous solutions. The ν(V≡O) stretch for this solution-phase material is, however, observable at 993 cm^{-1} as a weakly absorbing feature (see Figure 2.2). Solid-state samples were prepared by removing the solvent *in vacuo*, affording powdered material suitable for analysis. The ν(V≡O) stretch for this material was observed at 989 cm^{-1}, as seen in Figure 2.3. Furthermore, Figure 2.4 provides a visual comparison of **[VO,Li]** solution-phase IR data in comparison with the cations featured in Chapter 1, specifically through the relation between the ν(V≡O) stretch and Lewis acidity. As apparent from this figure, the lithium complex does not follow the trend measured for the other complexes. This suggests that the lithium cation interacts with the vanadyl core in a different manner than the other complexes in the series.

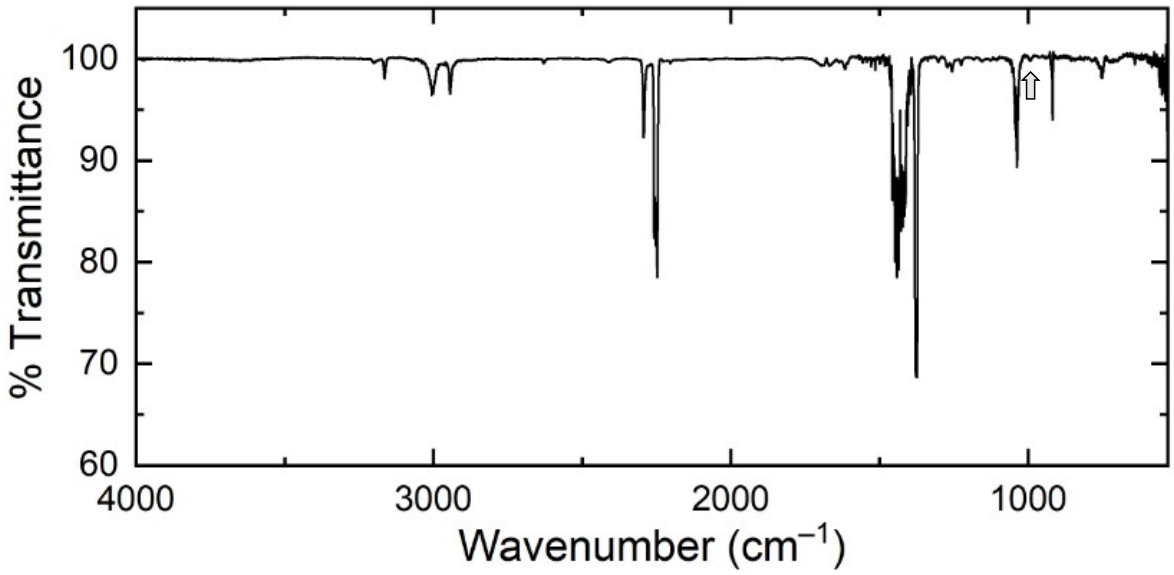

Figure 2.2. Solution-phase infrared spectrum of 1.25 mM solution of **[VO,Li]** in CH_3CN. Block arrow indicates the apparent V–O stretch.

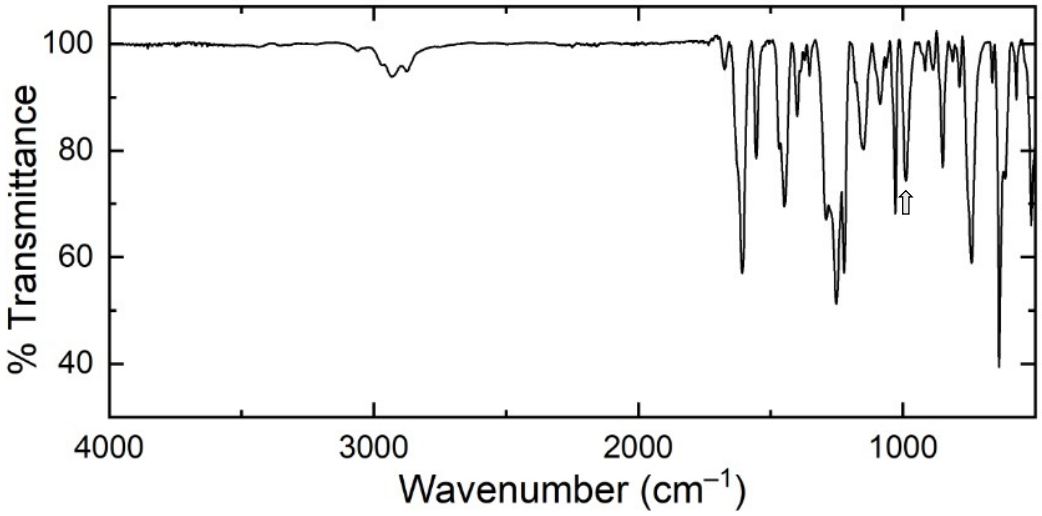

Figure 2.3. Solid-state infrared spectrum of **[VO,Li]**. Block arrow indicates V–O stretch.

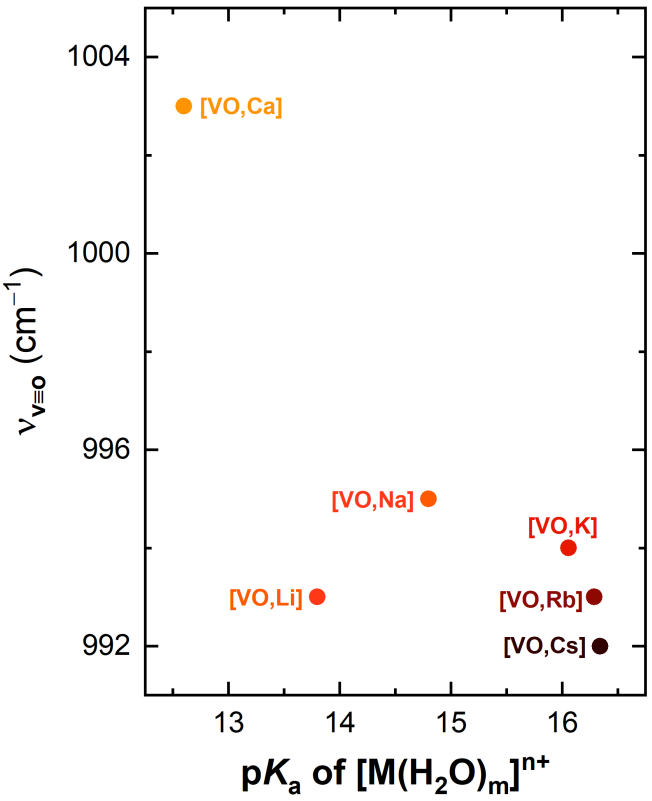

Figure 2.4. Dependence of ν(V≡O) solution-phase IR stretch on Lewis acidity.

Electronic Paramagnetic Resonance

EPR experiments for **[VO,Li]** were conducted in an identical fashion to the measurements carried out in Chapter 1. A 10 mM solution of **[VO, Li]** was prepared in acetonitrile under inert atmosphere in an N_2 glove box. A capillary tube was then filled with this solution, plugged, and then inserted into an EPR tube for experimentation. See Figure 2.5 for the experimental measurement conducted at room temperature (25°C) in addition to a simulated spectrum prepared using EasySpin. After obtaining these data, we next related experimental outcomes to one another, such as examining the relationship between *g*-value and A_{iso}, as well as A_{iso} vs. pK_a. Figures 2.6

and 2.7 illustrate these dependencies for the mono- and di-valent series of Chapter 1 while showing clearly that Li^+ is a distinct outlier in both plots. These findings underscore our conclusion that the lithium cation interacts differently with the paramagnetic vanadyl core than the other cations presented in Chapter 1.

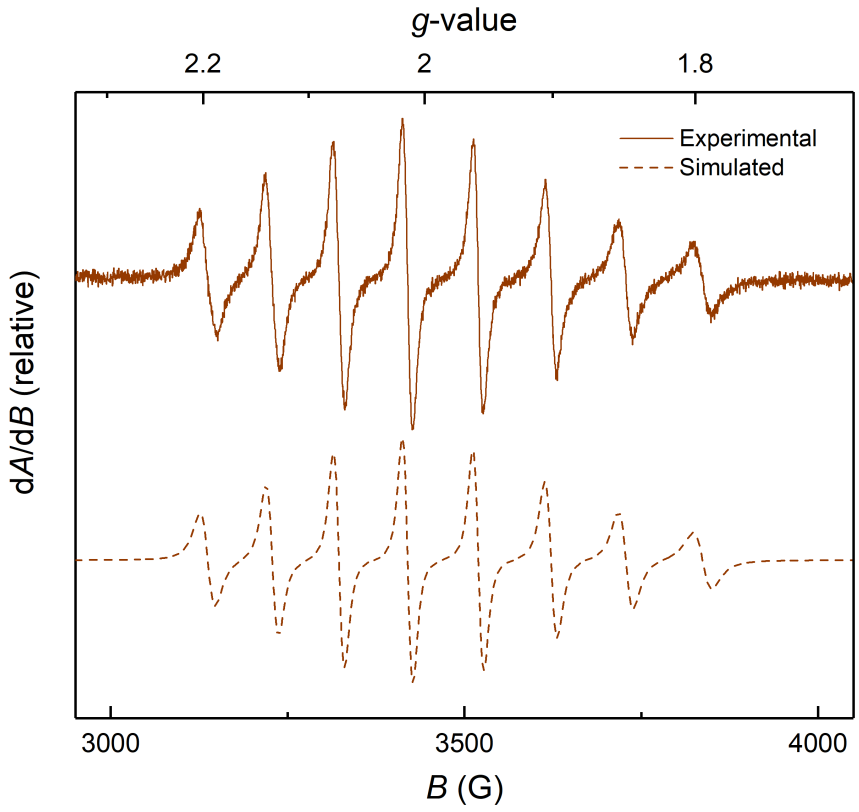

Figure 2.5. Experimental: X-band EPR spectrum of **[VO,Li]** 10mM solution in MeCN (Temperature = 298 K, Frequency = 9.6405 GHz, Power = 2mW). Simulated: Easyspin simulation using *garlic* function. Best fit values: $g_{\|}$= 1.97, $g_{\perp}$ = 1.98, A_{avg} = 275.9 MHz, $A_{\|}$ = 349.5 MHz, logtcorr = −9.30. RMSD = 0.026.

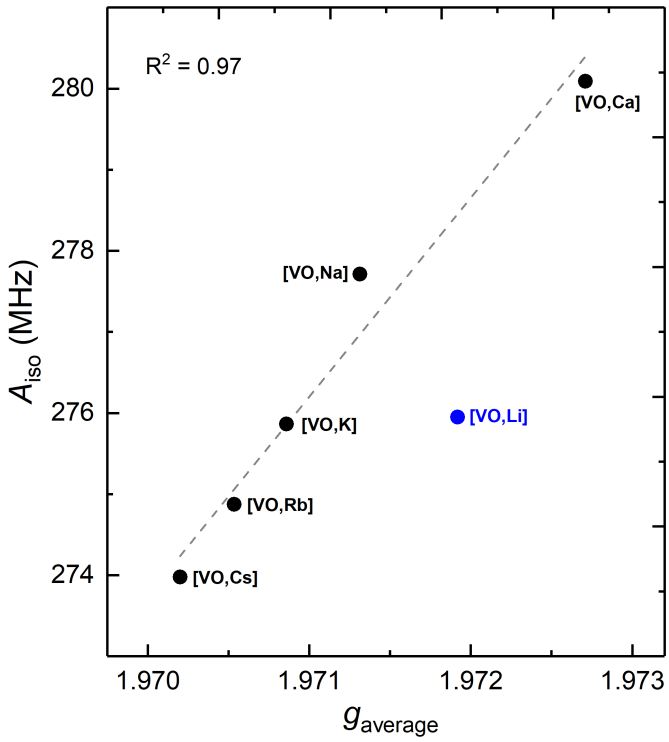

Figure 2.6. Plot of isotropic *A* values as a function of the average *g*-value.

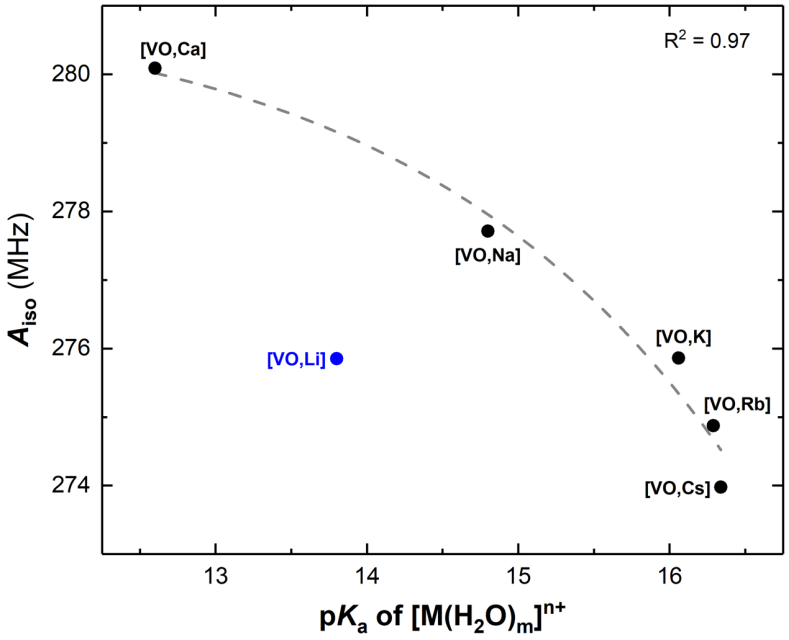

Figure 2.7. Plot of isotropic *A* values as a function of Lewis acidity.

Electrochemical Studies

Cyclic voltammetry experiments with **[VO,Li]** proved to be just as interesting as the spectroscopic methods used to probe the complex. These experiments were conducted at a 2 mM concentration in 0.1 M $[^nBu_4]^+[PF_6]^-$ in acetonitrile. As mentioned in Chapter 1, monometallic **[VO]** exhibits an $E_{1/2}$ value of 55 mV vs $Fc^{+/0}$. This $E_{1/2}$ value shifts by less than 20 mV total to just 68 mV vs $Fc^{+/0}$ upon incorporation of Li^+, as seen in Figure 2.8. This shift is incredibly modest as compared to what would be expected in relation to the Lewis acidity of this secondary metal. Considering the reduction potential measurements presented in Table 1.3, we would expect to observe the process for the **[VO,Li]** complex near 350 mV vs $Fc^{+/0}$ if the lithium cation were exerting a Lewis acidic effect similar to those found for the other cations. As solubility was an issue, scan rate dependent studies could be performed only by wiping the working electrode clean between each scan to avoid the influence of electrode fouling (see Figure 2.9). Nonetheless the data obtained from these scan rate dependent studies confirm that both the oxidized and reduced forms of **[VO,Li]** are freely diffusing at the electrode surface.

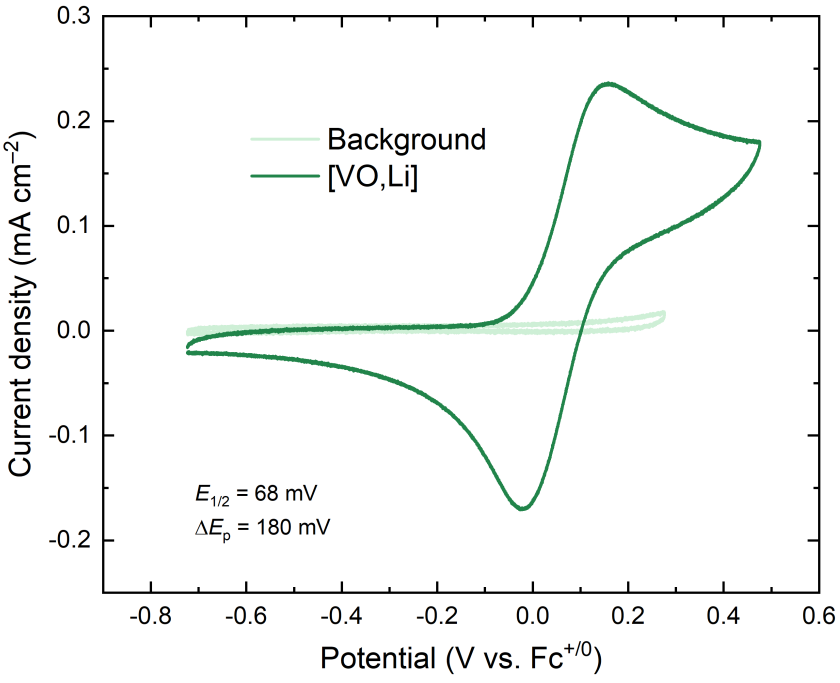

Figure 2.8. CV data for **[VO,Li]** in CH_3CN (0.1 M $[^nBu_4]^+[PF_6]^-$, 100 mV/s).

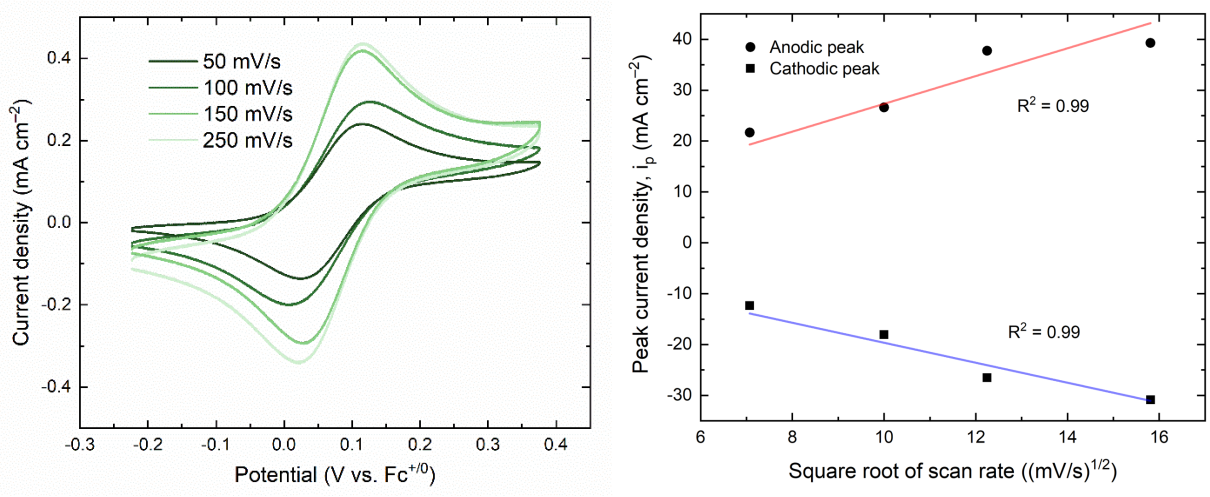

Figure 2.9. Left panel: scan rate dependence data for **[VO,Li]**. Right panel: plot of peak current density vs. (scan rate)$^{1/2}$, demonstrating the diffusional nature of the oxidized species involved.

2.3 Discussion

There exists an overarching theme amongst the data collected for **[VO,Li]** this chapter: poor solubility leads to skewed and unexpected results. However, we decided this issue must be probed further, and without a crystal structure, we must look to the literature to find existing explanations. One possibility for such insolubility may be a poor size match between the Li^+ ion and the [O_6] binding cavity. Studies in the literature point to this small ion having a greater affinity for a 15-crown-5 or an 8-crown-4 species.[43] Because of this difference in size, it is possible that the Li^+ cation dissociates from the crown in solution and during redox activity. Another explanation for such strange behavior is the possibility that Li^+ interacts with the terminal oxo present on vanadium.[44] Either of these ideas are feasible and open discussion up with regards to what is truly happening in solution. We know that addition of Li^+ causes shifts in the measured properties versus what would be expected for the pure monometallic complex, so certainly Li^+ is interacting with the precursor in some way. In cyclic voltammetry, for example, **[VO,Li]** shifts 68 mv vs $Fc^{+/0}$, a paltry 13 mV more positive than **[VO]**. This suggests some sort of equilibrium between bound and unbound cation, or that the cation is simply bound in another fashion, such as a direct interaction with the oxo moiety. Figures 1.7, 2.4, 2.6, and 2.7 exhibit **[VO,Li]** being nonconforming to the otherwise certain trends that exist in various spectroscopic methods. The UV-visible data discussed in Chapter 1 suggests incomplete binding as both the charge transfer and d-d transitions for **[VO,Li]** were expected to be found at higher energies than those displayed from the obtained experimental data. By extrapolating the linear fit curve, **[VO,Li]** is expected to have a CT band of near 3.35 eV in energy, but instead this value is closer to 3.25 eV. In IR spectroscopy, one would come to expect **[VO,Li]** to have a higher energy ν(V≡O) stretch than the bimetallics containing less Lewis acidic secondary metals, as the attenuated donor power of the bridging ligands results

in a stronger pull of the vanadium on the electron density donated by the oxo oxygen. However, if Li^+ were to bind to the oxo, its Lewis acidic properties would pull that electron density towards itself, resulting in a weaker than expected bond between vanadium and oxygen. In EPR spectroscopy, the A_{iso} value for **[VO,Li]** does not appear to be on trend with its neighboring complexes either. A_{iso}, the isotropic hyperfine coupling constant, is a value that directly correlates with bridging ligand donor strength; the lower this value, the stronger the bridging ligand donor strength. As **[VO,Li]** does not fit into either plot shown in Figures 2.6 or 2.7, the conclusion can be drawn that the ligand donor strength of the framework of the Li^+ analogue is not attenuated in the same manner that the other bimetallics are. These studies together all tie into the conclusion that **[VO]** and LiOTf do not exhibit clean reactivity due to the lithium cation's lack of binding affinity for such a large crown.

2.4 Conclusions

Following the interrogation of spectroscopic and electrochemical properties of **[VO,Li]**, it can be concluded that Li^+ is not a good fit for binding to form the targeted multimetallic system. The large size difference between this secondary metal cation and the 18-crown-6 binding site suggests that Li^+ falls out of this cavity and/or interacts with the terminal oxo moiety on vanadium. Either of these possibilities may result in the strange spectroscopic behavior observed in UV-Vis, IR, and EPR spectroscopic experiments, in addition to the modest $E_{1/2}$ value of 68 mV vs $Fc^{+/0}$ observed in cyclic voltammetry. To further probe a lithium-containing heterobimetallic vanadyl complex, it will be necessary to construct the ligand framework in a manner that better suits the small cation, such as the use of a smaller crown-like site.

Chapter 3

Interrogating the Spectroscopic Influence of Trivalent Lewis Acidic Cations on the Vanadyl Moiety

3.1 Abstract

Throughout the work presented in this thesis, we have probed the effects of several Lewis acidic cations on the vanadyl ion, including both mono- and di-valent cations. In order to expand on the previous work and further investigate Lewis acid tuning effects in heterobimetallic complexes, considering incorporation of trivalent secondary metals was an obvious next step. This chapter reports the synthesis of a small family of heterobimetallic vanadyl complexes that feature La^{3+}, Y^{3+}, and Lu^{3+} as incorporated secondary metal cations. ^{1}H nuclear magnetic resonance (NMR) experiments have yielded spectra that are similar to those for the analogues reported in Chapter 1, suggesting that the added trivalent cations do bind and interact with the monometallic vanadyl starting material; little else can be confirmed about the structures of the adducts of the trivalent secondary cations, however, due to the paramagnetic nature of the samples. Therefore, other spectroscopic techniques have been utilized to quantify the properties of the adducts. Solution-phase infrared spectra of the adducts exhibit a shift in ν(V≡O) towards higher wavenumbers, a trend that agrees well with data on the adducts reported in Chapter 1. In addition, electronic absorption spectroscopy confirms a linear relationship between the energies of charge transfer transitions for the adducts and the Lewis acidities of the incorporated cations. To compare with mono- and di-valent cations, **[VO,Na]** and **[VO,Ca]** data points have been included in trendline analyses to enable comparison across the cations' charges explored here. We conclude that tuning effects in our vanadyl complexes are accessible for mono-, di-, and tri-valent cations and that the trivalent cations appear to exert the largest tuning effects, as could be predicted on the basis of other work from our group.[33,34,63]

3.2 Results

Synthesis and NMR characterization of trivalent heterobimetallic complexes

To expand the existing library of heterobimetallic vanadyl complexes, analogues containing trivalent secondary cations were synthesized using the same methodology as that previously detailed in Chapter 1. To derive complexes containing La^{3+}, Y^{3+}, and Lu^{3+}, **[VO]** monometallic and the corresponding metal triflate salts were combined in acetonitrile in a 1:1 fashion. This synthetic procedure generates the desired product *in situ*, which was subjected to spectroscopic characterization as described below.

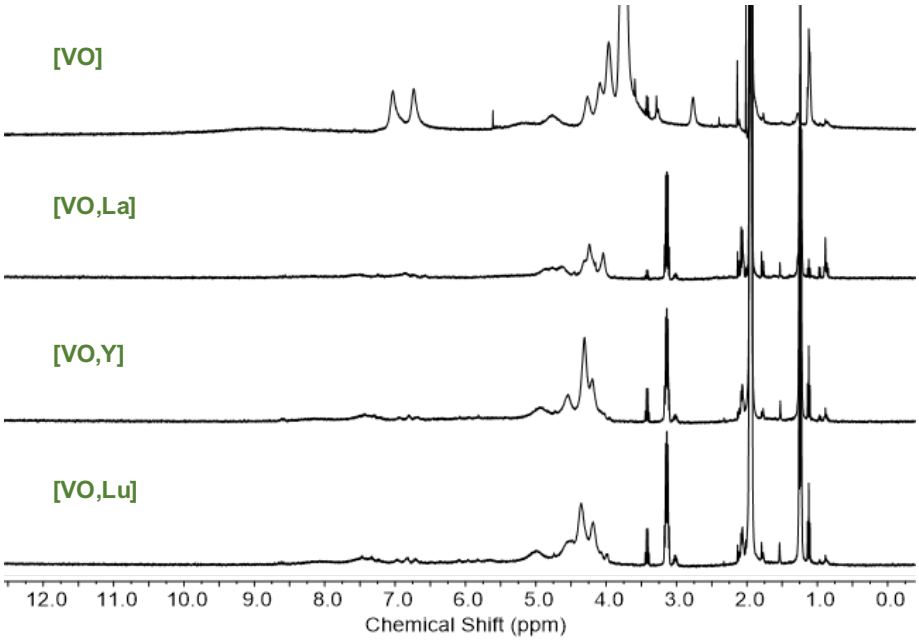

Figure 3.1. ^{1}H NMR spectrum (400 MHz, CD_3CN, 298 K) of **[VO], [VO,La], [VO,Y],** and **[VO,Lu]**. Grease (δ0.96, 0.88), diethyl ether (δ= 3.42 ppm, δ = 1.12 ppm), and water (δ= 2.13 ppm) impurities are found in the NMR solvent.

Figure 3.1 allows for comparison of the ^{1}H NMR spectra for the monometallic precursor **[VO]** and the adducts of trivalent cations. While these complexes are paramagnetic and alter the nature of the NMR spectra that may have been expected, there are still interpretations that can be extracted from the data. For example, the signal at 3.78 ppm in the monometallic spectrum apperas to undergo a shift to 4.04 ppm upon incorporation with La^{3+}. In additon, the signals present throughout the aromatic region broaden, resulting in lower apparent signal intensities upon binding with a trivalent metal. Analysis of these NMR spectra lead to the conclusion that the monometallic complex has reacted with the cations, but the completeness of the reactions cannot be judged using this method. We therefore moved on to electronic absorption spectroscopy.

Electronic Absorption Spectroscopy

UV-Visible data obtained on the *in situ* generated trivalent complexes revealed two distinct bands, a charge transfer (CT) and a d-d transition. Instrument capabilities permitted only the CT band to be probed further, as an in-depth analysis of the d-d band could require the use of an instrument with better signal-to-noise characteristics beyond 600-800 nm. Figures 3.2-3.4 reveal spectra for each trivalent adduct complex at concentrations ranging from 0.025 to 0.5 mM, along with the corresponding absorbance vs. concentration plots to determine molar absorptivity.

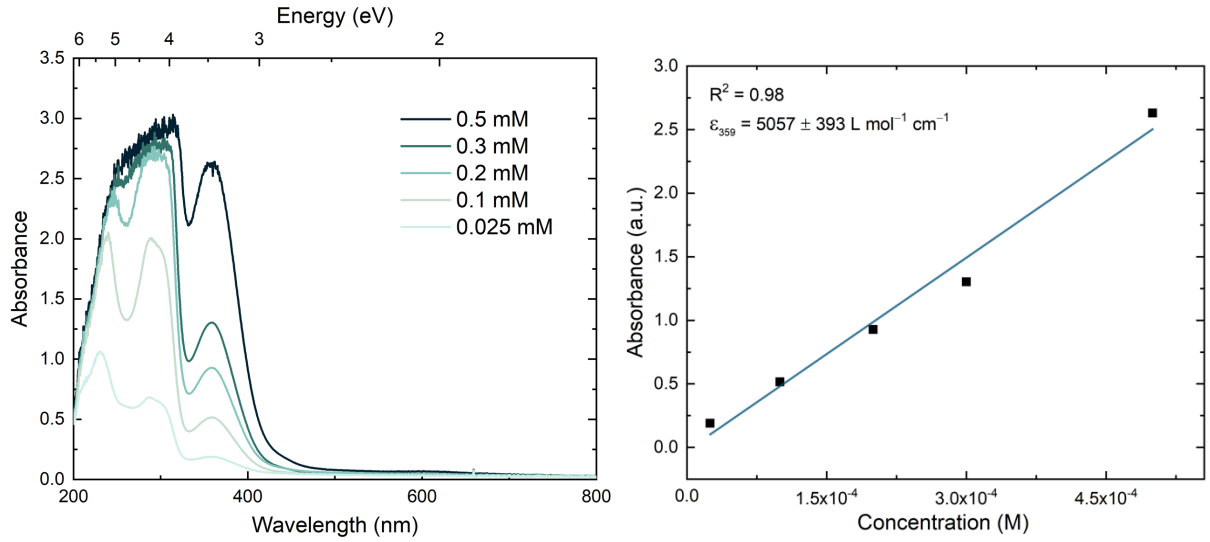

Figure 3.2. Left panel: Electronic absorption spectra of **[VO,La]** in CH_3CN. Right panel: Absorbance vs concentration plot of **[VO,La]** in CH_3CN monitored at 359 nm.

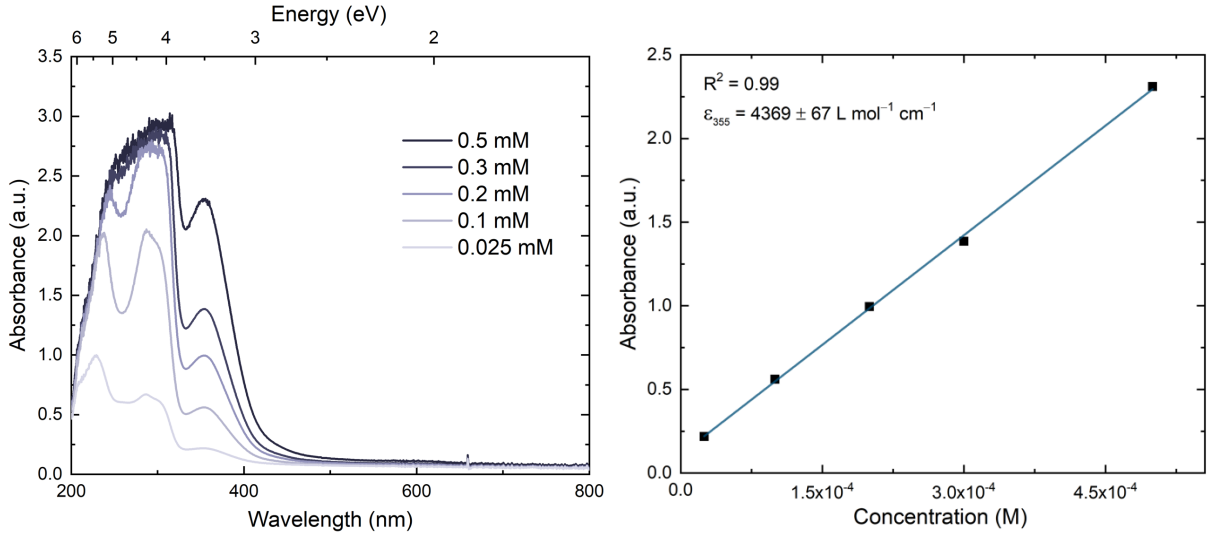

Figure 3.3. Left panel: Electronic absorption spectra of **[VO,Y]** in CH_3CN. Right panel: Absorbance vs concentration plot of **[VO,Y]** in CH_3CN monitored at 355 nm.

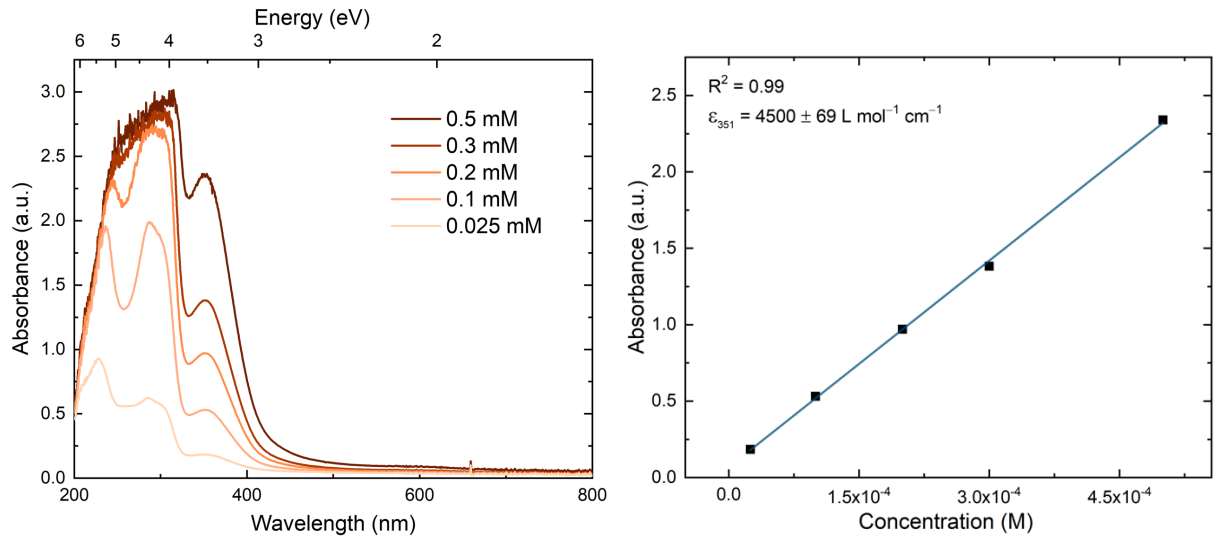

Figure 3.4. Left panel: Electronic absorption spectra of **[VO,Lu]** in CH_3CN. Right panel: Absorbance vs concentration plot of **[VO,Lu]** in CH_3CN monitored at 351 nm.

Each of these figures reveals a linear relationship between absorbance and concentration, leading to the straightforward determination of molar absorptivity. There also exists a linear relationship between the energy of the CT band and pK_a of incorporated secondary Lewis acid, as seen in Figure 3.5. **[VO,Na]** and **[VO,Ca]** are included to convey that this trend exists not only within the trivalent ions, but across the entire series of compounds explored here. The family of trivalent, highly Lewis acidic complexes exhibit higher CT energy than any of the previously synthesized analogues, but the slope of this linear relationship, –31 ± 3 meV/pK_a, remains similar to the –30 ± 5 meV/pK_a slope of the mono- and di-valent series in Chapter 1. This suggests that the La^{3+}, Y^{3+}, and Lu^{3+} ions bind in the [O_6] crown in the same fashion as in previous studies. With this knowledge in hand, we moved on to infrared spectroscopy to interrogate the ν(V≡O) stretch.

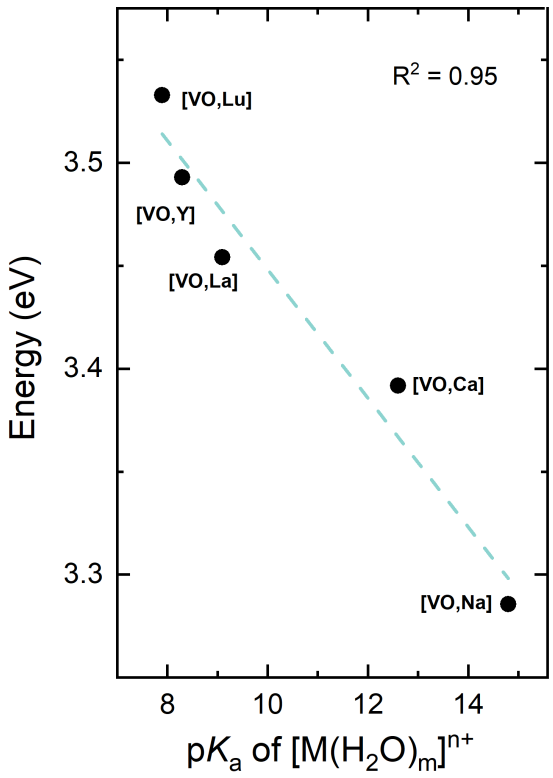

Figure 3.5. Dependence of CT band energy on Lewis acidity of the secondary metal cation.

Infrared Spectroscopy

In situ prepared samples were studied by FTIR spectroscopy in order to interrogate for the possible cation-induced shifts in the ν(V≡O) stretch. **[VO,La]** exhibits ν(V≡O) at 1009 cm^{-1}, a shift of 20 cm^{-1} from the monometallic precursor. This spectrum, along with those corresponding to **[VO,Y]** and **[VO,Lu]** is shown in Figures 3.6-3.9. Similar to Chapter 1, there exists a linear relationship between ν(V≡O) and the pK_a value of incorporated secondary ion, as seen in Figure 3.10. The location of the V≡O stretch, along with λ_{max} values for the series, can be found in Table 3.1.

Complex	pK_a of $[M(H_2O)_m]^{n+}$	λ_{max} (nm)	$\nu V{\equiv}O$ (cm^{-1})
[VO]	-	386	989
[VO,Na]	14.8	377	995
[VO,Ca]	12.6	365	1003
[VO,La]	9.1	359	1009
[VO,Y]	8.3	355	1010
[VO,Lu]	7.9	351	1011

Table 3.1. Table of compiled spectroscopic data for the **[VO,M]** series.

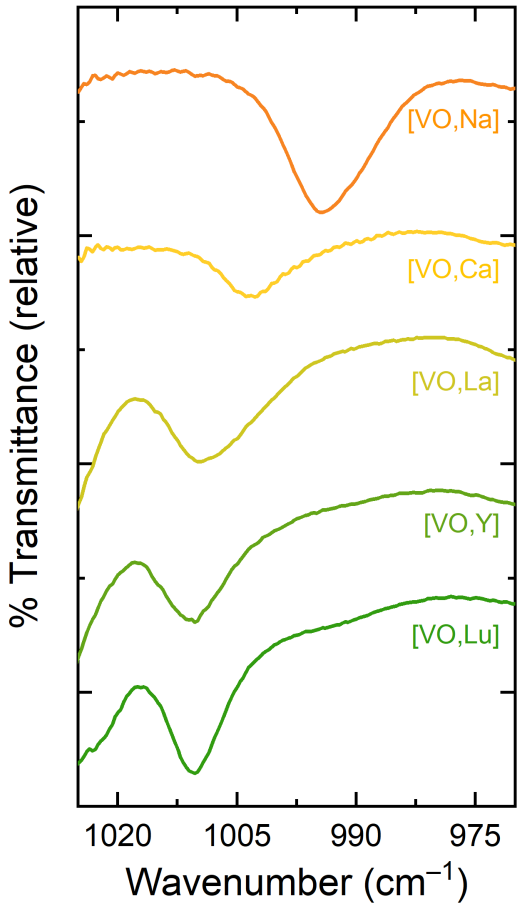

Figure 3.6. Infrared spectra of 10 mM solutions of **[VO,M]** complexes

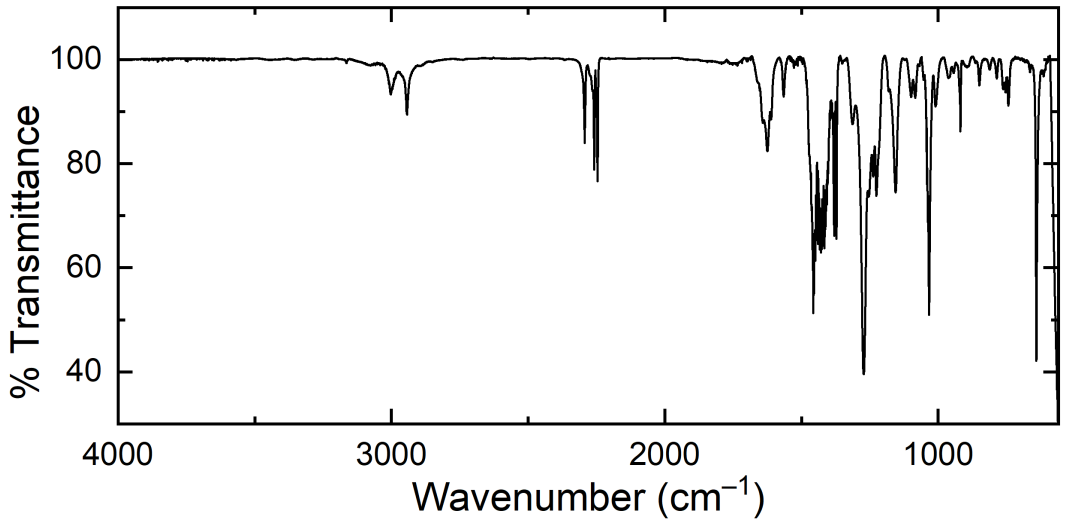

Figure 3.7. Infrared spectrum of a 10 mM solution of **[VO,La]** in CH_3CN.

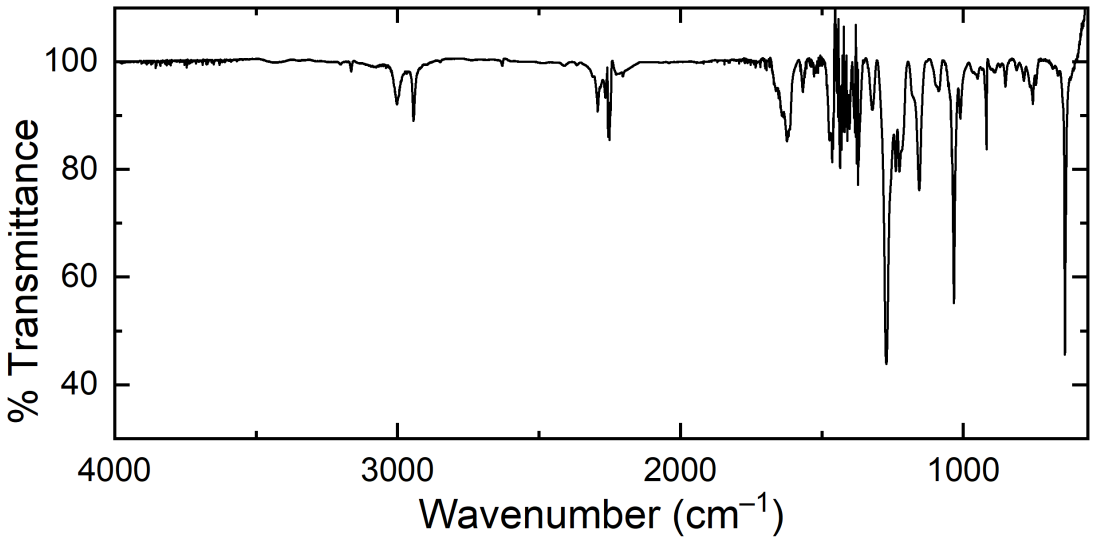

Figure 3.8. Infrared spectrum of a 10 mM solution of **[VO,Y]** in CH_3CN.

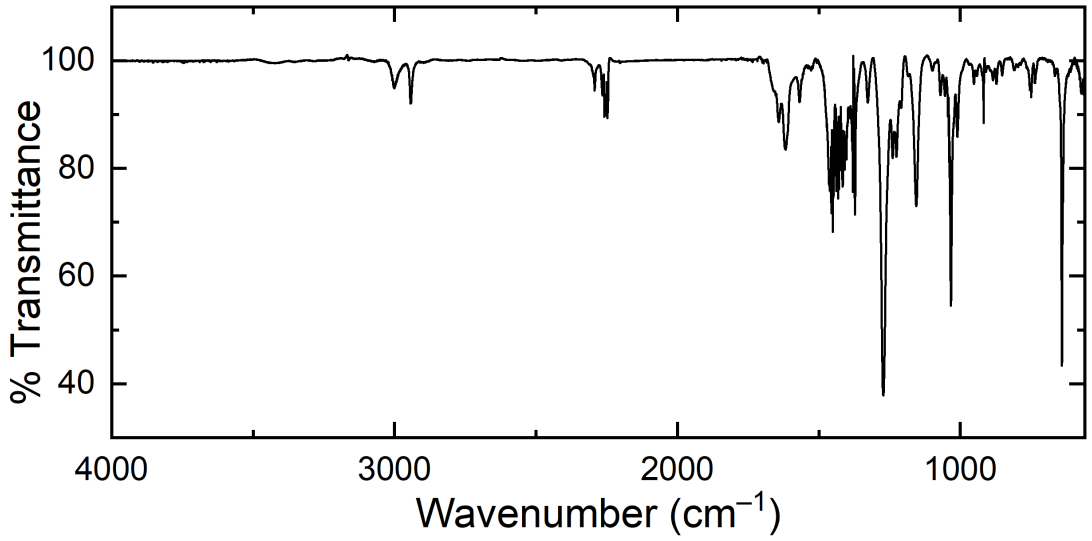

Figure 3.9. Infrared spectrum of a 10 mM solution of **[VO,Lu]** in CH_3CN.

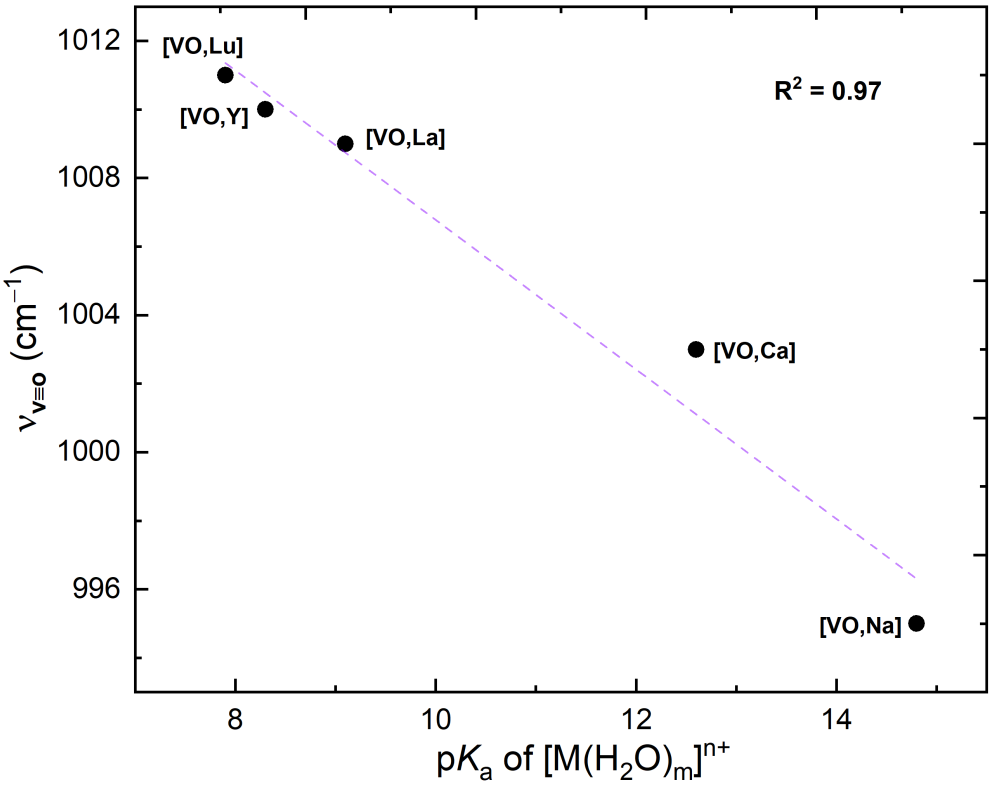

Figure 3.10. Dependence of ν(V≡O) on Lewis acidity.

3.3 Discussion

While synthesizing and obtaining spectroscopic data on these three new complexes, it was expected that the Lewis acidic cations would bind in the [O_6] crown site, much like the series discussed in Chapter 1. The resulting trends from these data give a strong suggestion that this expectation was confirmed. ^{1}H NMR spectra for the complexes, despite their paramagnetic nature, show shifts and broadening of signals corresponding to some level of chemical interaction between the cations and the monometallic vanadyl complex. To further probe this, electronic absorption data in the UV-Visible region was obtained to confirm a blue shifted charge transfer band, which would also point to incorporation of the secondary metal. As seen in Figure 3.5 and Table 3.1, the λ_{max} of this CT band systematically shifts to lower values, and in turn, the energy of this transition increases as a function of Lewis acidity. This trend persists not only with the mono- and di-valent series, but is also now confirmed with these even stronger trivalent Lewis acids. When looking to IR spectroscopy, a definitive shift is seen in the frequency of the terminal oxo stretch. This supports the claim that ligand donor strength is attenuated by the secondary Lewis acidic metal bound in the [O_6] site, especially for these metals that have a greater potential for polarizing the electron density of the bridging phenoxide ligands. More data should be collected on these complexes to make stronger claims, but when considering the spectroscopic characterization that has been done, it is clear that these trivalent ions *i*) cleanly incorporate into the [O_6] binding site and *ii*) directly influence the properties of vanadyl by their Lewis acidic nature.

3.4 Future Work

To complete the characterization of these complexes, much more data needs to be acquired in order to make full comparisons to the information presented in Chapter 1. Room temperature EPR experiments and cyclic voltammetry could be pursued in order to make more complete arguments

that these more strongly Lewis acidic cations are more effective at attenuating ligand donor strength in comparison to the cations associated with the series of complexes discussed in Chapter 1. Solid-state EPR experiments could give insight into the behavior of these complexes when not freely tumbling in solution and allow for the quantification of the anisotropic hyperfine coupling constants. Quantification of these parameters could provide an interesting comparison to the isotropic coupling values obtained in the work in Chapter 1. ^{51}V NMR could be conducted to analyze the shielding or deshielding of the ^{51}V chemical shift that may result from incorporation of secondary metals. Crystallographic information could be useful to definitively confirm the structures of the trivalent adducts and, perhaps most importantly, confirm changes in the bonding about the vanadium center. The expected shortening of the vanadium - terminal oxo bond as a function of the Lewis acidity of the secondary metal cations could be confirmed by obtaining such data and it is therefore of high interest.

3.5 Conclusions

We have obtained a limited set of spectroscopic data on a family of new heterobimetallic vanadyl complexes containing La^{3+}, Y^{3+}, and Lu^{3+} ions. The data paint a picture that broadly confirms the findings given in Chapters 1 and 2. Namely, the strongly Lewis acidic character of these trivalent cations results in chemical changes to the vanadyl core of the complexes that are greater than those encountered upon incorporation of mono- and di-valent cations. Confirmation that the cations bind in the [O_6] cavity underscores the useful ability of our ligand framework to support cation incorporation and suggests that the ligand could be useful for further studies of cation-modulated chemistry of other species in the future.

Appendix 1

General Considerations

All manipulations were carried out in dry N_2-filled gloveboxes (Vacuum Atmospheres Co., Hawthorne, CA) or under N_2 atmosphere using standard Schlenk techniques unless otherwise noted. All solvents were of commercial grade and dried over activated alumina using a PPT Glass Contour (Nashua, NH) solvent purification system prior to use, and were stored over molecular sieves. All chemicals were from major commercial suppliers and used as received. CD_3CN was purchased from Cambridge Isotope Laboratories and dried over 3 Å molecular sieves. ^1H and ^{19}F NMR spectra were collected on 400 and 500 MHz Bruker spectrometers and referenced to the residual protio-solvent signal[65] in the case of ^1H. ^{19}F NMR spectra were referenced and reported relative to CCl_3F as an external standard following the recommended scale based on ratios of absolute frequencies (Ξ).[66,67] Chemical shifts (δ) are reported in units of ppm. UV-visible spectra were collected with an Ocean Optics Flame spectrometer in a 1-cm path length quartz cuvette. Elemental analyses were performed at Midwest Microlab, Inc. (Indianapolis, IN, USA) and at the University of Memphis (Memphis, TN, USA).

Infrared Spectroscopy. Spectra were collected with a Shimadzu IRSpirit FTIR spectrometer equipped with a QATR-S single-reflection attenuated total reflectance (ATR) accessory and diamond prism plate, as well as accessories for conventional transmission measurements in cells with KBr windows. IR spectra were collected under an inert atmosphere in a dry N_2-filled glovebox (Vacuum Atmospheres Co., Hawthorne, CA).

Electron Paramagnetic Resonance Spectroscopy. Electron paramagnetic resonance (EPR) spectra were collected at room temperature on a Bruker EMXplus spectrometer in quartz capillaries placed into conventional quartz EPR tubes. The concentration of analyte in each EPR sample was 10 mM.

Electrochemistry. Electrochemical experiments were carried out in a N_2-filled glovebox. Dry, degassed CH_3CN containing 0.10 M tetra(n-butylammonium) hexafluorophosphate ($[^nBu_4N]^+[PF6]^-$); Sigma-Aldrich, electrochemical grade) served as the electrolyte for the experiments. Measurements were carried out with a Gamry Reference 600+ Potentiostat/Galvanostat (Gamry Instruments, Warminster, PA, USA), using a standard three-electrode configuration. The working electrode was the basal plane of highly oriented pyrolytic graphite (HOPG) (GraphiteStore.com, Buffalo Grove, Ill.; surface area: ca. 0.1 cm^2), the counter electrode was a platinum wire (Kurt J. Lesker, Jefferson Hills, PA; 99.99%, 0.5 mm diameter), and a silver wire immersed in electrolyte served as a pseudoreference electrode (CH Instruments). The reference was separated from the working solution by a Vycor frit (Bioanalytical Systems, Inc., West Lafayette, IN, USA). Ferrocene (Sigma-Aldrich, St. Louis, MO, USA; twice-sublimed) was added to the electrolyte solution prior to the beginning of each experiment; the midpoint potential of the ferrocenium/ferrocene couple (denoted as $Fc^{+/0}$) served as an external standard for comparison of the recorded potentials. Concentrations of analytes for cyclic voltammetry were typically 2 mM unless otherwise noted. Experiments were conducted by first scanning anodically, then cathodically on the return sweep.

Appendix 2

Supplementary Information

Contents

NMR Spectra

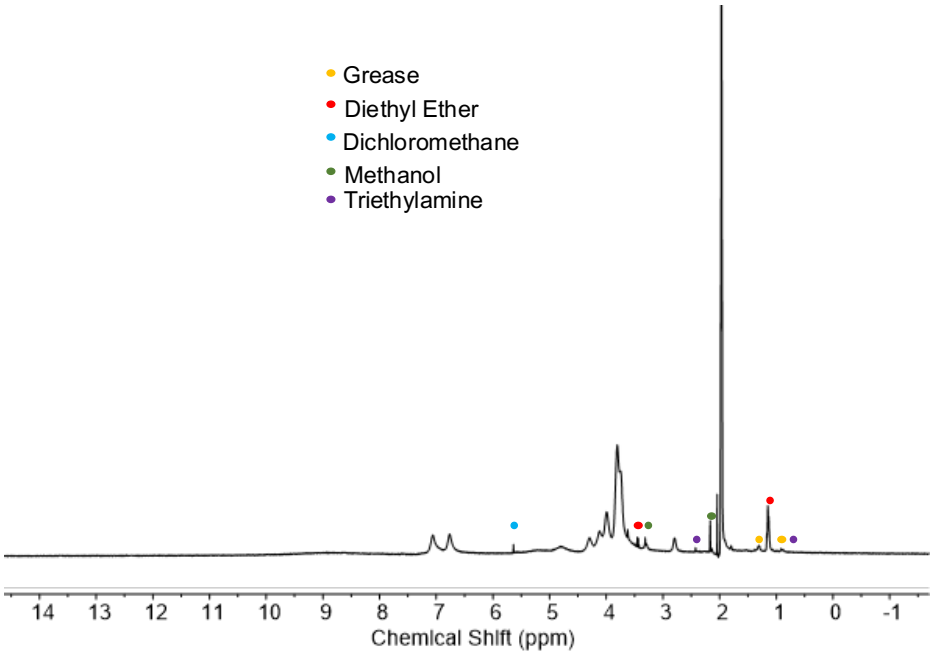

Figure S1. ^{1}H NMR spectrum (400 MHz, CD_3CN) of **[VO]**. Grease, diethyl ether, and dichloromethane are present in the NMR solvent.

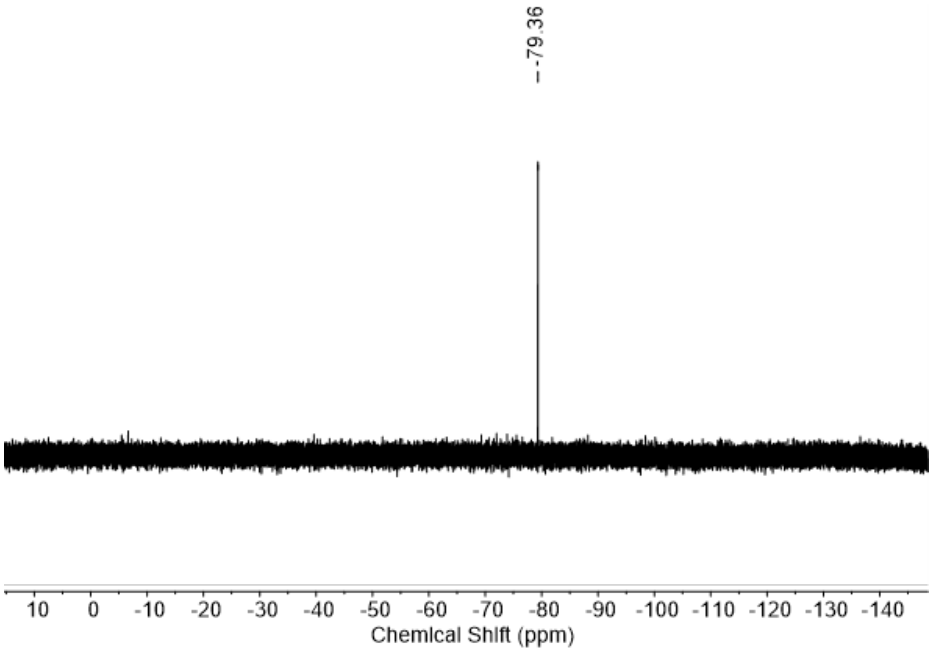

Figure S2. ^{19}F NMR spectrum (376 MHz, CD_3CN) of **[VO]**.

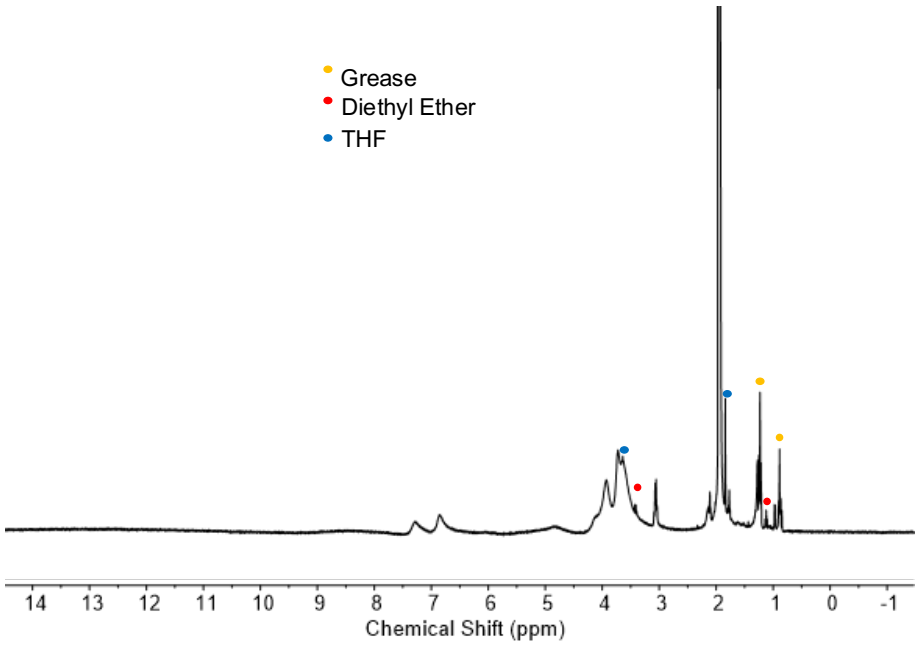

Figure S3. ^{1}H NMR spectrum (400 MHz, CD_3CN) of **[VO,Cs]**. Grease and diethyl ether are present in the NMR solvent.

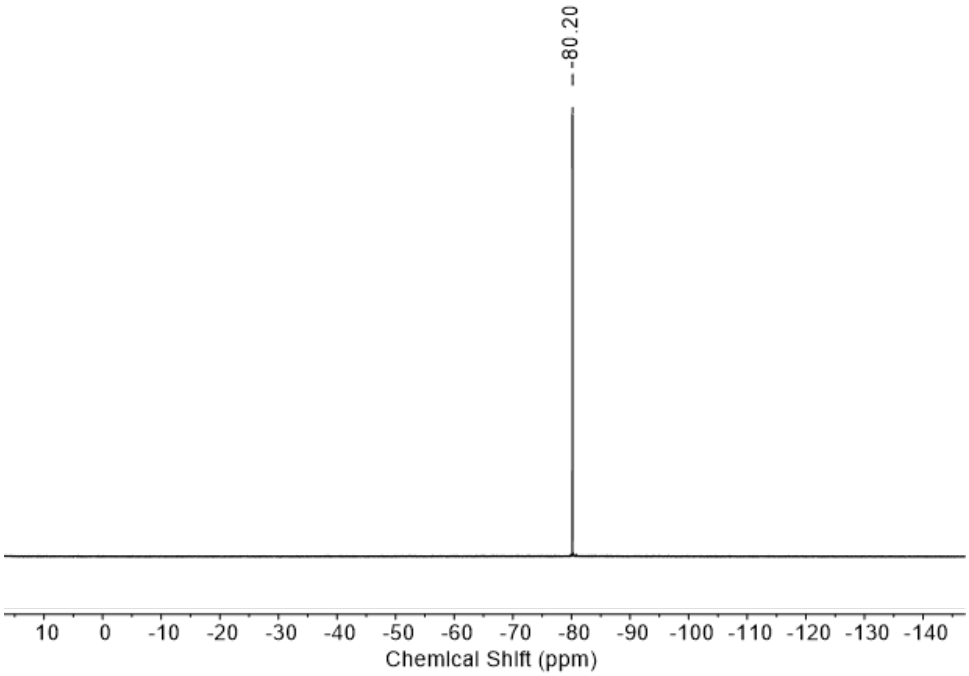

Figure S4. ^{19}F NMR spectrum (376 MHz, CD_3CN) of **[VO,Cs]**.

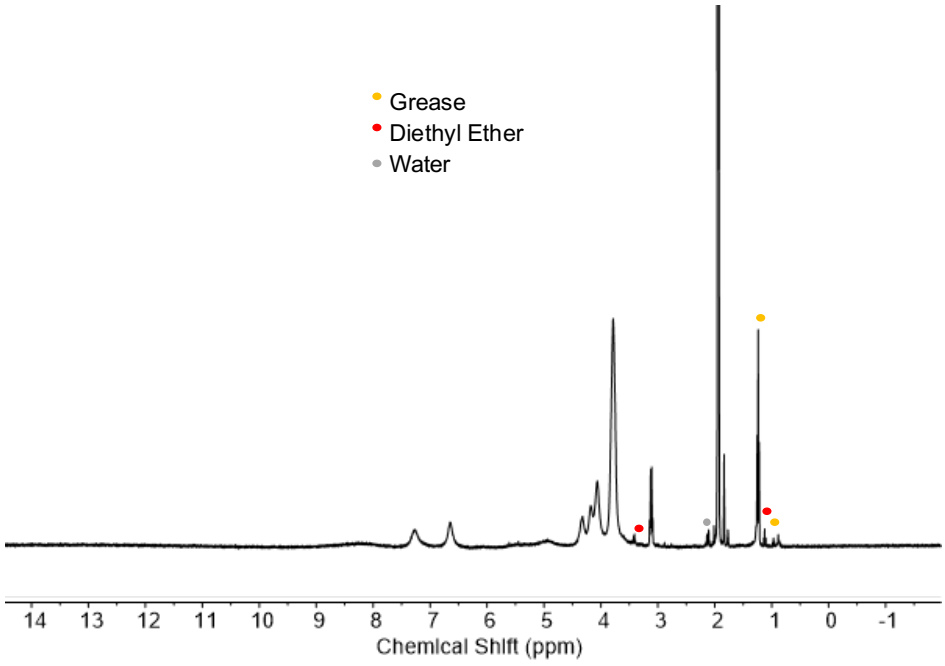

Figure S5. ^{1}H NMR spectrum (400 MHz, CD_3CN) of **[VO,Na]**. Grease, diethyl ether, and water are present in the NMR solvent.

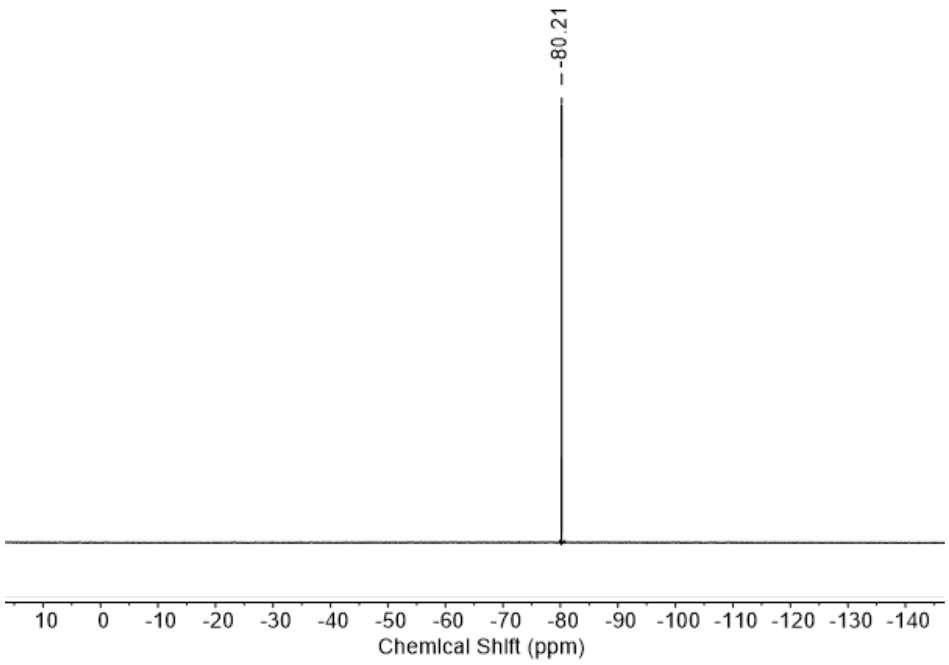

Figure S6. ^{19}F NMR spectrum (376 MHz, CD_3CN) of **[VO,Na]**.

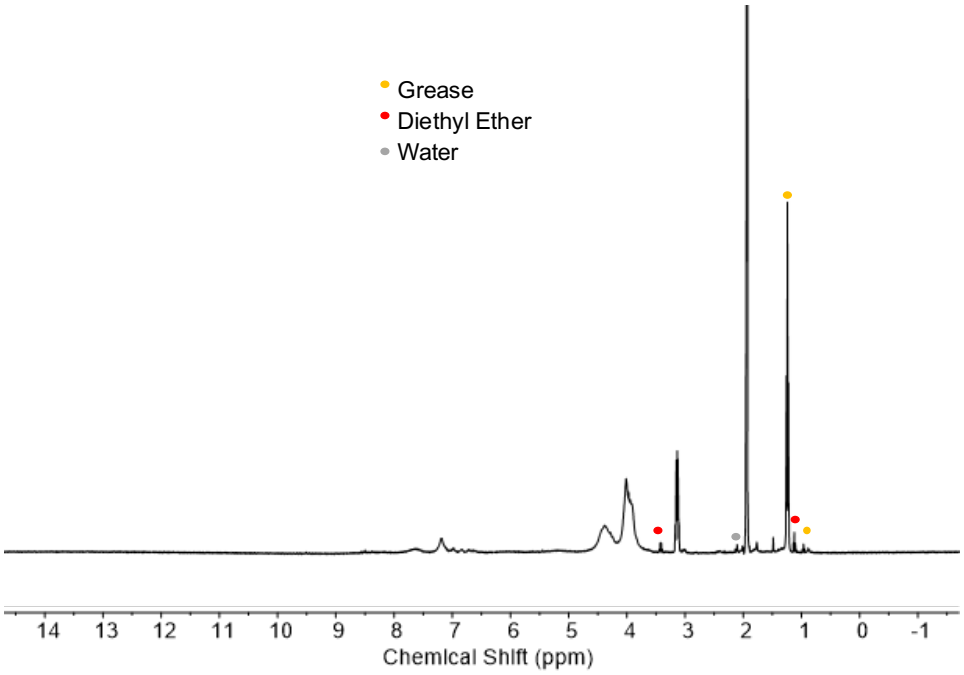

Figure S7. ^{1}H NMR spectrum (400 MHz, CD_3CN) of **[VO,Ca]**. Grease, diethyl ether, and water are present in the NMR solvent.

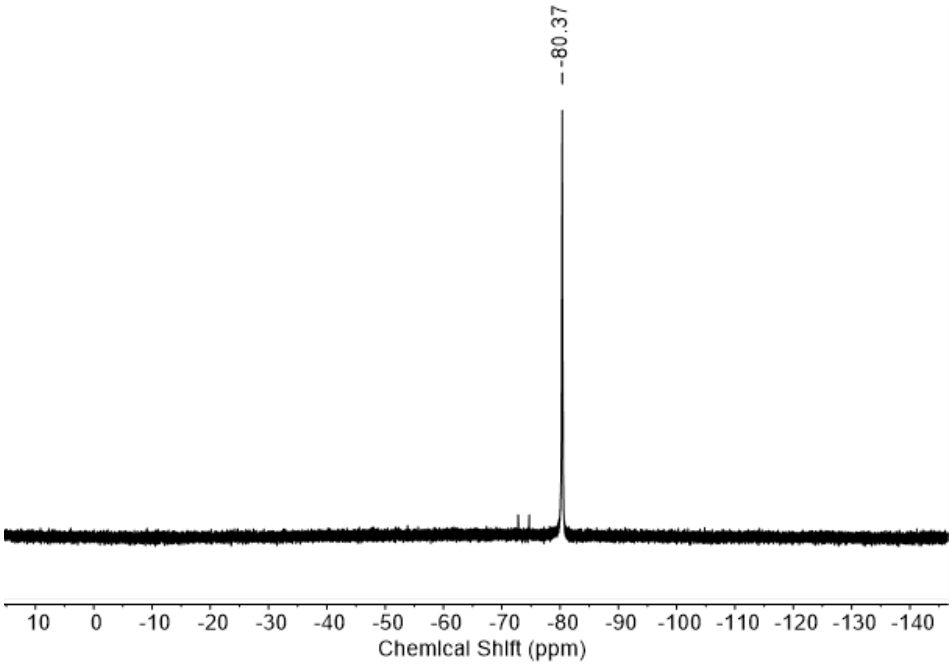

Figure S8. ^{19}F NMR spectrum (376 MHz, CD_3CN) of **[VO,Ca]**.

Electronic Absorption Spectra

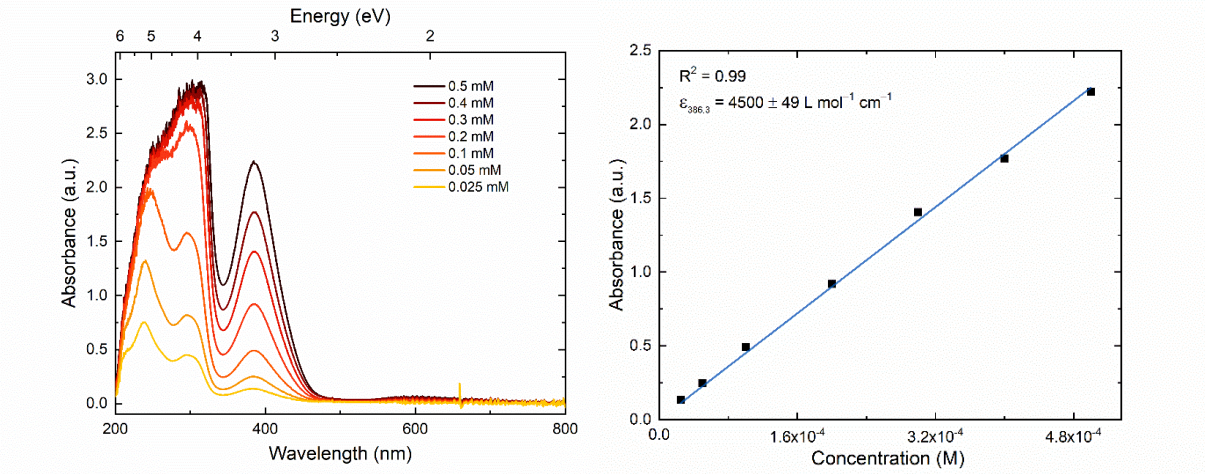

Figure S9. Left panel: Electronic absorption spectra of **[VO]** in CH_3CN. Right panel: Absorbance vs concentration plot of **[VO]** in CH_3CN monitored at 386 nm.

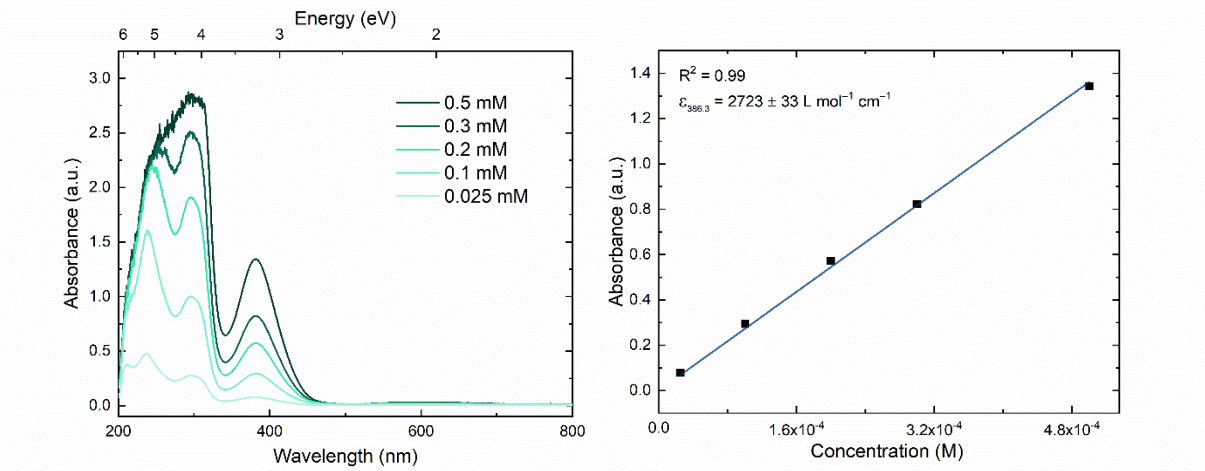

Figure S10. Left panel: Electronic absorption spectra of **[VO,Cs]** in CH_3CN. Right panel: Absorbance vs concentration plot of **[VO,Cs]** in CH_3CN monitored at 386 nm.

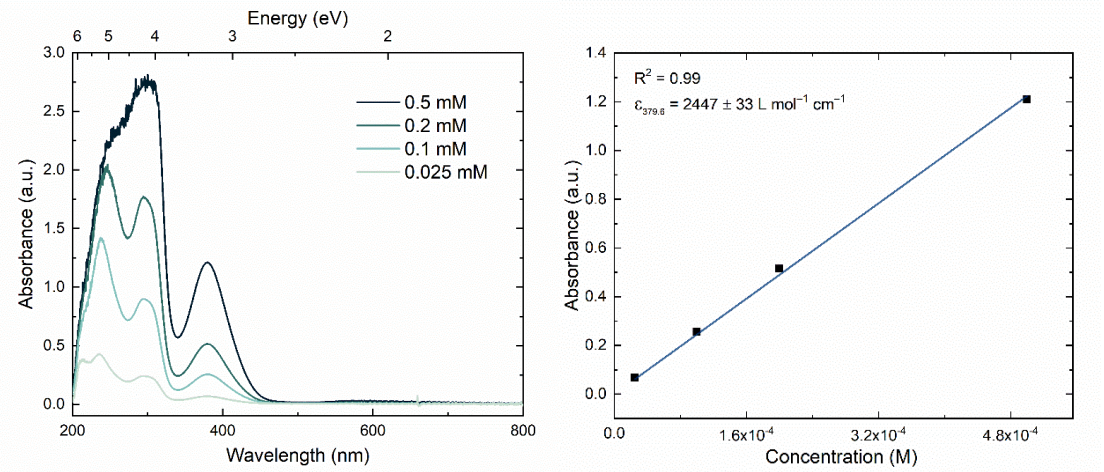

Figure S11. Left panel: Electronic absorption spectra of **[VO,Rb]** in CH_3CN. Right panel: Absorbance vs concentration plot of **[VO,Rb]** in CH_3CN monitored at 386 nm.

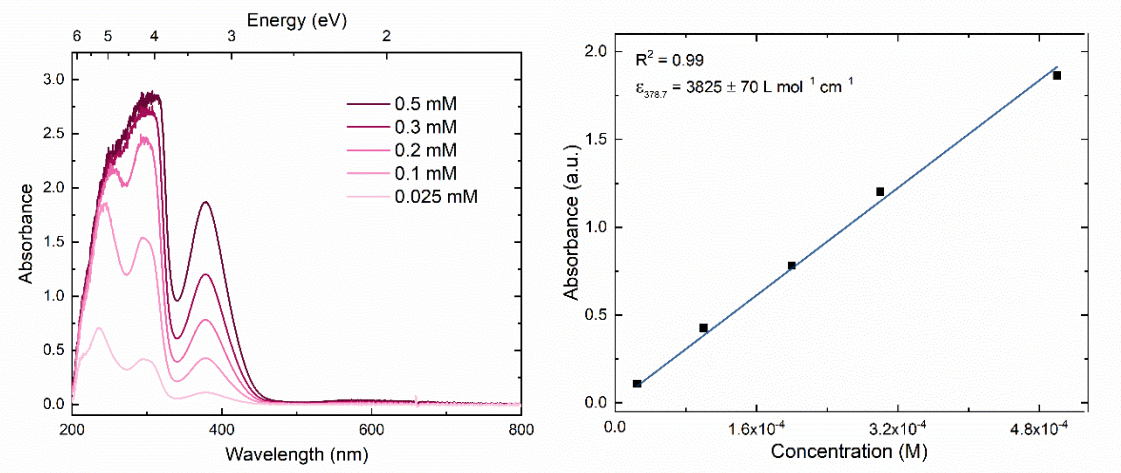

Figure S12. Left panel: Electronic absorption spectra of **[VO,K]** in CH_3CN. Right panel: Absorbance vs concentration plot of **[VO,K]** in CH_3CN monitored at 379 nm.

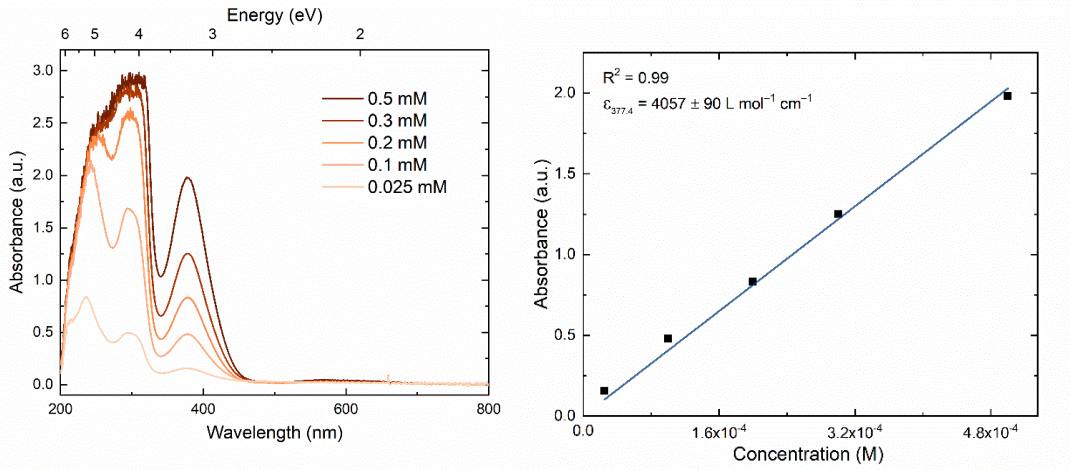

Figure S13. Left panel: Electronic absorption spectra of **[VO,Na]** in CH_3CN. Right panel: Absorbance vs concentration plot of **[VO,Na]** in CH_3CN monitored at 377 nm.

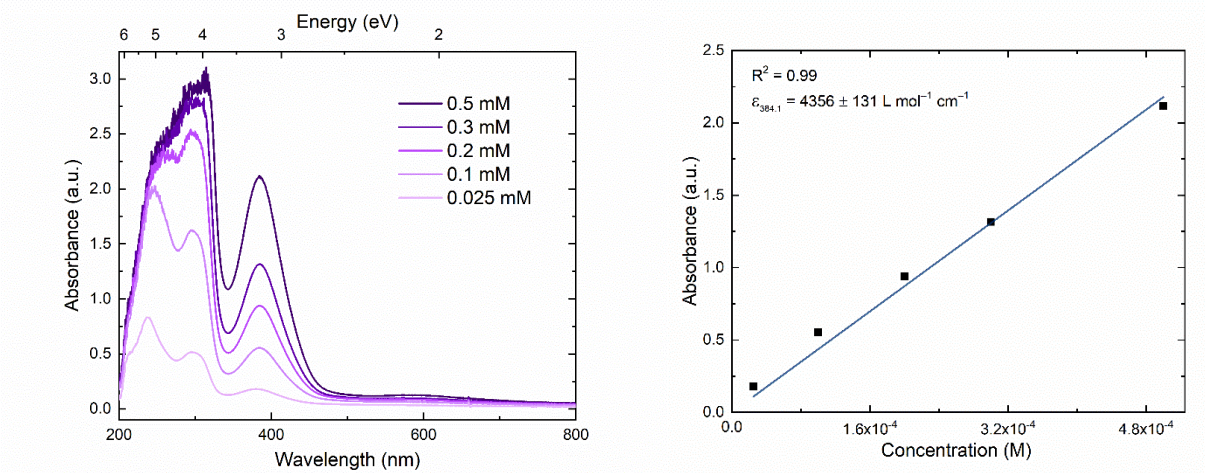

Figure S14. Left panel: Electronic absorption spectra of **[VO,Li]** in CH_3CN. Right panel: Absorbance vs concentration plot of **[VO,Li]** in CH_3CN monitored at 384 nm.

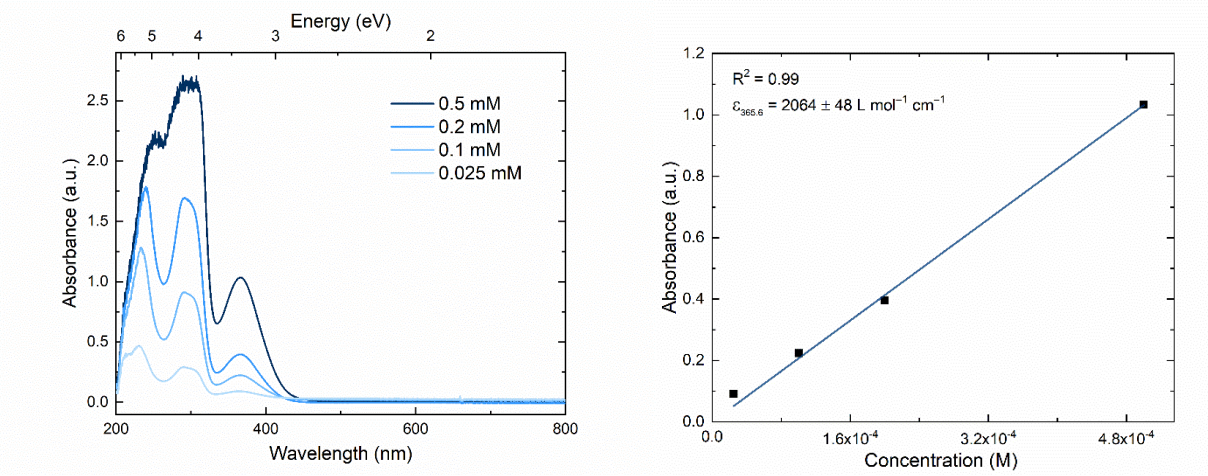

Figure S15. Left panel: Electronic absorption spectra of **[VO,Ca]** in CH_3CN. Right panel: Absorbance vs concentration plot of **[VO,Ca]** in CH_3CN monitored at 366 nm.

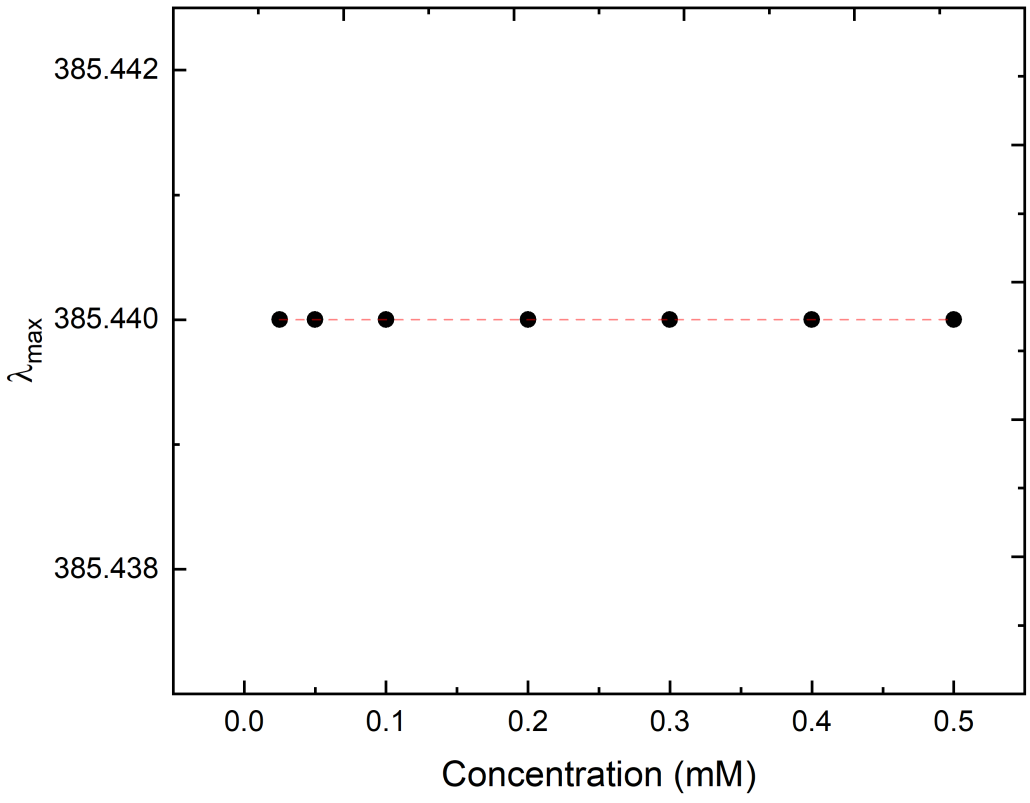

Figure S16. Dependence of λ_{max} on concentration for **[VO]**.

Solution-State Infrared Spectroscopy

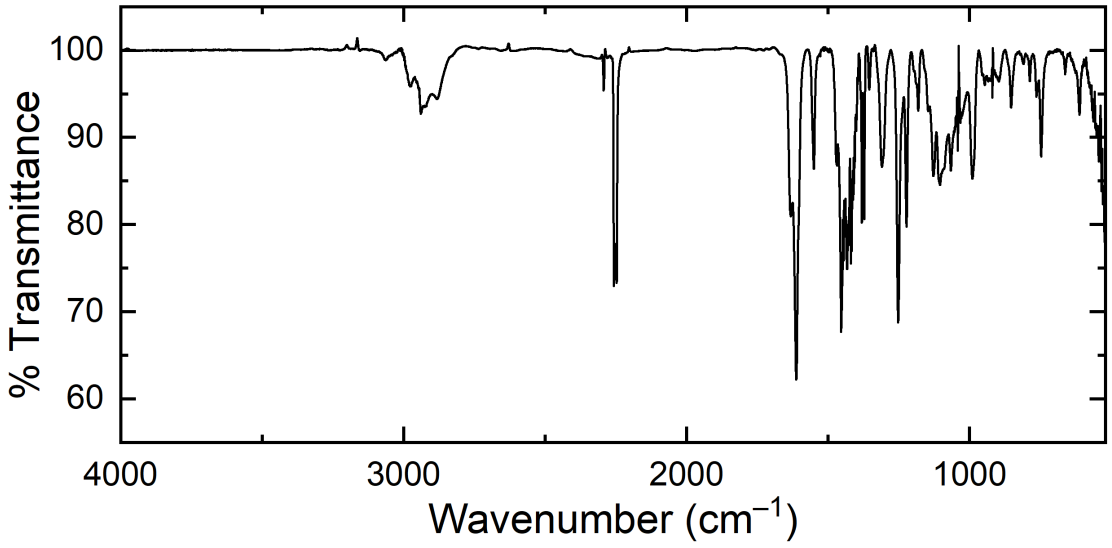

Figure S21. Infrared spectrum of 10mM solution of **[VO]** in CH_3CN.

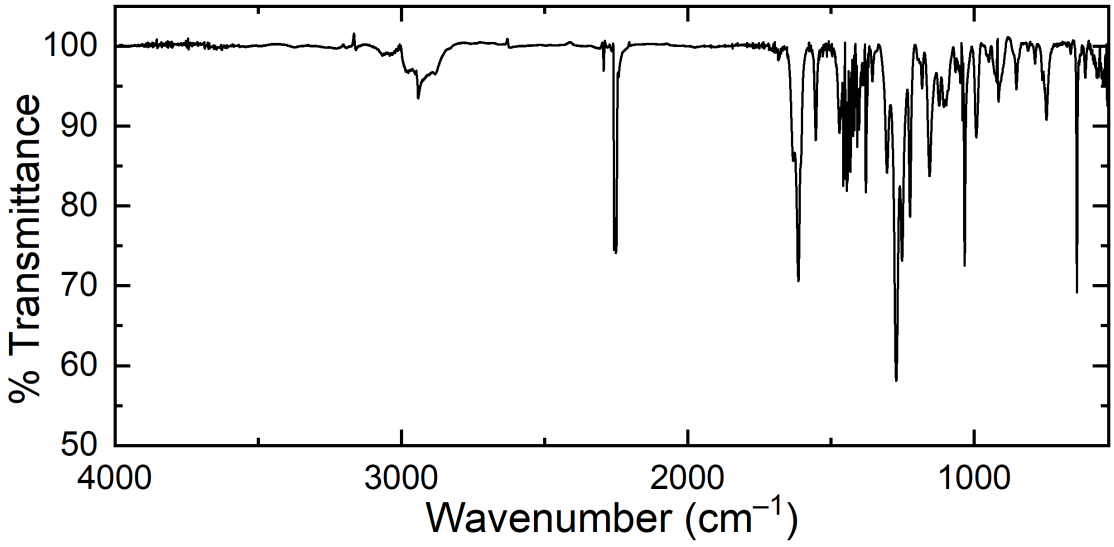

Figure S22. Infrared spectrum of 10mM solution of **[VO,Cs]** in CH_3CN.

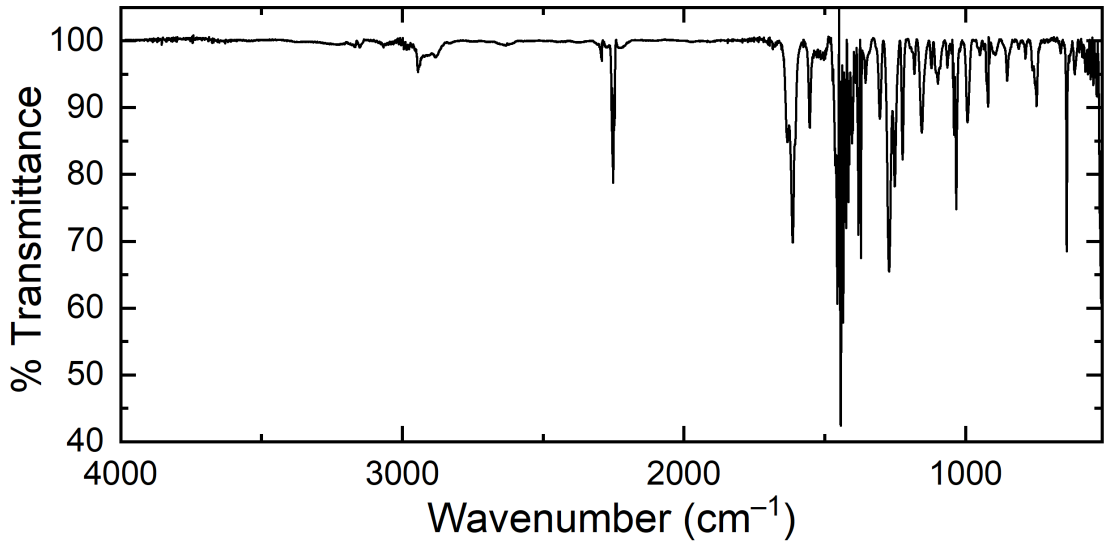

Figure S23. Infrared spectrum of 10mM solution of **[VO,Rb]** in CH_3CN.

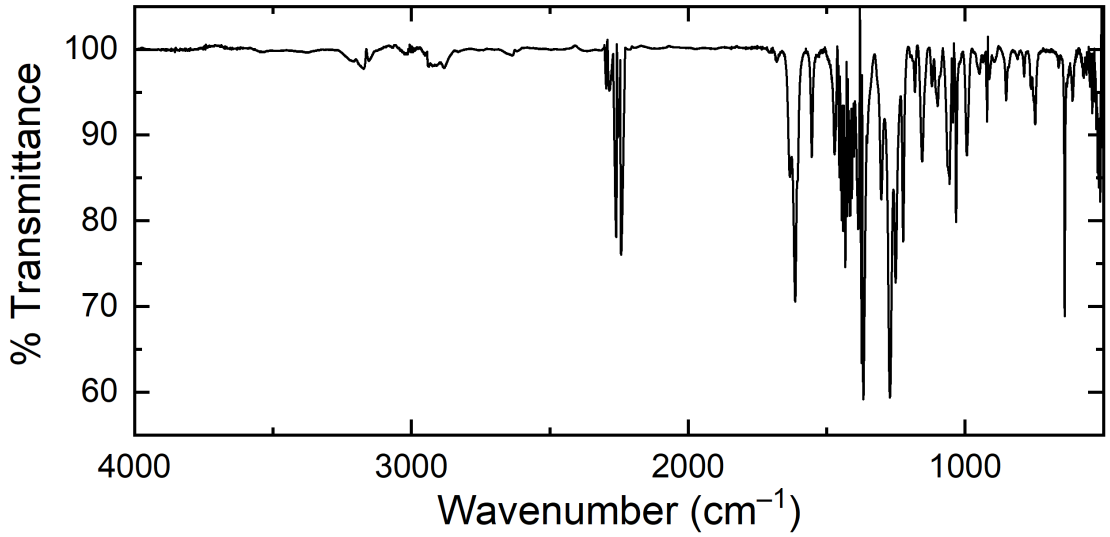

Figure S24. Infrared spectrum of 10mM solution of **[VO,K]** in CH_3CN.

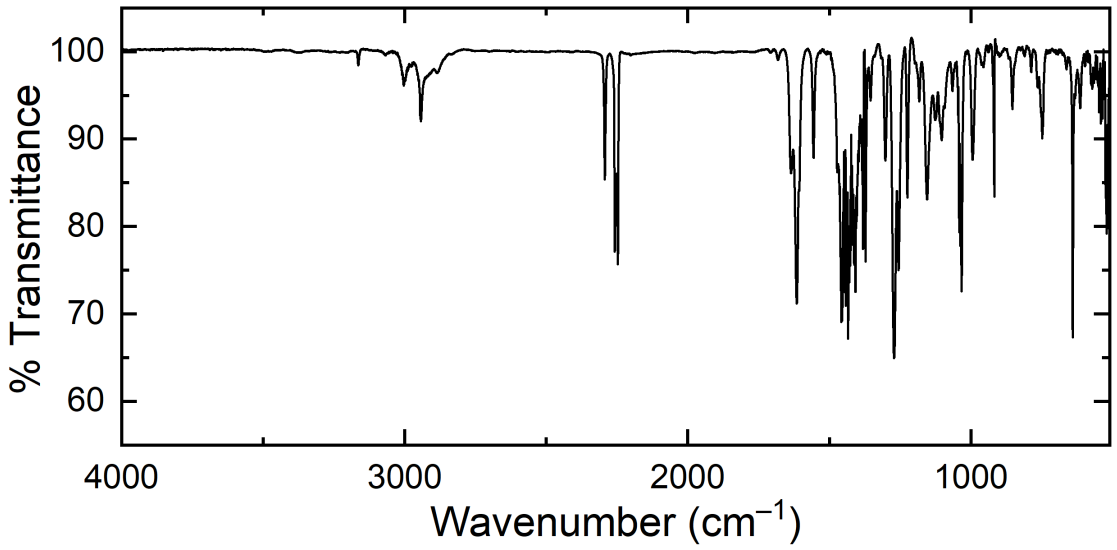

Figure S25. Infrared spectrum of 10mM solution of **[VO,Na]** in CH_3CN.

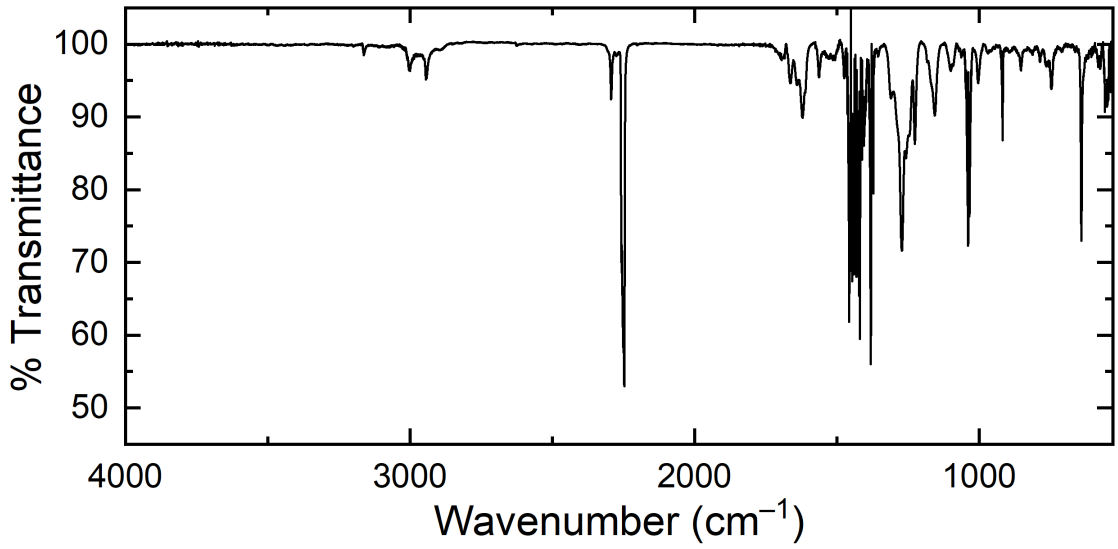

Figure S26. Infrared spectrum of 10mM solution of **[VO,Ca]** in CH_3CN.

Solid-State Infrared Spectroscopy

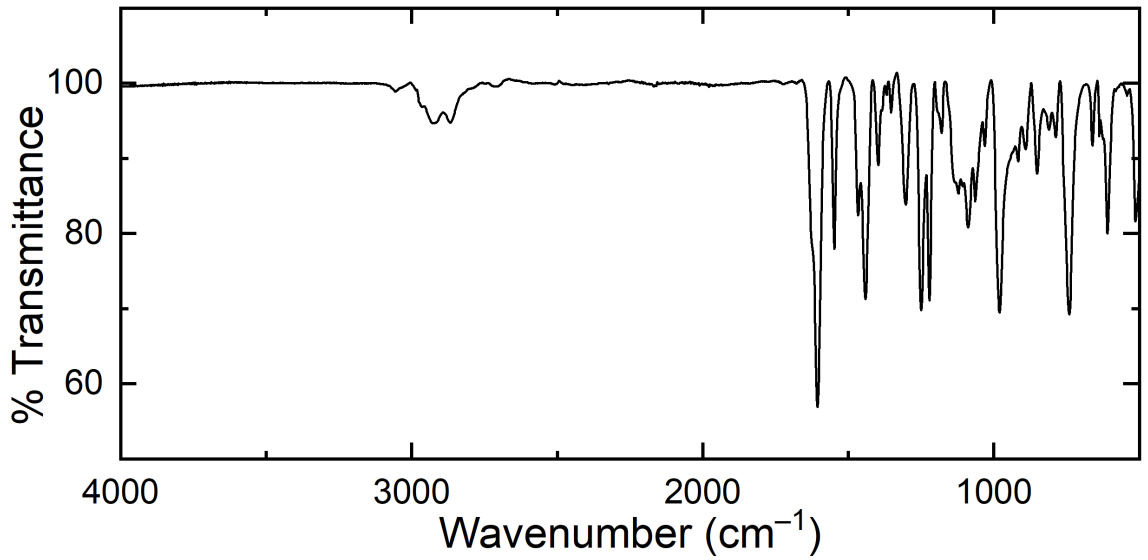

Figure S27. Solid-state infrared spectrum of **[VO]**.

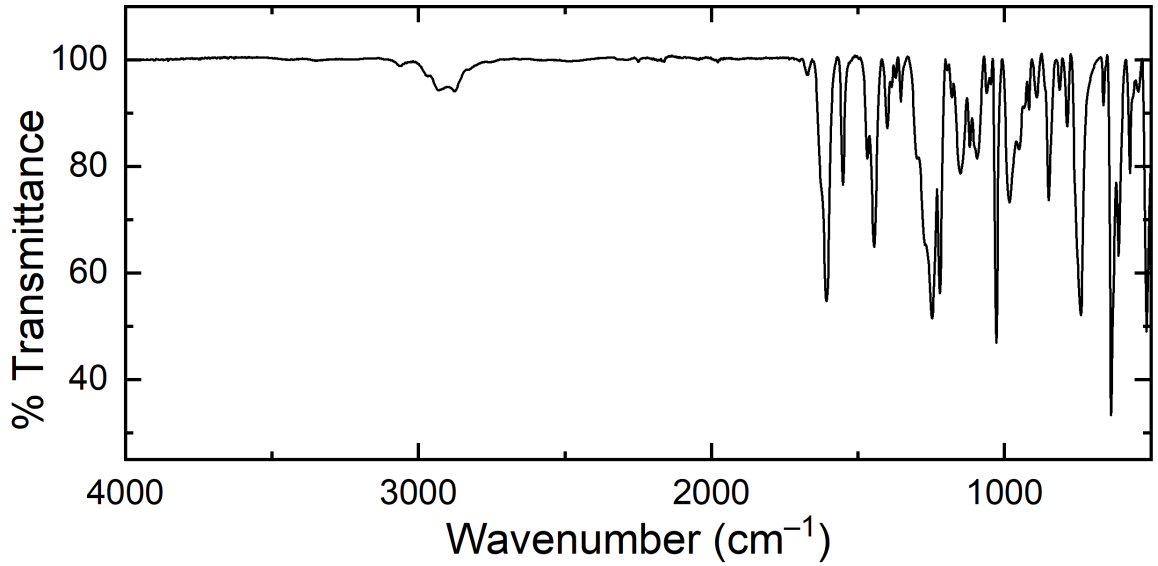

Figure S28. Solid-state infrared spectrum of **[VO,Cs]**.

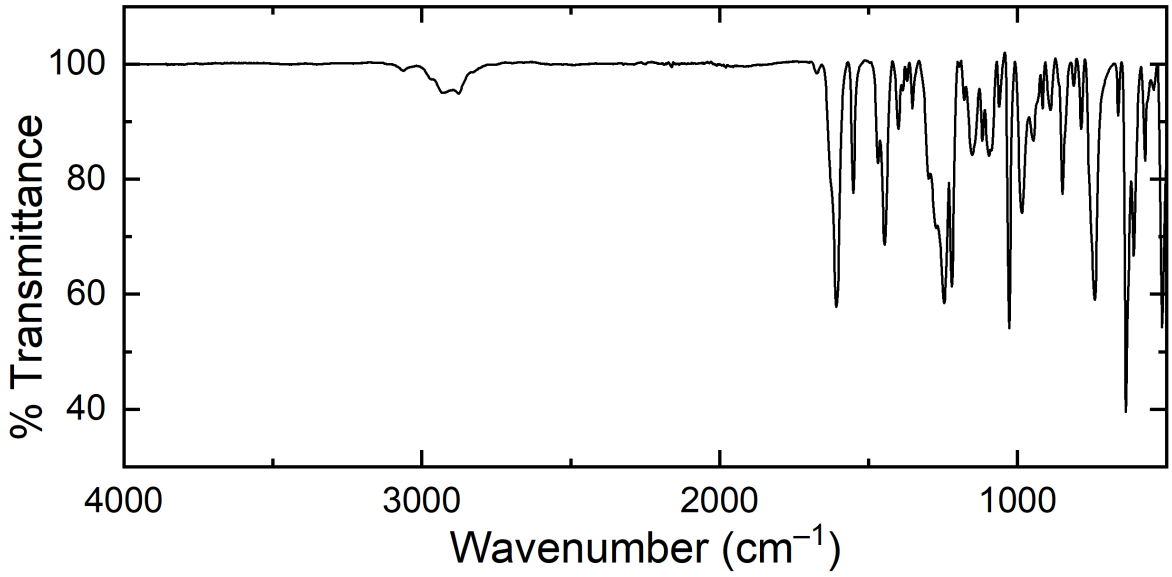

Figure S29. Solid-state infrared spectrum of **[VO,Rb]**.

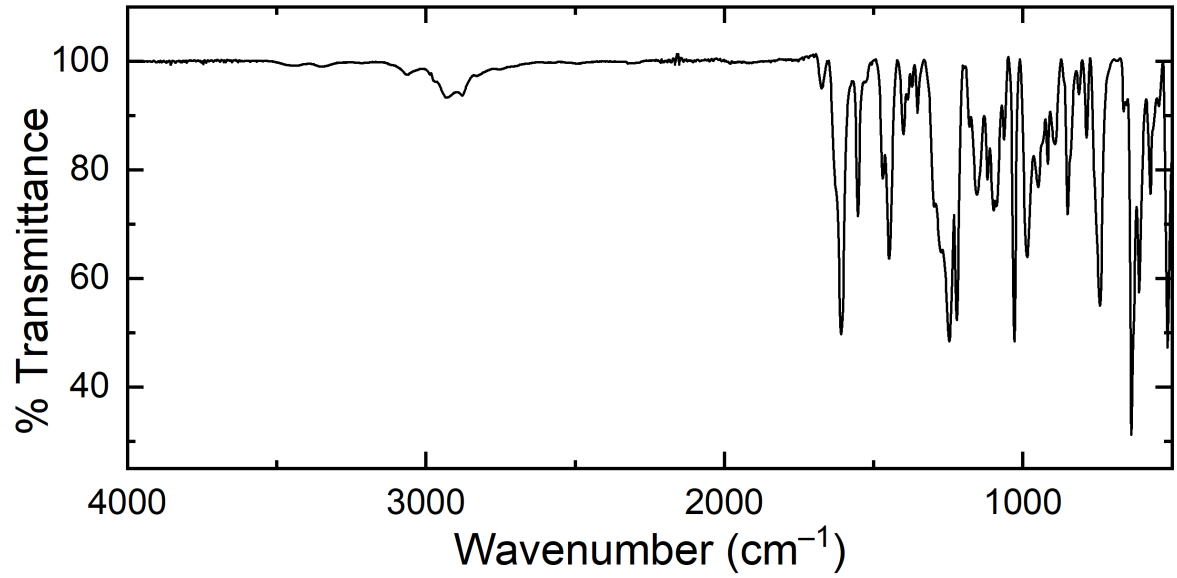

Figure S30. Solid-state infrared spectrum of **[VO,K]**.

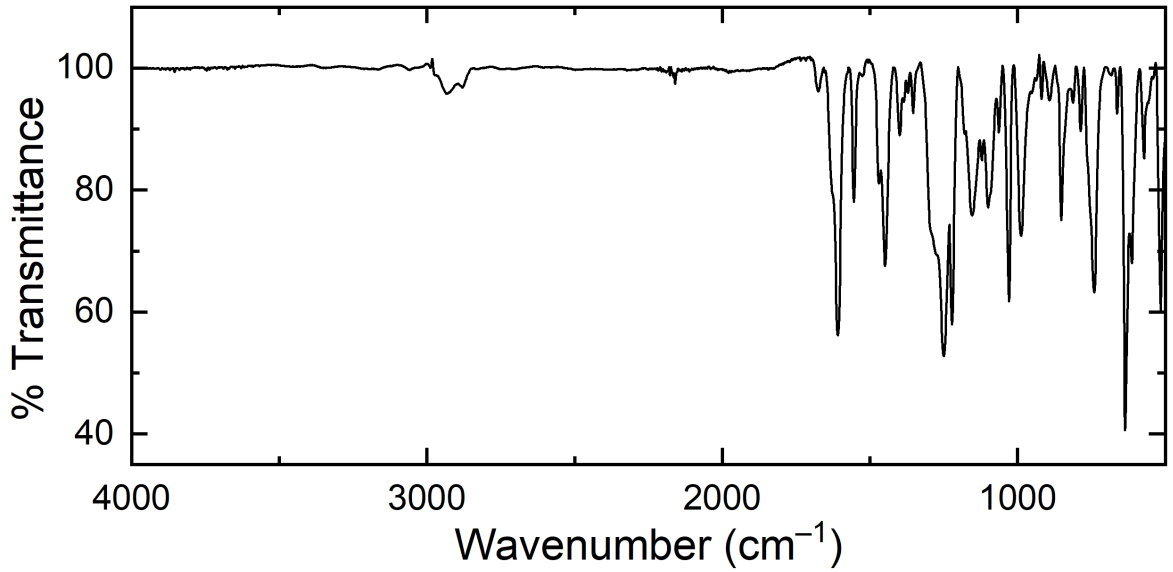

Figure S31. Solid-state infrared spectrum of **[VO,Na]**.

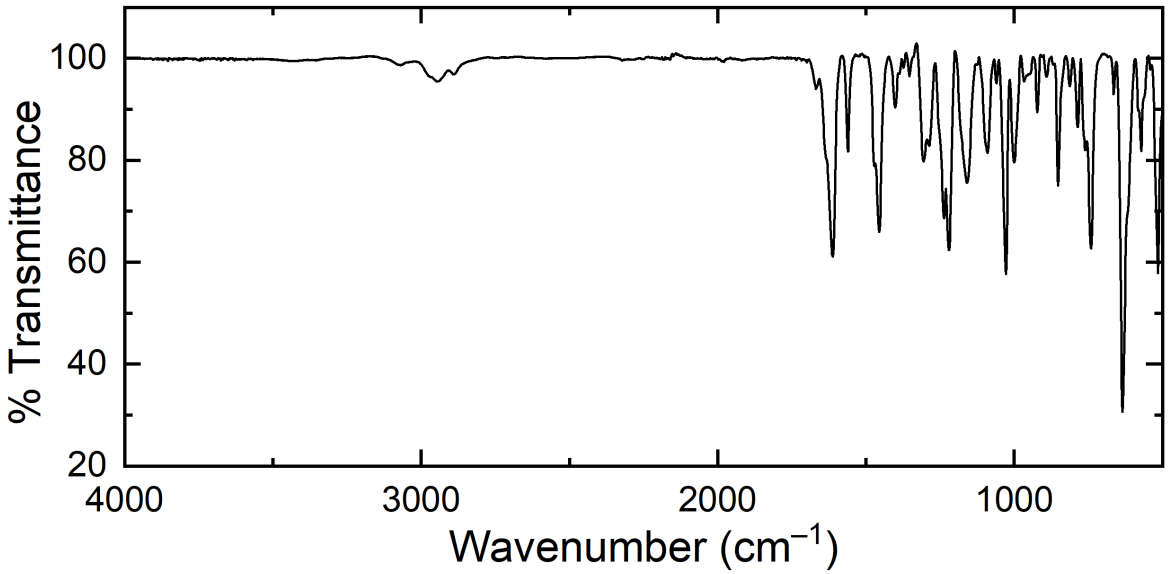

Figure S32. Solid-state infrared spectrum of **[VO,Ca]**.

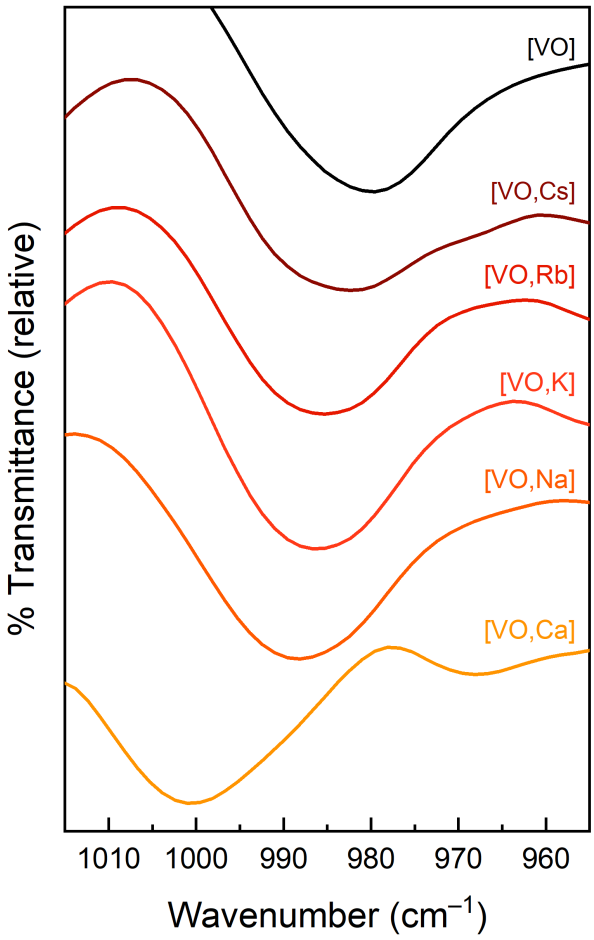

Figure S33. Comprehensive stack of solid-state infrared spectra in the V–O stretching region.

Analysis of Infrared Spectroscopy

Complex	ν(V–O) (cm^{-1}) *Solution State*	ν(V–O) (cm^{-1}) *Solid State*	Δν(V–O) (cm^{-1})
[VO]	991	979	12
[VO,Cs]	992	982	10
[VO,Rb]	993	985	8
[VO,K]	994	986	8
[VO,Na]	995	988	7
[VO,Ca]	1003	1001	2

Table S1. Comparison between V≡O stretching frequencies in the solution and solid states.

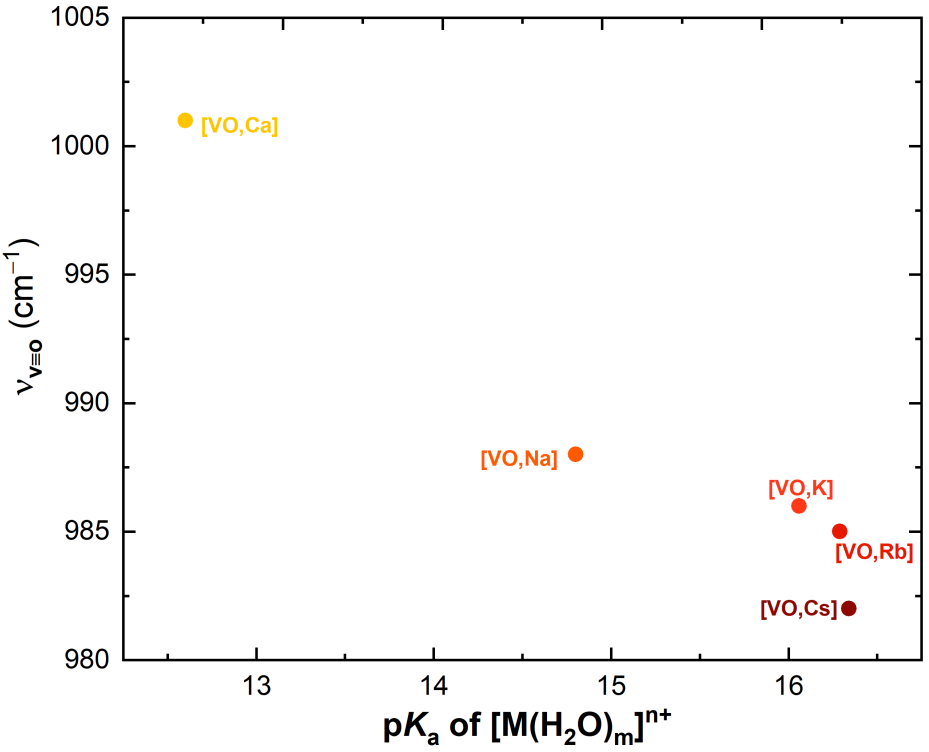

Figure S34. Plot of V≡O stretching frequencies in solid-phase IR as a function of pK_a.

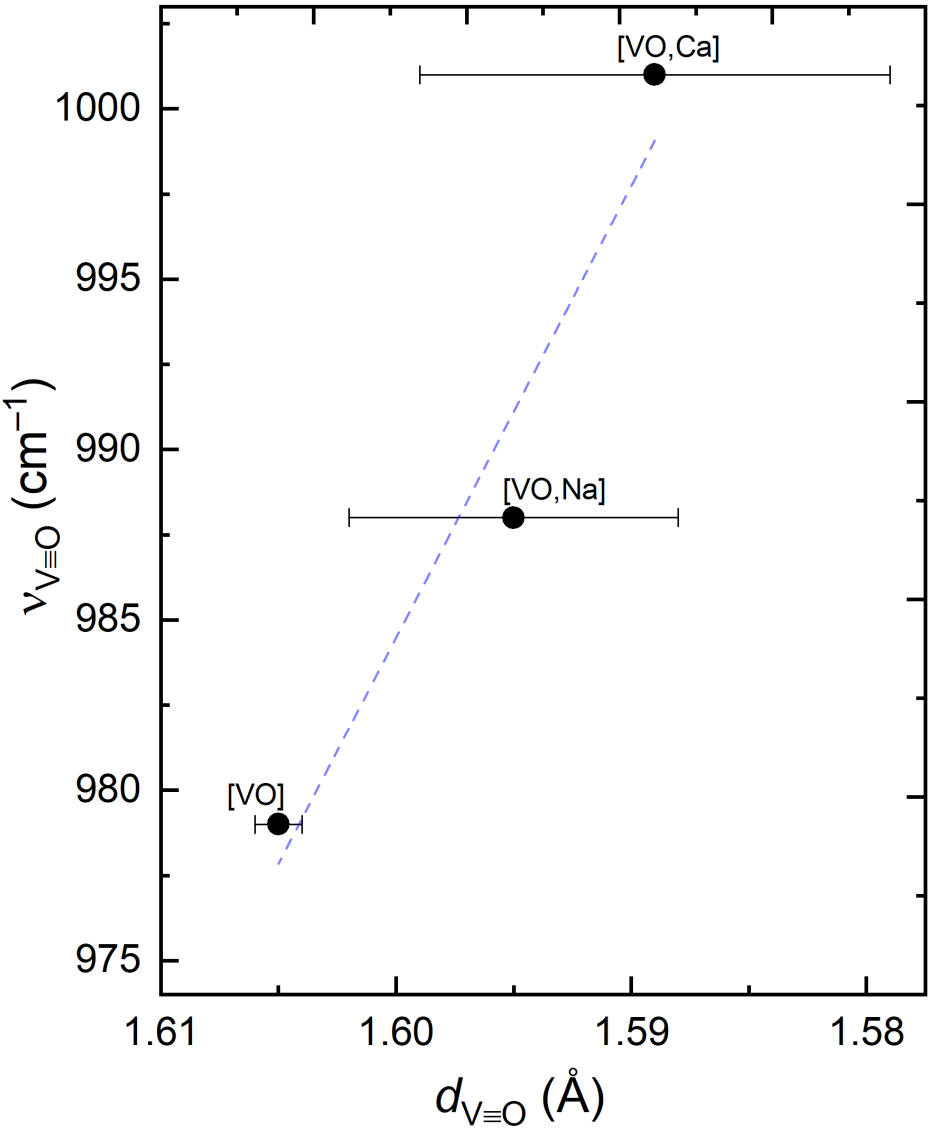

Figure S35. Dependence of the solid-state V≡O stretching frequency on V≡O bond length. The bond lengths for the individual compounds were derived from the structures reported here: **a03a**, **[VO]**; **a04d-No1**, **[VO,Na]**; **b31b-No7**, **[VO,Ca]**. Uncertainties associated with the bond lengths are represented with the error bars, which are the e.s.d.'s determined for each compound in the indicated structures. Details on determination of these e.s.d.'s are given in Table 1.1 in Chapter 1.

Electronic Paramagnetic Resonance Spectroscopy

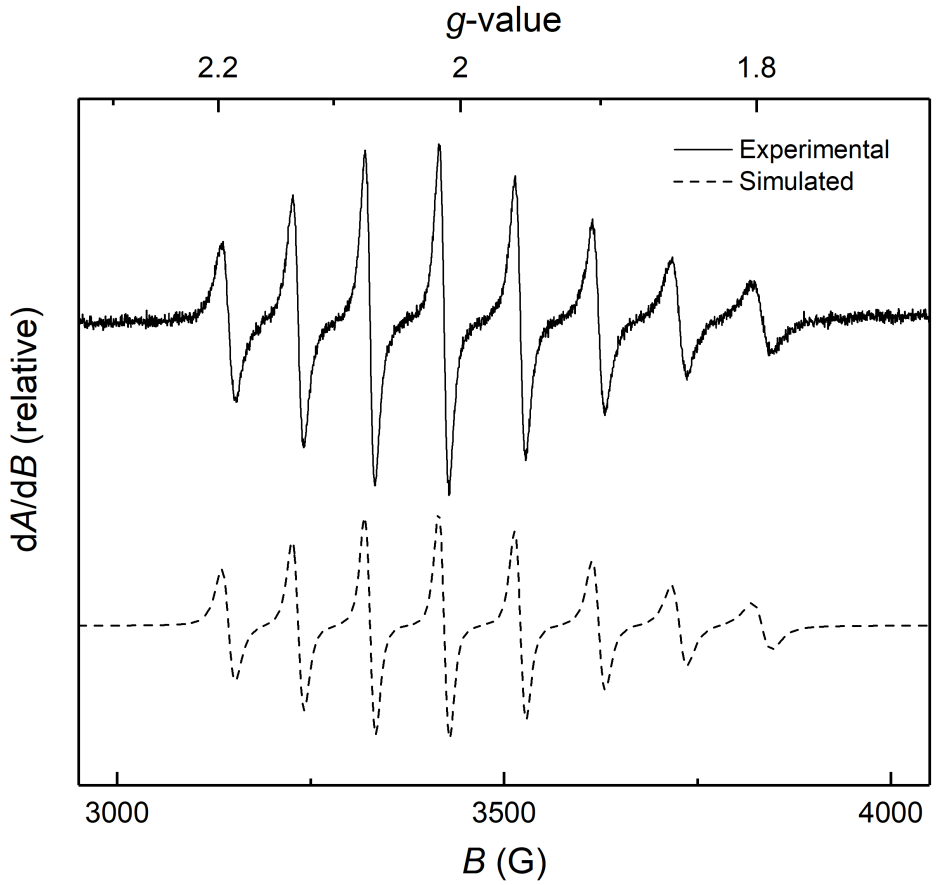

Figure S36. Experimental: X-band EPR spectrum of **[VO]** 10mM solution in MeCN (Temperature = 298 K, Frequency = 9.6405 GHz, Power = 2mW). Simulated: EasySpin simulation using *garlic* function. Best fit values: $g_{\|}$= 1.96, $g_{\perp}$ = 1.98, A_{iso} = 271.9 MHz, $A_{\|}$ = 372.0 MHz, logtcorr = −9.64. RMSD = 0.023.

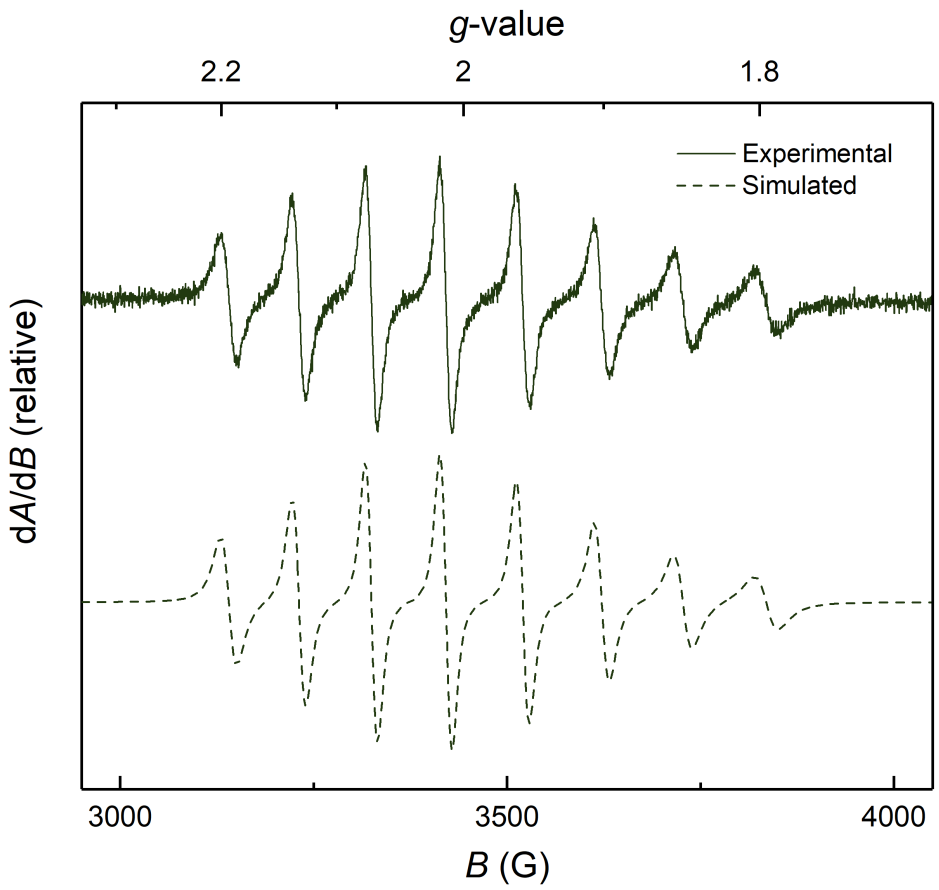

Figure S37. Experimental: X-band EPR spectrum of **[VO,Cs]** 10mM solution in MeCN (Temperature = 298 K, Frequency = 9.6405 GHz, Power = 2mW). Simulated: EasySpin simulation using *garlic* function. Best fit values: $g_{\|}$= 1.96, $g_{\perp}$ = 1.98, A_{iso} = 274.0 MHz, $A_{\|}$= 368.7 MHz, logtcorr = −9.48. RMSD = 0.031.

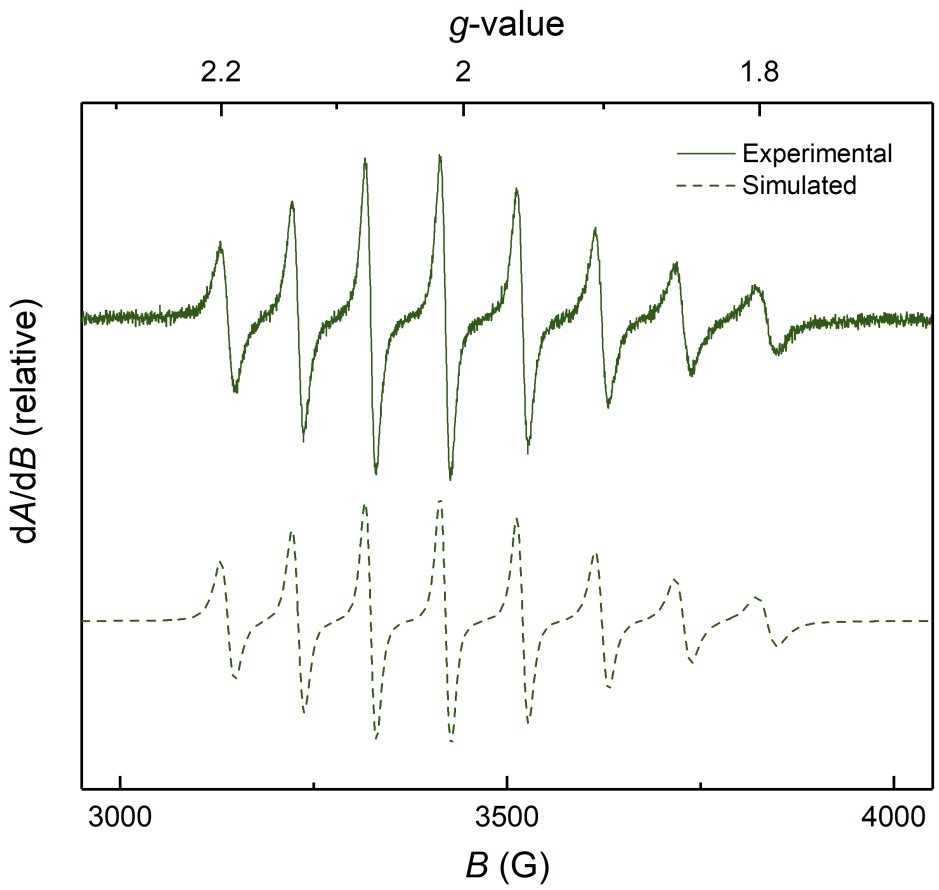

Figure S38. Experimental: X-band EPR spectrum of **[VO,Rb]** 10mM solution in MeCN (Temperature = 298 K, Frequency = 9.6405 GHz, Power = 2mW). Simulated: EasySpin simulation using *garlic* function. Best fit values: $g_{\|}$= 1.96, $g_{\perp}$ = 1.98, A_{iso} = 274.9 MHz, $A_{\|}$ = 357.5 MHz, logtcorr = −9.45. RMSD = 0.023.

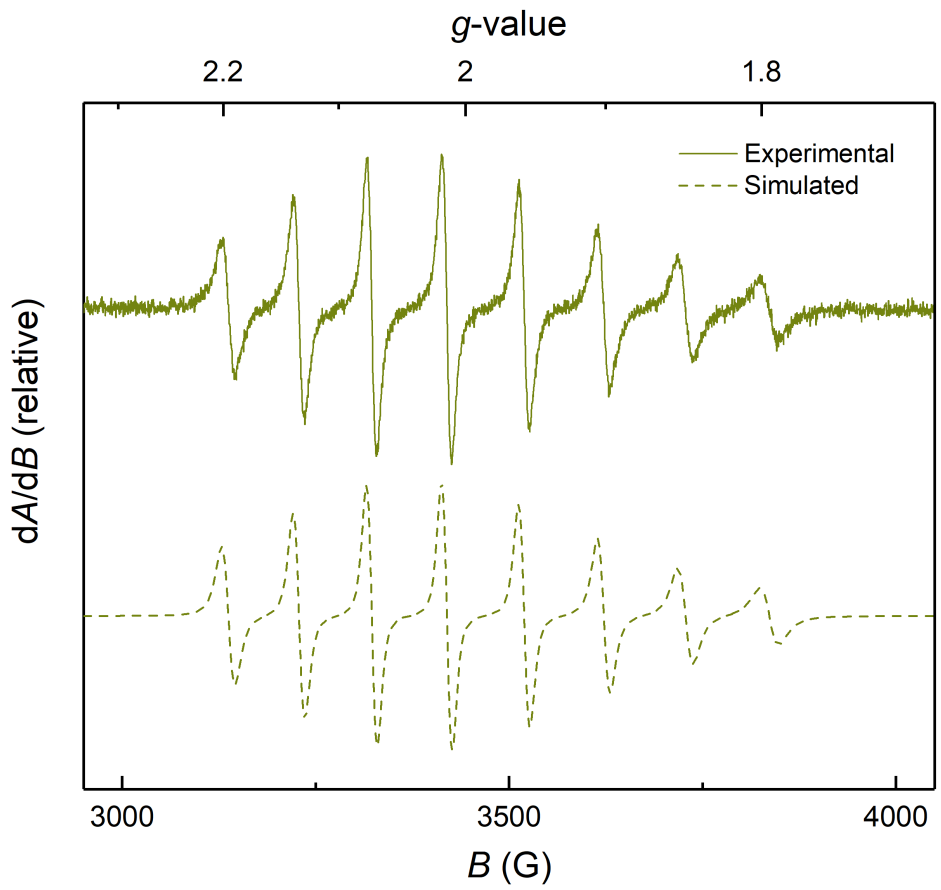

Figure S39. Experimental: X-band EPR spectrum of **[VO,K]** 10mM solution in MeCN (Temperature = 298 K, Frequency = 9.6405 GHz, Power = 2mW). Simulated: EasySpin simulation using *garlic* function. Best fit values: $g_{\|}$= 1.96, $g_{\perp}$ = 1.968, A_{iso} = 275.9 MHz, $A_{\|}$ = 353.8 MHz, logtcorr = −9.45. RMSD = 0.029.

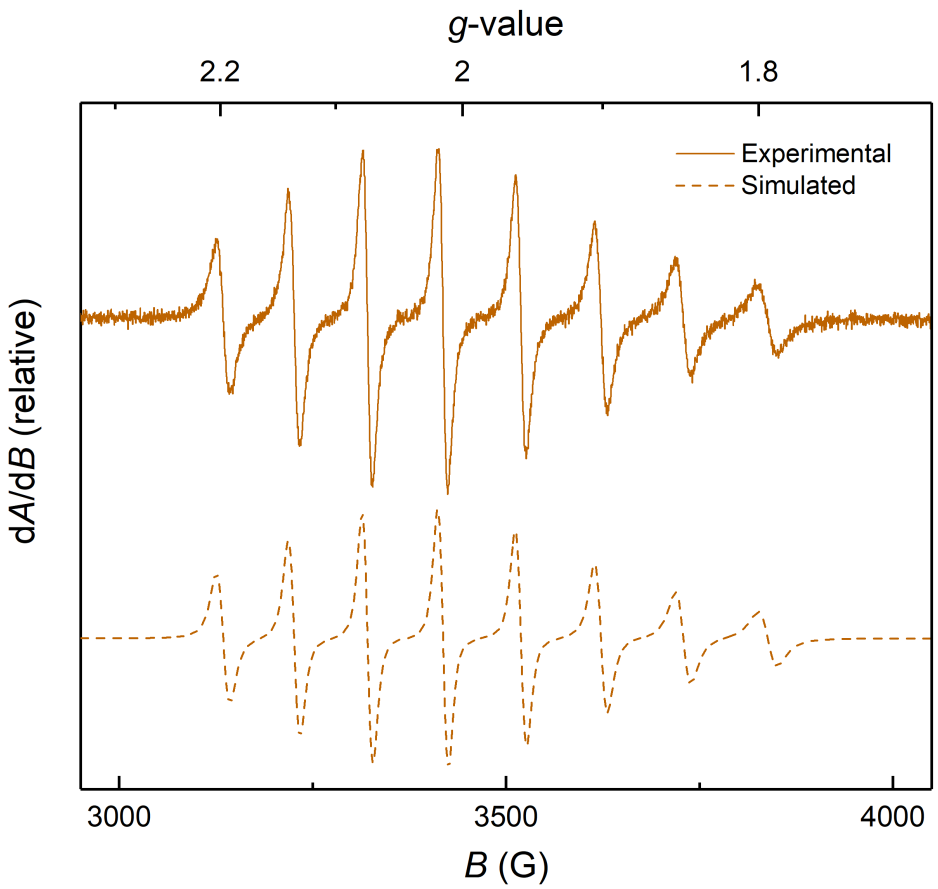

Figure S40. Experimental: X-band EPR spectrum of **[VO,Na]** 10mM solution in MeCN (Temperature = 298 K, Frequency = 9.6405 GHz, Power = 2mW). Simulated: EasySpin simulation using *garlic* function. Best fit values: $g_{\|}$= 1.97, $g_{\perp}$ = 1.98, A_{iso} = 277.7 MHz, $A_{\|}$ = 349.8 MHz, logtcorr = −9.37. RMSD = 0.024.

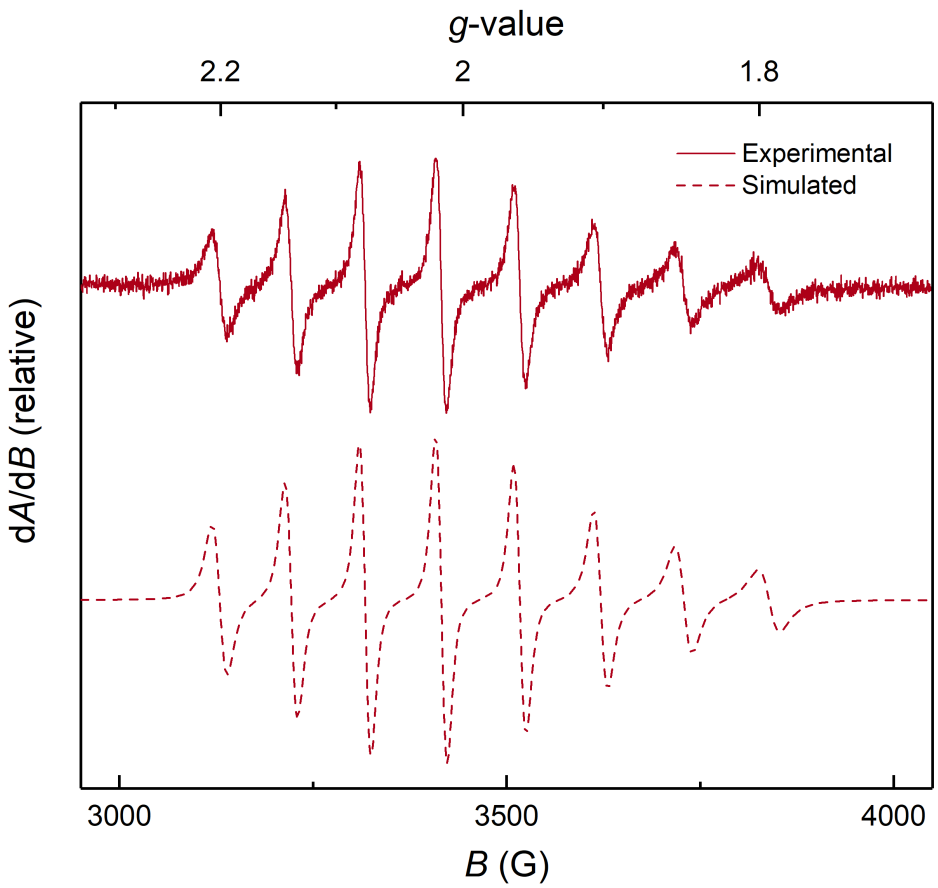

Figure S41. Experimental: X-band EPR spectrum of **[VO,Ca]** 10mM solution in MeCN (Temperature = 298 K, Frequency = 9.6405 GHz, Power = 2mW). Simulated: EasySpin simulation using *garlic* function. Best fit values: $g_{\|}$= 1.97, $g_{\perp}$ = 1.98, A_{iso} = 280.1 MHz, $A_{\|}$ = 346.3 MHz, logtcorr = −9.22. RMSD = 0.038.

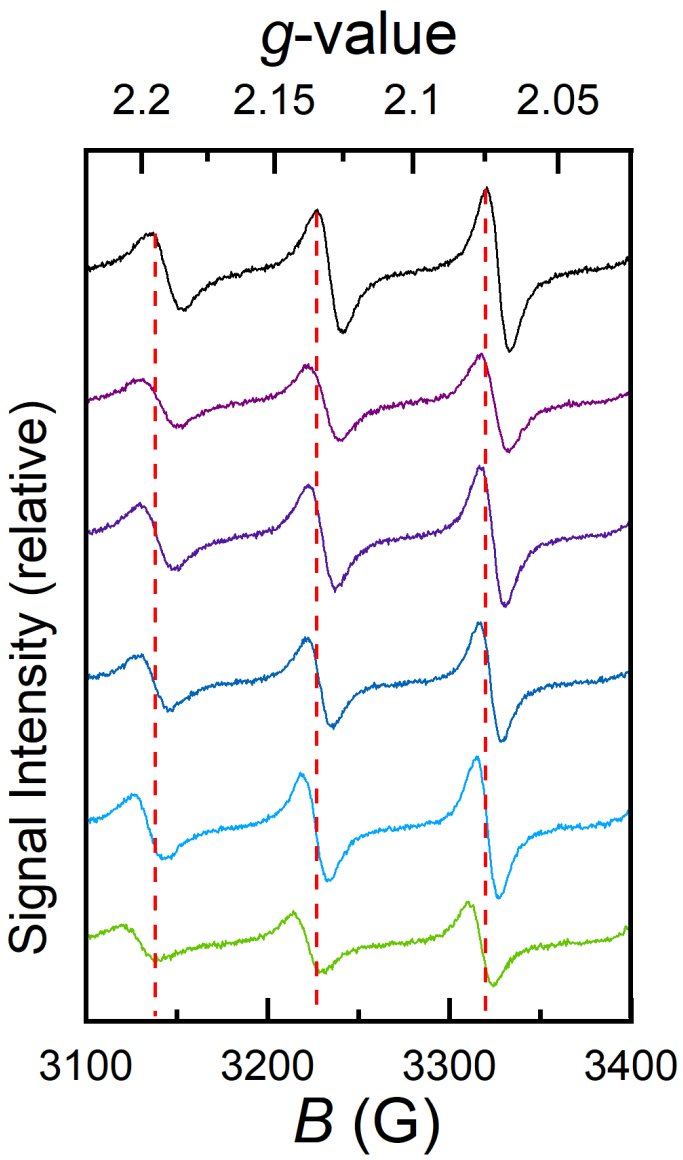

Figure S42. Comprehensive stacked spectra of experimental EPR data. Straight dashed red lines (g = 2.19, 2.14, 2.08) highlight the systematic broadening of the hyperfine coupling throughout the series. Lines correspond to the compounds by color as indicated in Figure S36.

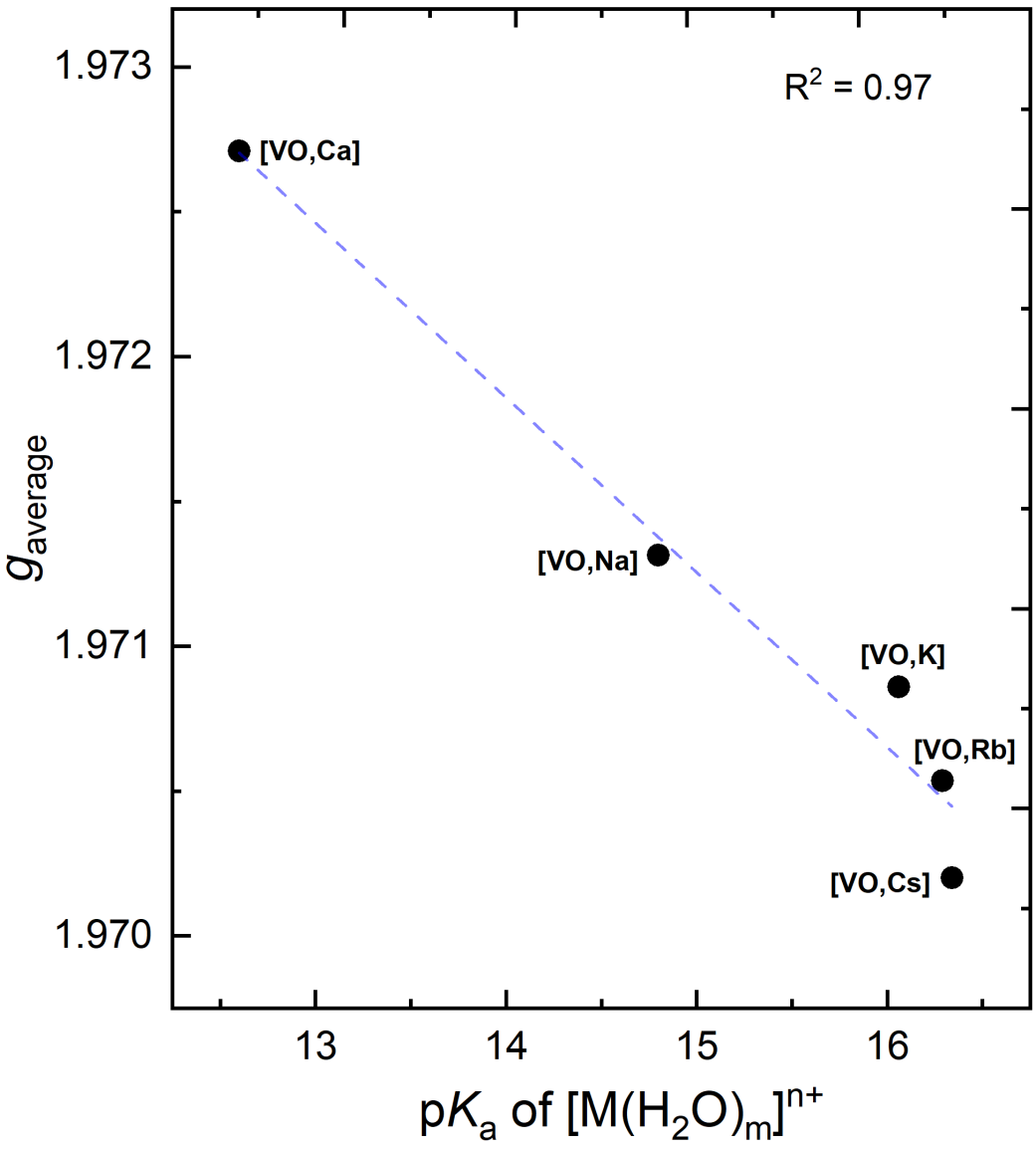

Figure S43. Plot of average *g*-values as a function of pK_a.

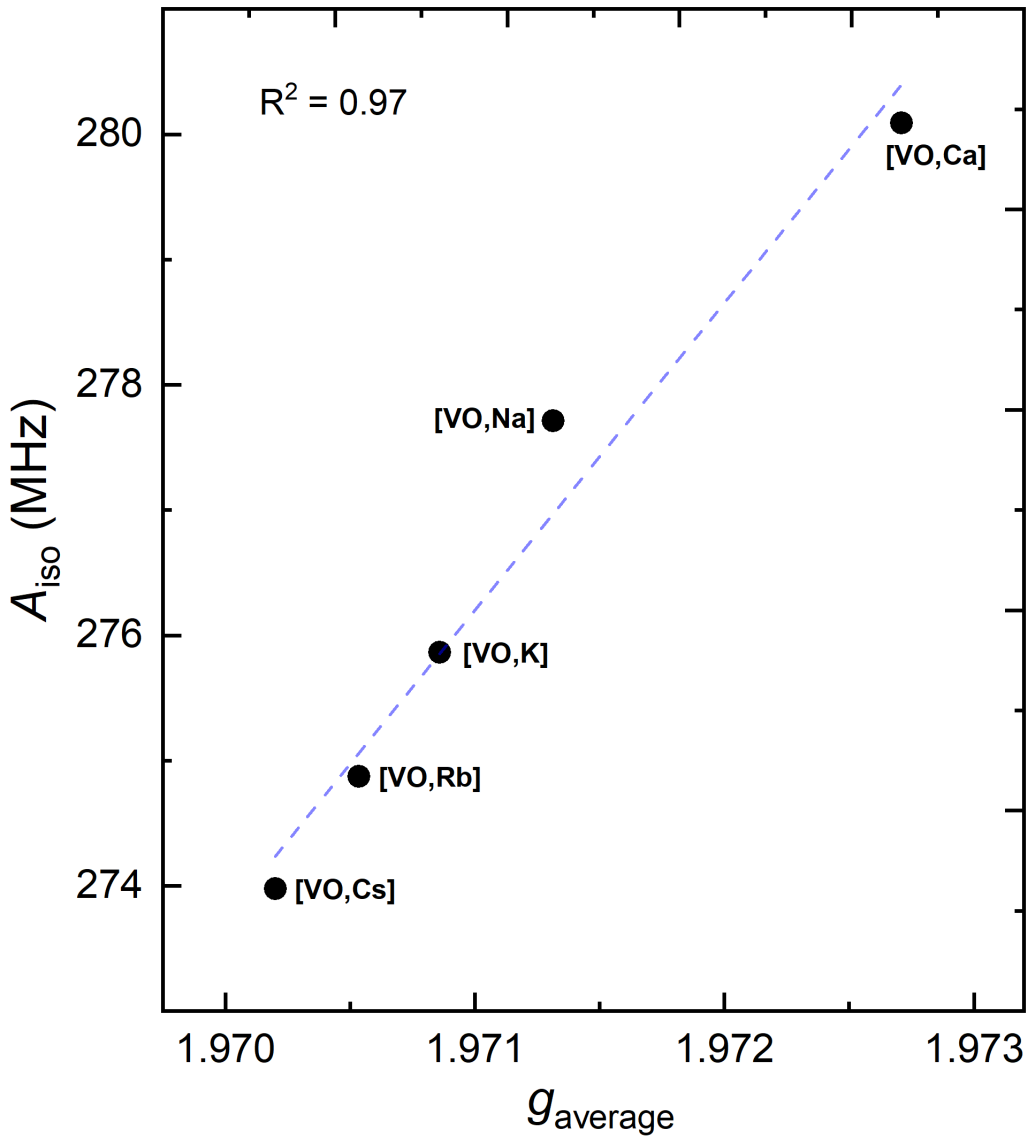

Figure S44. Plot of isotropic *A* values as a function of the average *g*-value.

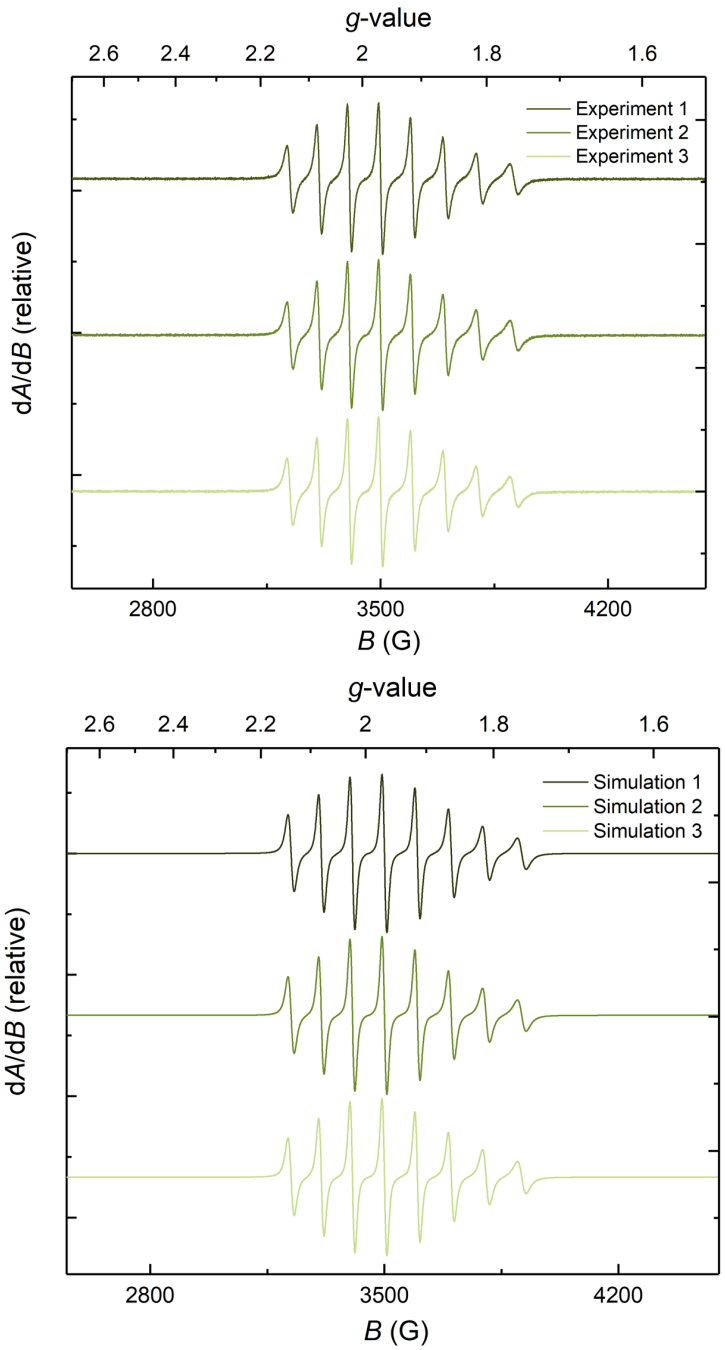

Figure S45. Upper panel: Triplicate X-band EPR spectra of **[VO]** 10 mM solution in MeCN (Temperature = 298 K, Frequency = 9.6405 GHz, Power = 2mW). Spectra are averaged over a total 30 scans. Lower panel: Triplicate X-band EPR simulation spectra of **[VO]**. Simulated using EasySpin for MATLAB with the *garlic* function.

Simulation #	A_{iso} (MHz)	$g_{average}$	RMSD
1	271.873	1.96979	0.014669
2	271.871	1.96975	0.014541
3	271.837	1.96867	0.014766
Average	271.860	1.96940	0.014658
STDEV	0.02023	0.00064	0.000113

Table S2. Comparison of the A_{iso} $g_{average}$, and RMSD values resulting from the three **[VO]** simulations.

EasySpin EPR Simulation Script

```
% load data

[B,spc,p] = eprload('CD-1-VO-10mM_9.64GHz_30scans_smaller
sweep width.DTA');

%% gentle BC & normalization
spcbc = basecorr(spc,1,1);
s=normalize(B,spcbc);
g=b2g(B/10,p.MWFQ);

%plot(B/10,spcbc,'k')
plot(B/10,s,'k')
xlim([300 400])

%% plot g as x-axis

plot(g,s,'k')
set(gca,'xdir','reverse')
xlim([1.7 2.3])

%% VO fit

Aave = 275; %MHz
gpar=1.9;
gperp=2;

Apar= Aave*2; %MHz
Aperp = (1/2)*(3*Aave-Apar); %MHz
                            %Aave=(2*Aperp+Apar)/3
Sys.S=1/2;
Sys.Nucs='V';
Sys.g=[gperp gpar];
Sys.A=[Aperp Apar];
Sys.lwpp=1;
Sys.logtcorr=-10.5; %10 = 100 ps
Exp.mwFreq = p.MWFQ/10^9;
Exp.Range = [B(1)/10 B(5000)/10];
Exp.nPoints = p.XPTS;
Exp.Temperature = 298;
[Bs,Ss]=garlic(Sys,Exp);

%% fit
Sys.myApar=Apar;
Sys.myAave=Aave;
Vary.myAave=Aave/20;
Vary.myApar=Apar/3;
Vary.g=[0.1 0.1];
Vary.logtcorr=1;
```

Figure S46. MATLAB script used to simulate EPR spectra using the EasySpin package.

Electrochemical Studies

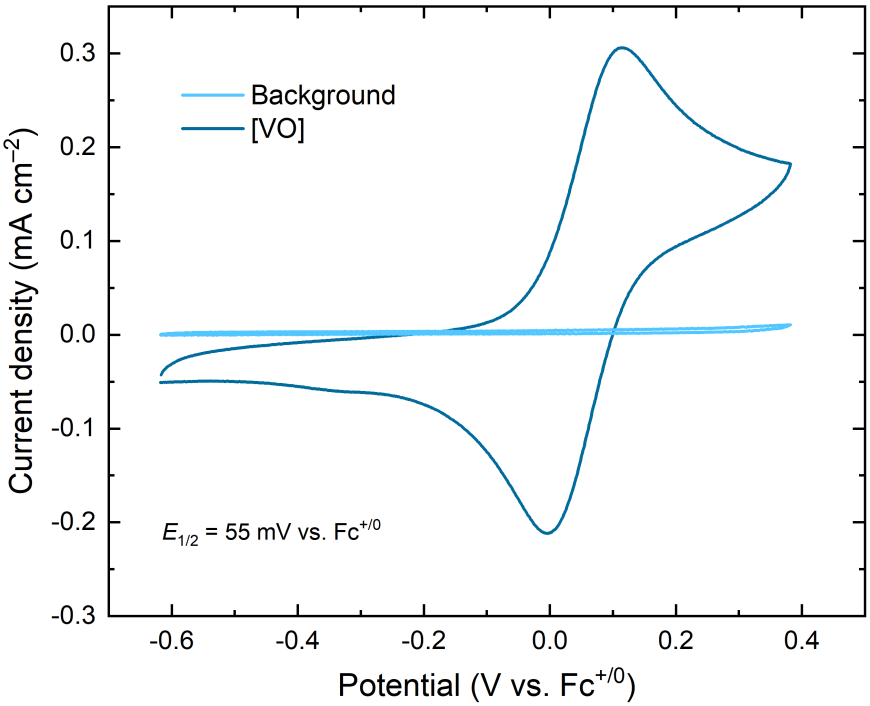

Figure S47. CV data for **[VO]** in CH_3CN (0.1 M $[^nBu_4]^+[PF_6]^-$, 100 mV/s).

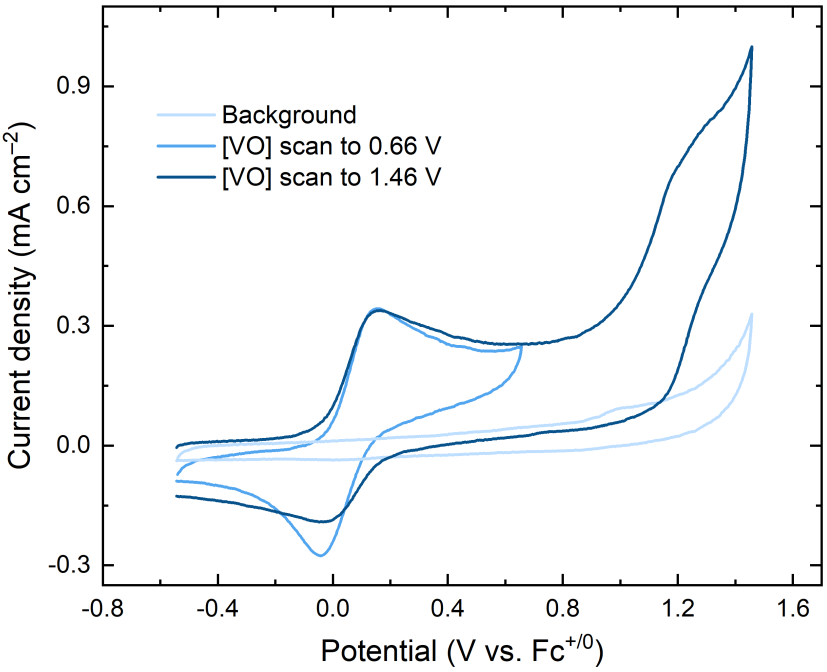

Figure S48. CV data for **[VO]** showing ligand oxidation when scanned to more positive potentials.

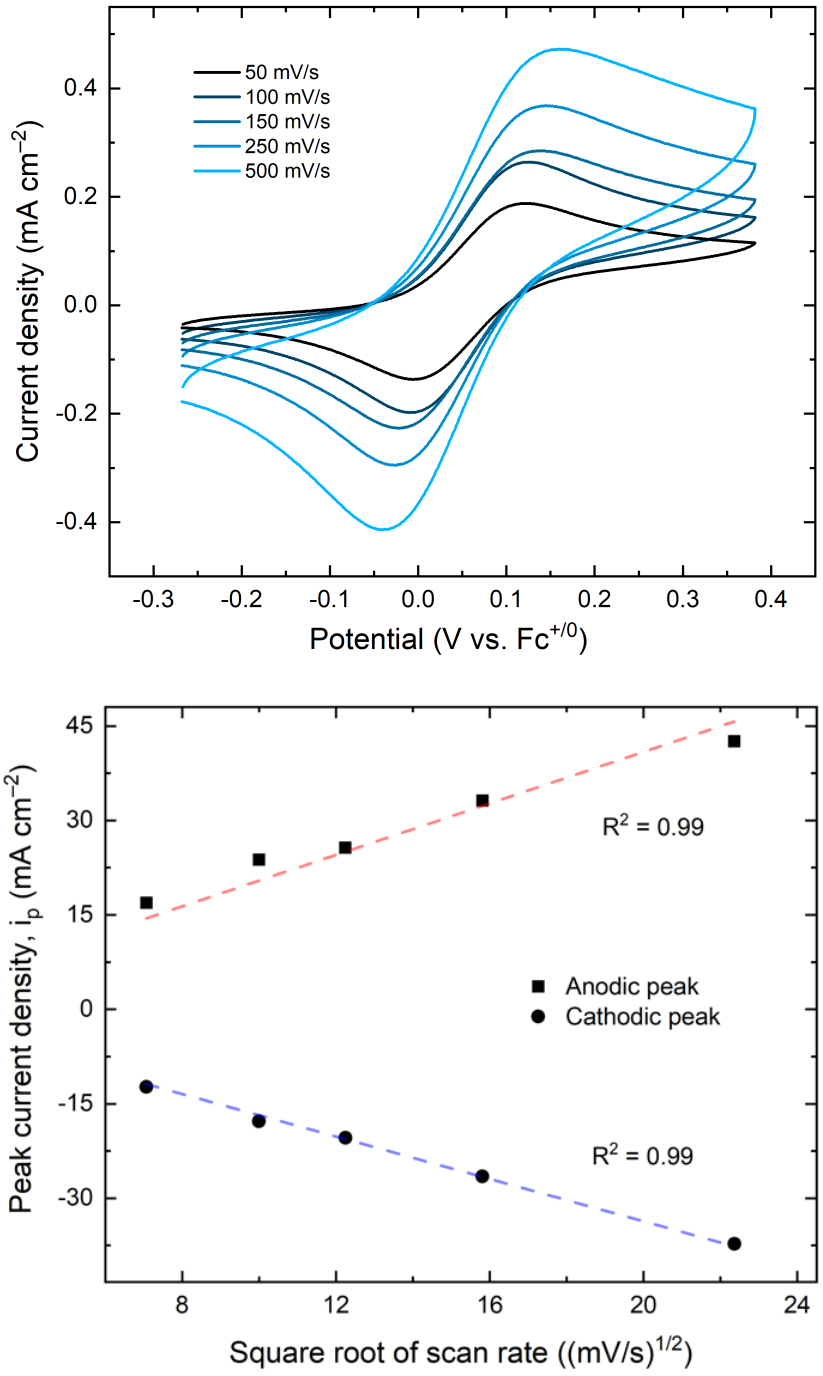

Figure S49. Top panel: scan rate dependence data for **[VO]**. Bottom panel: plot of peak current density vs. (scan rate)$^{1/2}$, demonstrating the diffusional nature of the oxidized species involved.

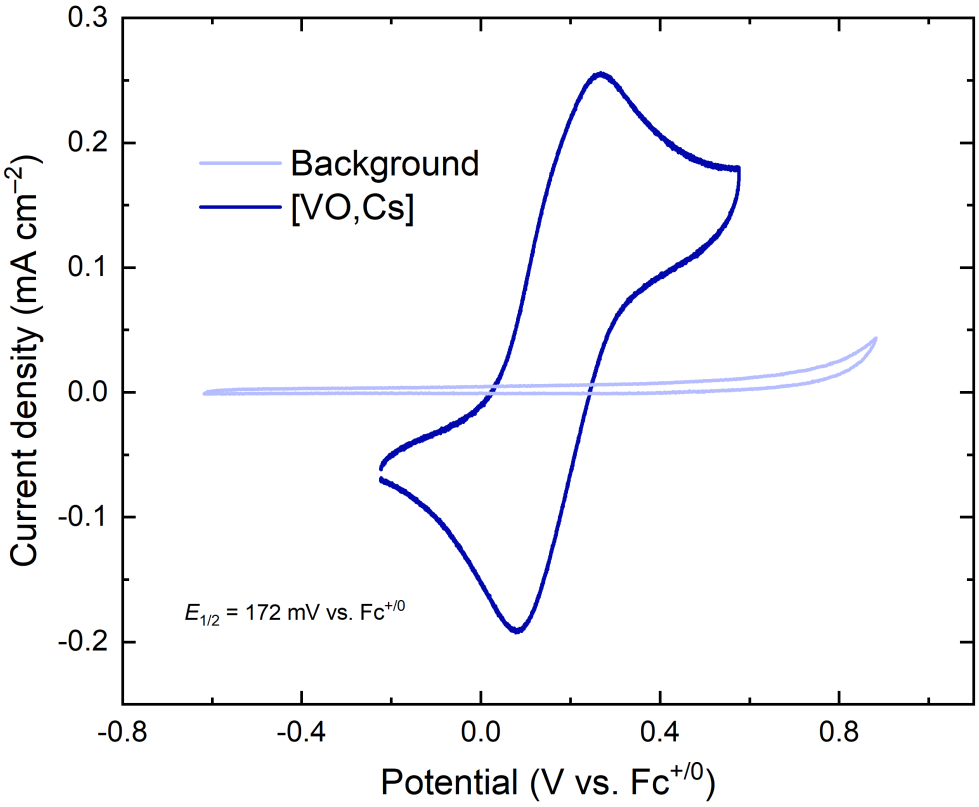

Figure S50. CV data for **[VO,Cs]** in CH_3CN (0.1 M $[^nBu_4]^+[PF_6]^-$, 100 mV/s).

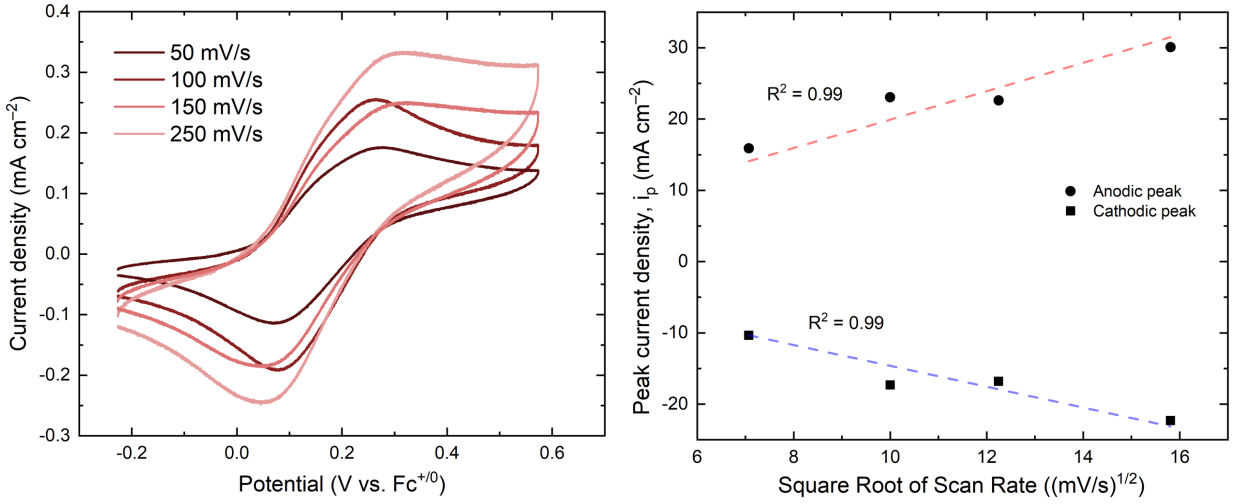

Figure S51. Left panel: scan rate dependence data for **[VO,Cs]**. Right panel: plot of peak current density vs. (scan rate)$^{1/2}$, demonstrating the diffusional nature of the oxidized species involved.

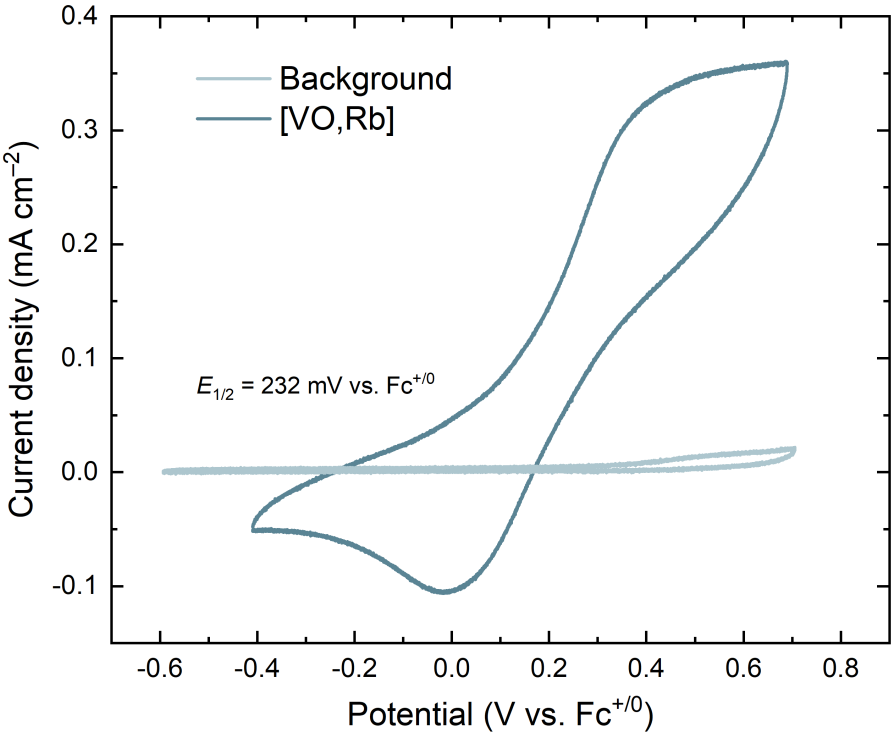

Figure S52. CV data for **[VO,Rb]** in CH_3CN (0.1 M $[^nBu_4]^+[PF_6]^-$, 100 mV/s).

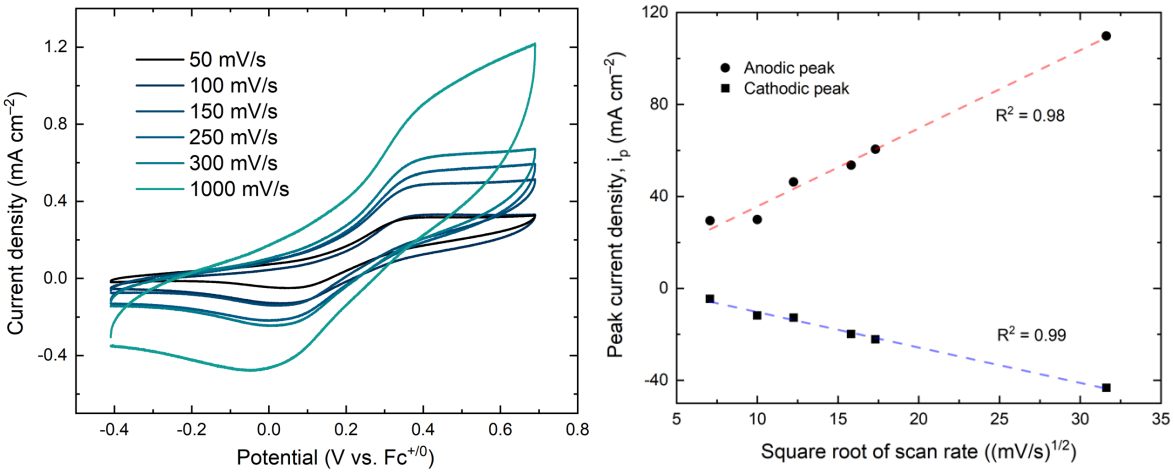

Figure S53. Left panel: scan rate dependence data for **[VO,Rb]**. Right panel: plot of peak current density vs. (scan rate)$^{1/2}$, demonstrating the diffusional nature of the oxidized species involved.

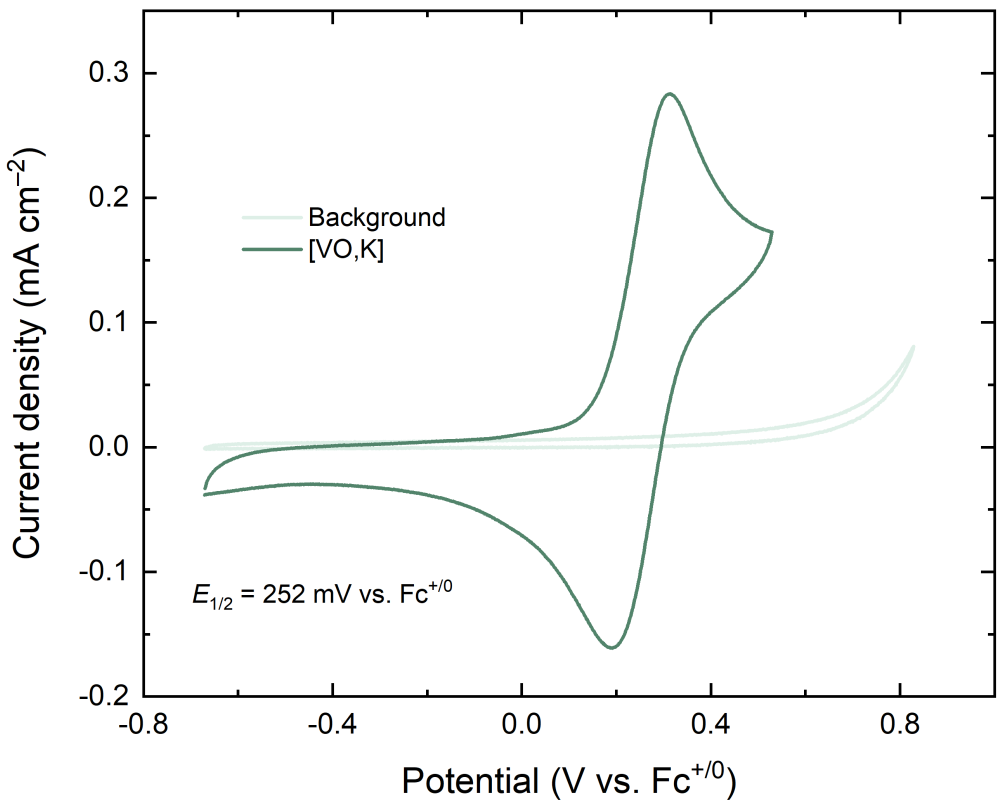

Figure S54. CV data for **[VO,K]** in CH_3CN (0.1 M $[^nBu_4]^+[PF_6]^-$, 100 mV/s).

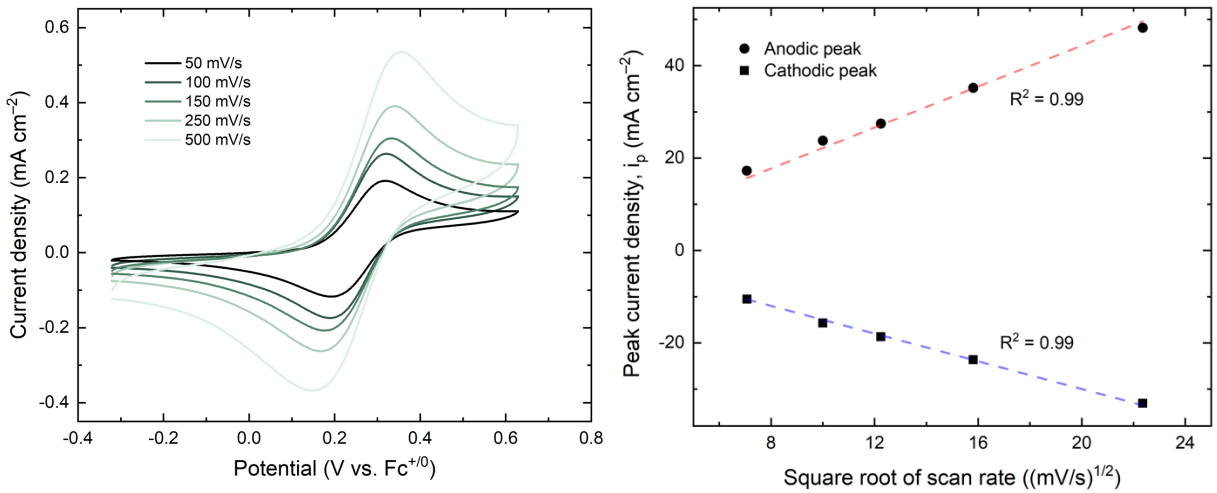

Figure S55. Left panel: scan rate dependence data for **[VO,K]**. Right panel: plot of peak current density vs. (scan rate)$^{1/2}$, demonstrating the diffusional nature of the oxidized species involved.

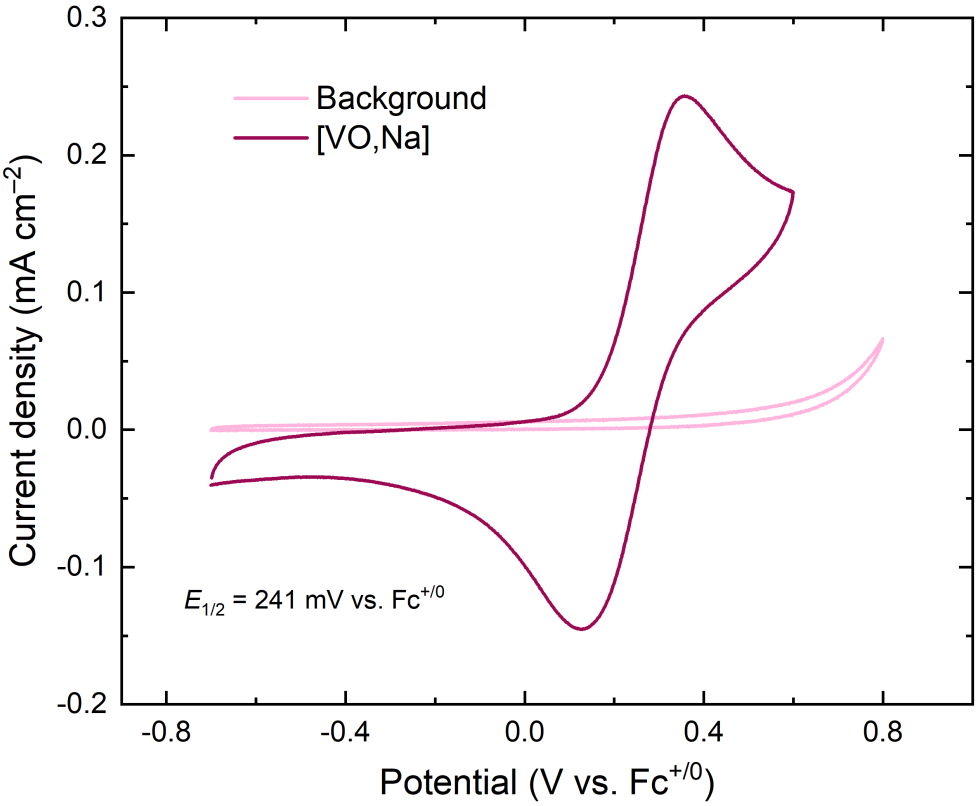

Figure S56. CV data for **[VO,Na]** in CH_3CN (0.1 M $[^nBu_4]^+[PF_6]^-$, 100 mV/s).

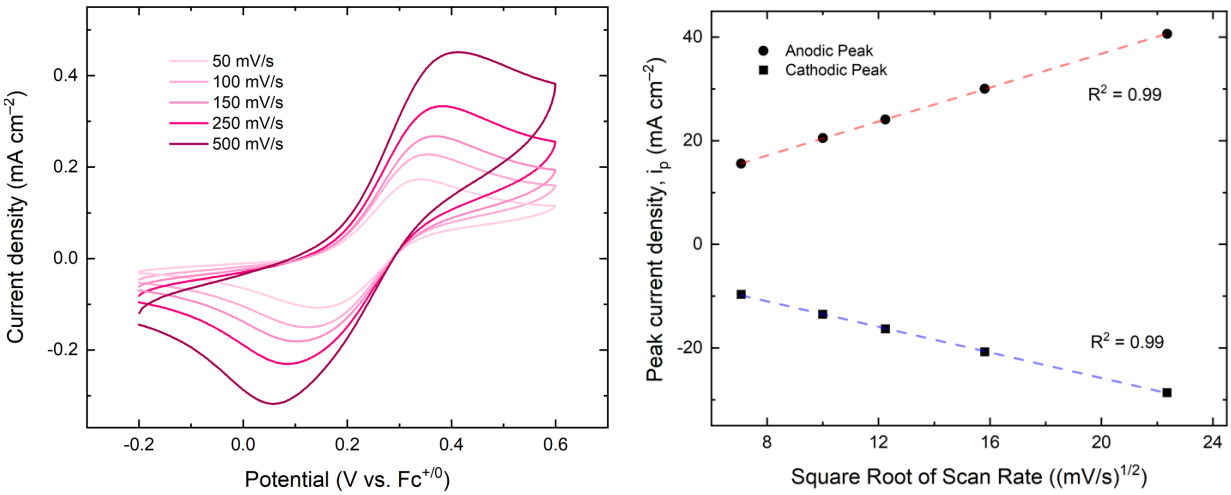

Figure S57. Left panel: scan rate dependence data for **[VO,Na]**. Right panel: plot of peak current density vs. (scan rate)$^{1/2}$, demonstrating the diffusional nature of the oxidized species involved.

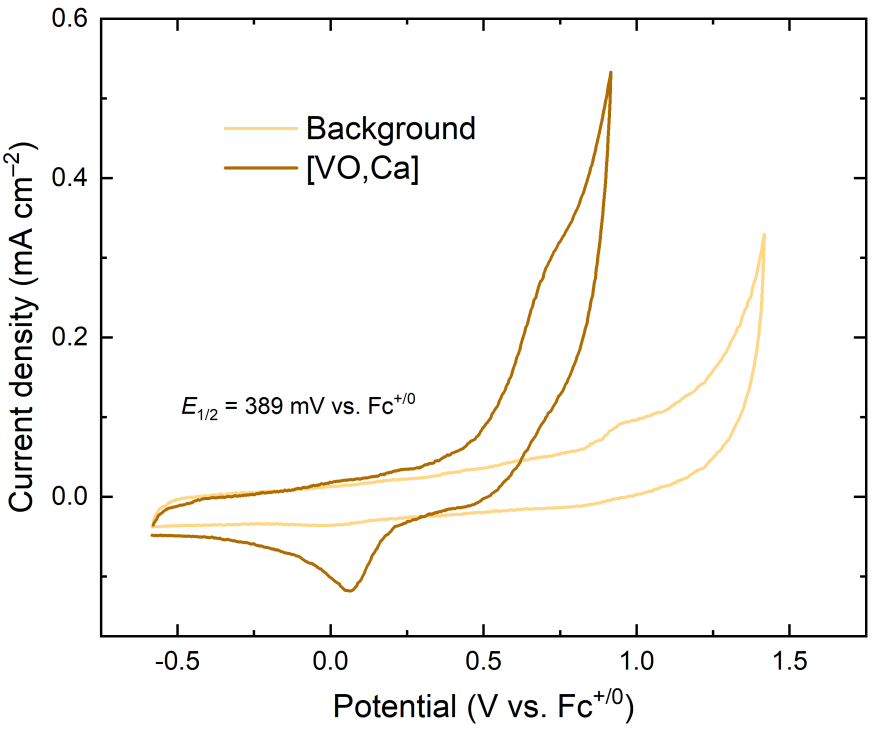

Figure S58. CV data for **[VO,Ca]** in CH_3CN (0.1 M $[^nBu_4]^+[PF_6]^-$, 100 mV/s).

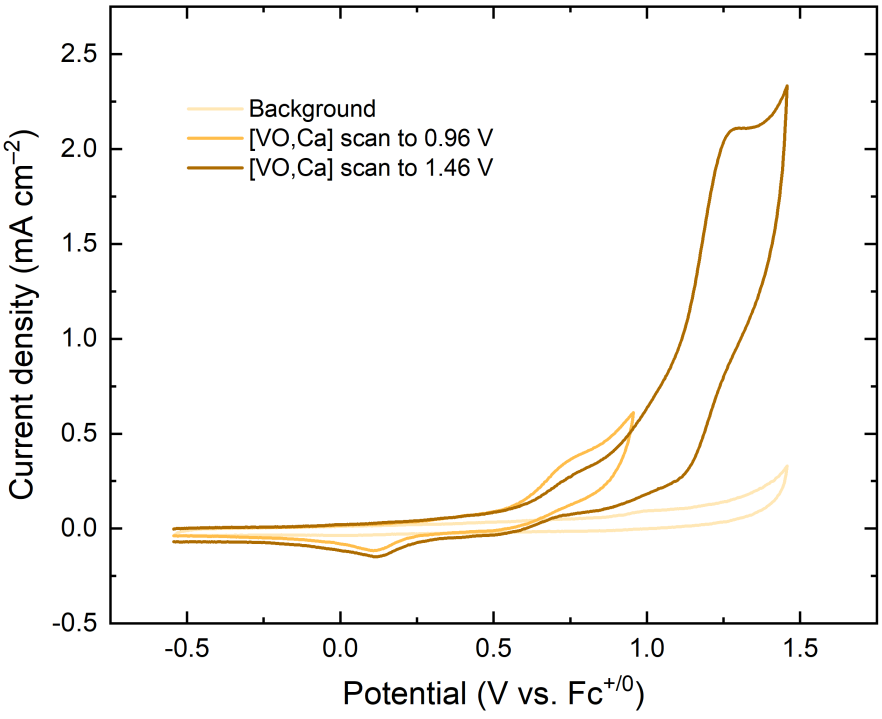

Figure S59. CV data for **[VO,Ca]** demonstrating ligand oxidation when scanned to more positive potentials.

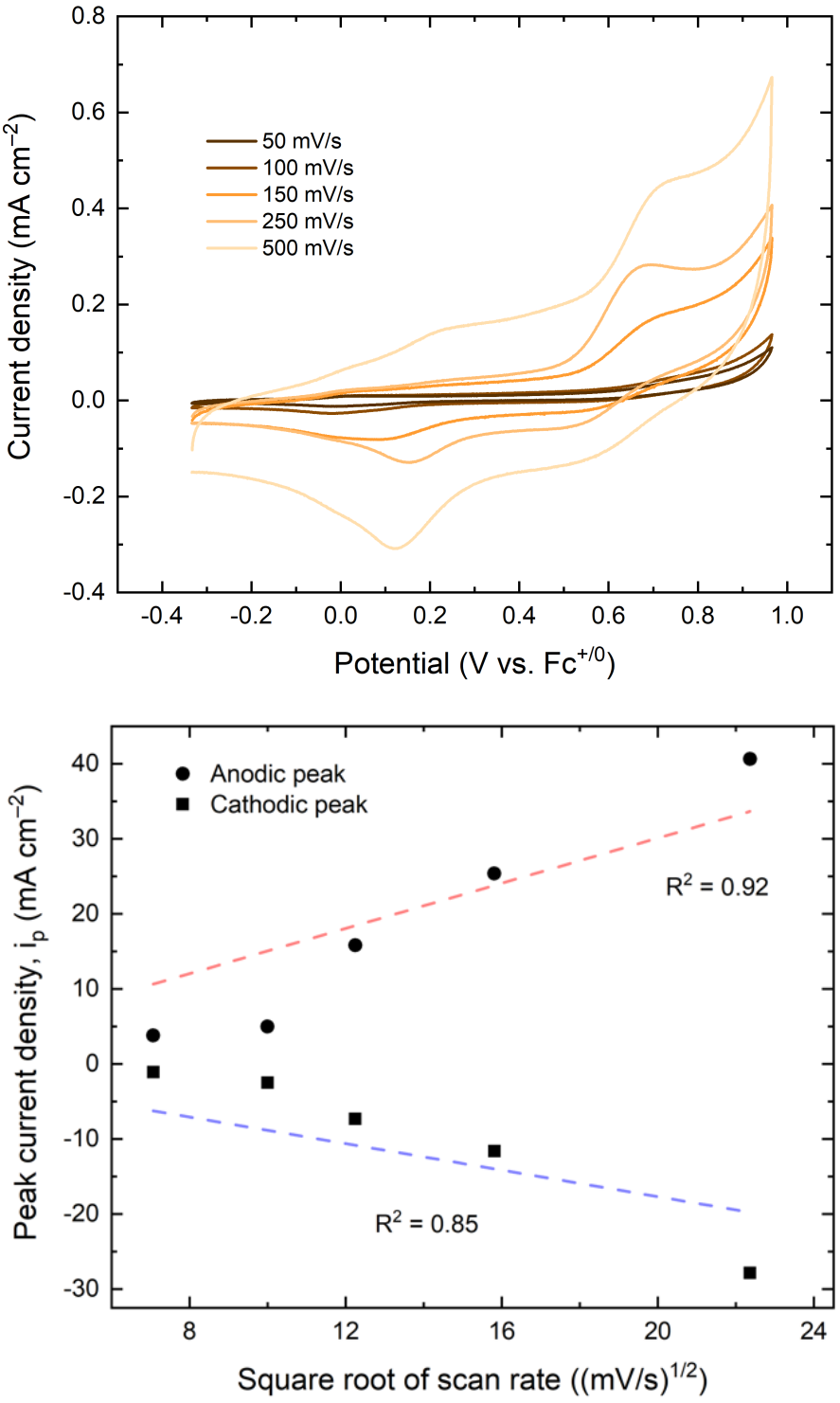

Figure S60. Top panel: scan rate dependence data for **[VO,Ca]**. Bottom panel: plot of peak current density vs. (scan rate)$^{1/2}$, demonstrating the diffusional nature of the oxidized species involved.

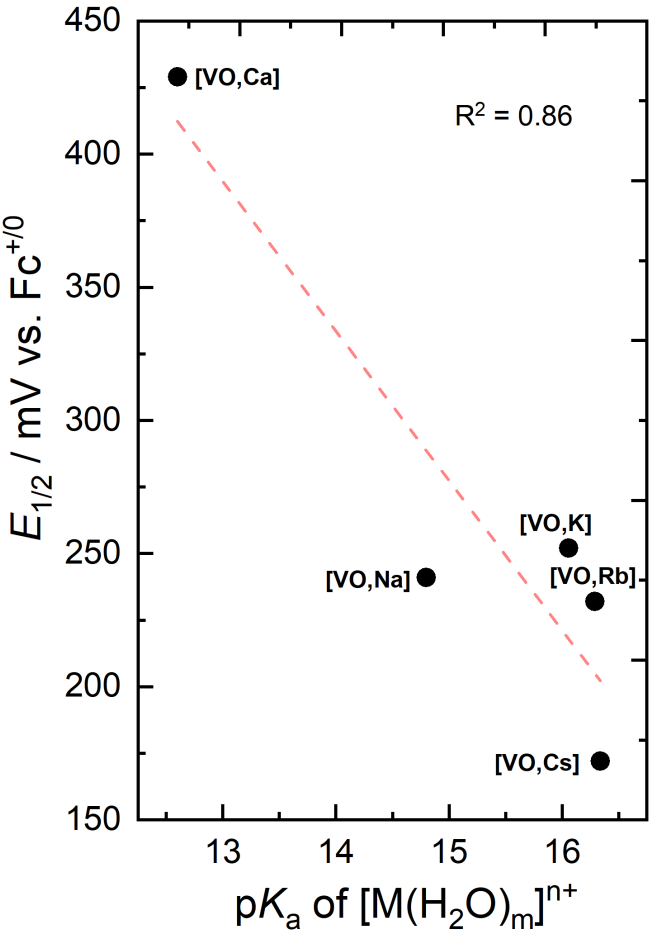

Figure S61. Dependence of $E_{1/2}$ on Lewis acidity. Trendline exhibits a slope of -56 ± 13 mV/pK_a

X-Ray Crystallography

General Considerations

Crystals were mounted using Paratone oil with MiTeGen loops and placed under a nitrogen stream for data collection. For **[VO]** (**a03a**) and **[VO,Na]** (**a04d**) low temperature (120 K) X-ray data were collected using 0.5°-wide ω- or φ-scans on a Bruker D8 3-circle diffractometer with a PHOTON-II detector. X-rays were provided by a fine-focus Mo-sealed tube running at 50 kV and 35 mA (Mo Kα = 0.71073 Å). All diffractometer manipulations for these structures, including data collection, integration, and scaling, were carried out using the Bruker APEX4 Software Suite.[68,69] For **[VO,Ca]** (**b31b**), low temperature (194 K) X-ray data were collected using 1.0°-wide ω- or φ-scans on a Bruker Smart APEX diffractometer equipped with a Bruker Smart APEX CCD detector and graphite monochromator. X-rays were provided by a fine-focus Mo sealed tube running at 50 kV and 30 mA (Mo Kα = 0.71073 Å). All data manipulations for **b31b** were carried out using the Bruker APEX3 Software Suite.[70] The data set for **b31b** was corrected for absorption using the multi-scan method by SADABS,[71] while numerical face-indexed absorption corrections were used for **a03a** and **a04d**. SHELXT was used to solve each structure using intrinsic phasing methods.[72] Final stages of weighted full-matrix least-squares refinement were conducted using F_o^2 data with SHELXL in SHELXle.[73]

The final structural model for each compound incorporated anisotropic thermal parameters for all ordered full-occupancy and disordered partial-occupancy nonhydrogen atoms; isotropic thermal parameters were used for all included hydrogen atoms. Hydrogen atoms in each complex were fixed at idealized riding model sp^2- or sp^3-hybridized positions with C–H bond lengths of 0.95 – 0.99 Å. Methyl groups were incorporated into the structural models either as sp^3-hybridized riding model groups with idealized "staggered" geometry and a C-H bond length of 0.98 Å or as idealized riding model rigid rotors (with a C–H bond length of 0.98 Å) that were allowed to rotate freely about their C–C bonds in least-squares refinement cycles. The isotropic thermal parameters of idealized hydrogen atoms in all three structures were fixed at values 1.2 (non-methyl) or 1.5 (methyl) times the equivalent isotropic thermal parameter of the carbon or oxygen atom to which they are covalently bonded.

CCDC entries 2219364–2219366, 2240872, and 2243380 contain the supplementary crystallographic data for this paper. These data can be obtained free of charge from the Cambridge Crystallographic Data Centre.

The relevant crystallographic and structure refinement data for all three compounds are given in Tables S3–S5.

Special Refinement Details for [VO] (a03a)

No special refinement was required. Two outer-sphere co-crystallized molecules of acetonitrile were found in the asymmetric unit; these acetonitrile molecules are presumably derived from the conditions of crystallization, as the crystals of **[VO]** were grown by vapor diffusion of diethyl ether into a concentrated solution of the compound in acetonitrile.

Solid-State Structure of [VO]

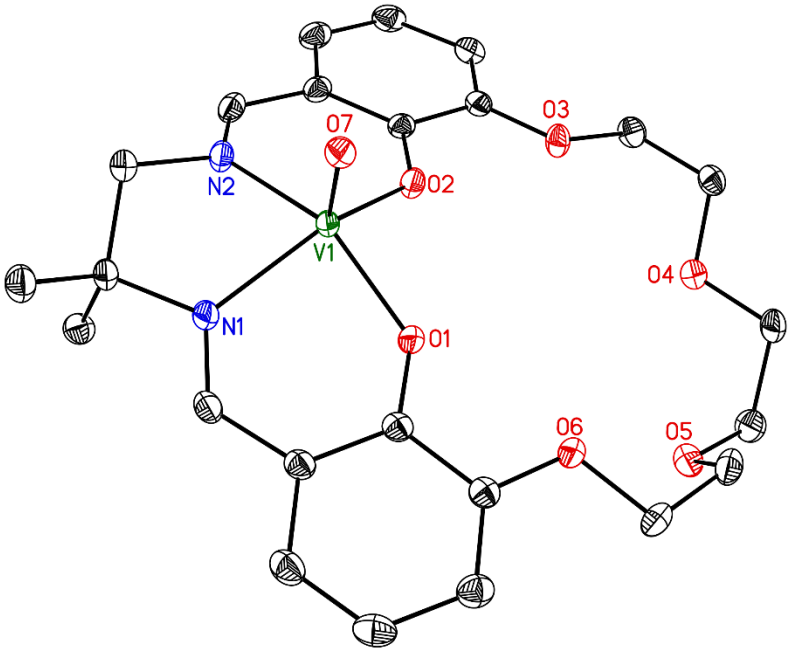

Figure S62. Solid-state structure from XRD of **[VO]**. All H-atoms and two co-crystallized outer-sphere acetonitrile solvent molecules are omitted for clarity. Displacement ellipsoids are shown at the 50% probability level.

Full Solid-State Asymmetric Unit of [VO]

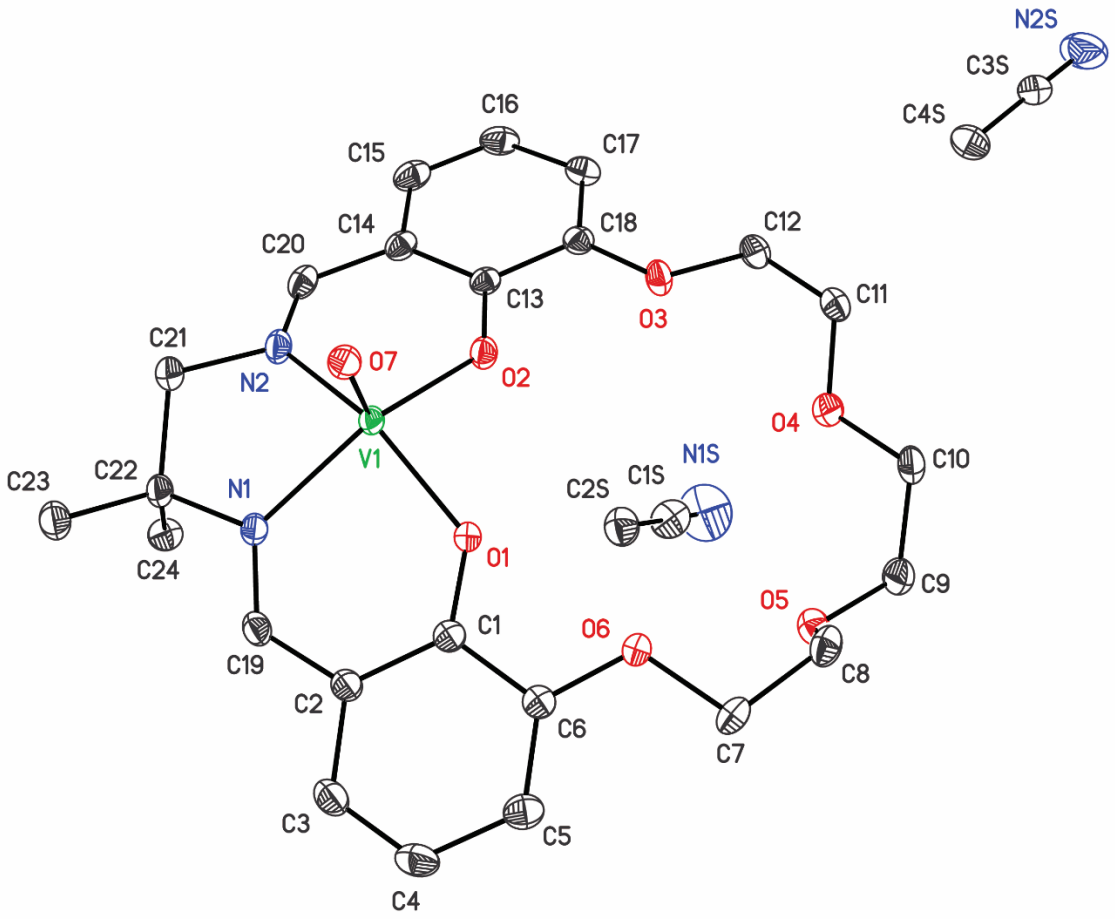

Figure S63. Full solid-state structure of the asymmetric unit from XRD of **[VO]**. All H-atoms are omitted for clarity, and displacement ellipsoids are shown at the 50% probability level.

This figure shows the systematic and consistent macrocycle labeling convention used throughout this work. The only exception to this naming convention is molecule B of structure a04d-No1 in *P-1*. See p. S48 for details on this naming "anomaly."

Special Refinement Details for [VO,Na] (a04d-No1 and a04d-No2)

Vapor diffusion of diethyl ether into a concentrated acetonitrile solution of **[VO,Na]** afforded single crystals of the heterobimetallic complex suitable for XRD analysis. Four inner-sphere molecules of acetonitrile, each bound to a separate Na^+ and derived from the crystal growth conditions, were found in the final structure. A single outer-sphere molecule of water was also found; this water is presumably derived from adventitious water present under the crystal growth conditions or could have been incorporated during sample handling, as the crystals had to be transported from Lawrence, KS to South Bend, IN for data collection.

The **a04d** structure was initially solved and fully refined to give the anticipated atom-to-atom connectivity and a reasonable R_1 (8.7%) value. The asymmetric unit contained two crystallographically-independent monomeric macrocyclic **[VO,Na]** moieties that form dimers about crystallographic inversion centers in the centrosymmetric triclinic space group *P-1* (No. 2). In this **a04d-No2** structure, the first dimer utilizes the inversion center at (½, 1, ½) and the second dimer utilizes the inversion center at (1, 0, 0). Both independent **[VO,Na]** moieties feature formally 8-coordinate hexagonal bipyramidal Na^+ ions. The axial coordination sites are occupied by one inner-sphere molecule of acetonitrile solvent (likely derived from the conditions of crystallization) and the oxo-type oxygen of a nearby inversion-related **[VO,Na]** monomer. In **a04d-No2**, the average Na•••O_{oxo} interaction is 2.304(3) Å while the average V–O_{oxo} bond is significantly shorter at 1.597(3) Å.

Although the structural and refinement details obtained in the case of **a04d-No2** were quite acceptable, the refinement required 60/40 disordering of the 4-carbon -$CH_2C(CH_3)_2$- bridge in one of the two **[VO,Na]** monomers comprising the asymmetric unit. This was assumed to be due to the dimer at that inversion center being "flipped" nearly half of the time. In projection, the Na-containing macrocycle would have C_{2v} symmetry without the methyl groups of the 4-carbon -$CH_2C(CH_3)_2$- bridge between the two imine nitrogens. For **[VO,Na]**, the methyl groups destroy the "vertical" mirror plane containing the vanadyl group, while the coordination of a vanadyl group to the *[N_2,O_2]* core destroys the remaining "horizontal" mirror plane containing the macrocyclic nitrogens and oxygens when the methyls are present. The vanadyl-macrocycle unit is therefore chiral and each dimer in the **a04d-No2** structure would contain both enantiomers, herein designated **I** and **II**.

These enantiomers **I** and **II** would be related by rigorous crystallographic symmetry in **a04d-No2** and the disordered dimer site could have the **I** and **II** halves interchanged in the lattice nearly half of the time. This could manifest itself as an *apparent*, and observed, mirror reflection of the macrocycle in the "vertical" plane coincidentally containing diimine methyl carbon atom C48 (C24 of the second independent molecule) due to tilting of the ethylene link, V2, O14 (vanadyl oxygen), and Na1A in **a04d-No2**. Although the entire macrocycle would actually have two different orientations, the "disorder" could be modeled quite well by incorporating alternate bridges between the imine groups. This could be achieved with 4-carbon -$CH_2C(CH_3)_2$- moieties bridging the two nitrogen centers in opposite directions, similar to the case of our prior structure of a monometallic palladium complex in the same ligand (**q35i**).[34] However, unlike the case of that prior structure, the model for **a04d-No2** coincidentally displays one shared methyl group (C48) for both disordered bridging moieties.

In any case, the structure of **a04d-No2** can presumably be concluded to be problematic due to the presence of a short, 2.918 Å intermolecular contact between a disordered atom and an ordered atom: C47(disordered methyl)•••O32(ordered) (O32 asymmetric unit: 1565); this separation should likely be 3.40 Å or larger considering the probable van der Waals nature of this packing interaction.[74] This suggested the possibility that the space group could actually be *P1* (No. 1).

This proved to be correct and the structure of **[VO,Na]** was solved and refined in the non-centrosymmetric space group *P1* (No. 1). In the final structure, denoted here as **a04d-No1**, there are two crystallographically-independent dimers or four crystallographically- independent monomeric **[VO,Na]** moieties (denoted A, B, C, and D) in the triclinic asymmetric unit (and unit cell). The first dimer contains the A and C monomers and the second dimer contains the B and D monomers. All four monomers confirm the expected atom-to-atom connectivity for **[VO,Na]** without the diimine backbone disorder observed for the refinement in centrosymmetric *P-1* (No. 2). The most significant difference in the two structures is that the **a04d-No1** structure has *two distinctly different dimers* while this was not obvious in the **a04d-No2** structure. The dimer with A and C labeled monomers contains a *pseudo*-inversion-center-related **I** and **II** enantiomeric pair. But in the second dimer (B and D labeled monomers), both monomers are the same enantiomer (**I** and **I**, or **II** and **II**). It should be noted that either of these latter two combinations for the second dimer would produce the disorder that was observed for the *incorrect centrosymmetric* **a04d-No2** structure that imposed a center of symmetry. Notably, the data crystal was a 51/49 inversion twin, meaning that the twinned crystal used for data collection overall contains equal quantities of enantiomers **I** and **II**, consistent with the racemic nature of the product mixture generated for synthesis of **[VO,Na]**. If monomer A in the asymmetric unit of **a04d-No1** is enantiomer **I**, then monomers C, B and D are all enantiomer **II**.

Most of the correct **a04d-No1** structure possesses a *pseudo*-inversion center. The only major departure from *pseudo*-inversion symmetry for the metal complexes is for the 4-carbon bridge between the two imine nitrogens in the second B/D dimer. This *pseudo*-symmetry produced strong correlations between parameters of the *pseudo*-inversion related atoms and necessitated the use of 67 ISOR restraints for C, N and O atoms as well as 11 mild SADI bond length restraints for individual C-N or C-C bonds and mild SAME restraints requiring the metrics for the 4-carbon diimine bridges of the B and D monomers to be similar to those of the A monomer to avoid A- and B-level alerts in CheckCIF. Additionally, the acetonitrile ligands for the B and D monomers were restrained to have near idealized geometries by setting the bond lengths and N•••C_{methyl} separation for the nonhydrogen atoms to appropriate multiples of the C-N bond length that was included in the refinement as a free variable that refined to a final value of 1.203(5) Å.

The final R_1 value (6.8%) as well as the ratio of restraints-to-parameters (460 to 1668) are quite reasonable in **a04d-No1**. Anisotropic thermal parameters were incorporated for all nonhydrogen atoms in the final structural model, and the relevant crystallographic and structural refinement details for **a04d-No1** are given in Table S4. Details for the alternative refinement **a04d-No2** are also given in Table S4 for comparison.

The final .hkl-format file used for refinement of both **a04d-No1** and **a04d-No2** contains the available Friedel pair data that were averaged for the **a04d-No1** refinement. For ease of structural

comparison, the unit cell origin for **a04d-No1** was chosen to be essentially the same as the one for **a04d-No2** with the **a04d-No1** *pseudo*-inversion centers coinciding with the crystallographic inversion centers of **a04d-No2.**

The asymmetric unit of **a04d-No1** is also distinguished from that found in **a04d-No2** as it contains one outer-sphere molecule of H_2O (associated with O1W) that is engaged in H-bonding interactions with nearby outer-sphere triflate counter-anions. O1W was not modeled in the final solution for **a04d-No2**. However, it appears that Peak #2 in the final *P-1* difference Fourier (1.65 electrons) could be associated with this H_2O. Peak #2 is about 0.44 Å away from the position for the non-centrosymmetric O1W and could make what would be two H-bonds to triflate oxygens: a reasonably short one (2.88 Å) and a rather long one (3.42 Å) with a subtended angle of 126.5°.[75] For **a04d-No1**, in the end, the occupancy of O1W refined to a value of 1.05, albeit with a large temperature factor. So, the final occupancy value was set to 1.00. This water molecule probably plays a key role in the structure, as it appears to not only be tying the two nearby triflates together through clearcut hydrogen-bonding interactions, but it also appears to be important in determining the packing of the two different, but sterically similar, types of dimers found in **a04d-No1**.

The possible importance of this water molecule to the observed non-centrosymmetric structure was investigated by checking for bad contacts when a second (inversion-related) water molecule was artificially generated (refer to a04d+water.res accompanying the published manuscript upon which Chapter 1 is based). Such a water molecule, labeled O1W' in the accompanying file, is also in a position to hydrogen bond to the oxygen atoms of two triflate groups. Unfortunately, it makes a 2.817 Å contact with a C23D methyl carbon that is significantly shorter than the anticipated van der Waal's contact of 3.40 Å.[74] Thus, we concluded that the absence of O1W' in the non-centrosymmetric structure allows the needed packing room for C23D from the second half of the rigorously non-centrosymmetric dimer formed from two monomers of the *same* enantiomer.

In the final model for **a04d-No1**, the first dimeric unit of **[VO,Na]** has A and C monomers that are related quite closely by a *pseudo*-inversion center. These would be related by a rigorous inversion center in **a04d-No2**. The second dimer in **a04d-No1** has B and D monomers that are *only nearly* related by a *pseudo*-inversion center; the *pseudo*-inversion symmetry of monomers B and D is broken by a "flipping" of the C21-C24 bridges in the packing of the diimine units. This means that unlike the first dimer, both halves of the second dimer are the *same* enantiomer. To show this clearly in the final model, the B monomer is intentionally labeled with a different convention than that used for the other macrocyclic species A, C, and D present in the asymmetric unit (see Figure S43 for the full atom naming of the regular convention). All atoms except the C21-C24 bridge in monomer B are labeled to reflect the *pseudo*-inversion center present for that dimer. The flipping of the diimine bridge thus results in both halves of the corresponding dimer (composed of monomers B and D) having the *same* stereochemical configuration. This situation contrasts with monomers A and C, which are related fully by a *pseudo*-inversion center, and thus have *opposite* stereochemical configurations. The labeling "anomaly" has been used here to emphasize the stereochemical difference between the two dimeric species in the asymmetric unit of **a04d-No1**. The bridge behavior destroys one of the macrocyclic C_{2v} mirror planes for a 2-dimensional projection of these species, highlighting the challenges induced by use of the diimine bridge containing a dimethyl-methylene moiety for crystallographic studies. The steric impact of these

two methyl groups on packing a large macrocycle into a crystal lattice is small, and inclusion of these moieties can lead to disorder or *pseudo*-symmetry. However, these methyl groups are required by our synthetic route, which relies on the Thorpe-Ingold effect to drive macrocycle generation for preparation of the monometallic precursor complex **[VO]**.

Notably, the same short intermolecular packing contact between a (previously) disordered methyl group of the heteroditopic ligand of **[VO,Na]** and a fully ordered triflate counter-anion that was present in the centrosymmetric structure was also present in the totally-ordered lower-symmetry non-centrosymmetric structure in *P1*. With both the methyl and triflate being ordered in the *P1* structure, it was possible to identify this interaction as a probable C–H•••O hydrogen bond.[76] The C23B•••O12B separation is 2.966 Å and the C23B-H32G•••O12B angle is 172.8°, statistics that are not inconsistent with weak hydrogen bonding. However, the C23B methyl group orientation was "idealized" about the C22B-C23B bond in full refinement of **a04d-No1** (via an AFIX 33 command), meaning that the C23B•••O12B separation of 2.966 Å is the structural parameter most relevant to indication of a weak H-bond in this case. The presence of this C-H•••O H-bond would be expected to make disorder of C23B and/or C23D less likely. A search of the Cambridge Structural Database[77] revealed 115 hits on a search for C(methyl)•••O(triflate) contacts of ≤ 3 Å. Restriction of the search results to structures with $R_1 \leq 5\%$ gives 26 hits. Among these, several show strikingly similar non-solvent methyl-to-triflate contacts for comparison to the case of C23B•••O12B in **a04d-No1**.[78,79,80] The C–H•••O hydrogen bond found in this case could stabilize the observed crystalline arrangement, along with the two hydrogen bonds involving O1W. The C23B•••O12B hydrogen bond also appears to be instrumental in promoting the co-crystallization of the two different types of dimers of **[VO,Na]**.

In summary, the structure **a04d** can be solved and refined in both *P-1* (No. 2) and *P1* (No. 1), and indeed the average $V–O_{oxo}$ bond distance determined in *P-1* is similar to the average value when the structure is solved in *P1* (1.597(3) Å in *P-1* vs. 1.595(7) Å in *P1*). Along this line, the ADDSYM alert of PLATON suggests the possible space group of *P-1* with a 97% fit when **a04d-No1** is run through CheckCIF. This is fully consistent with the structural refinements reported herein as well as with their *quite* different structural interpretations.

Solid-State Structure of [VO,Na] in a04d-No1

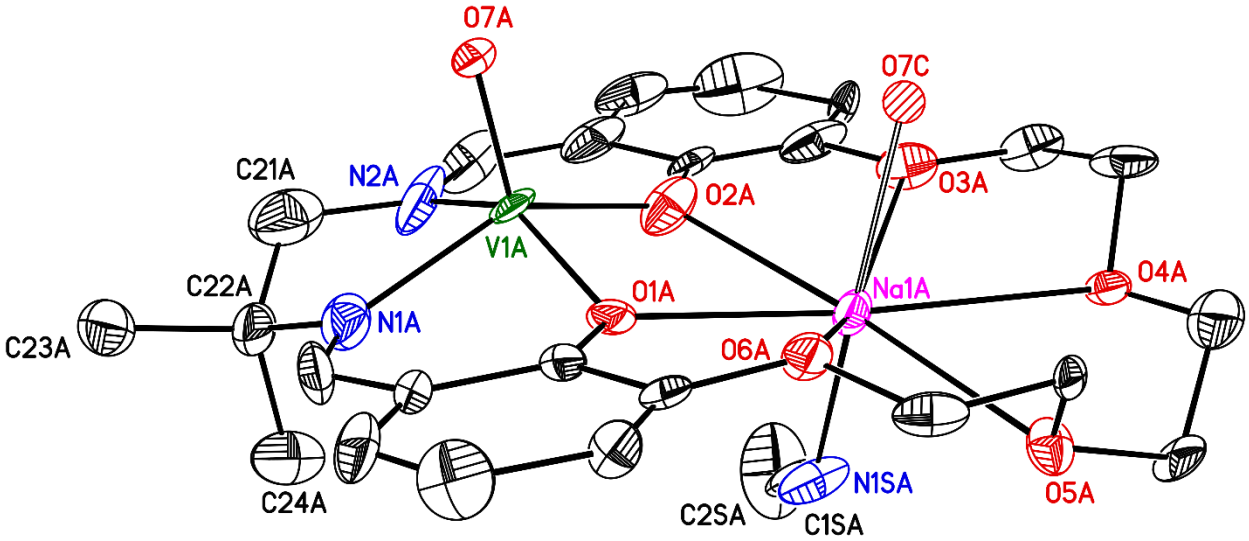

Figure S64. Solid-state structure from XRD of the first monomeric unit of **[VO,Na]** (monomer A). All H-atoms, four outer-sphere triflate counter-anions, an outer-sphere water molecule, most of the second monomeric unit (monomer C) of the dimeric species composed of heterobimetallic complexes, and the second dimeric species (monomers B and D) found in the asymmetric unit are omitted for clarity. Displacement ellipsoids are shown at the 50% probability level. Atom O7C is the vanadium oxo of the adjacent C monomer of **[VO,Na]** in the dimeric species.

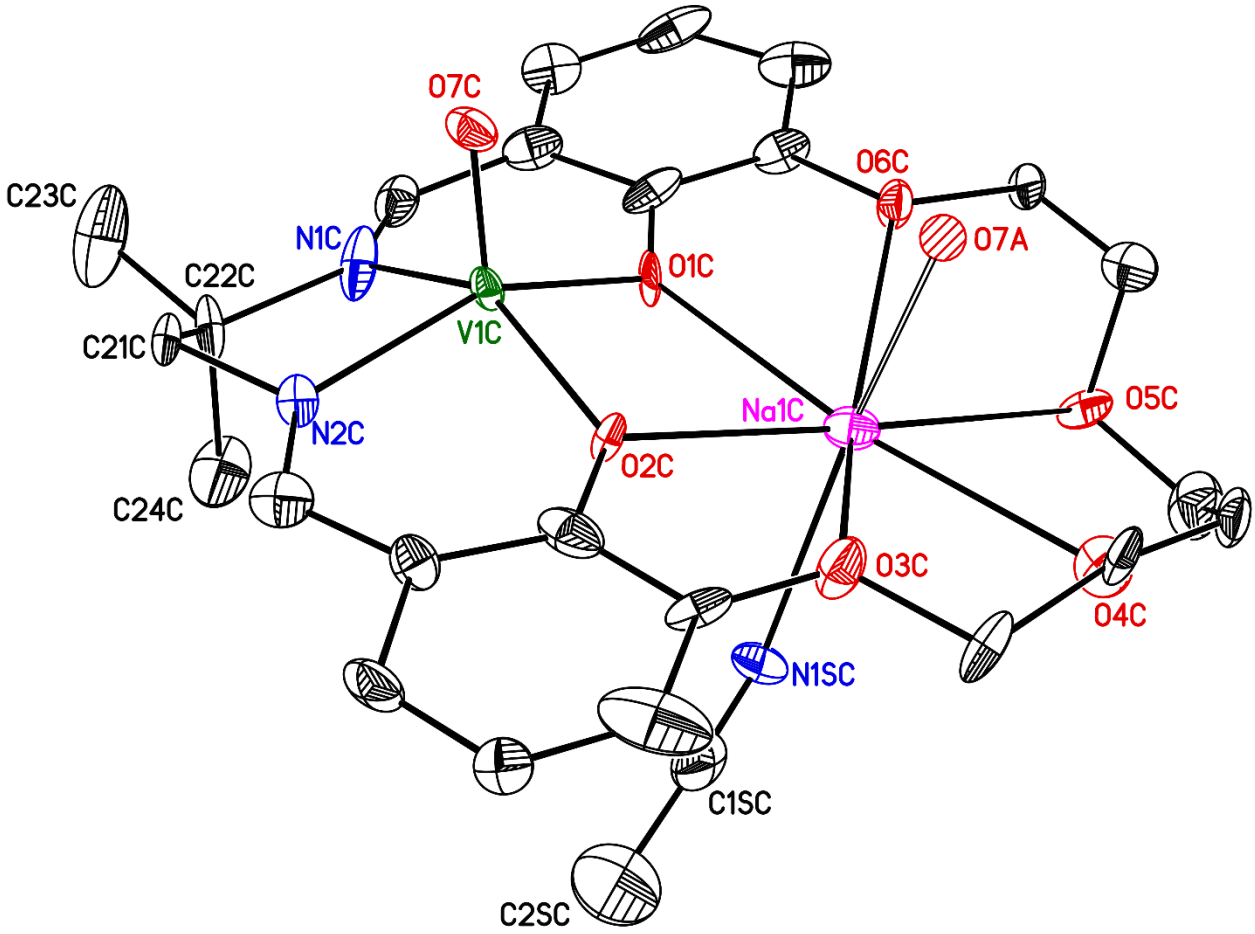

Figure S65. Solid-state structure from XRD of the third monomeric unit of **[VO,Na]** (monomer C). All H-atoms, four outer-sphere triflate counter-anions, an outer-sphere water molecule, most of the second monomeric unit (monomer A) of the dimeric species composed of heterobimetallic complexes, and the second dimeric species (monomers B and D) found in the asymmetric unit are omitted for clarity. Displacement ellipsoids are shown at the 50% probability level. Atom O7A is the vanadium oxo of the adjacent monomer of **[VO,Na]** in the dimeric species.

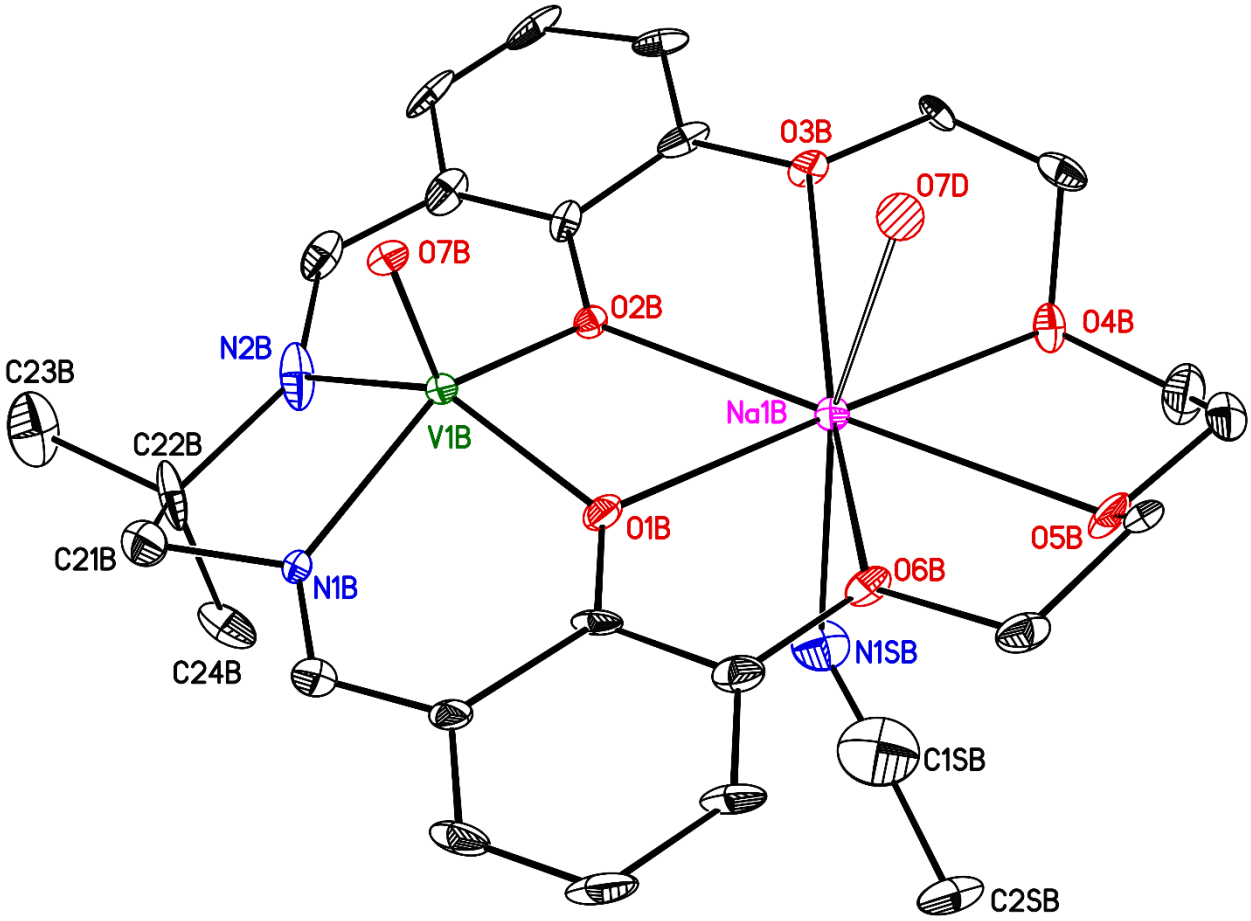

Figure S66. Solid-state structure from XRD of the second monomeric unit of **[VO,Na]** (monomer B). All H-atoms, four outer-sphere triflate counter-anions, an outer-sphere water molecule, most of the second monomeric unit (monomer D) of the dimeric species composed of heterobimetallic complexes, and the second dimeric species (monomers A and C) found in the asymmetric unit are omitted for clarity. Displacement ellipsoids are shown at the 20% probability level. Atom O7D is the vanadium oxo of the adjacent monomer of **[VO,Na]** in the dimeric species.

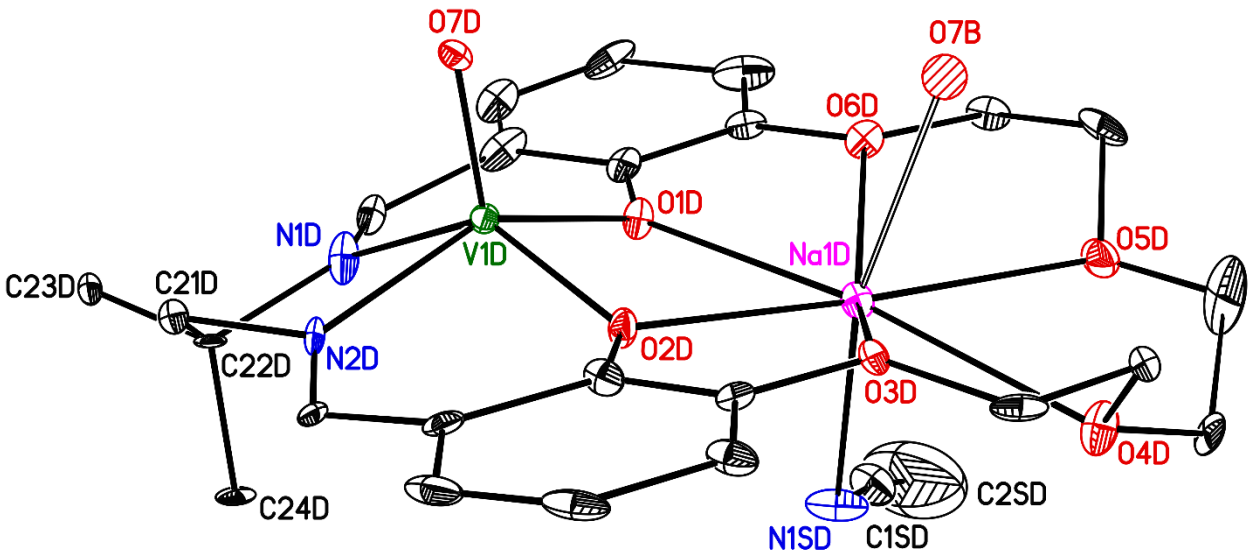

Figure S67. Solid-state structure from XRD of the fourth monomeric unit of **[VO,Na]** (monomer D). All H-atoms, four outer-sphere triflate counter-anions, an outer-sphere water molecule, most of the second monomeric unit (monomer B) of the dimeric species composed of heterobimetallic complexes, and the second dimeric species (monomers A and C) found in the asymmetric unit are omitted for clarity. Displacement ellipsoids are shown at the 20% probability level. Atom O7B is the vanadium oxo of the adjacent monomer of **[VO,Na]** in the dimeric species.

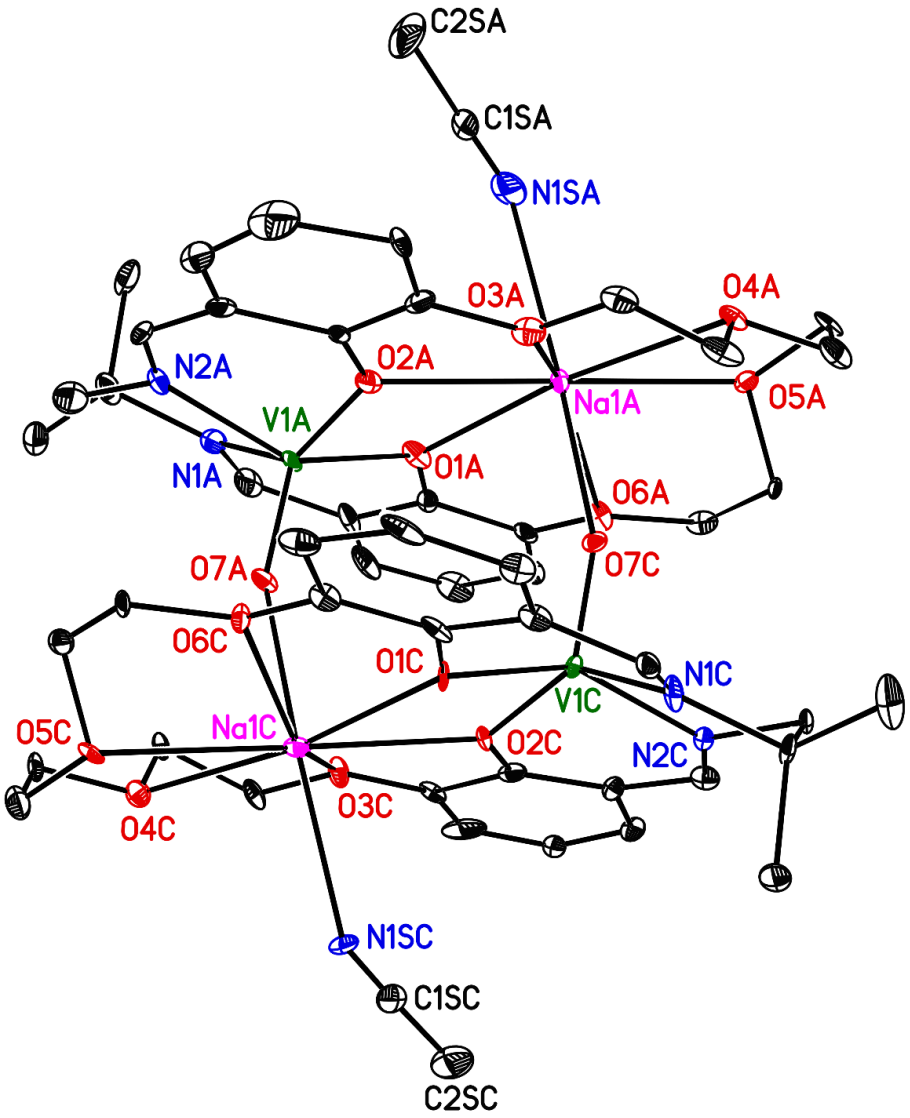

Figure S68. Solid-state structure from XRD of the first dimeric species (composed of **[VO,Na]** monomers A and C) found in the asymmetric unit of structure **a04d-No1**. All H-atoms, four outer-sphere triflate counter-anions, an outer-sphere water molecule, and a second dimeric species (composed of **[VO,Na]** monomers B and D) present in the asymmetric unit are omitted for clarity. Displacement ellipsoids are shown at the 20% probability level.

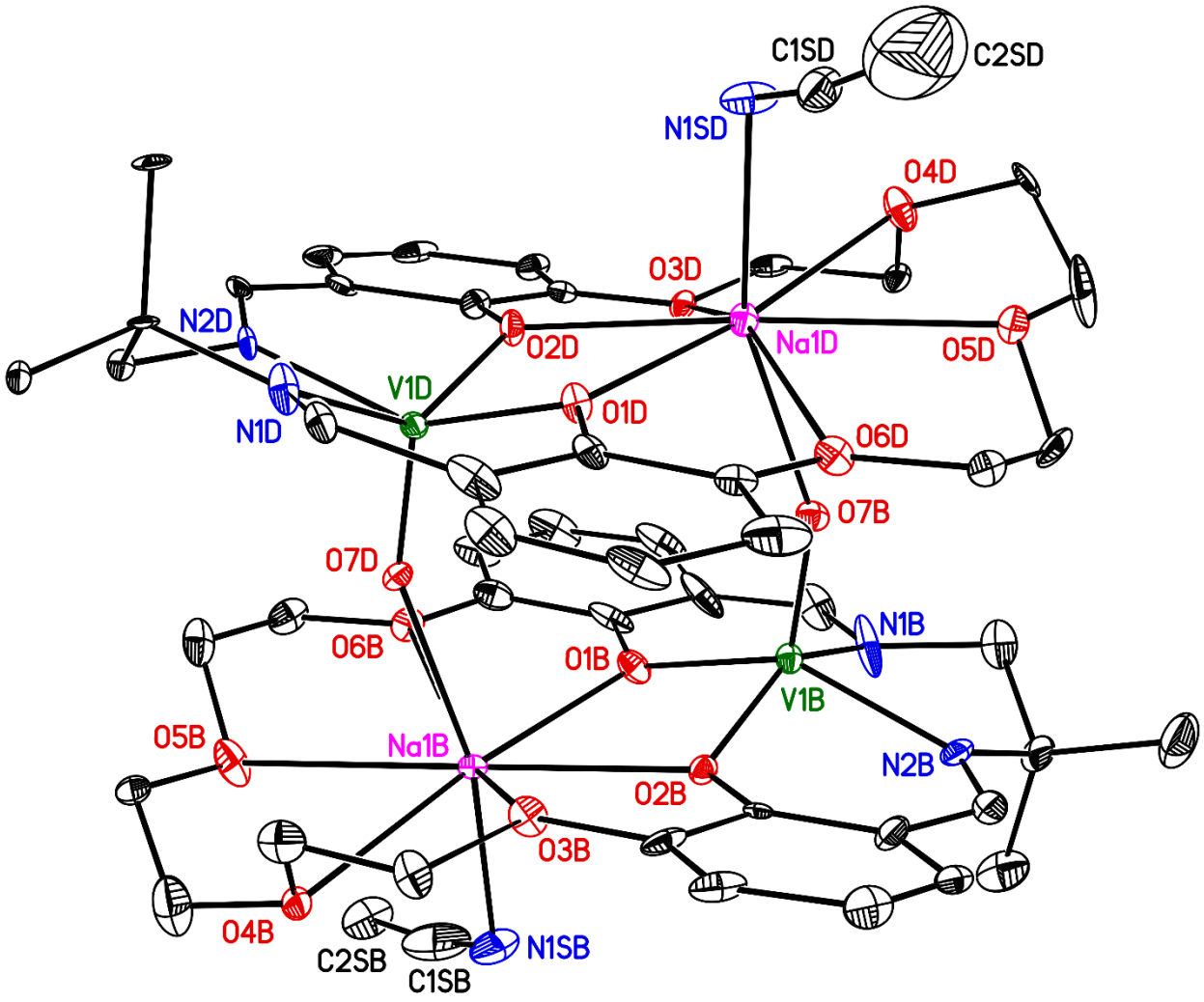

Figure S69. Solid-state structure from XRD of the second dimeric species (composed of **[VO,Na]** monomers B and D) found in the asymmetric unit of structure **a04d-No1**. All H-atoms, four outer-sphere triflate counter-anions, an outer-sphere water molecule, and a second dimeric species (composed of **[VO,Na]** monomers A and C) present in the asymmetric unit are omitted for clarity. Displacement ellipsoids are shown at the 20% probability level.

Full Solid-State Asymmetric Unit of [VO,Na] in a04d-No1

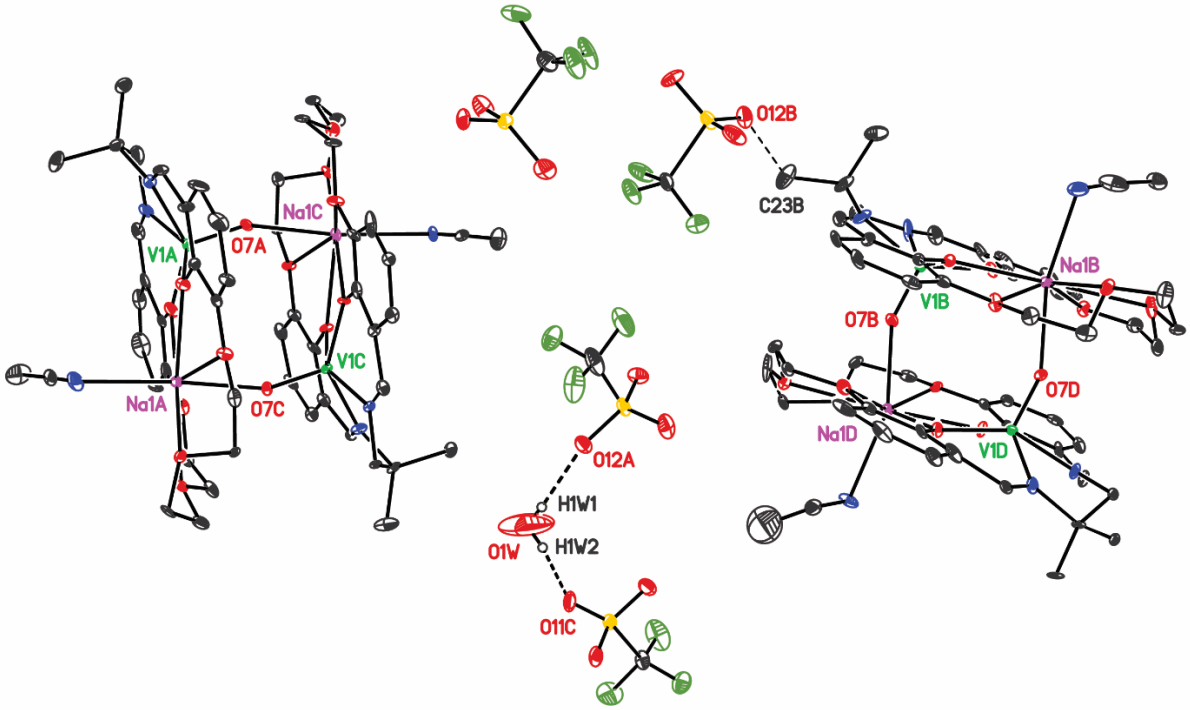

Figure S70. Solid-state structure from XRD of **[VO,Na]** showing the presence of both dimeric species composed of **[VO,Na]** monomers that are present in the asymmetric unit. All H-atoms except those associated with the water molecule (O1W) are omitted for clarity. Displacement ellipsoids are shown at the 20% probability level.

The hydrogen atoms (H1W1 and H1W2) of the outer-sphere water molecule (O1W) are engaged in moderately strong intermolecular hydrogen bonds with oxygen atoms of nearby outer-sphere triflate counter-anions (O1W···O12A distance of 3.04 Å; O1W···O11C distance of 3.17 Å; O12A···O1W···O11C angle of 130°).[75] These interactions are shown with solid dashed lines.

One methyl group (associated with C23B) on monomer B is engaged in an intrinsically weak C-H•••O hydrogen bond with the nearby triflate counter-anion (C23B···O12B distance of 2.97 Å). This interaction is shown with a thin dashed line.

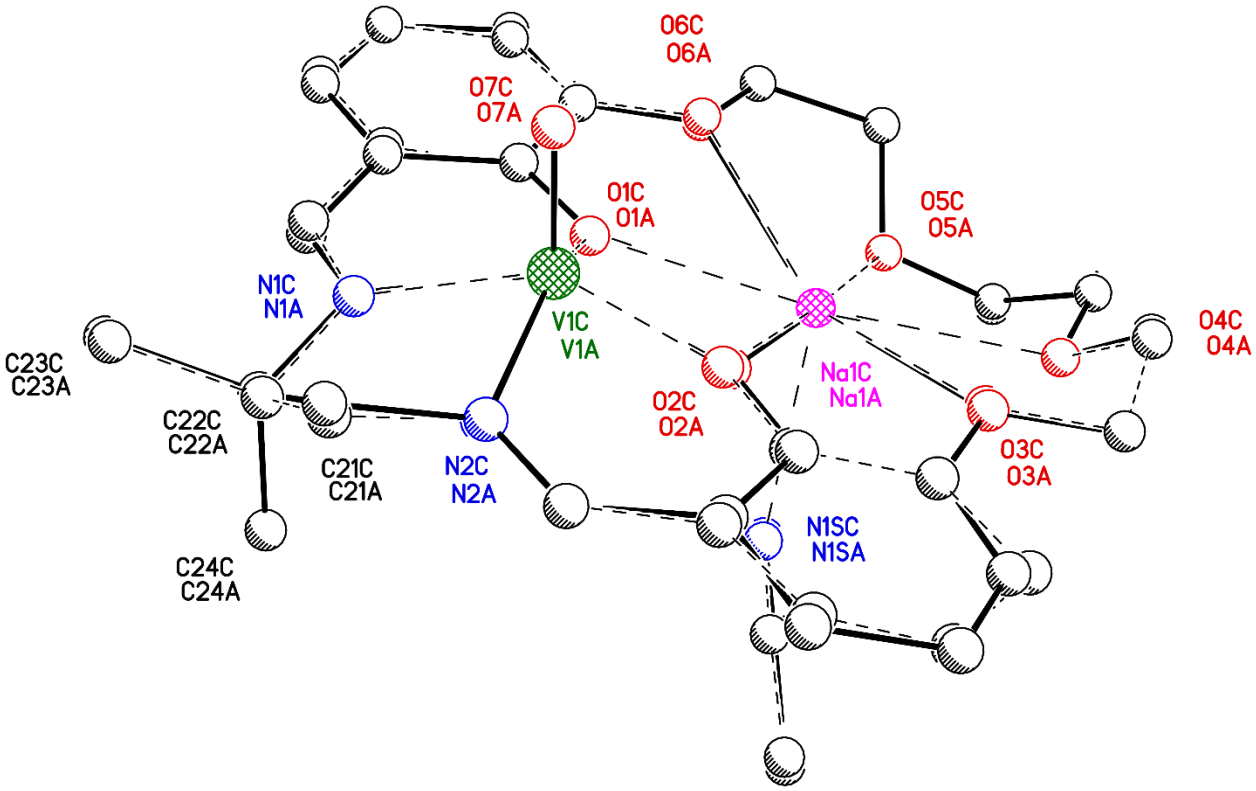

Figure S71. Drawing showing the superposition of inverted monomer A in **a04d-No1** with monomer C. The 38 nonhydrogen atoms of each monomer superimpose with a rms deviation of 0.08 Å.

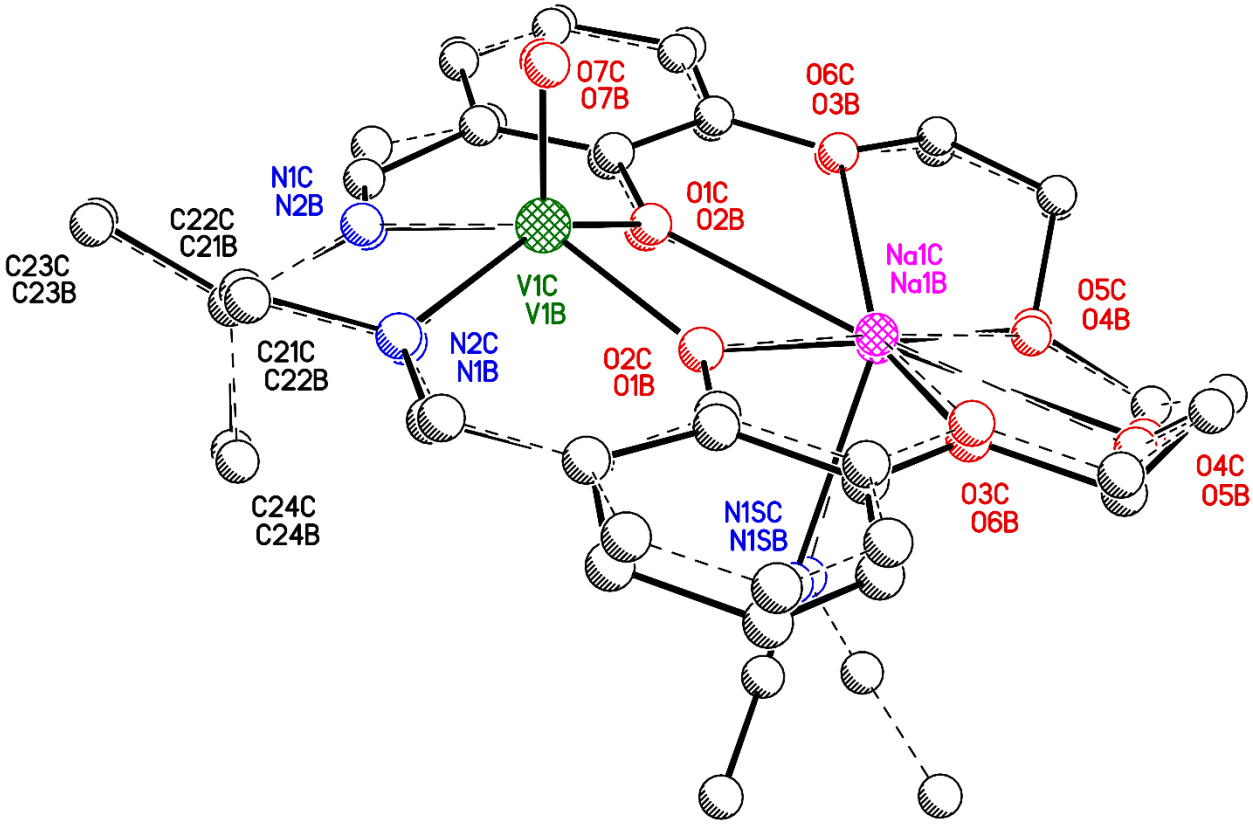

Figure S72. Drawing showing the superposition of monomer B in **a04d-No1** with monomer C. The V, O_{oxo}, Na and macrocyclic N and O atoms of each monomer superimpose with a rms deviation of 0.11 Å.

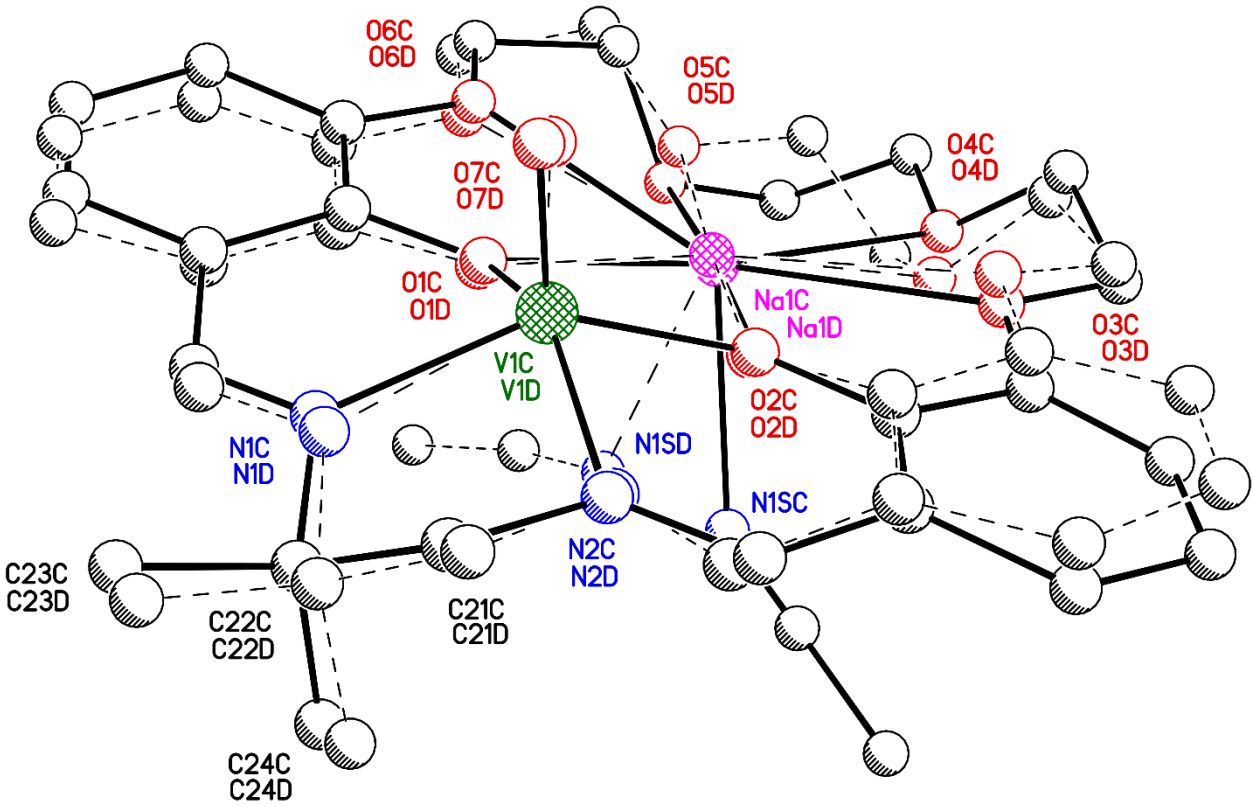

Figure S73. Drawing showing the superposition of monomer D in **a04d-No1** with monomer C. The V, O_{oxo}, Na and macrocyclic N and O atoms of each monomer superimpose with a rms deviation of 0.22 Å.

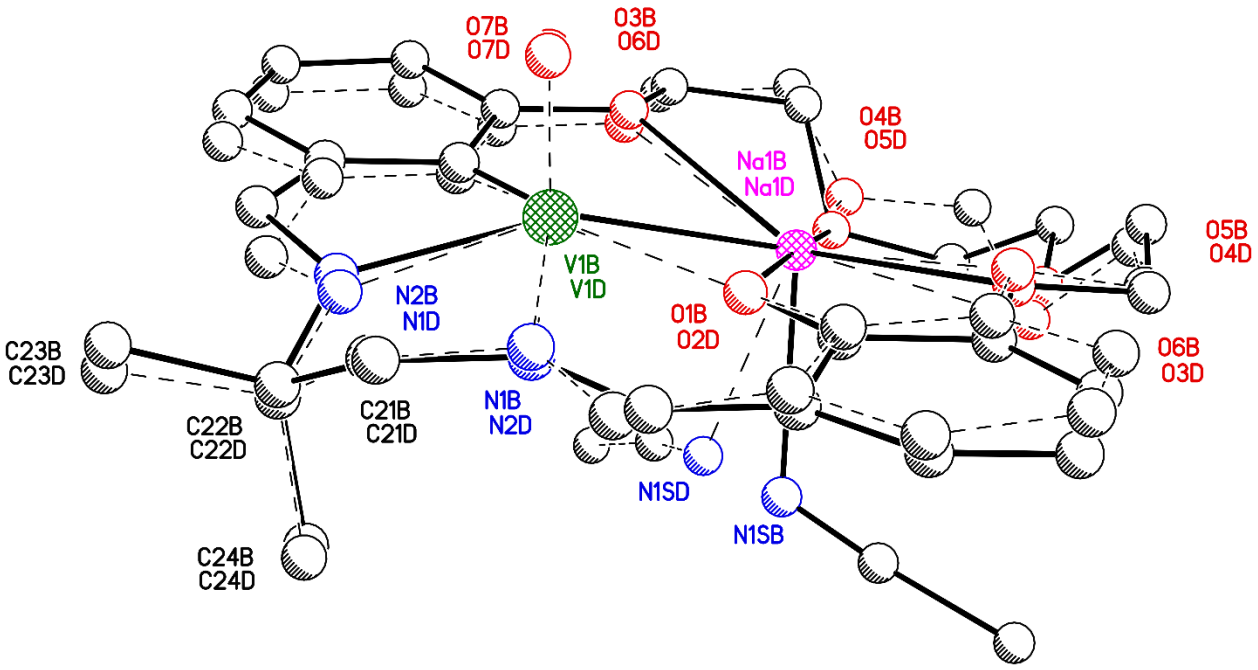

Figure S74. Drawing showing the superposition of monomer D in **a04d-No1** with monomer B. The V, O_{oxo}, Na, and macrocyclic N and O atoms of each monomer superimpose with a rms deviation of 0.19 Å.

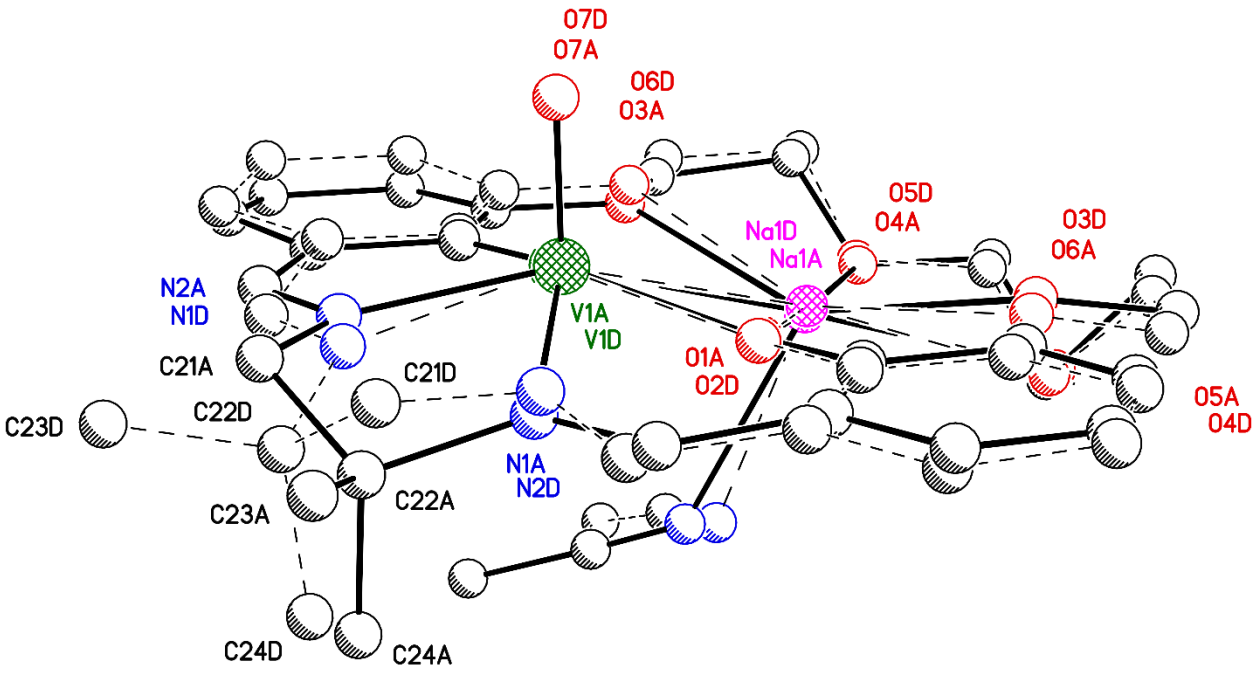

Figure S75. Drawing showing the superposition of monomer D in **a04d-No1** with monomer A. The V, O_{oxo}, Na and macrocyclic N and O atoms of each superimpose with a rms deviation of 0.16 Å.

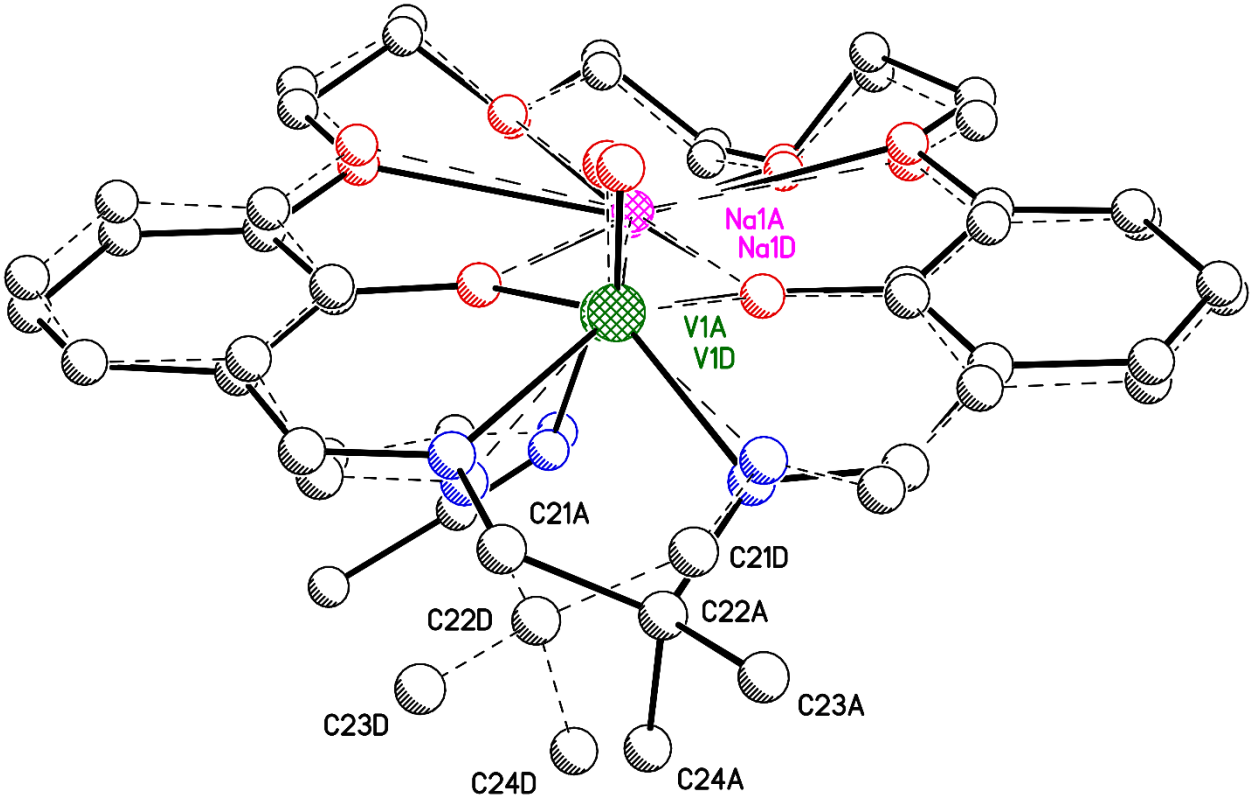

Figure S76. Drawing showing the superposition of monomer D in **a04d-No1** with monomer A, highlighting the imine bridge carbon atoms. The V, O_{oxo}, Na and macrocyclic N and O atoms of each superimpose with a rms deviation of 0.16 Å.

Solid-State Structure of [VO,Na] in a04d-No2

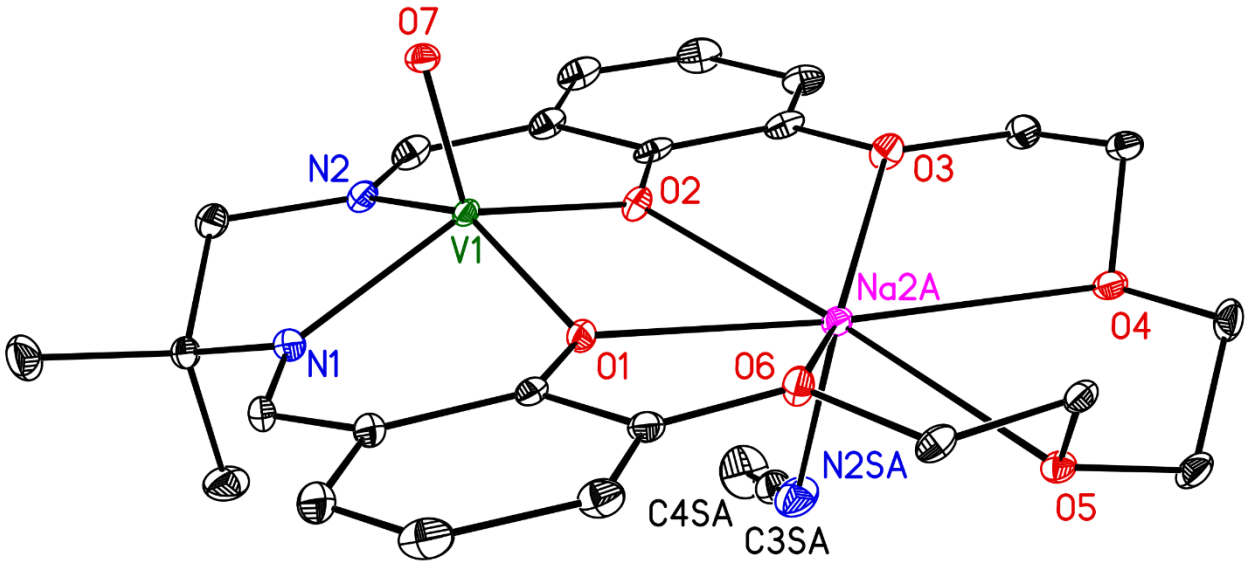

Figure S77. Solid-state structure from XRD of the first of two monomeric units of **[VO,Na]** present in the **a04d-No2** asymmetric unit. All H-atoms, outer-sphere triflate anions, and the second (disordered) monomeric unit of the complex found in the asymmetric unit are omitted for clarity. Displacement ellipsoids are shown at the 20% probability level.

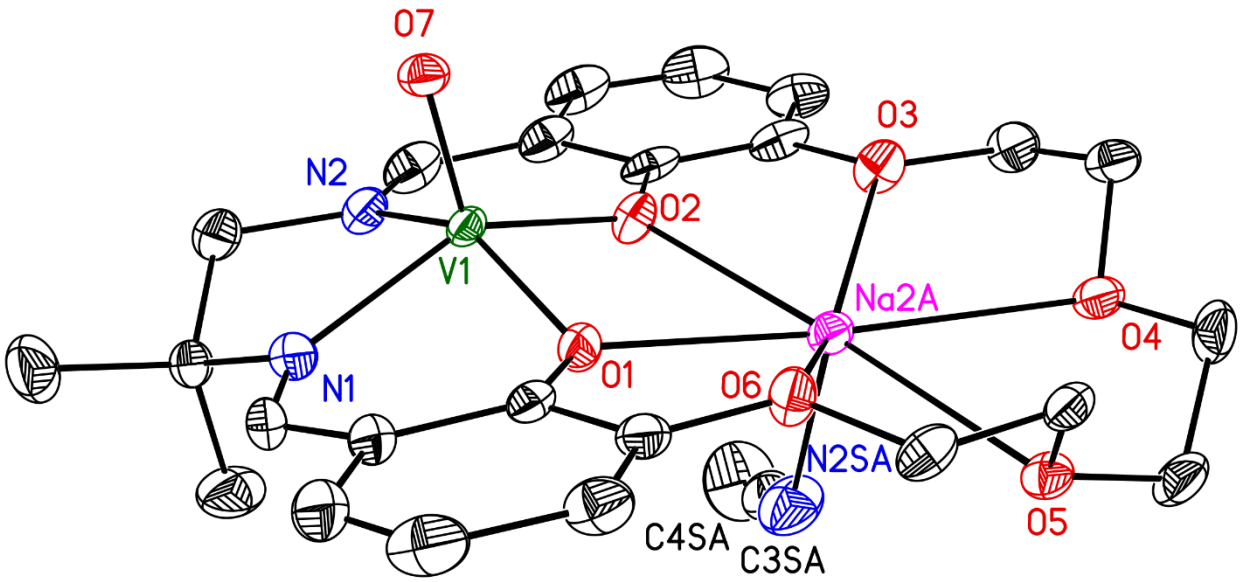

Figure S78. Solid-state structure from XRD of the first of two monomeric units of **[VO,Na]** present in the **a04d-No2** asymmetric unit. All H-atoms, outer-sphere triflate anions, and the second (disordered) monomeric unit of the complex found in the asymmetric unit are omitted for clarity. Displacement ellipsoids are shown at the 50% probability level.

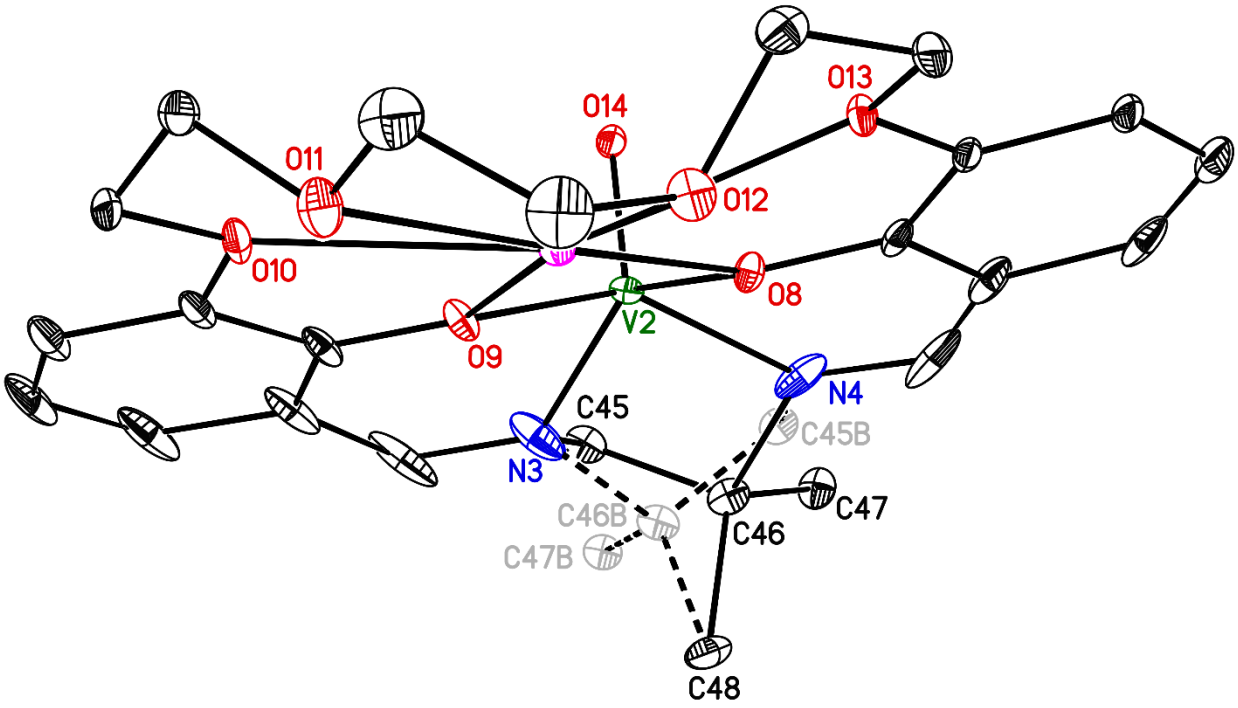

Figure S79. Solid-state structure from XRD of the metal/ligand framework present in the second monomeric unit of **[VO,Na]** found in the **a04d-No2** asymmetric unit. All H-atoms, outer-sphere triflate anions, acetonitrile moieties, and the first, fully-ordered independent monomer of **[VO,Na]** found in the asymmetric unit are omitted for clarity. Displacement ellipsoids are shown at the 20% probability level. The minor orientation (40%) of the bridging moiety between the imine groups is shown with solid bonds. The major orientation (60%) is shown with dashed bonds, and the associated atoms are labeled with 'B' suffixes. Methyl carbon C48 is common to both orientations and was included in the structural model with an occupancy factor of 1.00.

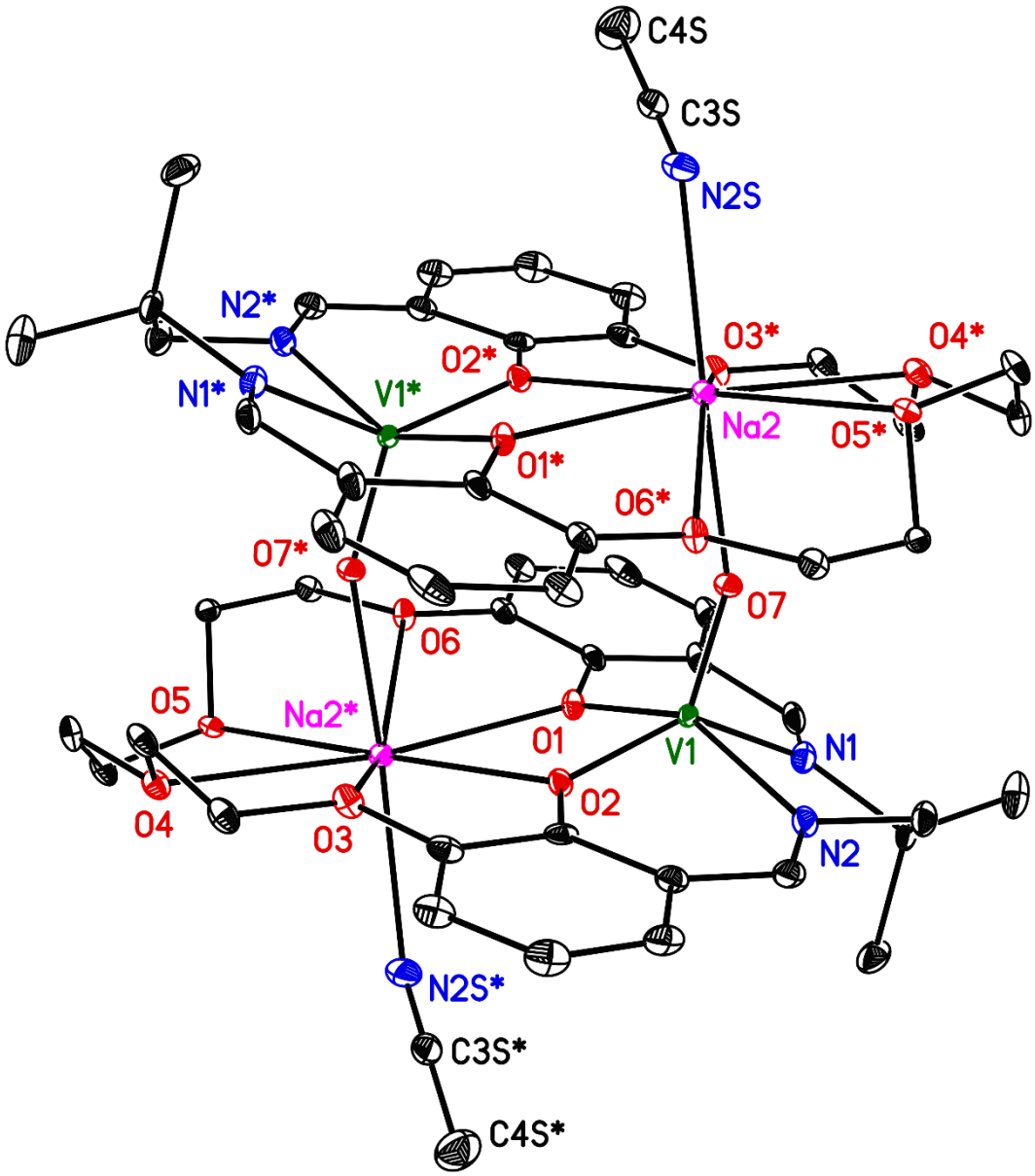

Figure S80. Solid-state structure from XRD of one ordered dimer of **[VO,Na]** found in the **a04d-No2** structure. Atoms labeled with an asterisk are generated by a crystallographic center of symmetry. All H-atoms, outer-sphere triflate anions, and a second (disordered) dimer of **[VO,Na]** present in the unit cell are omitted for clarity. Displacement ellipsoids are shown at the 20% probability level.

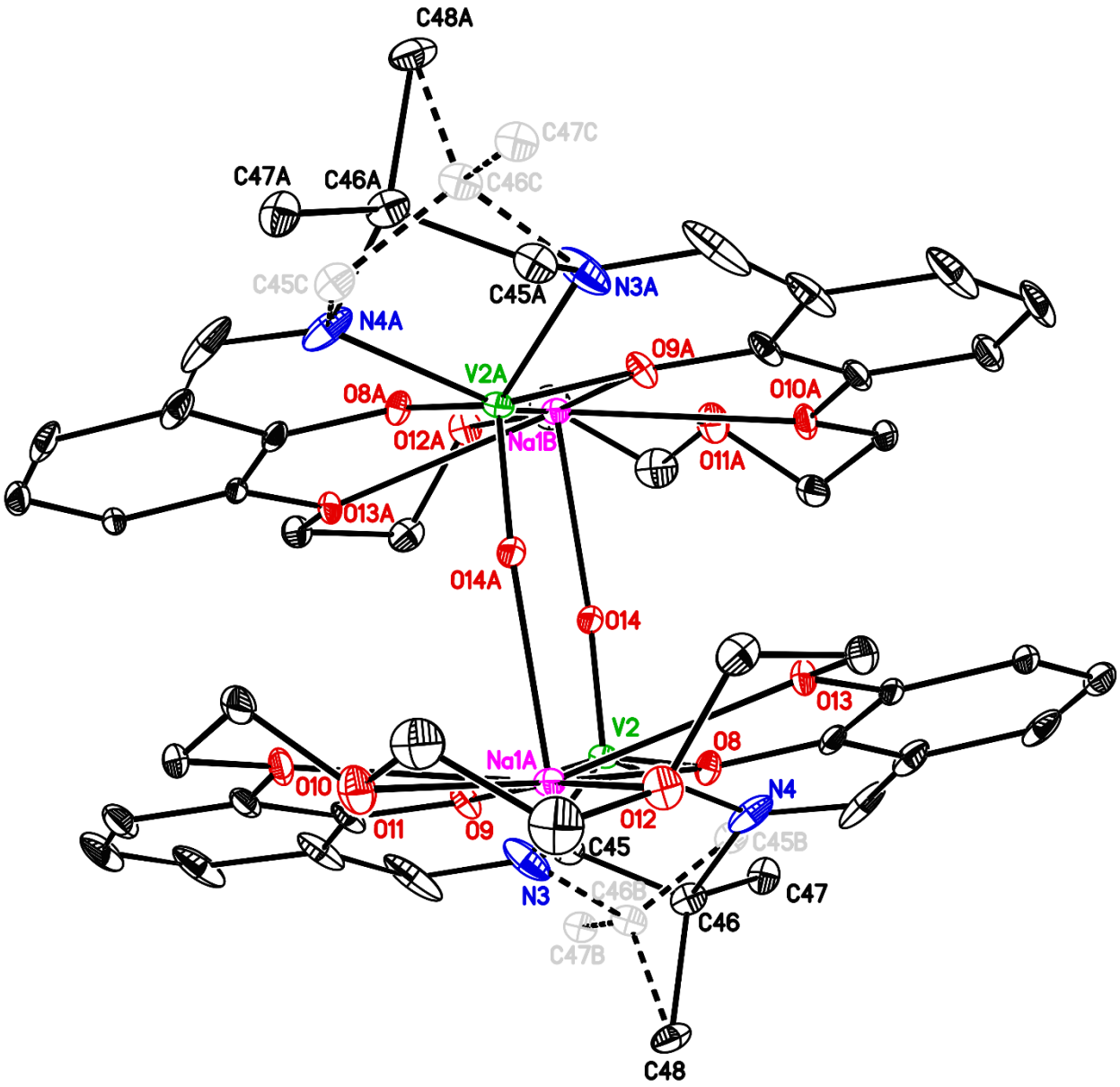

Figure S81. Solid-state structure from XRD for the metal-macrocycle cores of the second dimeric unit of **[VO,Na]** found in the **a04d-No2** structure. Inversion-symmetry-generated V, C, N and O atoms are labeled with an 'A' suffix to differentiate them from their mates in the asymmetric unit. Na1B is the inversion-related mate of Na1A. Carbon atoms labeled with a 'B' suffix are for the major orientation of the 4-carbon diimine bridge in the asymmetric unit and carbons labeled with a 'C' suffix are their inversion-related mates. All H-atoms, outer-sphere triflate anions, and the first, fully-ordered independent dimer of **[VO,Na]** found in the unit cell are omitted for clarity. Displacement ellipsoids are shown at the 20% probability level. The minor orientation (40%) of the bridging moieties between the imine groups is shown with solid bonds, while the major orientation (60%) is shown with dashed bonds.

Solid-State Structure Showing Packing Arrangement of Two [VO,Na] Dimers and Four Nearby Triflate Counter-Anions in a04d-No2

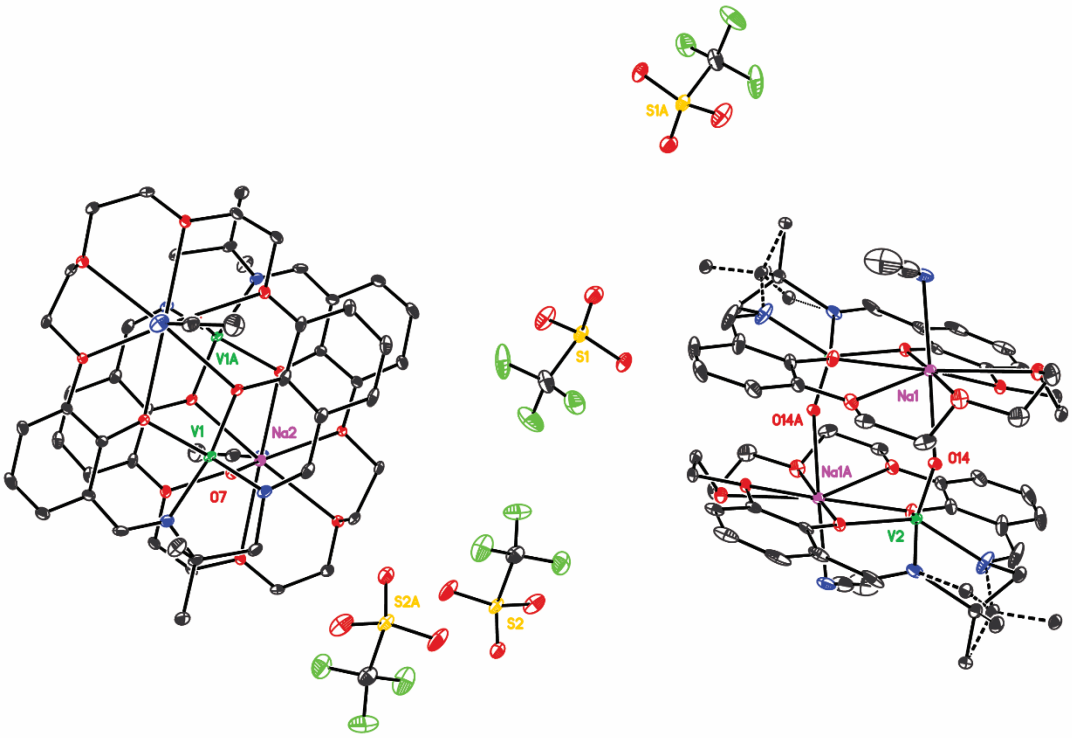

Figure S82. Solid-state structure from XRD of **[VO,Na]** in **a04d-No2** showing packing of the dimers of the complex with four nearby triflate counter-anions. Four triflates are shown here for direct comparison of this view to that given in Figure S50 which shows the full solid-state asymmetric unit of **a04d-No1**. The triflate molecules associated with S1 and S2 are located in the asymmetric unit, while those associated with S1A and S2A are generated by inversion and translation of S1 and S2. All other inversion-symmetry-generated atoms are also labeled with an 'A' suffix to differentiate them from atoms present in the asymmetric unit. All H-atoms are omitted for clarity, and displacement ellipsoids are shown at the 20% probability level.

Special Refinement Details for [VO,Ca] (b31b-No7 and b31b-No14).

Vapor diffusion of diethyl ether into a concentrated acetonitrile solution of **[VO,Ca]** afforded single crystals of the heterobimetallic complex suitable for XRD analysis. One outer-sphere partial-occupancy molecule of acetonitrile that is presumably derived from crystal growth was found in the structure.

The **b31b** structure was initially solved and fully refined with the anticipated atom-to-atom connectivity and a reasonable R_1 value (ca. 7.1%) with an asymmetric unit containing a single macrocyclic **[VO,Ca]** complex in the centrosymmetric monoclinic space group *P2₁/c* (No. 14). In this **b31b-No14** structure, two triflate counter-anions are bound to the formally 8-coordinate Ca^{2+} atom, and both are bound in the κ^1-fashion. A partial occupancy (33%) acetonitrile solvent molecule of crystallization was also present.

However, several of the structural and refinement details obtained in the case of **b31b-No14** suggested that the imposed symmetry might be too high in *P2₁/c* (No. 14). Full refinement of the structure in *P2₁/c* required a model with significant disorder to obtain a reasonable structure, including three-fold disorder (75/35/8) for the first triflate (containing S1), two-fold (55/45) disorder for the second triflate (containing S2), and 56/44 disorder for the atoms in the crown-ether-like moiety of **[VO,Ca]**. Modeling this disorder to yield a metrically-reasonable molecule produced a high ratio of restraints-to-parameters (1272 to 802). The extensive and nearly 50/50 disorder in the crown-ether-like moiety and second triflate suggested the possibility that the structure might utilize a lower-symmetry non-centrosymmetric space group. The reasonable yield of high-resolution data was also more consistent with a structure that did not contain so much disorder. While we have previously encountered triflates with two orientations in the asymmetric unit in our work with heterobimetallic complexes, we have not before been required to model disorder with three orientations to obtain reasonable structures. Similarly, we have not before encountered significant disorder in just the crown-ether-like portion of our ligands. On the other hand, our structure of a macrocyclic palladium complex containing the divalent cation Ca^{2+} displays a *pseudo*-center of symmetry that impacted final refinement.[34]

Consequently, the final structural refinement of **[VO,Ca]** utilizes the non-centrosymmetric space group *Pc* (No. 7). This choice was made in light of structural and refinement details elucidated during re-solving the structure in *Pc*. In the final structure, denoted here as **b31b-No7**, there are two crystallographically independent molecules (denoted A and B) of **[VO,Ca]** in the monoclinic asymmetric unit. Both molecules confirm the expected atom-to-atom connectivity of **[VO,Ca]** without the crown-ether-like disorder observed for the refinement in centrosymmetric *P2₁/c* (No. 14). The final R_1 value (6.4%) as well as the ratio of restraints-to-parameters (217 to 1096) are reasonable in **b31b-No7**. Anisotropic thermal parameters were incorporated for all nonhydrogen atoms in the final structural model, and the relevant crystallographic and structural refinement details for **b31b-No7** are given in Table S5. (Details for the alternative refinement **b31b-No14** are also given in Table S5 for comparison.)

Full refinement of the structure in *Pc* revealed that less disorder modeling was required than in the case of *P2₁/c*. Each molecule of **[VO,Ca]** displays two bound κ^1- triflate counterions; one of these in each case is ordered, while the other two are disordered over two orientations (55/45 and 54/46).

The asymmetric unit also contains a partial-occupancy (61%) acetonitrile solvent molecule of crystallization. Most notably, disorder modeling was *not required* for atoms in the crown-ether-like moieties, but was *still required* for the triflate and acetonitrile moieties. These findings are consistent with the conclusion that the crystal of **[VO,Ca]** is impacted by a *pseudo*-inversion center located at (0,½,0). The Y and Z coordinates of most atoms obey inversion symmetry quite closely, whereas the X coordinates generally obey it more approximately.

The structure can be solved in both $P2_1/c$ and *Pc*, and indeed the $V–O_{oxo}$ bond distance determined in $P2_1/c$ is similar to the average value when the structure is solved in *Pc* (1.583(3) Å in $P2_1/c$ vs. 1.589(10) Å in *Pc*). Consistent with this situation, the ADDSYM alert of PLATON suggests the possible space group of $P2_1/c$ with an 89% fit when **b31b-No7** is run through CheckCIF, underscoring the relationship between the structural refinements reported herein.

Each triflate was restrained to have near idealized bond lengths and angles by setting the interatomic separations to appropriate multiples of the S-O bond length that was included in the refinement as a free variable that refined to a final value of 1.424(2) Å. The acetonitrile solvent molecule of crystallization was restrained to have near-idealized geometry by setting the bond lengths and $N•••C_{methyl}$ separation for the nonhydrogen atoms to appropriate multiples of the C-N bond length that was included in the refinement as a free variable that refined to a final value of 1.08(2) Å.

Solid-State Structure of [VO,Ca] in b31b-No7

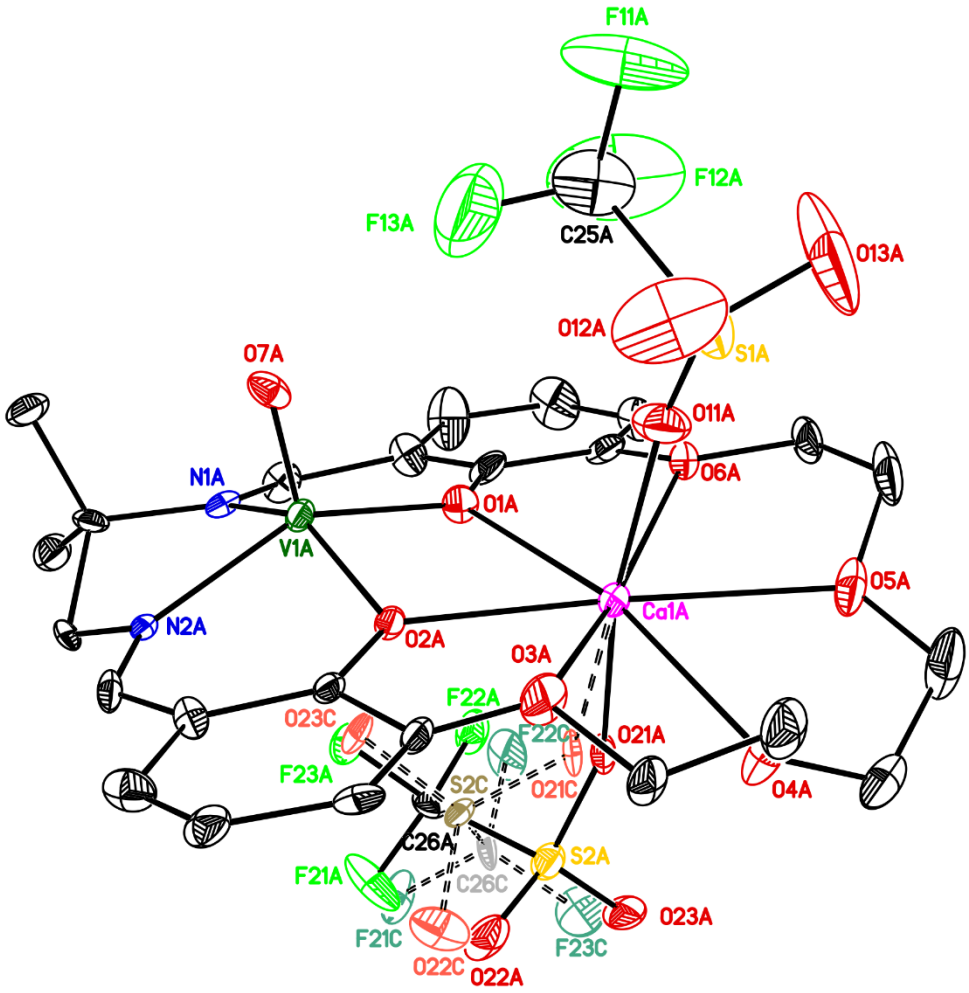

Figure S83. Solid-state structure from XRD of the first (A) of two molecules of **[VO,Ca]** found in the asymmetric unit of **b31b-No7**. All H-atoms, a co-crystallized outer-sphere acetonitrile molecule with partial (61%) occupancy, and the second molecule of **[VO,Ca]** found in the asymmetric unit are omitted for clarity. Displacement ellipsoids are shown at the 20% probability level. Disorder associated with the second triflate counter-anion bound to calcium is shown; the atoms for the major (55%) isomer are connected with solid lines; those for the minor (45%) species are colored more lightly and connected with dashed lines.

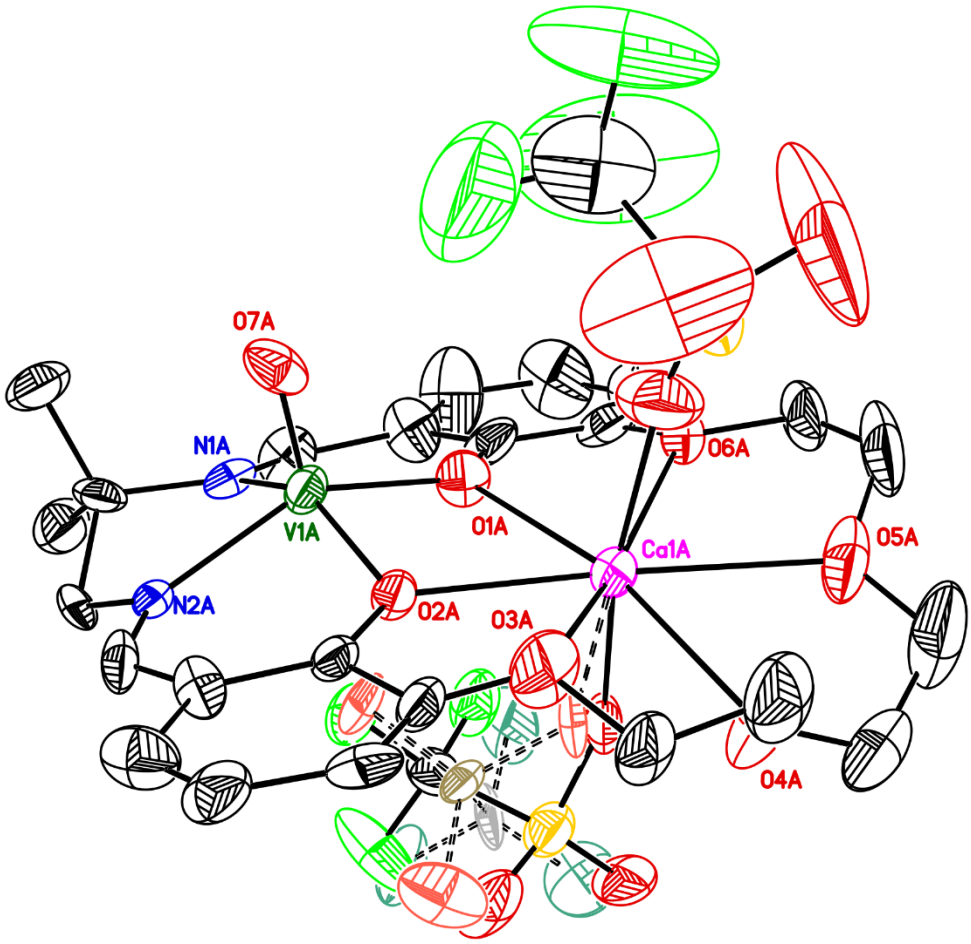

Figure S84. Solid-state structure from XRD of the first (A) of two molecules of **[VO,Ca]** found in the asymmetric unit of **b31b-No7**. All H-atoms, a co-crystallized outer-sphere acetonitrile molecule with partial (61%) occupancy, and the second molecule of **[VO,Ca]** found in the asymmetric unit are omitted for clarity. Displacement ellipsoids are shown at the 50% probability level. Disorder associated with the second triflate counter-anion bound to calcium is shown; the atoms for the major (55%) isomer are connected with solid lines; those for the minor (45%) species are colored more lightly and connected with dashed lines.

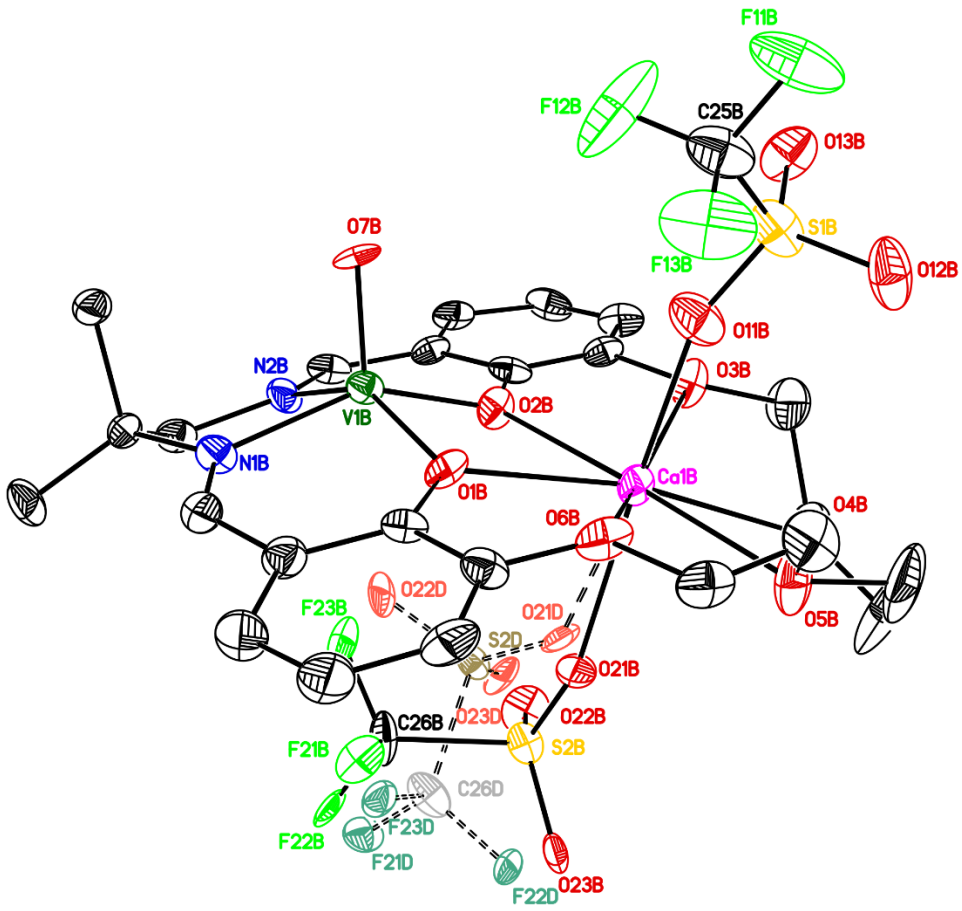

Figure S85. Solid-state structure from XRD of the second (B) of two molecules of **[VO,Ca]** found in the asymmetric unit of **b31b-No7**. All H-atoms, a co-crystallized outer-sphere acetonitrile molecule with partial (61%) occupancy, and the first molecule of **[VO,Ca]** found in the asymmetric unit are omitted for clarity. Displacement ellipsoids are shown at the 20% probability level. Disorder associated with the second triflate counter-anion bound to calcium is shown; the atoms for the major (54%) isomer are connected with solid lines; those for the minor (46%) species are colored more lightly and connected with dashed lines.

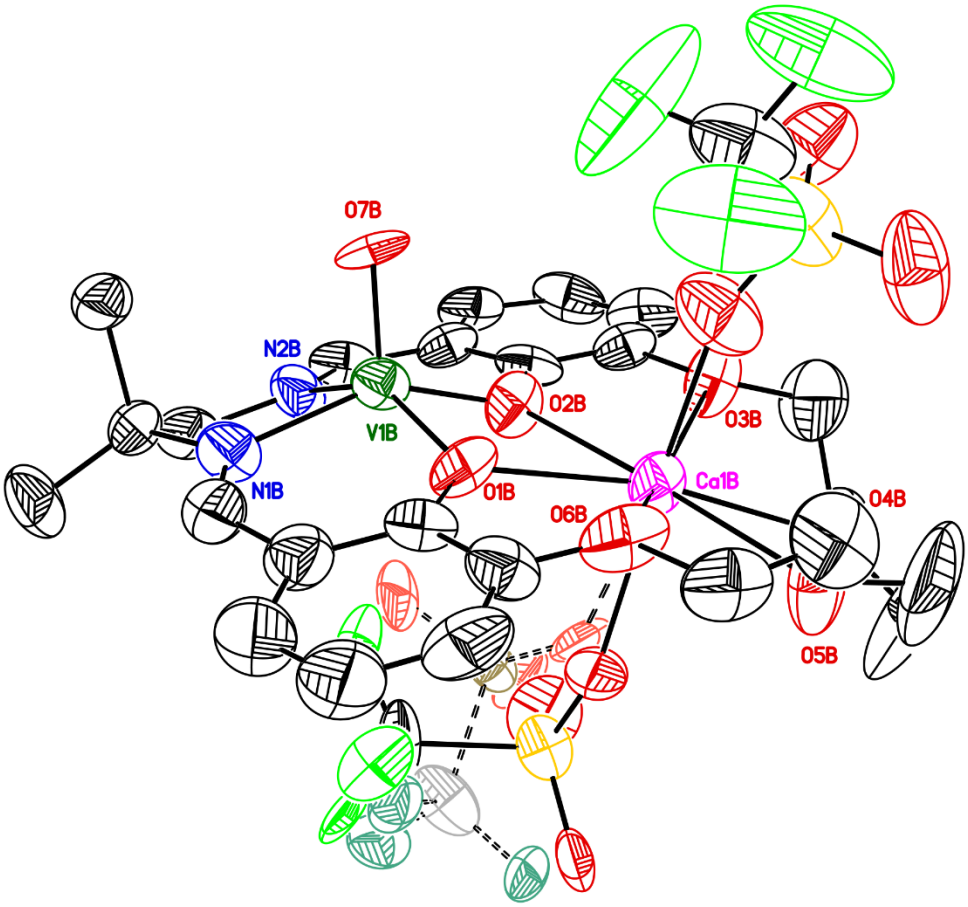

Figure S86. Solid-state structure from XRD of the second (B) of two molecules of **[VO,Ca]** found in the asymmetric unit of **b31b-No7**. All H-atoms, a co-crystallized outer-sphere acetonitrile molecule with partial (61%) occupancy, and the first molecule of **[VO,Ca]** found in the asymmetric unit are omitted for clarity. Displacement ellipsoids are shown at the 50% probability level. Disorder associated with the second triflate counter-anion bound to calcium is shown; the atoms for the major (54%) isomer are connected with solid lines; those for the minor (46%) species are colored more lightly and connected with dashed lines.

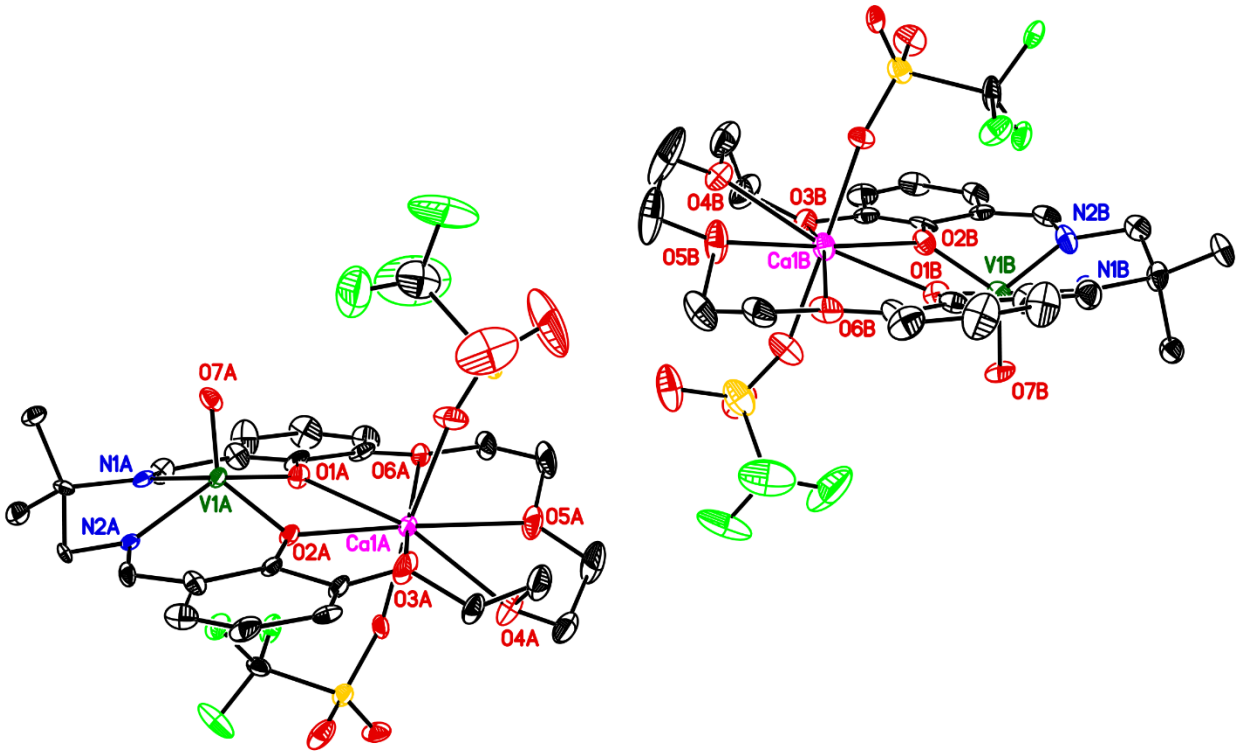

Figure S87. Solid-state structure from XRD of the two molecules of **[VO,Ca]** (A and B) found in the asymmetric unit of **b31b-No7**. All H-atoms, a co-crystallized outer-sphere acetonitrile molecule with partial (61%) occupancy, and disorder associated with one bound triflate counter-anion on each calcium di-cation are omitted for clarity. Displacement ellipsoids are shown at the 20% probability level.

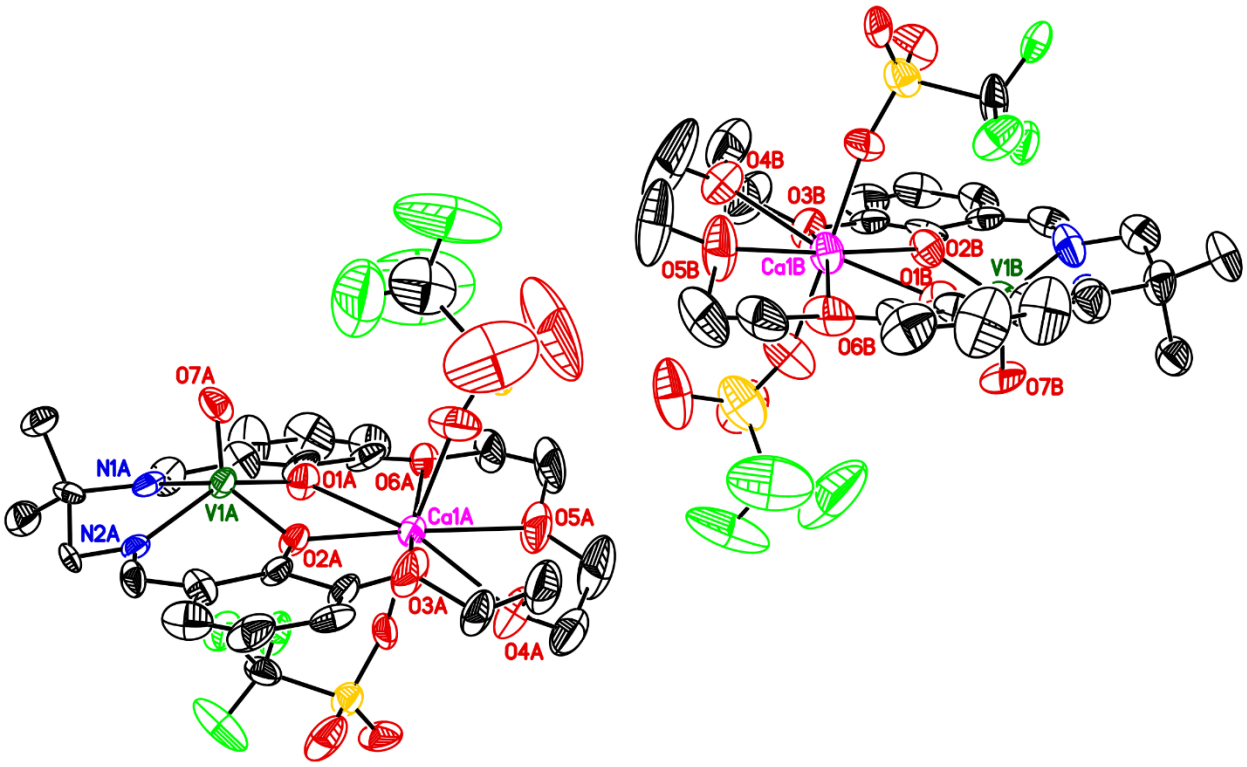

Figure S88. Solid-state structure from XRD of the two molecules of **[VO,Ca]** (A and B) found in the asymmetric unit of **b31b-No7**. All H-atoms, a co-crystallized outer-sphere acetonitrile molecule with partial (61%) occupancy, and disorder associated with one bound triflate counter-anion on each calcium di-cation are omitted for clarity. Displacement ellipsoids are shown at the 50% probability level.

Full Solid-State Asymmetric Unit of [VO,Ca] in b31b-No7

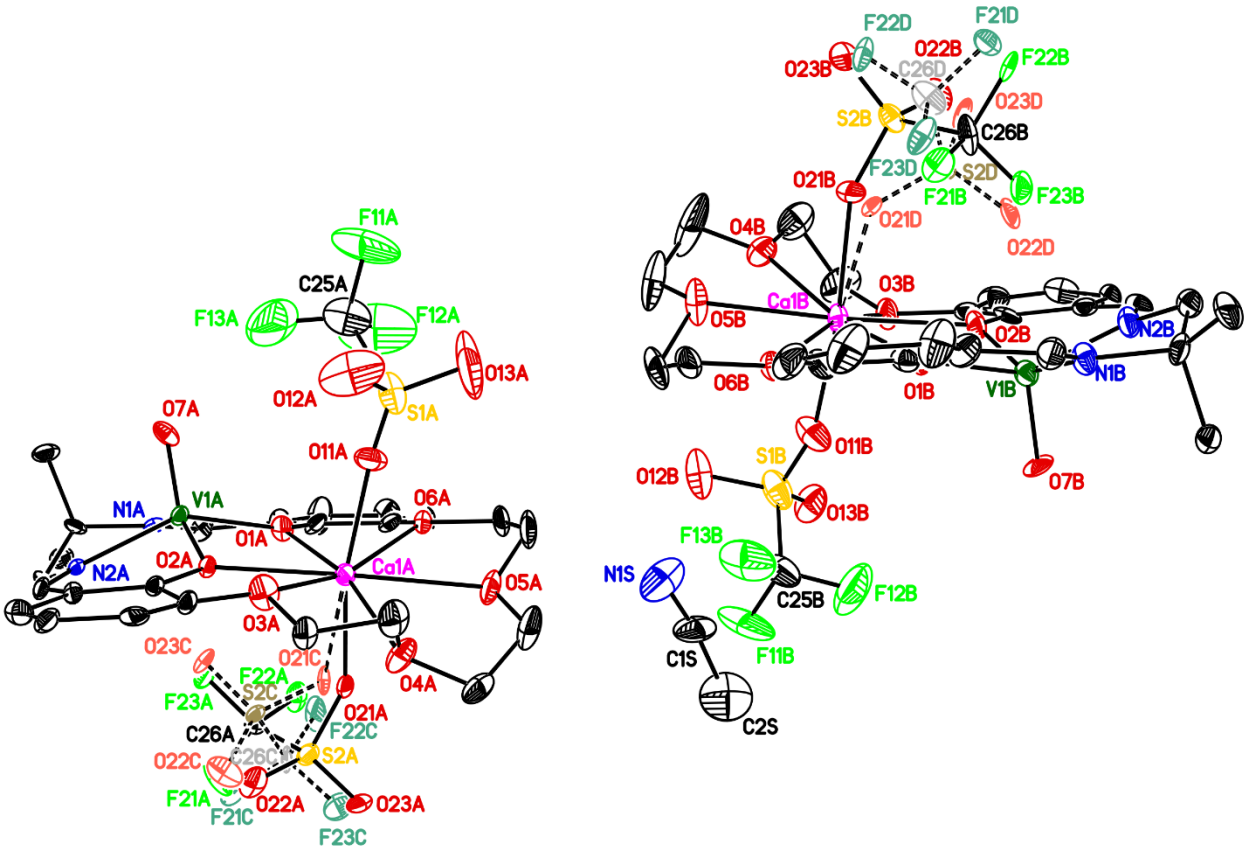

Figure S89. Solid-state structure from XRD of the two molecules of **[VO,Ca]** (A and B) found in the asymmetric unit of **b31b-No7**. All H-atoms omitted for clarity. Each macrocyclic complex has one ordered κ-1 triflate, and one disordered κ-1 triflate. For the disordered triflates, the atoms for the major isomers are connected with solid lines and those for the minor species are colored more lightly and connected with dashed lines. These triflates are 55/45 disordered on molecule A and 54/46 disordered on molecule B. A co-crystallized outer-sphere acetonitrile molecule with partial (61%) occupancy is also shown. Displacement ellipsoids are shown at the 20% probability level.

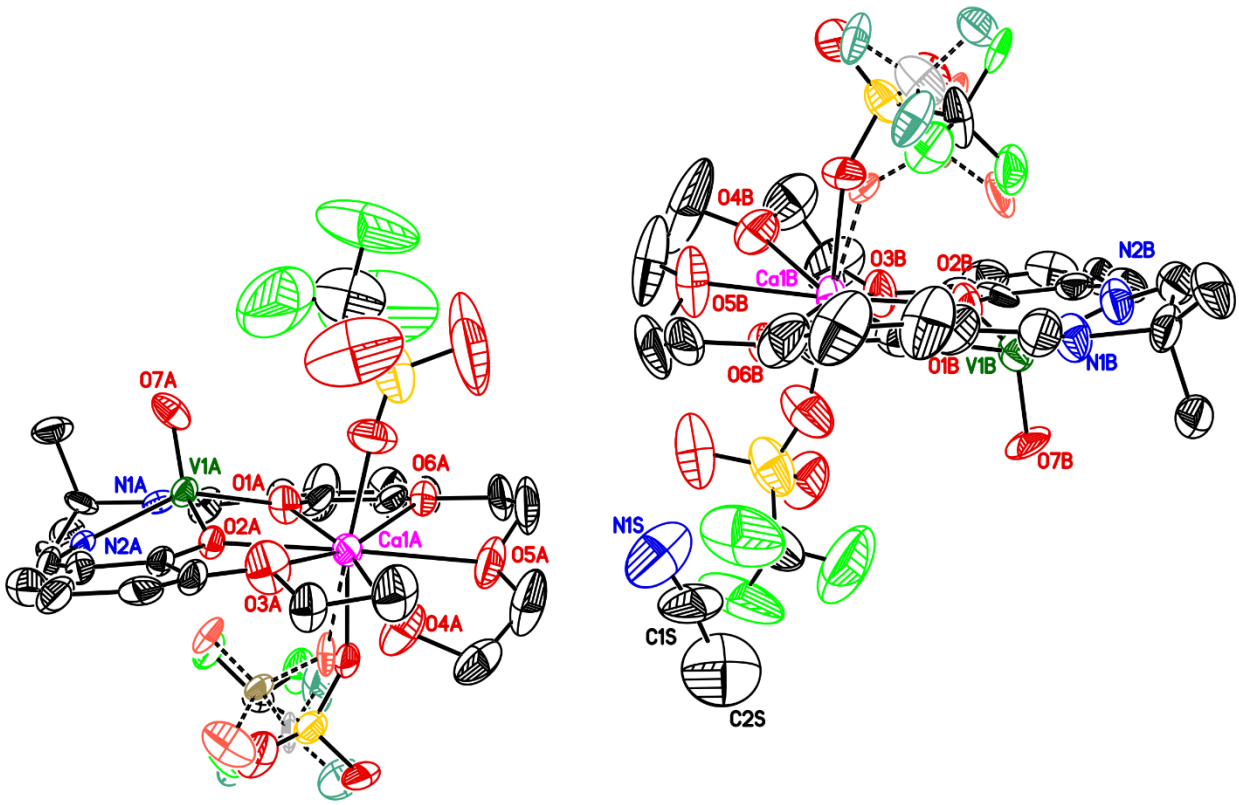

Figure S90. Solid-state structure from XRD of the two molecules of **[VO,Ca]** (A and B) found in the asymmetric unit of **b31b-No7**. All H-atoms omitted for clarity. Each macrocyclic complex has one ordered κ-1 triflate, and one disordered κ-1 triflate. For the disordered triflates, the atoms for the major isomers are connected with solid lines and those for the minor species are colored more lightly and connected with dashed lines. These triflates are 55/45 disordered on molecule A and 54/46 disordered on molecule B. A co-crystallized outer-sphere acetonitrile molecule with partial (61%) occupancy is also shown. Displacement ellipsoids are shown at the 50% probability level.

Solid-State Structure of [VO,Ca] in b31b-No14

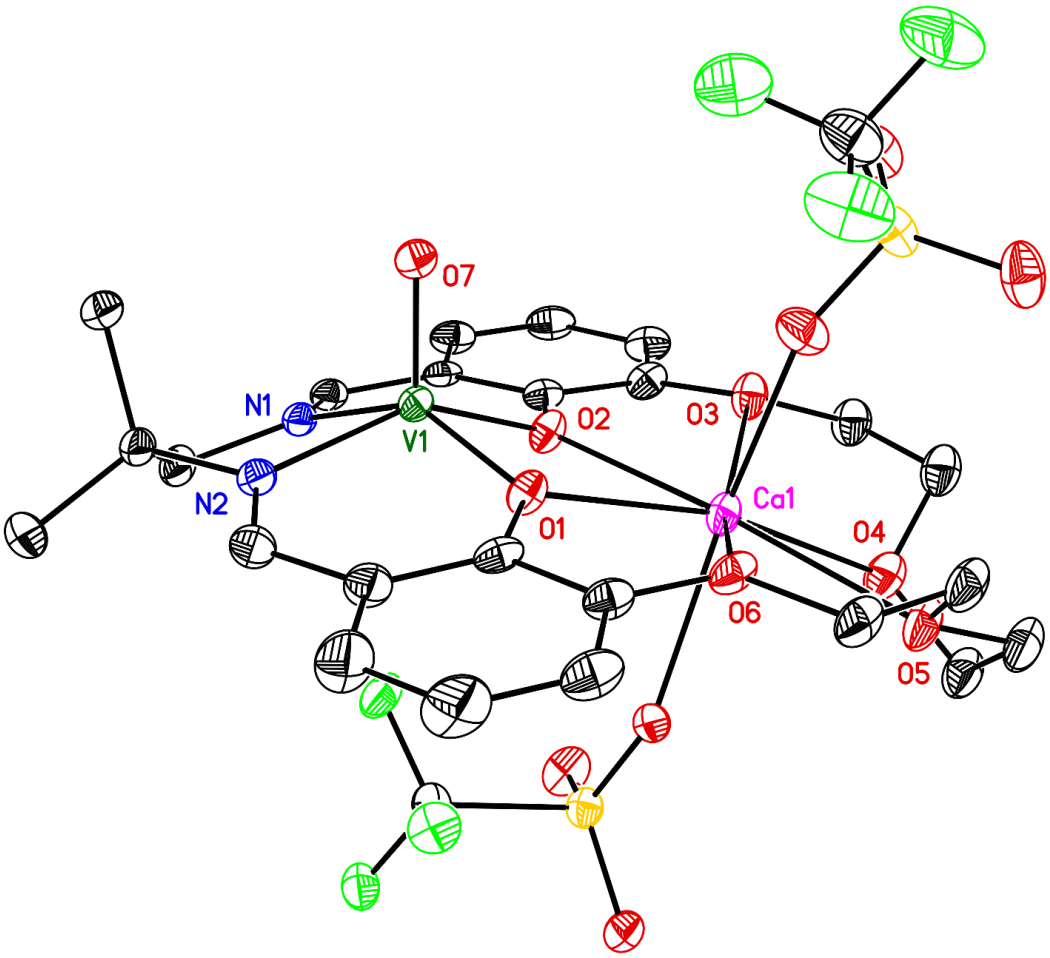

Figure S91. Solid-state structure from XRD of **[VO,Ca]**. All H-atoms, a co-crystallized outer-sphere acetonitrile solvent molecule with partial occupancy, and the minor components of disorder associated with the crown-ether-like moiety and the triflates are omitted for clarity. Displacement ellipsoids are shown at the 20% probability level.

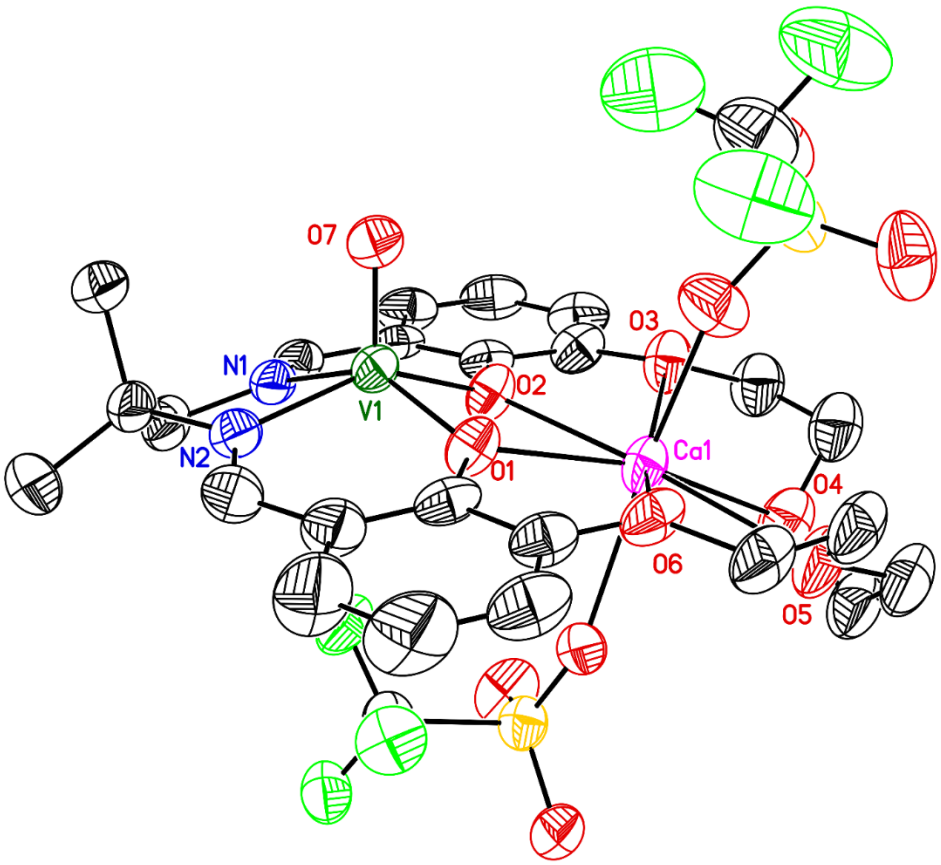

Figure S92. Solid-state structure from XRD of **[VO,Ca]**. All H-atoms, a co-crystallized outer-sphere acetonitrile solvent molecule with partial occupancy, and the minor components of disorder associated with the crown-ether-like moiety and the triflates are omitted for clarity. This is the same as Figure S71 except the displacement ellipsoids are shown at the 50% probability level.

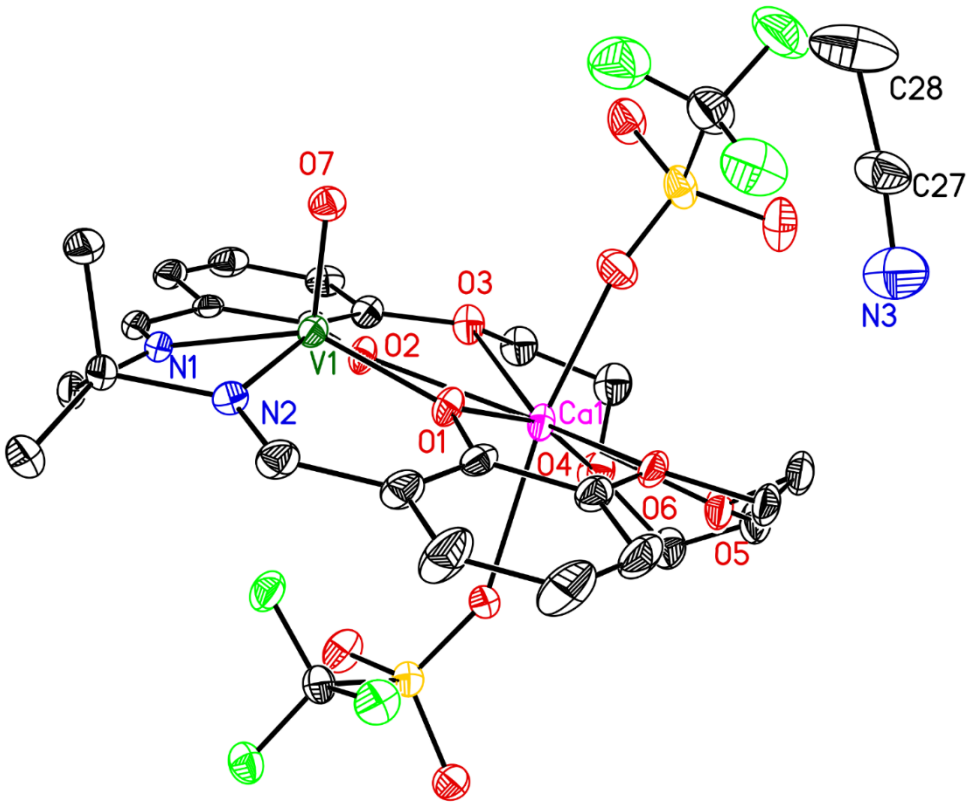

Figure S93. Solid-state structure from XRD of **[VO,Ca]** highlighting a co-crystallized outer-sphere acetonitrile solvent molecule with partial occupancy (33%). All H-atoms and the minor components of disorder associated with the crown-ether-like moiety and the triflates are omitted for clarity. Displacement ellipsoids are shown at the 20% probability level.

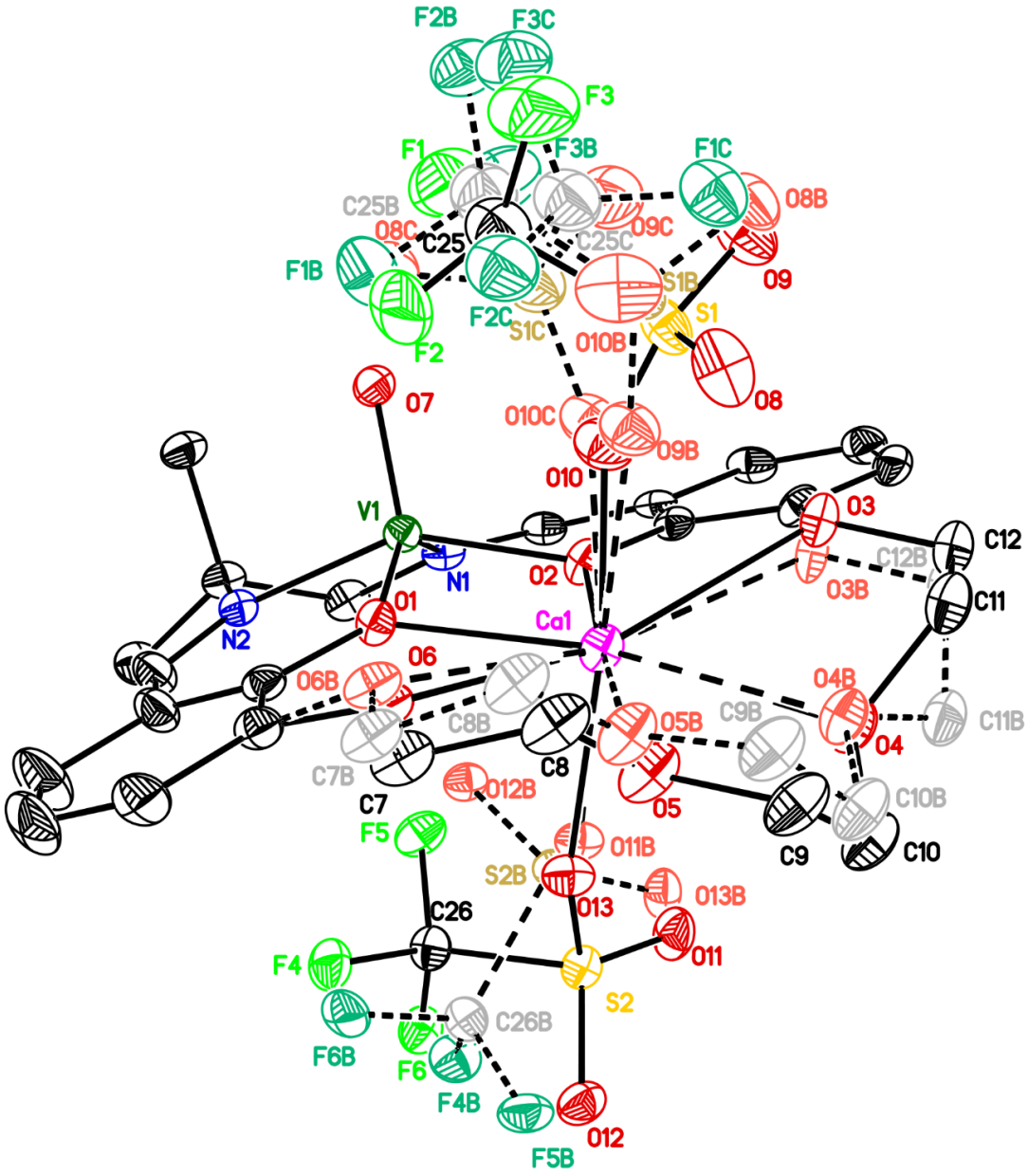

Figure S94. Solid-state structure from XRD of **[VO,Ca]** highlighting the 57/35/8 disordered packing for the first triflate (S1), 55/45 disordered packing for the second triflate (S2), and 56/44 disordered packing for atoms in the crown-ether-like moiety of **[VO,Ca]**. Atoms for the minor occupancy sites are labeled with 'B' and 'C' suffixes; the major occupancy species are connected with solid lines and those for the minor occupancy species are colored more lightly and connected with dashed lines A partial-occupancy co-crystallized outer-sphere acetonitrile solvent molecule and all H-atoms are omitted for clarity. Displacement ellipsoids are shown at the 20% probability level.

Table S3. Crystal and Refinement Data for **[VO].**

	[VO] (a03a)
CCDC accession code	2219364
Empirical formula	$C_{28}H_{34}N_4O_7V$
Formula weight	589.53
Temperature	120(2) K
Wavelength	0.71073 Å
Crystal system	Monoclinic
Space group	$P2_1/c$ – No. 14
a	9.3666(5) Å
b	27.2431(15) Å
c	11.3241(7) Å
α	90°
β	105.708(2)°
γ	90°
Volume	2781.7(3) $Å^3$
Z	4
Density (calculated)	1.408 g/cm^3
Absorption coefficient	0.410 mm^{-1}
F(000)	1236.0
Crystal size	0.223 × 0.189 × 0.072 mm^3
Theta range	1.495 to 28.317°
Index ranges	$-12\leq h\leq 12, -36\leq k\leq 36, -15\leq l\leq 15$
Reflections collected	52803
Independent reflections	6910 [R_{int} = 0.0504, R_{sigma} = 0.0283]
Completeness/θ_{max}	100.0%/ 25.242°
Absorption correction	Numerical
Max./Min. Transmission	0.979 and 0.941
Refinement method	Full-matrix least-squares on F^2
Data/restraints/parameters	6910/0/365
Goodness-of-fit on F^2	1.031
Final R indices [I>2σ(I)]	R_1 = 0.040, wR_2 = 0.089
R indices (all data)	R_1 = 0.054, wR_2 = 0.096
Largest diff. peak & hole	0.67 and –0.40 e.$Å^{-3}$

Table S4. Crystal and Refinement Data for **[VO,Na].**

	[VO,Na] (a04d-No1)	**[VO,Na] (a04d-No2)**
CCDC accession code	2219365	2243380
Empirical formula	$C_{54}H_{63}N_6O_{20.50}V_2Na_2F_6S_2$	$C_{54}H_{62}N_6O_{20}V_2Na_2F_6S_2$
Formula weight	1450.08	1441.07
Temperature	120(2) K	120(2) K
Wavelength	0.71073 Å	0.71073 Å
Crystal system	Triclinic	Triclinic
Space group	*P1* – No. 1	*P-1* – No. 2
a	13.0653(12) Å	13.0653(12) Å
b	13.2970(13) Å	13.2970(13) Å
c	18.7535(16) Å	18.7535(16) Å
α	94.498(3)°	94.498(3)°
β	90.881(3)°	90.881(3)°
γ	101.071(3)°	101.071(3)°
Volume	3186.0(5) $Å^3$	3186.0(5) $Å^3$
Z	2	2
Density (calculated)	1.512 g/cm^3	1.502 g/cm^3
Absorption coefficient	0.468 mm^{-1}	0.467 mm^{-1}
F(000)	1494.0	1484.0
Crystal size	0.168×0.118×0.085 mm^3	0.168 × 0.118 × 0.085 mm^3
Theta range	3.13 to 56.84°	1.566 to 28.422°
Index ranges	−17≤h≤17,−17≤k≤17,−25≤l≤25	–17≤h≤17,–17≤k≤17,–25≤l≤25
Reflections collected	102597	102597
Independent reflections	30638 [R_{int} = 0.066, R_{sigma} = 0.076]	15929 [R_{int} = 0.072, R_{sigma} = 0.052]
Completeness/θ_{max}	100.0 %/ 25.24°	100.0%/ 25.24°
Absorption correction	Numerical	Numerical
Max./Min. Transmission	0.986 and 0.936	1.000 and 0.897
Refinement method	Full-matrix least-squares on F^2	Full-matrix least-squares on F^2
Data/restraints/parameters	30638/460/1668	15929/90/864
Goodness-of-fit on F^2	1.047	1.120
Final R indices [I>2σ(I)]	R_1 = 0.068, wR_2 = 0.138	R_1 = 0.087, wR_2 = 0.187
R indices (all data)	R_1 = 0.105, wR_2 = 0.156	R_1 = 0.113, wR_2 = 0.199
Largest diff. peak & hole	1.12 and -0.71 e.$Å^{-3}$	1.78 and –0.74 e.$Å^{-3}$

Table S5. Crystal and Refinement Data for **[VO,Ca].**

	[VO,Ca] (b31b-No7)	**[VO,Ca] (b31b-No14)**
CCDC accession code	2219366	2240872
Empirical formula	$C_{26.61}H_{28.92}N_{2.31}O_{13}VCaF_6S_2$	$C_{26.67}H_{29}N_{2.33}O_{13}VCaF_6S_2$
Formula weight	858.27	859.31
Temperature	194(2) K	194(2) K
Wavelength	0.71073 Å	0.71073 Å
Crystal system	Monoclinic	Monoclinic
Space group	*Pc* – No. 7	*P2₁/c* – No. 14
a	9.1030(12) Å	9.1030(12) Å
b	33.158(4) Å	33.158(4) Å
c	11.7733(15) Å	11.7733(15) Å
α	90°	90°
β	103.6157(14)°	103.6157(14)°
γ	90°	90°
Volume	3453.7(8) $Å^3$	3453.7(8) $Å^3$
Z / Z′	2 / 2	4 / 1
Density (calculated)	1.651 g/cm^3	1.653 g/cm^3
Absorption coefficient	0.655 mm^{-1}	0.655 mm^{-1}
F(000)	1751.0	1753.0
Crystal size	0.304 × 0.188 × 0.132 mm^3	0.304 × 0.188 × 0.132 mm^3
Theta range	3.55 to 25.64°	3.55 to 25.64°
Index ranges	–11≤h≤11,–40≤k≤40,–14≤l≤14	–11≤h≤11,–40≤k≤40,–14≤l≤14
Reflections collected	42091	42026
Independent reflections	12967 [R_{int} = 0.052, R_{sigma} = 0.061]	6494 [R_{int} = 0.057, R_{sigma} = 0.040]
Completeness/θ_{max}	99.7%/25.24°	99.7%/25.24°
Absorption correction	Multi-scan	Multi-scan
Max./Min. Transmission	0.745 and 0.659	0.745 and 0.659
Refinement method	Full-matrix least-squares on F^2	Full-matrix least-squares on F^2
Data/restraints/parameters	12967/217/1096	6494/1272/802
Goodness-of-fit on F^2	1.018	1.125
Final R indices [I>2σ(I)]	R_1 = 0.064, wR_2 = 0.148	R_1 = 0.071, wR_2 = 0.141
R indices (all data)	R_1 = 0.104, wR_2 = 0.173	R_1 = 0.095, wR_2 = 0.152
Largest diff. peak & hole	0.91 and –0.72 $eÅ^{-3}$	0.69 and –0.71 $eÅ^{-3}$

Table S6. Selected bond lengths and interatomic distances in Å for the two alternative refinements **a04d-No1** and **a04d-No2** of the structure of **[VO,Na]**.

Structure code	**a04d-No1**	**a04d-No2**
CCDC accession code	2219365	2243380
Space group	*P1* (No. 1)	*P-1* (No. 2)
C.N. of M^{n+}	8	8
$d_{V\text{-}Oxo}$ [a]	1.595(7)	1.596(3)
$d_{V\cdots M}$ [a]	3.532(4)	3.530(2)
$d_{O\cdots O}$ [a]	2.603(12)	2.604(4)
$d_{V\text{-}N1}$ [a]	2.034(10)	2.037(4)
$d_{V\text{-}N2}$ [a]	2.058(11)	2.050(4)
$d_{V\text{-}O1}$ [a]	1.932(8)	1.930(3)
$d_{V\text{-}O2}$ [a]	1.920(8)	1.925(3)
$d_{Na\text{-}O1}$ [a]	2.482(9)	2.490(3)
$d_{Na\text{-}O2}$ [a]	2.509(9)	2.496(3)

[a] Average values of the interatomic distances were calculated as the arithmetic mean of the values for the four (**a04d-No1**) or two (**a04d-No2**) independent molecular species present in the asymmetric unit. The stated e.s.d.'s on these distances are taken as the larger of the individual values in the refined data for the independent molecular species.

Table S7. Selected bond lengths and interatomic distances in Å for the two alternative refinements **b31b-No14** and **b31b-No7** of the structure of **[VO,Ca]**.

Structure code	**b31b-No7**	**b31b-No14**
CCDC accession code	2219366	2240872
Space group	*Pc* (No. 7)	$P2_1/c$ (No. 14)
C.N. of M^{n+}	8	8
$d_{V\text{-}Oxo}$	1.589(10) [a]	1.583(3)
$d_{V\cdots M}$	3.524(4) [a]	3.524(1)
$d_{O\cdots O}$	2.580(15) [a]	2.583(5)
$d_{V\text{-}N1}$	2.060(15) [a]	2.052(4)
$d_{V\text{-}N2}$	2.050(14) [a]	2.058(4)
$d_{V\text{-}O1}$	1.934(10) [a]	1.934(3)
$d_{V\text{-}O2}$	1.951(11) [a]	1.952(3)
$d_{Ca\text{-}O1}$	2.448(11) [a]	2.450(3)
$d_{Ca\text{-}O2}$	2.455(10) [a]	2.454(3)

[a] Average values of the interatomic distances for **b31b-No7** were calculated as the arithmetic mean of the values for the two independent molecular species present in the asymmetric unit. The stated e.s.d.'s on these distances are taken as the larger of the individual values in the refined data for the independent molecular species.

References

[1] (a) Horwitz, C. P.; Ciringh, Y. Synthesis and electrochemical properties of oxo-bridged manganese dimers incorporating alkali and alkaline earth cations. *Inorg. Chim. Acta* **1994,** *225*, 191-200. (b) Horwitz, C. P.; Ciringh, Y.; Weintraub, S. T. Formation pathway of a Mn(IV),Mn(IV) bis(μ-oxo) dimer that incorporates alkali and alkaline earth cations and electron transfer properties of the dimer. *Inorg. Chim. Acta* **1999,** *294*, 133-139.

[2] Kanady, J. S.; Tsui, E. Y.; Day, M. W.; Agapie, T. A Synthetic Model of the Mn_3Ca Subsite of the Oxygen-Evolving Complex in Photosystem II. *Science* **2011,** *333*, 733-736.

[3] Buss, J. A.; VanderVelde, D. G.; Agapie, T. Lewis Acid Enhancement of Proton Induced CO_2 Cleavage: Bond Weakening and Ligand Residence Time Effects. *J. Am. Chem. Soc.* **2018,** *140*, 10121-10125.

[4] (a) Matsunaga, S.; Shibasaki, M. Multimetallic Schiff base complexes as cooperative asymmetric catalysts. *Synthesis* **2013,** *45*, 421-437. (b) Matsunaga, S.; Shibasaki, M. Recent advances in cooperative bimetallic asymmetric catalysis: dinuclear Schiff base complexes. *Chem. Commun.* **2014,** *50*, 1044-1057.

[5] (a) Deacy, A. C.; Moreby, E.; Phanopoulos, A.; Williams, C. K. Co(III)/Alkali-Metal(I) Heterodinuclear Catalysts for the Ring-Opening Copolymerization of CO_2 and Propylene Oxide. *J. Am. Chem. Soc.* **2020,** *142*, 19150-19160. (b) Lindeboom, W.; Fraser, D. A. X.; Durr, C. B.; Williams, C. K. Heterodinuclear Zn(II), Mg(II) or Co(III) with Na(I) Catalysts for Carbon Dioxide and Cyclohexene Oxide Ring Opening Copolymerizations. *Chem. - Eur. J.* **2021,** *27*, 12224-12231.

[6] Barlow, J. M.; Ziller, J. W.; Yang, J. Y. Inhibiting the Hydrogen Evolution Reaction (HER) with Proximal Cations: A Strategy for Promoting Selective Electrocatalytic Reduction. *ACS Catal.* **2021,** *11*, 8155-8164.

[7] Tsui, E. Y.; Agapie, T. Reduction potentials of heterometallic manganese-oxido cubane complexes modulated by redox-inactive metals. *Proc. Nat. Acad. Sci. U.S.A.* **2013,** *110*, 10084-10088.

[8] (a) Reath, A. H.; Ziller, J. W.; Tsay, C.; Ryan, A. J.; Yang, J. Y. Redox Potential and Electronic Structure Effects of Proximal Nonredox Active Cations in Cobalt Schiff Base Complexes. *Inorg. Chem.* **2017,** *56*, 3713-3718. (b) Kang, K.; Fuller, J.; Reath, A. H.; Ziller, J. W.; Alexandrova, A. N.; Yang, J. Y. Installation of internal electric fields by non-redox active cations in transition metal complexes. *Chem. Sci.* **2019,** *10*, 10135-10142.

[9] Shannon, R. D. Revised effective ionic radii and systematic studies of interatomic distances in halides and chalcogenides. *Acta Cryst. A* **1976,** *32*, 751-767.

[10] Perrin, D. D. *Ionisation Constants of Inorganic Acids and Bases in Aqueous Solution*. Pergamon Press: New York, 1982; pp. 180.

[11] Fukuzumi, S.; Ohkubo, K. Quantitative evaluation of Lewis acidity of metal ions derived from the g values of ESR spectra of superoxide: metal ion complexes in relation to the promoting effects in electron transfer reactions. *Chem. - Eur. J.* **2000,** *6*, 4532-4535

[12] Gaffen, J. R.; Bentley, J. N.; Torres, L. C.; Chu, C.; Baumgartner, T.; Caputo, C. B. A Simple and Effective Method of Determining Lewis Acidity by Using Fluorescence. *Chem* **2019,** *5*, 1567-1583

[13] Kumar, A.; Blakemore, J. D. On the Use of Aqueous Metal-Aqua pK_a Values as a Descriptor of Lewis Acidity. *Inorg. Chem.* **2021,** *60*, 1107-1115.

[14] Golwankar, R. R.; Curry, T. D., II; Paranjothi, C. J.; Blakemore, J. D. Molecular Influences on the Quantification of Lewis Acidity with Phosphine Oxide Probes. *Inorg. Chem.* **2023**, doi: 10.1021/acs.inorgchem.3c00084.

[15] Langeslay, R. R.; Kaphan, D. M.; Marshall, C. L.; Stair, P. C.; Sattelberger, A. P.; Delferro, M. Catalytic Applications of Vanadium: A Mechanistic Perspective. *Chem. Rev.* **2019,** *119*, 2128-2191.

[16] (a) Romakh, V. B.; Kozlov, Y. N.; Süss-Fink, G.; Shul'pin, G. B. The Kinetics and Mechanism of Oxidation of Isopropanol with the Hydrogen Peroxide-Vanadate Ion-Pyrazine-2-carboxylic Acid System. *Russ. J. Phys. Chem. A* **2007,** *81*, 1221-1229. (b) Maeda, Y.; Kakiuchi, N.; Matsumura, S.; Nishimura, T.; Kawamura, T.; Uemura, S. Oxovanadium Complex-Catalyzed Aerobic Oxidation of Propargylic Alcohols. *J. Org. Chem.* **2002,** *67*, 6718-6724.

[17] Digwal, C. S.; Yadav, U.; Ramya, P. V. S.; Sana, S.; Swain, B.; Kamal, A. Vanadium-Catalyzed Oxidative C(CO)–C(CO) Bond Cleavage for C–N Bond Formation: One-Pot Domino Transformation of 1,2-Diketones and Amidines into Imides and Amides. *J. Org. Chem.* **2017,** *82*, 7332-7345.

[18] Tang, J.; Yao, P.-F.; Xu, X.-L.; Li, H.-Y.; Huang, F.-P.; Nie, Q.-Q.; Luo, M.-Y.; Yu, Q.; Bian, H.-D. Asymmetric Catalytic Sulfoxidation by a Novel V^{IV}_8 Cluster Catalyst in the Presence of Serum Albumin: A Simple and Green Oxidation System. *RSC Advances* **2016,** *6*, 44154-44162.

[19] (a) Chapman, G.; Nicholas, K. M. Vanadium-catalyzed deoxydehydration of glycols. *Chem. Commun.* **2013,** *49*, 8199-8201. (b) Gopaladasu, T. V.; Nicholas, K. M. Carbon Monoxide (CO)- and Hydrogen-Driven, Vanadium-Catalyzed Deoxydehydration of Glycols. *ACS Catalysis* **2016,** *6*, 1901-1904. (c) Aksanoglu, E.; Lim, Y. H.; Bryce, R. A. Direct Deoxydehydration of Cyclic trans-Diol Substrates: An Experimental and Computational Study of the Reaction Mechanism of Vanadium(V)-based Catalysis. *ChemSusChem* **2021,** *14*, 1545-1553. (d) Kwok, K. M.; Choong, C. K. S.; Ong, D. S. W.; Ng, J. C. Q.; Gwie, C. G.; Chen, L.; Borgna, A. Hydrogen-Free Gas-Phase Deoxydehydration of 2,3-Butanediol to Butene on Silica-Supported Vanadium Catalysts. *ChemCatChem* **2017,** *9*, 2443-2447. (e) Petersen, A. R.; Nielsen, L. B.; Dethlefsen, J. R.; Fristrup, P. Vanadium-Catalyzed Deoxydehydration of Glycerol Without an External Reductant. *ChemCatChem* **2018,** *10*, 769-778

[20] (a) Chen, K.; Bell, A. T.; Iglesia, E. Kinetics and Mechanism of Oxidative Dehydrogenation of Propane on Vanadium, Molybdenum, and Tungsten Oxides. *J. Phys. Chem. B* **2000,** *104*, 1292-1299. (b) Cheng, M.-J.; Chenoweth, K.; Oxgaard, J.; van Duin, A.; Goddard, W. A. Single-Site Vanadyl Activation, Functionalization, and Reoxidation Reaction Mechanism for Propane Oxidative Dehydrogenation on the Cubic V_4O_{10} Cluster. *J. Phys. Chem. C* **2007,** *111*, 5115-5127.

[21] Chakraborty, S.; Petel, B. E.; Schreiber, E.; Matson, E. M. Atomically Precise Vanadium-Oxide Clusters. *Nanoscale Adv.* **2021,** *3*, 1293-1318.

[22] (a) Li, F.; VanGelder, L. E.; Brennessel, W. W.; Matson, E. M. Self-Assembled, Iron-Functionalized Polyoxovanadate Alkoxide Clusters. *Inorg. Chem.* **2016,** *55*, 7332-7334. (b)

Li, F.; Carpenter, S. H.; Higgins, R. F.; Hitt, M. G.; Brennessel, W. W.; Ferrier, M. G.; Cary, S. K.; Lezama-Pacheco, J. S.; Wright, J. T.; Stein, B. W.; Shores, M. P.; Neidig, M. L.; Kozimor, S. A.; Matson, E. M. Polyoxovanadate–Alkoxide Clusters as a Redox Reservoir for Iron. *Inorg. Chem.* **2017,** *56*, 7065-7080.

[23] (a) VanGelder, L. E.; Brennessel, W. W.; Matson, E. M. Tuning the redox profiles of polyoxovanadate-alkoxide clusters via heterometal installation: toward designer redox Reagents. *Dalton Trans.* **2018,** *47*, 3698-3704. (b) Meyer, R. L.; Brennessel, W. W.; Matson, E. M. Synthesis of a gallium-functionalized polyoxovanadate-alkoxide cluster: Toward a general route for heterometal installation. *Polyhedron* **2018,** *156*, 303-311.

[24] Meyer, R. L.; Anjass, M. H.; Petel, B. E.; Brennessel, W. W.; Streb, C.; Matson, E. M. Electronic Consequences of Ligand Substitution at Heterometal Centers in Polyoxovanadium Clusters: Controlling the Redox Properties through Heterometal Coordination Number. *Chem.-Eur. J.* **2020,** *26*, 9905-9914.

[25] (a) Krogman, J. P.; Foxman, B. M.; Thomas, C. M. Activation of CO_2 by a Heterobimetallic Zr/Co Complex. *J. Am. Chem. Soc.* **2011,** *133*, 14582-14585. (b) Kuppuswamy, S.; Powers, T. M.; Krogman, J. P.; Bezpalko, M. W.; Foxman, B. M.; Thomas, C. M. Vanadium–iron complexes featuring metal–metal multiple bonds. *Chem. Sci.* **2013,** *4*, 3557-3565. (c) Sharma, P.; Pahls, D. R.; Ramirez, B. L.; Lu, C. C.; Gagliardi, L. Multiple Bonds in Uranium–Transition Metal Complexes. *Inorg. Chem.* **2019,** *58*, 10139-10147.

[26] (a) Kanso, H.; Clarke, R. M.; Kochem, A.; Arora, H.; Philouze, C.; Jarjayes, O.; Storr, T.; Thomas, F. Effect of Distortions on the Geometric and Electronic Structures of One-Electron Oxidized Vanadium(IV), Copper(II), and Cobalt(II)/(III) Salen Complexes. *Inorg. Chem.* **2020,** *59*, 5133-5148. (b) Kolawole, G. A.; Patel, K. S. The stereochemistry of oxovanadium(IV) complexes derived from salicylaldehyde and polymethylenediamines. *J. Chem. Soc. Dalton Trans.* **1981,** 1241-1245.

[27] Ballhausen, C. J.; Gray, H. B. The Electronic Structure of the Vanadyl Ion. *Inorg. Chem.* **1962,** *1*, 111-122.

[28] Selbin, J. The Chemistry of Oxovanadium(IV). *Chem. Rev.* **1965,** *65*, 153-175.

[29] Selbin, J. Oxovanadium(IV) Complexes. *Coord. Chem. Rev.* **1966,** *1*, 293-314.

[30] (a) Tsuchida, E.; Yamamoto, K.; Oyaizu, K.; Iwasaki, N.; Anson, F. C. Electrochemical Investigations of the Complexes Resulting from the Acid-Promoted Deoxygenation and Dimerization of (N,N'-Ethylenebis(salicylideneaminato))oxovanadium(IV). *Inorg. Chem.* **1994,** *33*, 1056-1063. (b) Larin, G. M.; Zelentsov, V. V.; Rakitin, Y. V.; Dyatkina, M. E. EPR study of the effect of remote substituents in ligands on the nature of the metal-ligand chemical bond in vanadyl complexes. *Zh. Neorg. Khim.* **1972,** *17*, 2136-2139.

[31] (a) Van Staveren, C. J.; Van Eerden, J.; Van Veggel, F. C. J. M.; Harkema, S.; Reinhoudt, D. N. Cocomplexation of neutral guests and electrophilic metal cations in synthetic macrocyclic hosts. *J. Am. Chem. Soc.* **1988,** *110*, 4994-5008. (b) Van Veggel, F. C. J. M.; Harkema, S.; Bos, M.; Verboom, W.; Van Staveren, C. J.; Gerritsma, G. J.; Reinhoudt, D. N. Metallomacrocycles: synthesis, x-ray structure, electrochemistry, and ESR spectroscopy of mononuclear and heterodinuclear complexes. *Inorg. Chem.* **1989,** *28*, 1133-1148.

[32] (a) Zanello, P.; Cinquantini, A.; Guerriero, P.; Tamburini, S.; Vigato, P. A. Electrochemical behavior of acyclic and macrocyclic complexes of nickel(II), copper(II) and uranyl(VI). *Inorg. Chim. Acta* **1986,** *117*, 91-96 (b) Brianese, N.; Casellato, U.; Tamburini, S.; Tomasin,

P.; Vigato, P. A. Asymmetric compartmental macrocyclic ligands and related mononuclear and hetero-dinuclear complexes with d- and/or f-metal ions. *Inorg. Chim. Acta* **1999,** *293*, 178-194. (c) Vigato, P. A.; Tamburini, S. The challenge of cyclic and acyclic Schiff bases and related derivatives. *Coord. Chem. Rev.* **2004,** *248*, 1717-2128.

[33] Kumar, A.; Lionetti, D.; Day, V. W.; Blakemore, J. D. Trivalent Lewis Acidic Cations Govern the Electronic Properties and Stability of Heterobimetallic Complexes of Nickel. *Chem. – Eur. J.* **2018,** *24*, 141-149.

[34] Golwankar, R. R.; Kumar, A.; Day, V. W.; Blakemore, J. D. Revealing the Influence of Diverse Secondary Metal Cations on Redox-Active Palladium Complexes. *Chem. – Eur. J.* **2022,** *28*, e202200344.

[35] Rowe, R. A.; Jones, M. M. Vanadium(IV) oxy(acetylacetonate). *Inorg. Synth.* **1957,** *5*, 113-116.

[36] Addison, A. W.; Rao, T. N.; Reedijk, J.; van Rijn, J.; Verschoor, G. C. Synthesis, Structure, and Spectroscopic Properties of Copper(II) Compounds Containing Nitrogen–Sulphur Donor Ligands; The Crystal and Molecular Structure of Aqua[1,7-bis(N-methylbenzimidazol-2′-yl)-2,6-dithiaheptane]copper(II) perchlorate. *J. Chem. Soc., Dalton Trans.* **1984,** 1349-1356.

[37] Blackman, A. G.; Schenk, E. B.; Jelley, R. E.; Krenske, E. H.; Gahan, L. R. Five-coordinate Transition Metal Complexes and the Value of τ_5: Observations and Caveats. *Dalton Transactions* **2020,** *49*, 14798-14806.

[38] Marsh, R. Some Thoughts on Choosing the Correct Space Group. *Acta Cryst. B* **1995,** *51*, 897-907.

[39] Marsh, R., *P1* or *P-1*? Or Something Else? *Acta Cryst. B* **1999,** *55*, 931-936.

[40] Pauling, L. *The Nature of the Chemical Bond*. Cornell University Press: Ithaca, NY, 1960.

[41] Baran, E. J. Review: spectroscopic studies of oxovanadium coordination compounds. *J. Coord. Chem.* **2001,** *54*, 215-238.

[42] Kumar, A.; Lionetti, D.; Day, V. W.; Blakemore, J. D. Redox-Inactive Metal Cations Modulate the Reduction Potential of the Uranyl Ion in Macrocyclic Complexes. *J. Am. Chem. Soc.* **2020,** *142*, 3032-3041.

[43] (a) Pedersen, C. J. Cyclic polyethers and their complexes with metal salts. *J. Am. Chem. Soc.* **1967,** *89*, 7017-7036. (b) Blakemore, J. D.; Chitta, R.; D'Souza, F. Synthesis and study of crown ether-appended boron dipyrrin chemosensors for cation detection. *Tetrahedron Letters* **2007,** *48*, 1977-1982. (c) van der Ham, A.; Hansen, T.; Lodder, G.; Codée, J. D. C.; Hamlin, T. A.; Filippov, D. V. Computational and NMR Studies on the Complexation of Lithium Ion to 8-Crown-4. *ChemPhysChem* **2019,** *20*, 2103-2109.

[44] (a) Bjorklund, J. L.; Pyrch, M. M.; Basile, M. C.; Mason, S. E.; Forbes, T. Z. Actinyl-cation interactions: experimental and theoretical assessment of $[Np(VI)O_2Cl_4]^{2-}$ and $[U(VI)O_2Cl_4]^{2-}$ systems. *Dalton Trans.* **2019,** *48*, 8861-8871. (b) Bazhina, E. S.; Aleksandrov, G. G.; Kiskin, M. A.; Efimov, N. N.; Ugolkova, E. A.; Korlyukov, A. A.; Nikitin, O. M.; Magdesieva, T. V.; Minin, V. V.; Sidorov, A. A.; Miller, J. S.; Eremenko, I. L. Synthesis, crystal structure and spin exchange coupling in polynuclear carboxylates with $\{Li_2(VO)_2\}$ metal core. *Polyhedron* **2017,** *137*, 246-255. (c) Garwick, R. E.; Schreiber, E.; Brennessel, W. W.; McKone, J. R.; Matson, E. M. Surface ligands influence the selectivity

of cation uptake in polyoxovanadate–alkoxide clusters. *J. Mater. Chem. A* **2022,** *10*, 12070-12078.

[45] Chen, J.; Lee, Y.-M.; Davis, K. M.; Wu, X.; Seo, M. S.; Cho, K.-B.; Yoon, H.; Park, Y. J.; Fukuzumi, S.; Pushkar, Y. N.; Nam, W. A Mononuclear Non-Heme Manganese(IV)–Oxo Complex Binding Redox-Inactive Metal Ions. *J. Am. Chem. Soc.* **2013,** *135*, 6388-6391.

[46] Hong, S.; Lee, Y.-M.; Sankaralingam, M.; Vardhaman, A. K.; Park, Y. J.; Cho, K.-B.; Ogura, T.; Sarangi, R.; Fukuzumi, S.; Nam, W. A Manganese(V)–Oxo Complex: Synthesis by Dioxygen Activation and Enhancement of Its Oxidizing Power by Binding Scandium Ion. *J. Am. Chem. Soc.* **2016,** *138*, 8523-8532.

[47] Atzori, M.; Benci, S.; Morra, E.; Tesi, L.; Chiesa, M.; Torre, R.; Sorace, L.; Sessoli, R. Structural Effects on the Spin Dynamics of Potential Molecular Qubits. *Inorg. Chem.* **2018,** *57*, 731-740.

[48] Adão, P.; Maurya, M. R.; Kumar, U.; Avecilla, F.; Henriques, R. T.; Kusnetsov, M. L.; Pessoa, J. C.; Correia, I. Vanadium-salen and -salan Complexes: Characterization and Application in Oxygen-transfer Reactions. *Pure Appl. Chem.* **2009,** *81*, 1279-1296.

[49] King, A. E.; Nippe, M.; Atanasov, M.; Chantarojsiri, T.; Wray, C. A.; Bill, E.; Neese, F.; Long, J. R.; Chang, C. J. A Well-Defined Terminal Vanadium(III) Oxo Complex. *Inorg. Chem.* **2014,** *53*, 11388-11395.

[50] Hamilton, D. E. Reinvestigation of the Vanadium-oxygen Stretch in the IR Spectrum of bis[N-(4-chlorophenyl)salicylideneiminato]oxovanadium(IV). *Inorg. Chem.* **1991,** *30*, 1670-1671.

[51] Grant, C. V.; Geiser-Bush, K. M.; Cornman, C. R.; Britt, R. D. Probing the Molecular Geometry of Five-Coordinate Vanadyl Complexes with Pulsed ENDOR. *Inorg. Chem.* **1999,** *38*, 6285-6288.

[52] Weil, J. A.; Bolton, J. R. *Electron Paramagnetic Resonance: Elementary Theory and Practical Applications*. 2nd ed.; Wiley: Hoboken, NJ, 2007.

[53] Stoll, S.; Schweiger, A. EasySpin, a comprehensive software package for spectral simulation and analysis in EPR. *J. Magn. Res.* **2006,** *178*, 42-55.

[54] (a) Crans, D. C.; Smee, J. J.; Gaidamauskas, E.; Yang, L. The Chemistry and Biochemistry of Vanadium and the Biological Activities Exerted by Vanadium Compounds. *Chem. Rev.* **2004,** *104*, 849-902. (b) Yang, X.; Wang, K.; Lu, J.; Crans, D. C. Membrane transport of vanadium compounds and the interaction with the erythrocyte membrane. *Coord. Chem. Rev.* **2003,** *237*, 103-111.

[55] Amin, S. S.; Cryer, K.; Zhang, B.; Dutta, S. K.; Eaton, S. S.; Anderson, O. P.; Miller, S. M.; Reul, B. A.; Brichard, S. M.; Crans, D. C. Chemistry and Insulin-Mimetic Properties of Bis(acetylacetonate)oxovanadium(IV) and Derivatives. *Inorg. Chem.* **2000,** *39*, 406-416.

[56] Wüthrich, K. E.S.R. (Electron Spin Resonance) Investigation of VO^{2+} Complex Compounds in Aqueous Solution. II. *Helv. Chim. Acta* **1965,** *48*, 1012-1017.

[57] Chasteen, N. D., "Vanadyl(IV) EPR spin probes. Inorganic and Biochemical Aspects," in *Biol. Magn. Reson.*; Berliner, L. J., Reuben, J., Ed.; Plenum Press: New York, 1981; Chapter 2, Vol. 3, pp. 53-119.

[58] Dickson, F. E.; Petrakis, L. Application of electron spin resonance and electronic spectroscopy to the characterization of vanadium species in petroleum fractions. *Anal. Chem.* **1974,** *46*, 1129-1130.

[59] Smith, T. S.; LoBrutto, R.; Pecoraro, V. L. Paramagnetic spectroscopy of vanadyl complexes and its applications to biological systems. *Coord. Chem. Rev.* **2002,** *228*, 1-18

[60] Holyk, N. H. An Electron Paramagnetic Resonance Study of Model Oxovanadium(IV) Complexes in Aqueous Solution: Correlation of Magnetic Properties with Ligand Type and Metal Chelate Structure. M.S. Thesis, University of New Hampshire, Durham, NH, 1979.

[61] Savéant, J. M.; Costentin, C. *Elements of Molecular and Biomolecular Electrochemistry, An Electrochemical Approach to Electron Transfer Chemistry*. 2nd ed.; Wiley: Hoboken, NJ, 2019.

[62] Cornman, C. R.; Geiser-Bush, K. M.; Rowley, S. P.; Boyle, P. D. Structural and Electron Paramagnetic Resonance Studies of the Square Pyramidal to Trigonal Bipyramidal Distortion of Vanadyl Complexes Containing Sterically Crowded Schiff Base Ligands. *Inorg. Chem.* **1997,** *36*, 6401-6408.

[63] Kelsey, S. R.; Kumar, A.; Oliver, A. G.; Day, V. W.; Blakemore, J. D. Promotion and Tuning of the Electrochemical Reduction of Hetero- and Homobimetallic Zinc Complexes. *ChemElectroChem* **2021,** *8*, 2792-2802.

[64] Badger, R. M. A Relation between Internuclear Distances and Bond Force Constants. *J. Chem. Phys.* **1934,** *2*, 128-131.

[65] Fulmer, G. R.; Miller, A. J.; Sherden, N. H.; Gottlieb, H. E.; Nudelman, A.; Stoltz, B. M.; Bercaw, E.; Goldberg, K. I. NMR Chemical Shifts of Trace Impurities: Common Laboratory Solvents, Organics, and Gases in Deuterated Solvents Relevant to the Organometallic Chemist. *Organometallics.* **2010**, *29*, 2176-2179.

[66] Harris, R. K.; Becker, E. D.; Cabral De Menezes, S. M.; Goodfellow, R.; Granger, P. NMR nomenclature. Nuclear spin properties and conventions for chemical shifts (IUPAC recommendations 2001). *Pure Appl. Chem.* **2001,** *73*, 1795-1818

[67] Harris, R. K.; Becker, E. D.; Cabral De Menezes, S. M.; Granger, P.; Hoffman, R. E.; Zilm, K. W. Further conventions for NMR shielding and chemical shifts (IUPAC recommendations 2008). *Pure Appl. Chem.* **2008,** *80*, 59-84.

[68] APEX2, Version 2 User Manual, M86-E01078. Bruker Analytical X-ray Systems: Madison, WI, June 2006.

[69] SAINT Ver. 8.40A. Bruker Analytical X-ray Systems Inc.: Madison, WI, USA, 2022.

[70] SAINT. Ver. 8.34A. Bruker Analytical X-ray Systems: Madison, WI, June 2014.

[71] G. M. Sheldrick, SADABS (version 2008/1): Program for Absorption Correction for Data from Area Detector Frames, University of Göttingen, 2008.

[72] Sheldrick, G. M. SHELXT – Integrated Space-Group and Crystal-Structure Determination. *Acta Crystallogr., Sect. A: Found. Crystallogr.*, **2015**, *A71*, 3–8.

[73] Hübschle, C. B.; Sheldrick, G. M; Dittrich, B. ShelXle: a Qt Graphical User Interface for SHELXL. *J. Appl. Cryst.*, **2011**, *44*, 1281–1284.

[74] Pauling, L. *The Nature of the Chemical Bond.* Cornell University Press: Ithaca, NY, 1960.

[75] Jeffrey, G. A. *An Introduction to Hydrogen Bonding.* Oxford University Press: New York, NY, 1997. p. 12.

[76] https://journals.iucr.org/services/cif/hbonds.html

[77] Groom, C. R.; Bruno, I. J.; Lightfoot, M. P.; Ward, S. C. The Cambridge Structural Database. *Acta Cryst. B* **2016,** *72*, 171-179.

[78] (a) Schmitz, M.; Leininger, S.; Fan, J.; Arif, A.M.; Stang, P.J., CCDC 1170659: Experimental Crystal Structure Determination, 1999, database identifier: GULREK. (b) Schmitz, M.; Leininger, S.; Fan, J.; Arif, A.M.; Stang, P.J. *Organometallics*, **1999**, *18*, 4817-4824.

[79] (a) Mazloomi, Z.; Margalef, J.; Gil-Sepulcre, M.; Romero, N.; Albrecht, M.; Llobet, A.; Sala, X.; Pàmies, O.; Diéguez, M. CCDC 2003896: Experimental Crystal Structure Determination, **2020**, doi: 10.5517/ccdc.csd.cc2586th. (b) Mazloomi, Z.; Margalef, J.; Gil-Sepulcre, M.; Romero, N.; Albrecht, M.; Llobet, A.; Sala, X.; Pàmies, O.; Diéguez, M. *Inorg. Chem.* **2020,** *59*, 12337-12347.

[80] (a) Moelands, M. A. H.; Nijsse, S.; Folkertsma, E.; de Bruin, B.; Lutz, M.; Spek, A. L.; Klein Gebbink, R. J. M. CCDC 967066: Experimental Crystal Structure Determination, **2013**, doi: 10.5517/cc11g9ph. (b) Moelands, M. A. H.; Nijsse, S.; Folkertsma, E.; de Bruin, B.; Lutz, M.; Spek, A. L.; Klein Gebbink, R. J. M. *Inorg. Chem.* **2013,** *52*, 7394-7410.